ISSN 2458-973X

JSCMT

Journal of Sustainable Construction Materials and Technologies

Volume 7
Issue 4
Year 2022

YTÜ PRESS

www.jscmt.yildiz.edu.tr

Journal of Sustainable Construction Materials and Technologies
Web page info: https://jscmt.yildiz.edu.tr

Editor In Chief

Prof. Dr. Orhan CANPOLAT
Yildiz Technical University, Türkiye

Assistant Editor

Ekin Paylan
Kare Publishing, Türkiye

Contact

Journal of Sustainable Construction
Materials and Technologies (JSCMT)
Yildiz Technical University
Civil Engineering Department, 34220 Esenler
Istanbul – Türkiye
Web: https://dergipark.org.tr/en/pub/jscmt
E-mail: jscmt@yildiz.edu.tr

Journal of Sustainable Construction Materials and Technologies
Web page info: https://jscmt.yildiz.edu.tr

JSCMT
Journal of Sustainable Construction Materials and Technologies

Journal of Sustainable Construction Materials and Technologies
Web page info: https://jscmt.yildiz.edu.tr

Journal of Sustainable Construction Materials and Technologies

Journal of Sustainable Construction Materials and Technologies
Web page info: https://jscmt.yildiz.edu.tr

JSCMT
Journal of Sustainable Construction Materials and Technologies

TABLE OF CONTENTS

Journal of Sustainable Construction Materials and Technologies
Web page info: https://jscmt.yildiz.edu.tr

Review Articles

Journal of Sustainable Construction Materials and Technologies
Web page info: https://jscmt.yildiz.edu.tr
DOI: 10.47481/jscmt.1163963

JSCMT
Journal of Sustainable Construction Materials and Technologies

Research Article

Effects of single-walled carbon nanotubes and steel fiber on recycled ferrochrome filled electrical conductive mortars

Heydar DEHGHANPOUR[*,1], Fatih DOĞAN[2], Serkan SUBAŞI[3], Muhammed MARAŞLI[3]

[1]*Fibrobeton Company, R&D Center, Düzce, Türkiye*
[2]*Munzur University, Rare Earth Elements Application and Research Center, Tunceli, Türkiye*
[3]*Department of Civil Engineering, Düzce University Faculty of Engineering, Düzce, Türkiye*

ARTICLE INFO

Article history
Received: 18 August 2022
Revised: 11 October 2022
Accepted: 14 October 2022

Key words:
Carbon nanotube, conductive mortars, dynamic resonance, ferrochrome, SWCNT

ABSTRACT

The production of electrically conductive concrete was introduced years ago among construction materials, generally for anti-icing. The present study investigates the electrical, mechanical, dynamic, and microstructural properties of recycled ferrochrome filled cementitious mortars containing single-walled carbon nanotubes (SWCNTs) and steel fiber. Within the scope of the study, a total of 5 different mixtures were obtained. 7, 14, and 28-day non-destructive and 28-day compressive and bending tests of cementitious conductive mortars obtained from five different mixtures were performed. The two-point uniaxial method was used to determine the electrical conductivity properties of the samples. The damping ratio of the samples was obtained by performing dynamic resonance tests. Ultrasound pulse velocity (UPV) and Leeb hardness tests were performed as other non-destructive testing methods. Microstructure analysis at the interfaces of conductive concrete samples was characterized by scanning electron microscopy (SEM), EDS (Energy-Dispersive X-ray Spectroscopy), and X-ray diffraction (XRD). The results showed a logical agreement when comparing their mechanical, physical, and dynamic properties. When SWCNT is used with steel fiber, the conductive mortar samples exhibited good conductivity, while their compressive and bending strengths turned below.

Cite this article as: Dehghanpour, H., Doğan, F., Subaşi, S., & Maraşli, M. (2022). Effects of single-walled carbon nanotubes and steel fiber on recycled ferrochrome filled electrical conductive mortars. *J Sustain Const Mater Technol*, 7(4), 250–265.

1. INTRODUCTION

Cementitious composite materials show great interest in structural elements and large areas such as building facade cladding due to their relatively low cost and easy applicability [1, 2]. Recently, not only the mechanical properties of such applications in modern facade cladding but also their electrical properties have been the subject of research [3]. For some reason, it is preferred to use fine aggregate in building facade cladding. The most important reasons are that they are shell elements and the application of the spraying method [4]. Apart from spraying methods, it is preferred to use fine aggregate in ultra-high-performance concrete (UHPC) shells produced for facade cladding [5, 6]. Therefore, the use of conductive additives in a more suitable type and dosage should be investigated to improve the electrical conductivity properties in this building elements mixture.

***Corresponding author.**
*E-mail address: heydar.dehghanpour@fibrobeton.com.tr

Since 1965 [7], the discovery of electrically conductive cementitious materials, various research have been carried out in this field. Conductive cementitious materials are used in self-sensing [8] materials of buildings, electromagnetic radiation reflectors for electromagnetic interference shielding [9], and resistance materials in self-heating [10] cementitious systems. Electrically conductive cementitious materials have also been proposed as an alternative anti-icing method in snowy weather [11]. Conventional cementitious materials are known to have high electrical resistivity. According to the literature, the resistivity of concrete under room conditions has been reported as 6.54×10^5–11.4×10^5 Ω-cm [12], the resistivity of saturated concrete as 10^6 Ω-cm and the resistivity of thoroughly dried concrete as 10^9 Ω-cm [13, 14]. Using different conductive additives, the researchers even managed to reduce the resistivity values of cementitious materials to just below 100 Ω-cm [12, 13, 15]. Depending on the materials' type, dosage, and conductivity properties, it may vary.

Materials with good conductivity, such as steel fiber [16, 17], carbon fiber [18, 19], erosion wire [20], steel shaving [16], graphite powder [13, 21], carbon nanotube [22], carbon black [20] and graphene [23] can be used to increase the electrical conductivity of cementitious materials. Figure 1 represents the internal structure of electrically conductive concrete [24]. The study used various fibers and nanocarbon black (NCB) materials to provide electrical conductivity. The fibers are randomly placed between aggregates forming a complex network and acting as a bridge for electric current. Cement paste is defined as a matrix element for fibers between aggregates. It has been reported that the electrical conductivity of the fibers increased by combining cement paste with conductive materials in powder form. The NCB fills the intergranular spaces, thus increasing the interface area between the conductive fiber and the matrix. Therefore, it is ensured that the electrical current passes more quickly.

The electrical resistivity of cementitious materials can be measured using a two-point uniaxial, four-probe, or Wenner probe and C1760-12 ASTM [25]. The two-point uniaxial measurement method is the widely used method. In this method, the geometry of the sample can be cylindrical, prismatic, or cube-shaped. The four-probe method is often used to measure the surface resistivity of cylindrical or prismatic specimens. In this method, resistance is measured with four-probe equipment. A voltage difference is applied between the two internal probes, and the electrical current is measured between the two external probes. In the C1760-12 ASTM test method, the electrical resistivity of the hardened saturated cylinder concrete sample is obtained based on the diffusion of chloride ions. This is a two-point-uniaxial test method, but the resistivity may be a little low due to the chloride ion permeability.

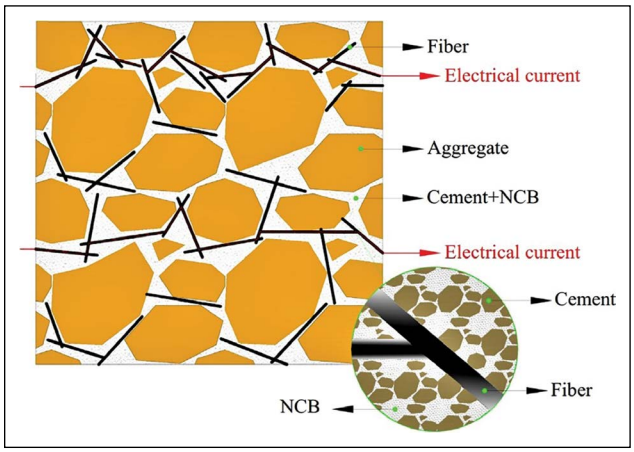

Figure 1. Schematic view of the internal structure of conductive concrete [24].

In the literature, there are many studies on the evaluation of the above-mentioned conductive additives in electrically conductive cementitious materials. However, there are still gaps in the literature on increasing the conductivity of cement and aggregate composition, which are matrix elements in concrete. Also, there are many studies on the evaluation of recycled aggregate and slag materials in concrete [26–28]. The present study investigates the electrical, mechanical, physical, and microstructural properties of electrical conductive mortars containing 100% recycled ferrochrome sand. SWCNT and steel fiber was used as nano and macro-scale conductive additives, respectively. Microstructures of SS-filled, FRC-filled, and FRC-CNT conductive concrete samples were characterized by scanning electron microscopy (SEM), EDS, and X-ray diffraction (XRD). The effects of composite materials on strength were analyzed.

2. MATERIAL AND METHODS

2.1. Used Material

100% silica sand was used as the filling material in the reference mixture, and 100% ferrochrome was used in all other mixtures. The specific gravity of silica sand and ferrochrome sand used were 2.55 and 3.33, respectively. CEM II-42.5 R white cement, preferred in facade cladding, was used as a binder. As a pozzolanic additive material, calcined kaolin was preferred in equal proportions in all mixtures. The chemical composition of Cement, Silica sand, and Calcined kaolin is given in Table 1, and the EDS analysis result of ferrochrome aggregate is shown in Table 2. The particle size ranges of aggregate, cement, and calcined kaolin were compared in Figure 2a, and images of SWCNT and steel fiber used are shown in Figure 2b and Figure 2c, respectively. Stainless steel fiber with a diameter of 80 micrometers and a length of 12 mm was used as the conductive fiber. With a length/diameter ratio of about 1000, SWCNT was added as the nano-sized conductive material. Since the SWCNT used is dispersed in a carboxymethyl cel-

Table 1. Chemical composition of cement, silica sand, and calcined kaolin

Component	Cement (%)	Silica sand (%)	Calcined kaolin (%)
SiO_2	17.460	98.570	59.78
Al_2O_3	3.2700	0.0000	10.23
Fe_2O_3	0.2100	0.1700	0.4400
CaO	63.0400	0.2900	9.9100
MgO	1.6700	0.0000	1.5900
K_2O	0.3400	0.0.16	0.9000
Na_2O	0.3000	0.0000	0.0500
SO_3	3.0200	0.0000	1.2500
P_2O_5	0.0400	0.0100	0.0400
TiO_2	0.0900	0.1200	0.1500
Cr_2O_3	0.0021	0.0137	0.0186
Mn_2O_3	0.0042	0.0029	0.0077
LOI	11.000	0.3900	16.240

lulose-based solution with a ratio of 0.4/1000, more water was used than necessary in the mixtures, according to the preferred 0.3% SWCNT dosage. Polycarboxylate-based superplasticizer was used to ensure adequate workability in all mixtures.

Table 2. EDS analysis result of ferrochrome aggregate

Element	Weight %	Weight % Sigma	Atomic %
O	41.85	0.95	49.66
C	12.08	0.49	19.1
Mg	16.7	0.66	13.04
Al	9.39	0.68	6.61
Cr	0	7.14	0
Si	14.29	1.02	9.66
Fe	5.68	1.12	1.93
Total	100		100

Details of materials used in electrically conductive mortars are given in Table 3. A reference mix is a regular premix mortar consisting of a filler, binder, pozzolanic, water, and plasticizer and is defined as the matrix for other mixtures. In the premix mixture, all dry ingredients are put into the mixer and mixed for 90 seconds; then plasticizer is added with water, remixed for 90 seconds, and placed in molds. In the mixtures containing SWCNT, the water of the solution with SWCNT was taken as the basis instead of mains water. In this case, approximately 88% of water usage will be higher than the reference mixture, and serious adverse effects

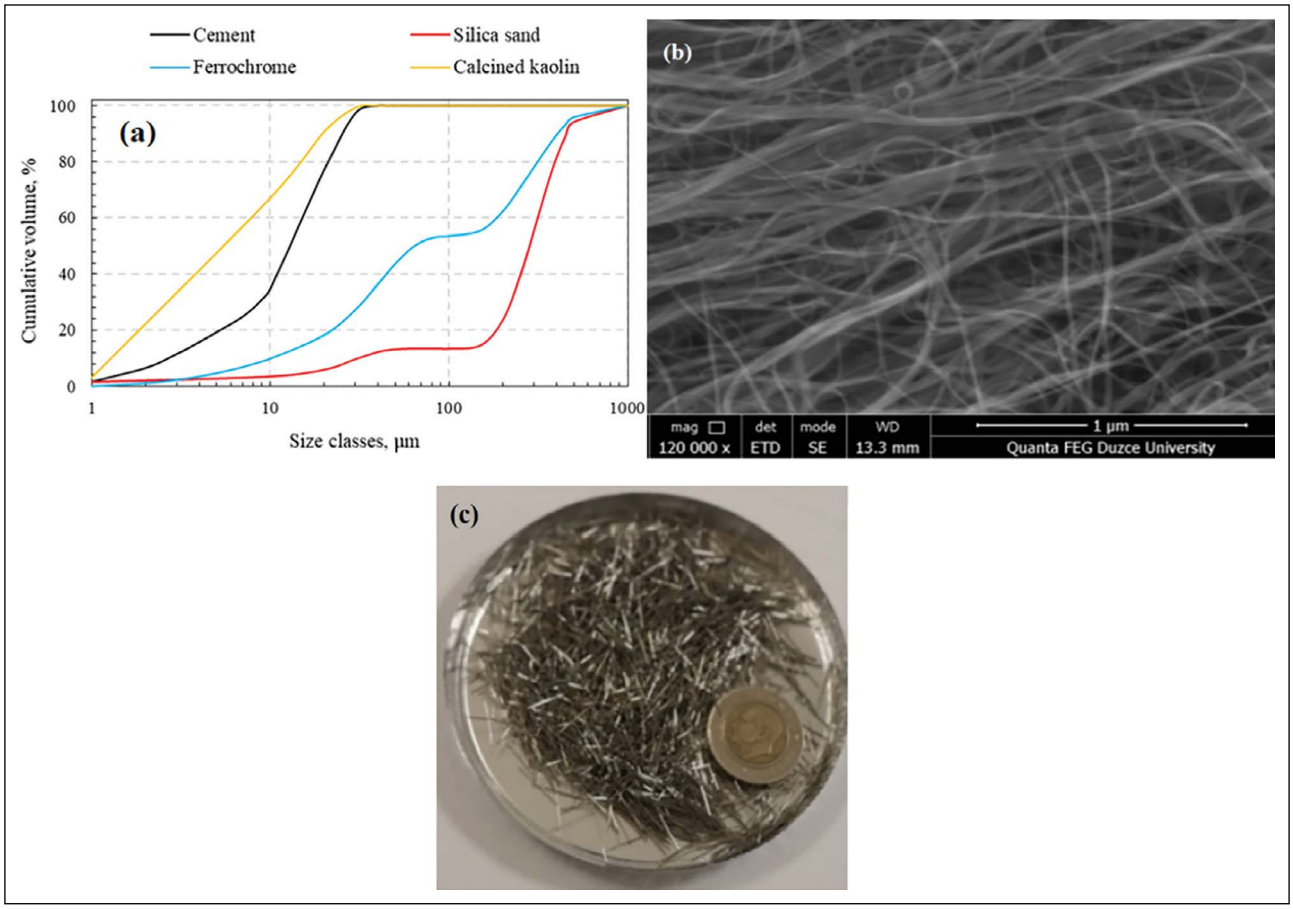

Figure 2. Grain size analysis curves of cement and filling materials **(a)**, SEM image of SWCNT **(b)**, and Steel fiber image **(c)**.

Table 3. Component ratios in electrically conductive mortars

No	Code	Silica sand (g)	Ferrochrome (g)	Cement (g)	Calcined kaolin (CK) (g)	Steel fiber (g)	Su (g)	SWCNT (%)	Superplasticizer (g)
1	SS (Ref)	1350	…	500	50	…	220	…	4
2	FRC	…	1350	500	50	…	220	…	4
3	FRC-SF	…	1245	500	50	105	220	…	4
4	FRC-CNT	…	1350	500	50	…	413	0.3	4
5	FRC-SF-CNT	…	1245	500	50	105	413	0.3	4

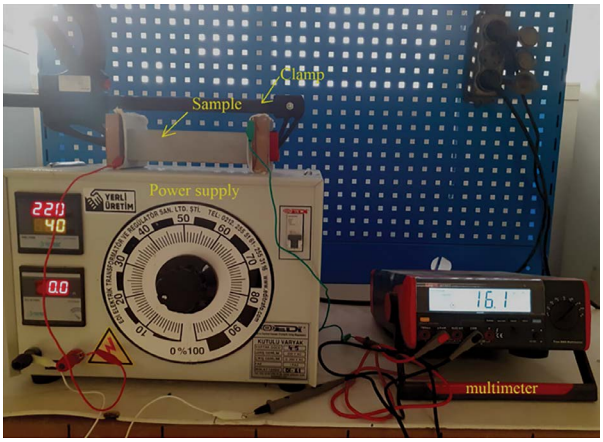

Figure 3. Two-point uniaxial electrical conductivity measuring test setup.

are expected on the strength, but since the aim of the study is electrical conductivity, this experiment was considered. After all the components came together in steel fiber mixtures, the fibers were added and mixed with a mixer for one minute when the matrix was ready.

2.2. Test Methods

The electrical conductivity measuring test setup is shown in Figure 3. The measurement of resistances of electrically conductive mortars was carried out by the two-point uniaxial method. This method is also used frequently in the literature [13, 15, 29]. This method applies a potential difference between the two ends of the specimen, and the amount of current realized is measured. The resistance of the specimen is obtained by putting the current value and applied voltage into ohm's law (Eq. 1). The resistivity is calculated from Eq. 2. The electrical conductivity obtained as the inverse of the resistivity is given in Eq. 3.

$$V=IR \tag{1}$$

$$\rho = R\frac{A}{L} \tag{2}$$

$$\sigma = \frac{1}{\rho} \tag{3}$$

The longitudinal resonance frequency analyses of the conductive mortar samples produced from the mixtures obtained within the scope of the study were carried out according to the ASTM C215 standard [30]. The experimental setup is given in Figure 4a. According to the resonance test results, firstly, the amplitude-frequency curve (Figure 4b) was drawn for each sample. The damping ratio values were calculated by considering the curve. Many structural problems are solved by determining the natural frequencies at which the structure resonates and the percentage of critical damping of each resonance [31].

In some cases, starting vibration is reduced by changing the active form of the system or shifting a resonant frequency (by stiffening the structure and mass loading) to avoid a frequency coincidence. Another way is to add damping treatments to the structure. Layers of isolation stabilize ground vibration, and installing a vibration absorber can "split" a resonance into two acceptably different frequencies. All these corrections are decided by applying a measured force to the problem structure and measuring and analyzing the response acceleration rate of that force as a function of frequency.

The flexural strengths of the conductive mortar samples were determined by a three-point bending test on three 40 x 40 x 160 mm prismatic samples obtained from each mixture. The parts obtained after the bending test were placed between the apparatus, as in Figure 5, and subjected to the compressive strength test. Bending and compressive strength tests were carried out by the TS EN 196-1 standard [32]. Ultrasonic pulse velocity (UPV) and Leeb hardness tests were performed as non-destructive methods before subjecting them to other tests on identical specimens. UPV tests were performed according to ASTM C597 [33]. The ASTM A956 standard [34] was used to determine the Leeb hardness of the produced samples. In addition, densities were calculated by measuring the dry weight and dimensions of all 28-day samples.

The surface morphologies of the conductive concrete samples were analyzed using HITACHI SU3500 Scanning Electron Microscopy (SEM). After mechanical testing, SEM analyzes were used to observe the porous, rough, and void structure at the sample interface. Elemental analyzes of composite concrete samples were carried out using the Energy-Dispersive X-Ray Spectroscopy (EDS) analysis method. Also, the X-ray Diffraction technique (XRD method) was used to identify the crystalline phases of the materials. XRD analyzes were performed using the RIKAGU device with a scanning range of 10°–70° at a scanning rate of 1°/min.

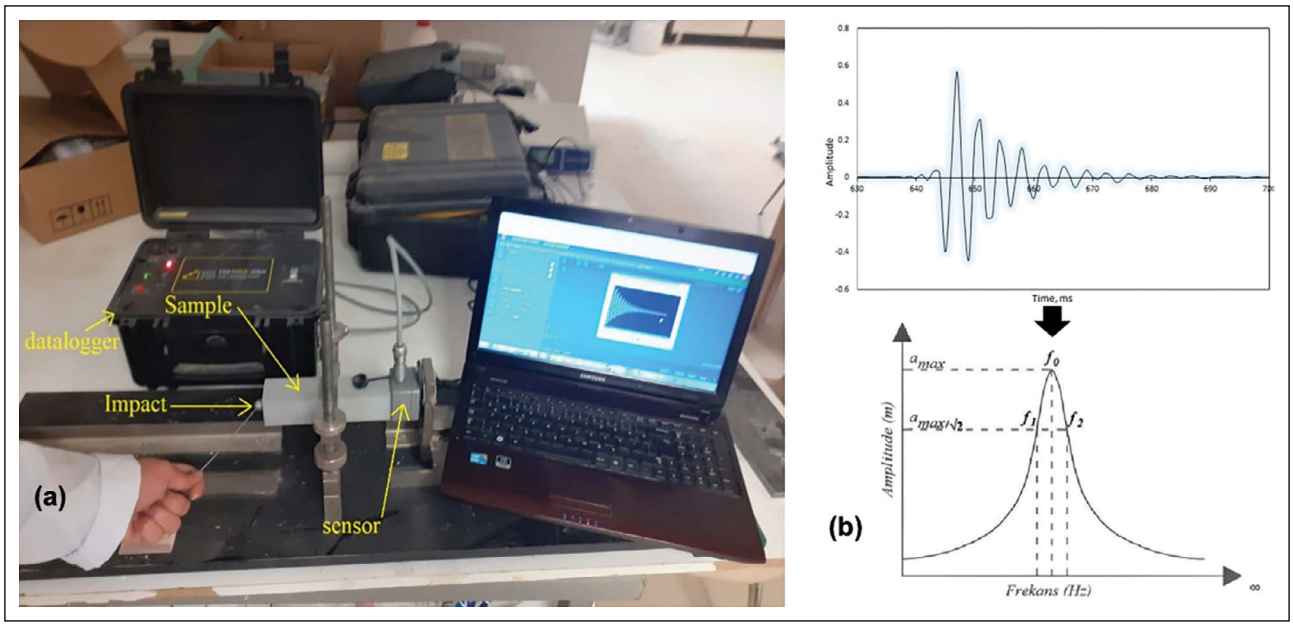

Figure 4. Dynamic resonance test setup **(a)** and schematic view of amplitude-frequency curve.

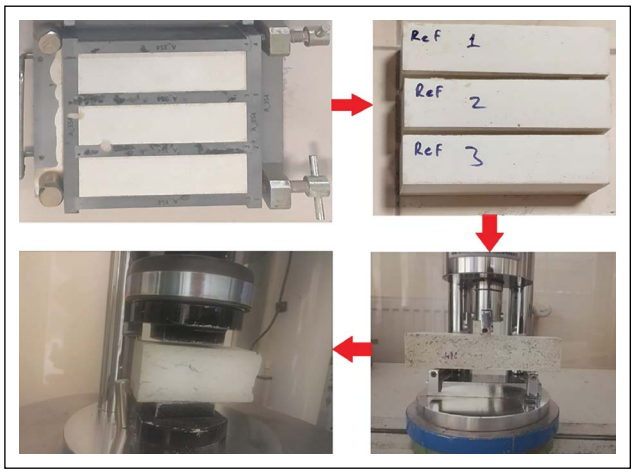

Figure 5. Flexural and compressive strength test setup.

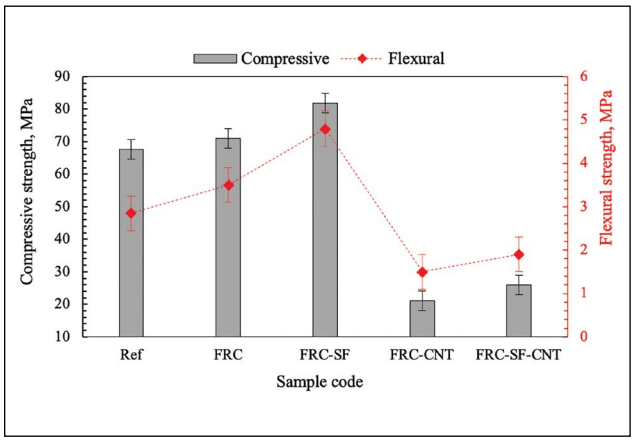

Figure 6. 28-Day compressive and flexural strength of conductive mortar samples.

3. RESULTS AND DISCUSSION

3.1. Mechanical Test Results

As mechanical test methods, 28-day flexural and compressive strength tests of electrically conductive mortar samples were performed, and the most substantial results were compared in Figure 6. The compressive and flexural strength of the ferrochrome (FRC) filled conductive mortar increased by 4.84%, and 22.81%, respectively, compared to the silica sand filled mortar (Ref). This is the significant increase provided by recycled aggregate. Adding five wt.% steel fiber (SF) to the FRC-filled mortar resulted in a 15.26% increase in compressive strength. Also, the strength of this sample was 20.87% higher than that of Ref. The SF contributed 37.14% to the FRC-filled sample's flexural strength, and this sample's flexural strength was 68.42% higher than the Ref. In the literature, there is information about the positive and negative effects of recycled ferrochrome aggregate on the strength of cementitious materials. In the study of Islam et al. [35], it was reported that the compressive and flexural strength of 100% FRC substituted concrete increased by 12% and 19.9%, respectively, compared to the compressive and flexural strength of concrete filled with natural aggregates. The increase in strength has been explained as the excellent bonding of FRC with cement paste since it has a rough surface [36]. Another reason is that since the FRC has a porous structure, it absorbs the excess water in the concrete and causes a denser matrix formation. At [37], the strength of the obtained concrete decreased with the addition of fine FRC. As a result, the positive or negative effect of FRC on concrete strength is related to factors such

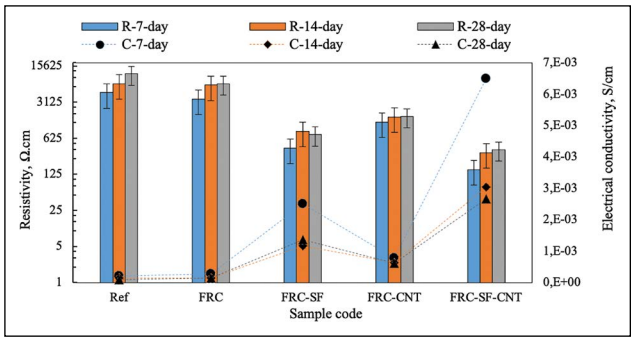

Figure 7. Resistivity and electrical conductivity results of conductive mortar samples.

as FRC's own physical and mechanical properties, granulometry, and water/binder ratio in concrete. According to the graphic, it is observed that carbon nanotube (CNT) has a remarkable negative effect on strength. However, as mentioned above, the high-water content (0.75 of binder) in the dispersed solution is the main reason for this decrease. The reason for using such a high rate of water is that it is aimed to investigate the use of 0.3% pure SWCNT in mixtures. The compressive strength of FRC-CNT decreased by 3.21 and 3.36 times compared to Ref and FRC samples, respectively.

Similarly, flexural strength decreased by 1.9 and 2.33 times, respectively, compared to the same samples. Naqi et al. [38] reported that the compressive strength of cementitious composites containing less than 0.05% MWCNT increased compared to the control sample. On the contrary, they reported that the compressive strength of cementitious composites containing more than 0.05% MWCNT was reduced compared to the control sample. The addition of 5% SF to the FRC-CNT mixture resulted in an increase of 23.41% and 26.67% in compressive and flexural strength, respectively. However, this sample's compressive and flexural strength (FRC-SF-CNT) decreased by 3.14 and 2.53 times, respectively, compared to FRC-SF. Another reason for the decrease in strength may be that the solution containing SWCNT has a high amount of carboxymethyl cellulose (CMC). CMC, which has good water retention, can cause permanent porosity in the matrix after the hydration process is completed when used at high rates in cementitious materials [20]. In a study [39], an increase in the strength of the cementitious composite was observed by using SWCNT dispersed with CMC. The related study used lower rates of CMC (0.3 wt.%) and SWCNT (0.04 wt.%).

3.2. Electrical Properties

7, 14, and 28-day electrical conductivity and resistivity values of the conductive mortar samples are summarized in Figure 7. Depending on the sample age, the resistivity value increased and the electrical conductivity decreased. However, while there was a more significant difference between the seven and 14-day values, the 14 and 28-day values approached each other. The reason for this is the presence of water in early concrete, which has been proven in previous studies [14, 20] with different voltages on different mixtures. Substitution of FRC sand for silica sand has provided a certain amount of advantage on electrical properties. Considering the 28-day electrical resistivity values, it was observed that the resistivity of the FRC-filled sample decreased by 35.55% compared to Ref. Without the use of conductive fiber, such an improvement in electrical properties is essential in cementitious materials. Because of the improved conductivity as a matrix, it is possible to provide a higher performance current in the presence of conductive fiber. With the addition of 5% SF to the FRC-filled mixture, the electrical resistivity values decreased by about 10-time. With the addition of 0.3 wt.% SWCNT to the FRC-filled mixture, a decrease of more than 4-times in the electrical resistivity values was observed. The electrical resistivity of the FRC-SWCNT-filled mixture decreased approximately four times with the addition of 5 wt.% SF. The resistivity of the same mixture was 19 times lower than the FRC-filled mixture.

The electrical properties of cementitious materials are generally studied for two purposes: durability and physical. It is characterized in terms of chloride penetration in concrete as durability [40]—chlorinated liquids penetrating concrete damage cement products and reinforcement bars. In order to prevent this, the impermeability of the concrete should be reduced. In the study [41], the electrical conductivity of concrete with different ratios of acceptable FRC substitutes instead of natural aggregate was investigated in terms of durability and low chloride ion permeability according to ASTM 1202 [42]. In the literature, there are no studies examining the physical conductivity of FRC filled conductive concretes. The electrical conductivity of natural aggregate-filled concrete varies with the resistivity of the matrix, the type, and ratio of voids, and the type and conductivity level of the conductive additives used. It is known that powder materials generally do not significantly affect concrete's electrical resistivity [20]. For example, El-Dieb et al. [13] found that using carbon powder alone had no significant effect on electrical conductivity. According to the studies, using conductive fiber is essential to increase the conductivity performance in concrete. In the [29] study, the length and ratio of carbon fiber used as conductive fiber were 12 mm and 1%, respectively. Yehia and Tuan [16] obtained optimum conductivity values by using 20% steel shaving and 1.5% steel fiber for an electrically conductive concrete study as a deicing application. Carbon nanotubes (CNT) have been widely used as conductivity-enhancing nanomaterials in cementitious materials [43–45]. Most studies observed the best electrical resistivity values at 1000 Ω.cm when CNT was used alone. However, the functionality of the conductive concrete obtained is divided into various classes accord-

ing to factors such as the purpose of use, CNT ratio, and sample size. It is not sufficient to use CNT alone for the production of heatable, conductive concrete. The best heat performance in heatable conductive concretes is obtained at power consumptions of approximately 500 watts. For this, the most suitable electrical resistivity values are between 200–800 Ω.cm.

Carbon nanotubes' usability in producing new-generation cementitious materials such as self-sensing has been confirmed in different studies [1, 46, 47]. Self-sensing is the ability of a material to respond to different conditions such as temperature, strain, stress, and damage [47]. For example, if a crack occurs in a cementitious material, the resistivity value increases due to the extension of the electric wave propagation way. Since cementitious materials have very high resistivity, it is not easy to measure the resistivity difference in such cases. The presence of conductive materials such as CNT in the cement paste ensures the high sensitivity of the lower resistivity cementitious product. In this study, the alternative mixture that can be used for this purpose may be FRC-CNT. In addition, FRC is a suitable filling material for self-sensing cementitious materials since it is a main part of the direct matrix, and its resistivity is low compared to natural aggregate.

3.3. Non-destructive Test Results

3.3.1. Dynamic Resonance Test Results

The resonant frequency is mainly related to a vibrating beam's dynamic elasticity modulus and density. For this reason, a beam's natural vibration frequency is also used to determine the beam's dynamic modulus of elasticity. In this study, post-resonance test Frequency-Amplitude curves of 7, 14, and 28-day mortars obtained from all mixtures were plotted, and damping ratios were calculated, as shown in Figure 8.

Small peaks at the beginning of the curves are due to ambient noise during testing. Considering the dynamic resonance test results, it is observed that the amplitude number decreases over time; however, the peaks are also narrow. From the amplitude-frequency curves, it can be concluded that the damping ratio increases as the amplitude decreases. In other words, the narrower and higher the curve, the lower the damping; the more comprehensive and lower the curve, the greater the damping [48]. From this information, it can be concluded that the damping ratio decreases with increasing curing time. For example, when the damping ratio of Ref is examined, the damping ratios of 14 and 28 days decreased by 30% and 53%, respectively, compared to 7-day. Considering the damping ratios of FRC and FRC-CNT samples, although CNT had a slight increase effect on the seven and 14-day values, it did not affect the damping ratio of the 28-day sample. When the damping ratios of the FRC and FRC-SF samples were examined, it was observed that SF had an increasing effect of around 40% on

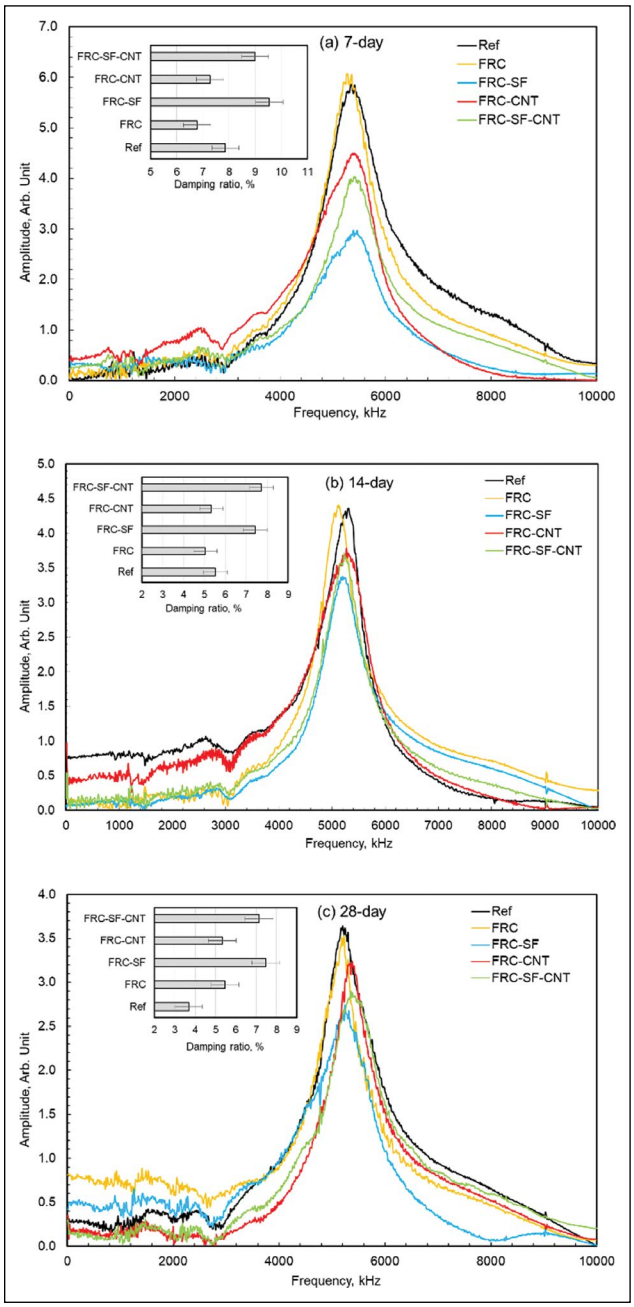

Figure 8. Dynamic resonance test results of conductive mortar samples.

the damping ratio. The damping ratios of the FRC-CNT-SF and FRC-SF samples were almost the same. The positive result obtained with the addition of SF is attributed to the minimization of the defect rate in the mortars [49]. With the increase in energy distribution, a higher capacity damping property emerges. When the damping rates are compared with the mechanical results, it is observed that there is a parallel relationship between them. As in the dynamic results, the maximum values in the mechanical results were obtained for the FRC-SF mixture.

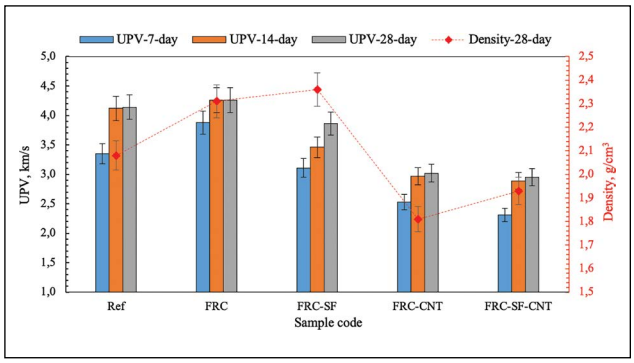

Figure 9. Density and UPV test results of conductive mortar samples.

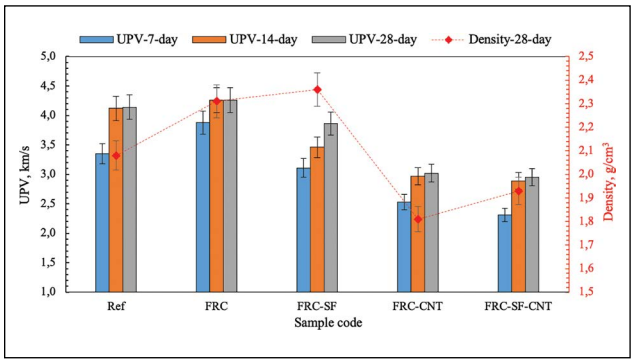

Figure 10. Leeb hardness test results of conductive mortar samples.

3.3.2. Ultrasonic Pulse Velocity

The ultrasonic pulse velocity results of the samples and the density results are summarized in Figure 9 to observe if there is any correlation between them. When UPV values were compared by age, a more significant incremental variation was observed between 7 and 14-day values, but there was little increase at 28-day values compared to 14-day values. This is due to faster hydration reactions at early ages in cementitious materials. In the early ages, there was more void and water in the matrix, and over time, the hydration products formed due to the hydration reaction filled most of the voids, creating a dense and rigid structure [50]. When the UPV values of the mixtures of FRC and Ref were compared, it was observed that the value of FRC was 2.9% higher than that of Ref. Also, the density value of FRC increased by 11.06% compared to Ref. This is because FRC sand has a denser structure compared to silica sand. As noted in the Material section, the specific gravity values of FRC and silica sand are 3.33 and 2.9 g/cm^3, respectively. With the addition of SF to the FRC mixture, the UPV values decreased by 9.39%. Due to the relatively high dosage of SF (5%), voids occur between the fibers in the mixture. This causes the sound transmission speed to decrease. Although steel fiber had a higher weight compared to concrete, the density of fibrous and fiberless FRC-filled mortars was similar, which is evidence of voids occurring. Due to the extra water used, SWCNT had adverse effects on UPV, density results, and other results. The 28-day UPV and density values of the FRC-CNT mixture decreased by 29.11% and 21.64% compared to the FRC. A similar situation was observed in FRC-CNT-SF. The water/binder ratio significantly affects the density of all cementitious materials [51].

3.3.3. Leeb Hardness Results

The Leeb hardness test, a non-destructive method, provides information about the hardness and estimated strength of construction materials, such as stone and concrete [52, 53]. In the present study, the hardness of prismatic specimens produced from different conductive mortar mixtures was measured at different ages and compared in Figure 10. Leeb hardness values increased in all mixtures depending on the sample age. For example, Leeb hardness values of 14 and 28-day Ref samples have increased by 7.8% and 13.8%, respectively, compared to 7-day. Age effect on Leeb hardness was less than others in the FRC mixture. Considering the hardness values of 28-day FRC and silica sand-filled mortars, it was observed that the hardness of FRC-filled mortars was 2% lower. The hardness value of the FRC-filled mortar with SF added was 1.6% higher than the fiberless sample. This is because thin SFs disperse in the mortar and form a network, creating a more rigid surface. SWCNT had a negative effect of 17% on the hardness of the FRC-filled mortar. However, not all of these adverse effects are directly related to SWCNT due to the extra amount of water and CMC used. As indicated in the results above, the amount of extra water used in the mortar caused a high rate of voids and defects in the internal structure. Adding SF to the FRC-CNT mixture increased the hardness value by 13%. When the hardness values were compared with the other results, it was observed that there was a parallel relationship consistent with the compressive, flexural, and density results.

Since there has been no hardness research about FRC filed mortars, it is impossible to compare the obtained hardness values with the literature. However, there are a few Leeb hardness studies on regular concretes, although limited. Song et al. [54] investigated the Leeb hardness of sodium silicate-based concrete and regular C30 concrete and concluded that the average hardness value of standard concrete was 362.4 HL, and that of sodium silicate-based concrete was 405.6 HL. The hardness values of the 28-day specimens produced in this study were measured between 369 and 454 HL. Therefore, the results prove to be compatible when compared to regular concrete. Gomez-Heras et al. [55] stated that the finer the grain size, the higher the Leeb hardness. Also, calcined kaolin improves the surface hardness of concrete [56]. This situation is directly related to filling fine-grained minerals into micro and macropores [57].

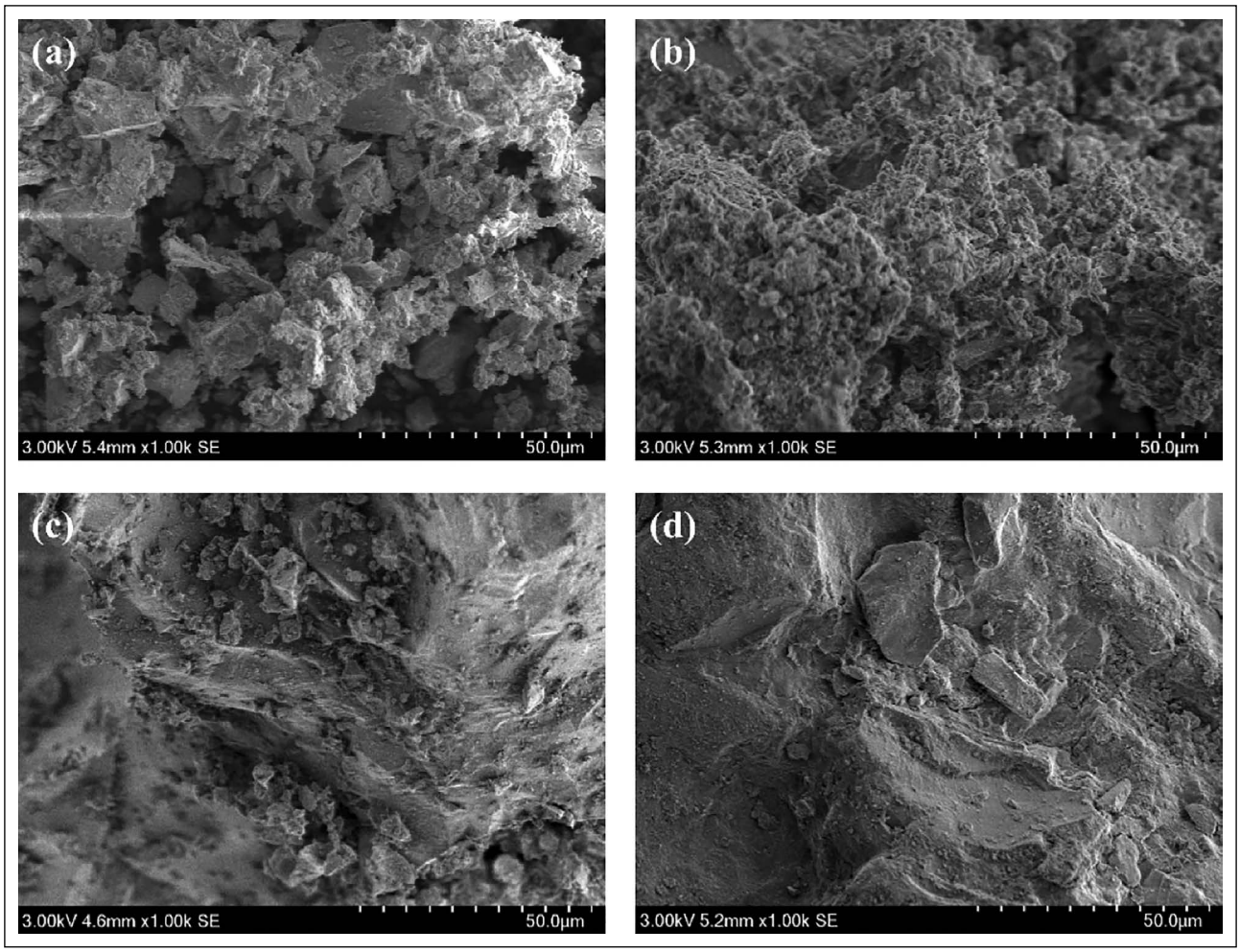

Figure 11. Microstructure images of raw particles; **(a)** cement, **(b)** CK, **(c)** ferrochrome, and **(d)** SS, respectively.

3.4. Microstructure Analysis Results

Figure 11 shows the morphologies of cement, CK, ferrochrome, and SS particles, respectively. The particle sizes were found to be about 5 µm. Ferrochrome and silica sand, used as reinforcement materials, were preferred for their effect on mechanical strength and dense structure formation. Especially the sharp-edged square crystals observed in silica sand reinforcement particles could improve the mechanical behavior of the mixture by strengthening the bond with the cement. It has been known that the micro-voids and micro-cracks formed by the interlocking aggregate particles cause the formation of the porous structure [58]. The effect of particles dispersed in cement on the microstructure was examined. In Figure 12, microstructures of cemented filler samples (SS-filled, FRC-filled, and FRC-CNT) at different magnifications were investigated by SEM analysis. It was observed that the micro-void distributions in the samples were not significant; accordingly, micro-cracks were not formed intensively. In this regard, the micro-voids in the high magnification image of the SS-filled sample (Fig. 12a) was nearly the same in diameter compared to the FRC-filled sample. It could be stated that the SS-filled sample showed fine microstructure since the microvoids were low compared to the particle size distributions. Fine particle-size silica sand with a large specific surface area increased C-S-H formation in the cement matrix. The increased strength of the compacted samples has been associated with the amount of calcium silicate hydrate (C-S-H) gel in the structure [59].

Aggregate particles were densely combined with the silica sand particles due to intense C-S-H formation. In addition, the silica sand particles in the SS-filled sample contributed to the high gel formation. The silica sand particles improved the morphology of the cementitious matrix and made the matrix denser. Consequently, silica sand particles improved compressive and flexural strength by preventing the formation and development of micro-voids and micro-cracks. Because C-S-H formations were relatively weaker in the FRC-filled cementitious structure microstructure than the SS-filled sample, porosity and roughness increased. The porous and rough structure could be attributed to the air content of the ferrochrome-reinforced cement-based mixture [60].

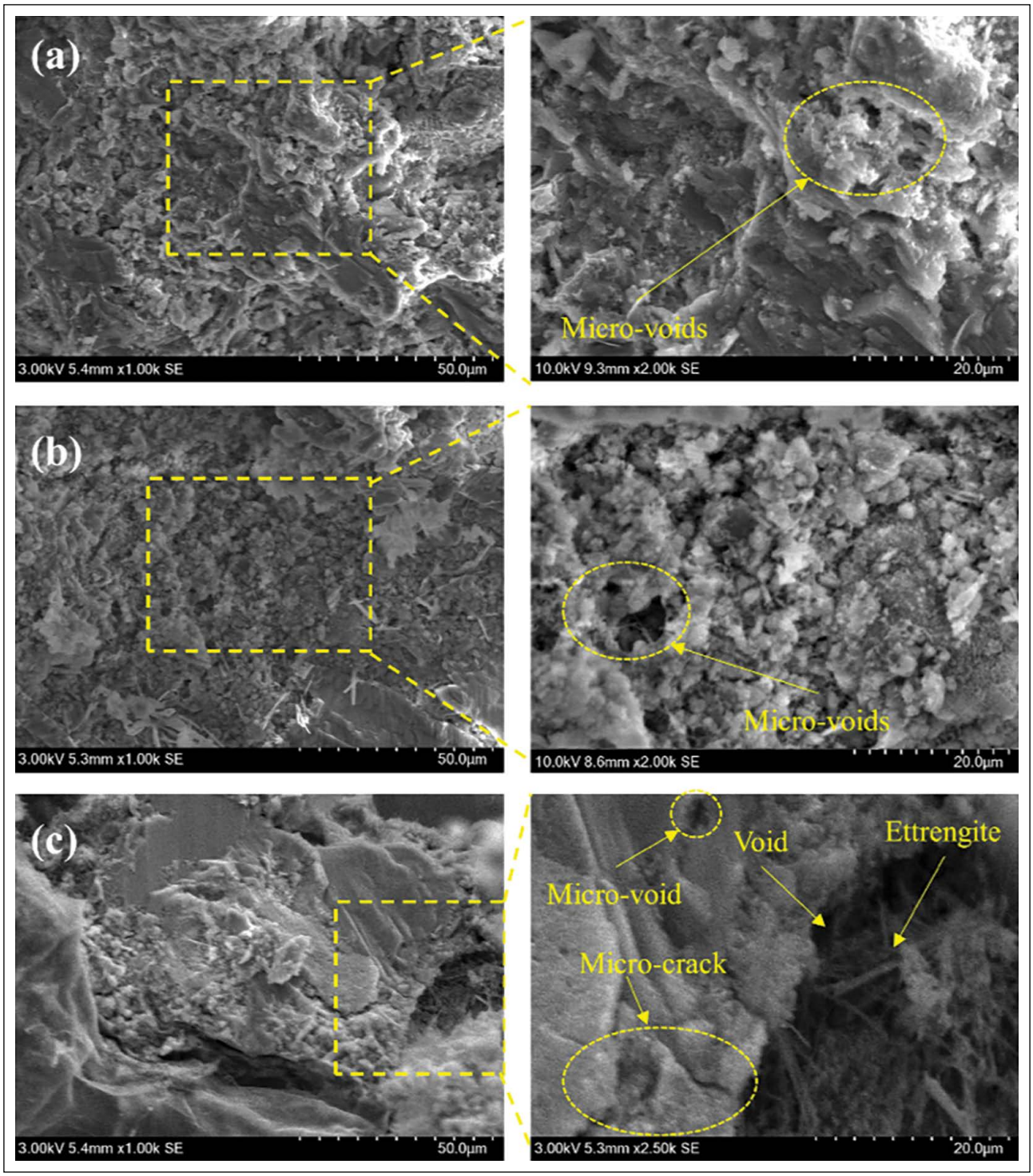

Figure 12. Low and high magnification SEM images of **(a)** SS-filled, **(b)** FRC-filled, and **(c)** FRC-CNT samples, respectively.

The increase in surface roughness compared to the SS-filled sample caused a change in morphology. Nevertheless, the formation of sharp-edged structures seen in the morphology of SS-filled and FRC-filled samples has been attributed to the bonding between aggregate and C-S-H, which increased the material's mechanical strength [61]. The increased compactness of the matrix decreased the tension at the matrix-aggregate interface, preventing the expansion of micro-cracks along with the aggregate. Thus, the reduction in micro-crack contributed to the increase in mortar strength [36]. It could be summarized that SS-filled and FRC-filled samples contained finer particles,

and microstructure deterioration was lower. It has been seen that the FRC-CNT sample was less dense than the other samples. This could be seen as a barrier to strength increase relative to other blends. With the addition of CNT to the mixture, the workability decreased due to the decrease in cement paste. It was observed that CNT particles dispersed in the aggregate could not prevent the formation of voids and cracks. The formation of a larger micro-void structure in FRC-CNT morphology could be attributed to the negative effect of CNT reinforcement on concrete strength. Since C-S-H crystals were collected at the interface, weak bonding in the cement matrix decreased the material's mechanical strength. Moreover, needle-like ettringite crystals observed in cement paste reduced compact structure formation. FRC-CNT sample also pointed out the weakest parameters about density, UPV, and strength tests. It could be said that the addition of CNT particles to the aggregate reduced C-S-H gel formation and made it difficult to form networks in a compact structure.

EDS analysis results of SS-filled, FRC-filled, and FRC-CNT samples are given in Figure 13. O, Si, and Ca elements formed the prominent peaks in the SS-filled sample. The silica in the mixture came from the hydration of the cement, while the gold and palladium came from the gold etching of the samples. The main constituent elements of cementitious products were O, Si, and Ca, and the C/S ratio was related to C-S-H gel formation. Cement-based material products have increased bonding energy by interacting with the matrix interface [62]. The low C/S ratio has been related to high strength [63]. The C/S ratios in the Si-filled, FRC-filled, and FRC-CNT were 1.01, 0.98, and 1.11, respectively. The silica sand added to increase the material durability contains high Si in C-S-H formation; it was observed that the C/S ratio decreased in spectrum-1. Since the increase in C-S-H polymerization increased the degree of interfacial bonding, it supported the formation of the dense and compact structure of the composite material [64]. It has been consistent with the compressive and flexural strength results shown in Figure 6. The absence of micro-cracks in the matrix and aggregate interface region indicated in Figure 12 was attributed to the low shrinkage in the compact structure formed by silica sand.

In spectrum-2, the formation of Cr and Fe element peaks in the FRC-filled sample indicated the presence of ferrochrome particles. Lower C/S level contributed to forming the bonding system between the aggregate/reinforcement particles and confirmed the strength increase noted in Figure 6. Ferrochrome particles containing chromium and iron elements contributed to the mechanical strength increase by collecting C-S-H crystals in the interfacial transition region. Moreover, ferrochrome with a high percentage of calcium forms high binding in aqueous media with Ca (OH)2 [65]. It could be stated that the intense Ca peak seen in spectrum-2 contributed to the formation of the dense structure of the composite material. The C peak seen in the EDS analysis of the FRC-CNT sample indicated the presence of CNTs in spectrum-3. It could be said that the percentages of Ca and Si were lower due to the high percentage of C that CNTs contain. Thus, it could be concluded that the bond between CNTs and Ca and Si was weak. It could be stated that the decrease in calcium, silicon, chromium, and iron peaks was a weak interaction between CNT and hydration products, and this result could be attributed to the low-density structure indicated in Figure 12. Moreover, CNT allowed the inclusion of more particles compared to chromium and iron elements due to their low density. This explains the increase in the carbon peak and the decrease in the chromium-iron peaks. As a result, as indicated in Figure 7, the conductive CNT particles contributed to the conductivity of the composite material by creating an electric field [66]. When the EDS results are compared with the cemented studies in the literature, the peaks and their grades have been confirmed by the results of several studies [67, 68].

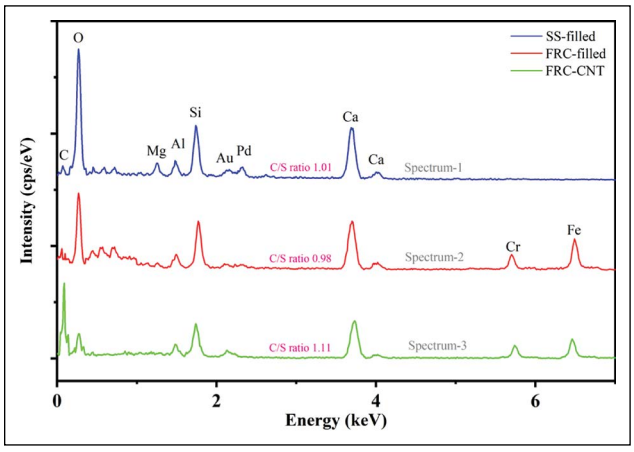

Figure 13. EDS analysis of SS-filled (spectrum-1), FRC-filled (spectrum-2), and FRC-CNT (spectrum-3) samples, respectively.

In Figure 14, the phase compositions of SS-filled, FRC-filled, and FRC-CNT samples were shown by XRD models. Origin Pro 2021 software was used to plot the diffraction angles on the X-ray diffraction plot. $CaCO_3$, one of the primary raw materials of cement, contributed to the formation of calcium-containing hydration products such as C-S-H and ettringite [69]. Although it was observed that the primary crystalline peaks in the conductive concrete samples were quartz and calcite, the C-S-H gel also showed characteristic peaks. The silica sand in the SS-filled sample explains the intensity of the quartz main phase. The silica sand content in the cement matrix reduced the ettringite formation and contributed to the compressive strength increase of the composite material. However, it could be

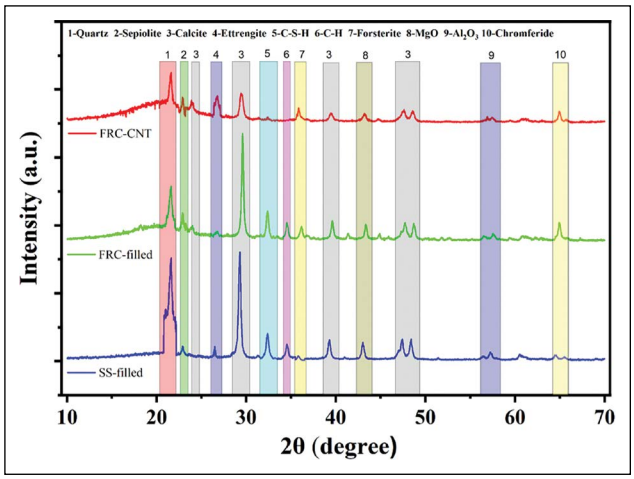

Figure 14. XRD patterns of SS-filled, FRC-filled, and FRC-CNT.

said that the formation of the ettringite phase in the structure prevented the formation of a porous structure in the composite concrete sample [70]. The reduction of ettringite growth increased the crosslinking within the matrix, thereby forming a compact structure with improved compressive and flexural strengths. The increase in the calcite peak intensity of the SS-filled sample indicated that the hydration process increased, and as a result, it showed that it supported the increase in strength. The increase in C-S-H gel density in the mixture containing silica sand could be explained by the reactivity of the silica sand particles and the high hydration product. Silica sand, which has high hydraulic activity, contributed to the formation of C-S-H gel, which was a product of cement hydration and facilitated the increase of the binding force in the matrix.

In the XRD analysis of ferrochrome-containing samples, forsterite (Mg_2SiO_4) and chromferide (Fe, Cr) mineral peaks were observed separately. Also, it was stated that the analyzed sepiolite mineral was a stable product that intensified the microstructure [71]. In the FRC-filled sample mentioned in Figure 12, the increase in the C-S-H gel content resulting from the hydration reaction was confirmed by the intensity of the calcium silicate hydrate peak observed in the XRD analysis. In addition, the high peak density of portlandite (CH) could be attributed to the conversion of ettringite and portlandite to C-S-H gel, depending on the curing age. In addition, this condition was associated with compressive and flexural strength [72]. The absence of a CNT diffraction peak in the FRC-CNT sample indicated no chemical reaction between the CNT and the cement [73]. Also, it was observed that the CH peak derived from the pozzolanic reactions did not occur. CNTs dispersed in the aggregate cannot be said to contribute to the growth of cement hydrates. It could be argued that CNTs inhibited the hydration process [74]. In addition, the C-H and C-S-H crystals formed because of hydration were not detected in the XRD analysis, which confirmed this. The ettringite formation confirmed in the SEM microstructural characterization was analyzed in the XRD characterization of the FRC-CNT sample. Although the calcite peak density was associated with the porous structure [75], the bond strength between cement and reinforcement particles did not increase since hydration product formation, such as C-S-H in the FRC-CNT sample, was weak. The decrease in calcite peak intensity could be attributed to the low mechanical strength of the composite concrete of the porous structure formed because of the continuous dissolution of Ca $(OH)_2$.

4. CONCLUSIONS

According to the experimental study, the recycled FRC aggregate positively affected the mechanical properties. The highest compressive and flexural strength results were obtained for the steel fiber-reinforced FRC-filled mixture. SWCNT had an apparent adverse effect on strength. This was primarily related to the CMC used as a dispersing agent. Using FRC sand, the electrical resistivity value was slightly decreased compared to the resistivity of the silica sand-filled reference sample. With the addition of 5% SF, the resistivity value of the FRC-filled mixture decreased significantly. Although SWCNT alone positively affected conductivity properties, it performed best in combination with SF. The presence of SF had an essential role in developing its dynamic properties. Sample age had a positive effect on dynamic properties. An increase of over 53% was observed in the 28-day damping ratio results. When the results obtained with non-destructive test methods are compared with the experimental test results, it has generally proven to be a successful study. A consistent correlation was observed between the UPV and density and strength results.

SEM-EDS and XRD analyses were evaluated together with strength analyses to determine the composite material's performance. The effect of the C/S ratio on compressive and flexural strengths in EDS analysis was discussed. In the SEM analysis, the inclusion of silica sand and ferrochrome particles in the cement mortar contributed to the densification of the composite matrix. XRD results of composite conductive concrete showed that C-S-H gel formation contributed to forming a compact and dense microstructure. It was stated that the C-S-H crystal structures formed because of hydration detected in the XRD analysis affected the increase in strength.

ETHICS

There are no ethical issues with the publication of this manuscript.

ACKNOWLEDGMENTS

This study was carried out within the scope of the project coded STB-072161 of the Fibrobeton R&D Center. Thank you to Fibrobeton Company for their support. We also thank Eti Krom Inc. for its support of ferrochrome materials.

DATA AVAILABILITY STATEMENT

The authors confirm that the data that supports the findings of this study are available within the article. Raw data that support the finding of this study are available from the corresponding author, upon reasonable request.

CONFLICT OF INTEREST

The authors declare that they have no conflict of interest.

FINANCIAL DISCLOSURE

The authors declared that this study has received no financial support.

PEER-REVIEW

Externally peer-reviewed.

REFERENCES

[1] You, I., Yoo, D. Y., Kim, S., Kim, M. J., & Zi, G. (2017). Electrical and self-sensing properties of ultra-high-performance fiber-reinforced concrete with carbon nanotubes. *Sensors* (*Switzerland*), 17(11) Article 2481. [CrossRef]

[2] Li, Z., Ding, S., Yu, X., Han, B., & Ou, J. (2018). Multifunctional cementitious composites modified with nano titanium dioxide: A review. *Composites Part A: Applied Science and Manufacturing*, 111, 115–137. [CrossRef]

[3] Wang, L., & Aslani, F. (2019). A review on material design, performance, and practical application of electrically conductive cementitious composites. *Construction and Building Materials*, 229, Article 116892. [CrossRef]

[4] Ates, A. O., Khoshkholghi, S., Tore, E., Marasli, M., & Ilki, A. (2019). Sprayed glass fiber–reinforced mortar with or without basalt textile reinforcement for jacketing of low-strength concrete prisms. *Journal of Composites for Construction*, 23(2), Article 04019003. [CrossRef]

[5] Marasli, M., Subasi, S., Dehghanpour, H., Ozdal, V., & Kohen, B. (2021). Experimental investigation of pull-out and shear behavior of lifting sockets in precast UHPC panels. *ALKU Journal of Science*, 3(2), 82–93. [CrossRef]

[6] Topbas, A., Tulen, F. Ö., Marasli, M., & Kohen, B. (2019). *A prefabricated GFRC-UHPC shell pedestrian Bridge*. IASS Annual Symposium 2019 – Structural Membranes.

[7] Barnard, E. H., & Tex, H. (1965). *Electrically conductive concrete. Patent No: US3166518A*, 1–2. United States Patent Office.

[8] Howser, R. N., Dhonde, H. B., & Mo, Y. L. (2011). Self-sensing of carbon nanofiber concrete columns subjected to reversed cyclic loading. *Smart Materials and Structures*, 20(8), Article 085031. [CrossRef]

[9] Wen, S., & Chung, D. D. L. (2004). Electromagnetic interference shielding reaching 70 dB in steel fiber cement. *Cement and Concrete Research*, 34(2), 329–332. [CrossRef]

[10] Gomis, J., Galao, O., Gomis, V., Zornoza, E., & Garcés, P. (2015). Self-heating and deicing conductive cement. Experimental study and modeling. *Construction and Building Materials*, 75, 442–449. [CrossRef]

[11] Dehghanpour, H., & Yilmaz, K. (2021). A more sustainable approach for producing less expensive electrically conductive concrete mixtures: Experimental and FE study. *Cold Regions Science and Technology*, 184, Article 103231. [CrossRef]

[12] Wu, J., Liu, J., & Yang, F. (2015). Three-phase composite conductive concrete for pavement deicing. *Construction and Building Materials*, 75, 129–135. [CrossRef]

[13] El-Dieb, A. S., El-Ghareeb, M. A., Abdel-Rahman, M. A. H., & Nasr, E. S. A. (2018). Multifunctional electrically conductive concrete using different fillers. *Journal of Building Engineering*, 15, 61–69. [CrossRef]

[14] Dehghanpour, H., & Yilmaz, K. (2020). Investigation of specimen size, geometry and temperature effects on resistivity of electrically conductive concretes. *Construction and Building Materials*, 250, Article 118864. [CrossRef]

[15] Dehghanpour, H., & Yilmaz, K. (2020). Heat behavior of electrically conductive concretes with and without rebar reinforcement. *Medziagotyra*, 26(4), 471–476. [CrossRef]

[16] Yehia, S. A., & Tuan, C. Y. (2000). Thin conductive concrete overlay for bridge deck deicing and anti-icing. *Transportation Research Record*, 1698(1), 45–53. [CrossRef]

[17] Rao, R., Wang, H., Wang, H., Tuan, C. Y., & Ye, M. (2019). Models for estimating the thermal properties of electric heating concrete containing steel fiber and graphite. *Composites Part B: Engineering*, 164, 116–120. [CrossRef]

[18] Hou, Z., Li, Z., & Wang, J. (2007). Electrical conductivity of the carbon fiber conductive concrete. *Journal Wuhan University of Technology, Materials Science Edition*, 22(2), 346–349. [CrossRef]

[19] Wang, Y. Z., Xu, Y. Z., & Sun, Y. (2012). Experimental study on electrical conductivity of carbon fiber reinforced concrete underwater. *Advanced Materials Research*, 461, 246–249. [CrossRef]

[20] Dehghanpour, H., Yilmaz, K., & Ipek, M. (2019). Evaluation of recycled nano carbon black and waste erosion wires in electrically conductive concretes. *Construction and Building Materials*, 221, 109–121. [CrossRef]

[21] Rao, R., Fu, J., Chan, Y., Tuan, C. Y., & Liu, C. (2018). Steel fiber confined graphite concrete for pavement deicing. *Composites Part B: Engineering*, 155, 187–196. [CrossRef]

[22] Farcas, C., Galao, O., Navarro, R., Zornoza, E., Baeza, F. J., Del Moral, B., Pla, R., & Garcés, P. (2021). Heating and deicing function in conductive concrete and cement paste with the hybrid addition of carbon nanotubes and graphite products. *Smart Materials and Structures*, 30(4), Article 045010. [CrossRef]

[23] Wang, X., Wu, Y., Zhu, P., & Ning, T. (2021). Snow melting performance of graphene composite conductive concrete in severe cold environment. *Materials*, 14(21), Article 6715. [CrossRef]

[24] Dehghanpour, H., Yilmaz, K., Afshari, F., & Ipek, M. (2020). Electrically conductive concrete: A laboratory-based investigation and numerical analysis approach. *Construction and Building Materials*, 260, Article 119948. [CrossRef]

[25] Dehghanpour, H., & Yilmaz, K. (2020). The relationship between resistances measured by two-probe, Wenner probe and C1760-12 ASTM methods in electrically conductive concretes. *SN Applied Sciences*, 2(1), Article 10. [CrossRef]

[26] Dilbas, H. (2022). An investigation on effect of aggregate distribution on physical and mechanical properties of recycled aggregate concrete (RAC). *Journal of Sustainable Construction Materials and Technologies*, 7(2), 108–118. [CrossRef]

[27] Canpolat, O., Uysal, M., Aygörmez, Y., Şahin, F., & Acıkök, F. (2018). Effect of fly ash and ground granulated blast furnace slag on the strength of concrete pavement. *Journal of Sustainable Construction Materials and Technologies*, 3(3), 278–285. [CrossRef]

[28] Dilbas, H. (2021). Application of finite element method on recycled aggregate concrete and reinforced recycled aggregate concrete: A review. *Journal of Sustainable Construction Materials and Technologies*, 6(4), 173–191. [CrossRef]

[29] Sassani, A., Ceylan, H., Kim, S., Gopalakrishnan, K., Arabzadeh, A., & Taylor, P. C. (2017). Influence of mix design variables on engineering properties of carbon fiber-modified electrically conductive concrete. *Construction and Building Materials*, 152, 168–181. [CrossRef]

[30] American Society for Testing and Materials C215. (2019). *Standard test method for fundamental transverse, longitudinal, and torsional resonant frequencies of concrete specimens*. American Society for Testing and Materials.

[31] Trifunac, M. D. (1972). Comparisons between ambient and forced vibration experiments. *Earthquake Engineering & Structural Dynamics*, 1(2), 133–150. [CrossRef]

[32] Turkish Standard EN 196-1. (2005). *Methods of testing cement–Part 1: Determination of strength*. Turkish Standard.

[33] American Society for Testing and Materials C597. (2009). *Standard test method for pulse velocity through concrete*. American Society for Testing and Materials.

[34] American Society for Testing and Materials A956. (2006). *Standard test method for leeb hardness testing of steel products*. American Society for Testing and Materials.

[35] Islam, M. Z., Sohel, K. M. A., Al-Jabri, K., & Al Harthy, A. (2021). Properties of concrete with ferrochrome slag as a fine aggregate at elevated temperatures. *Case Studies in Construction Materials*, 15, e00599. [CrossRef]

[36] Al-Jabri, K., & Shoukry, H. (2018). Influence of nano metakaolin on thermo-physical, mechanical and microstructural properties of high-volume ferrochrome slag mortar. *Construction and Building Materials*, 177, 210–221. [CrossRef]

[37] Dash, M. K., & Patro, S. K. (2018). Performance assessment of ferrochrome slag as partial replacement of fine aggregate in concrete. *European Journal of Environmental and Civil Engineering*, 25(4), 635–654. [CrossRef]

[38] Naqi, A., Abbas, N., Zahra, N., Hussain, A., & Qasim, S. (2018). Effect of multi-walled carbon nanotubes (MWCNTs) on the strength development of cementitious. *Integrative Medicine Research*, 8(1) 1203–1211. [CrossRef]

[39] Uchida, T. (2022). Development of CNT dispersion Al 2 O 3 ceramics. *Ceramics*, 45, 1–4.

[40] Fares, A. I., Sohel, K. M. A., & Al-mamun, A. (2021). Characteristics of ferrochrome slag aggregate and its uses as a green material in concrete – A review. *Construction and Building Materials*, 294, Article 123552. [CrossRef]

[41] Dash, M. K., & Patro, S. K. (2018). Effects of water cooled ferrochrome slag as fine aggregate on the properties of concrete. *Construction and Building Materials*, 177, 457–466. [CrossRef]

[42] American Society for Testing and Materials C1202. (1997). *Standard test method for electrical indication of concrete's ability to resist chloride ion penetration*. American Society for Testing and Materials.

[43] Alessandro, A. D., Tiecco, M., Meoni, A., & Ubertini, F. (2021). Improved strain sensing properties of cement-based sensors through enhanced carbon nanotube dispersion. *Cement and Concrete Composites*, 115, Article 103842. [CrossRef]

[44] Hong, G., Choi, S., Yoo, D., & Oh, T. (2021). Moisture dependence of electrical resistivity in under-percolated cement-based composites with multi-walled carbon nanotubes. *Journal of Materials Research and Technology*, 16, 47–58. [CrossRef]

[45] Dong, W., Guo, Y., Sun, Z., Tao, Z., & Li, W. (2021). Development of piezoresistive cement-based sensor using recycled waste glass cullets coated with carbon nanotubes. *Journal of Cleaner Production*, 314, Article 127968. [CrossRef]

[46] Gupta, S., Lin, Y., Lee, H., Buscheck, J., Wu, R., Lynch, J. P., Garg, N., & Loh, K. J. (2021). In situ crack mapping of large-scale self-sensing concrete pavements using electrical resistance tomography. *Cement and Concrete Composites*, 122, Article 104154. [CrossRef]

[47] Suchorzewski, J., Prieto, M., & Mueller, U. (2020). An experimental study of self-sensing concrete enhanced with multi- wall carbon nanotubes in wedge splitting test and DIC. *Construction and Building Materials, 262*, Article 120871. [CrossRef]

[48] Tian, J., Fan, C., Zhang, T., & Zhou, Y. (2019). Rock breaking mechanism in percussive drilling with the effect of high-frequency torsional vibration. Energy Sources, Part A: Recovery, *Utilization and Environmental Effects*, 44(1), 2510–2534. [CrossRef]

[49] Long, W.-J., Wu, Z., Khayat, K. H., Wei, J., Dong, B., Xing, F., & Zhang, J. (2022). Design, dynamic performance and ecological efficiency of fiber-reinforced mortars with different binder systems: Ordinary Portland cement, limestone calcined clay cement and alkali-activated slag. *Journal of Cleaner Production*, 337, Article 130478. [CrossRef]

[50] Marasli, M., Subasi, S., & Dehghanpour, H. (2022). Development of a maturity method for GFRC shell concretes with different fiber ratios. *European Journal of Environmental and Civil Engineering*, 26(15), Article 2028190. [CrossRef]

[51] Tassew, S. T., & Lubell, A. S. (2014). Mechanical properties of glass fiber reinforced ceramic concrete. *Construction and Building Materials*, 51, 215–224. [CrossRef]

[52] Mishra, D. A., & Basu, A. (2013). Estimation of uniaxial compressive strength of rock materials by index tests using regression analysis and fuzzy inference system. *Engineering Geology*, 160, 54–68. [CrossRef]

[53] Ortega, J. A., Gómez-Heras, M., Perez-López, R., & Wohl, E. (2014). Multiscale structural and lithologic controls in the development of stream potholes on granite bedrock rivers. *Geomorphology*, 204, 588–598. [CrossRef]

[54] Song, Z., Xue, X., Li, Y., Yang, J., He, Z., Shen, S., … Zhang, N. (2016). Experimental exploration of the waterproofing mechanism of inorganic sodium silicate-based concrete sealers. *Construction and Building Materials*, 104, 276–283. [CrossRef]

[55] Gomez-Heras, M., Benavente, D., Pla, C., Martinez-Martinez, J., Fort, R., & Brotons, V. (2020). Ultrasonic pulse velocity as a way of improving uniaxial compressive strength estimations from Leeb hardness measurements. *Construction and Building Materials*, 261, Article 119996. [CrossRef]

[56] Pangdaeng, S., Sata, V., Aguiar, J. B., Pacheco-Torgal, F., Chindaprasirt, J., & Chindaprasirt, P. (2016). Bioactivity enhancement of calcined kaolin geopolymer with CaCl2 treatment. *ScienceAsia*, 42(6), 407–414. [CrossRef]

[57] García-Del-Cura, M. Á., Benavente, D., Martínez-Martínez, J., & Cueto, N. (2012). Sedimentary structures and physical properties of travertine and carbonate tufa building stone. *Construction and Building Materials*, 28(1), 456–467. [CrossRef]

[58] Wu, J., Feng, M., Mao, X., Xu, J., Zhang, W., Ni, X., & Han, G. (2018). Particle size distribution of aggregate effects on mechanical and structural properties of cemented rockfill: Experiments and modeling. *Construction and Building Materials*, 193, 295–311. [CrossRef]

[59] Afzal, M. T., & Khushnood, R. A. (2021). Influence of carbon nano fibers (CNF) on the performance of high strength concrete exposed to elevated temperatures. *Construction and Building Materials*, 268, Article 121108. [CrossRef]

[60] Dehghanpour, H., Subasi, S., Guntepe, S., Emiroglu, M., & Marasli, M. (2022). Investigation of fracture mechanics, physical and dynamic properties of UHPCs containing PVA, glass and steel fibers. *Construction and Building Materials*, 328, Article 127079. [CrossRef]

[61] Sun, J., Lin, S., Zhang, G., Sun, Y., Zhang, J., Chen, C., Morsy A. M., & Wang, X. (2021). The effect of graphite and slag on electrical and mechanical properties of electrically conductive cementitious composites. *Construction and Building Materials*, 281, Article 122606. [CrossRef]

[62] Dehghanpour, H., Doğan, F., & Yılmaz, K. (2022). Development of CNT–CF–Al2O3-CMC gel-based cementitious repair composite. *Journal of Building Engineering*, 45(October 2021), 1–4. [CrossRef]

[63] Rhee, I., Lee, J. S., Kim, J. H., & Kim, Y. A. (2017). Thermal performance, freeze-and-thaw resistance, and bond strength of cement mortar using rice husk-derived graphene. *Construction and Building Materials*, 146, 350–359. [CrossRef]

[64] Wang, D., Wang, X., Ashour, A., Qiu, L., & Han, B. (2022). Compressive properties and underlying mechanisms of nickel coated carbon nanotubes modified concrete. *Construction and Building Materials*, 319, Article 126133. [CrossRef]

[65] Acharya, P. K., & Patro, S. K. (2016). Utilization of ferrochrome wastes such as ferrochrome ash and ferrochrome slag in concrete manufacturing. *Waste Management and Research*, 34(8), 764–774. [CrossRef]

[66] Lee, S.-J., You, I., Kim, S., Shin, H.-O., & Yoo, D.-Y. (2022). Self-sensing capacity of ultra-high-performance fiber-reinforced concrete containing conductive powders in tension. *Cement and Concrete Composites*, 125, Article 104331. [CrossRef]

[67] Doğan, F., Dehghanpour, H., Subaşi, S., & Maraşli, M. (2022). Characterization of carbon fiber reinforced conductive mortars filled with recycled ferrochrome slag aggregates. *Journal of Sustainable Construction Materials and Technologies*, 7(3), 145–157. [CrossRef]

[68] Islam, M. Z., Sohel, K. M. A., Al-Jabri, K., & Al Harthy, A. (2021). Properties of concrete with ferrochrome slag as a fine aggregate at elevated temperatures. Case *Studies in Construction Materials*, 15, e00599. [CrossRef]

[69] Akarsh, P. K., Marathe, S., & Bhat, A. K. (2021). Influence of graphene oxide on properties of concrete in the presence of silica fumes and M-sand. *Construction and Building Materials*, 268, Article 121093. [CrossRef]

[70] Pan, D., Yaseen, S. A., Chen, K., Niu, D., Ying Leung, C. K., & Li, Z. (2021). Study of the influence of seawater and sea sand on the mechanical and microstructural properties of concrete. *Journal of Building Engineering*, 42, Article 103006. [CrossRef]

[71] Dash, M. K., Patro, S. K., Acharya, P. K., & Dash, M. (2022). Impact of elevated temperature on strength and micro-structural properties of concrete containing water-cooled ferrochrome slag as fine aggregate. *Construction and Building Materials*, 323, Article 126542. [CrossRef]

[72] Zhang, B., Zhu, H., Shah, K. W., Feng, P., & Dong, Z. (2021). Optimization of mix proportion of alkali-activated slag mortars prepared with seawater and coral sand. *Construction and Building Materials*, 284, Article 122805. [CrossRef]

[73] Li, C. (2021). Chloride permeability and chloride binding capacity of nano-modified concrete. *Journal of Building Engineering*, 41, Article 102419. [CrossRef]

[74] Abedi, M., Fangueiro, R., Camões, A., & Gomes Correia, A. (2020). Evaluation of CNT/GNP's synergic effects on the Mechanical, Microstructural, and durability properties of a cementitious composite by the novel dispersion method. *Construction and Building Materials*, 260, Article 120486. [CrossRef]

[75] Bostanci, L. (2020). Effect of waste glass powder addition on properties of alkali-activated silica fume mortars. *Journal of Building Engineering*, 29, Article 101154. [CrossRef]

Journal of Sustainable Construction Materials and Technologies
Web page info: https://jscmt.yildiz.edu.tr
DOI: 10.47481/jscmt.1196292

JSCMT
Journal of Sustainable Construction Materials and Technologies

Research Article

Effects of exfoliation temperature for vermiculate aggregates modified by sodium ions on thermal and comfort properties of a new generation cementitious mortar

Lütfullah GÜNDÜZ, Şevket Onur KALKAN*

Department of Civil Engineering, İzmir Katip Çelebi University, İzmir, Türkiye

ARTICLE INFO

Article history
Received: 29 October 2022
Revised: 04 December 2022
Accepted: 04 December 2022

Key words:
Exfoliation, heating temperature, mortar, thermal comfort, thermal insulation, vermiculite

ABSTRACT

Vermiculite exfoliation is based on the principle that water between the layers evaporates and the crystal layers spread out, pressured by steam. As a result, elongated, curved particles are formed. The thermal properties of the final product formed are directly related to this exfoliation amount. In this experimental work, the exfoliation characteristic of natural vermiculate is studied. A series of experimental analyses were carried out to examine the expandability of natural vermiculite at different heating temperatures using the non-modification and Na^+ modification methods. The thermal expansion process was experimentally performed by recording the exfoliation states and times at six different heating temperature values of 350 °C, 450 °C, 530 °C, 620 °C, 710 °C, and 840 °C, respectively, in a laboratory environment. In the study's second phase, the thermal properties of new-generation composite mortars produced with exfoliated vermiculite aggregates were experimentally analyzed. Parameters such as thermal conductivity, heat storage capacity, specific heat, and heat dissipation coefficient of mortar test samples prepared with exfoliated vermiculite aggregates are analyzed and discussed here. Test results showed that Na^+-modified vermiculite samples expanded better than non-modified vermiculite samples for all expansion temperatures. When Na^+-modified expanded vermiculite is evaluated in composite mortars, it reduces the unit weight of the mortar as it expands more, and the unit weight decreases. Accordingly, the compressive strength of the mortar decreases relatively. However, it has been determined that the thermal comfort properties of mortars using Na^+-modified exfoliated vermiculite are better than those with non-modified exfoliated vermiculite.

Cite this article as: Gündüz, L., & Kalkan, ŞO. (2022). Effects of exfoliation temperature for vermiculate aggregates modified by sodium ions on thermal and comfort properties of a new generation cementitious mortar. *J Sustain Const Mater Technol*, 7(4), 266–281.

1. INTRODUCTION

The new generation composite mortars, developed to contribute to the insulation of wall surfaces, differ from traditional mortar uses due to technical features and superior advantages. For example, unit weight values are pretty low due to the porous aggregates used in their composition. In insulation design applications in buildings, it is possible to see the development of new types of products that raise awareness, such as thermal comfort, sound transmission

***Corresponding author.**
*E-mail address: onur_kalkan@hotmail.com

loss, and resistance to fire and water effects [1, 2]. In order to provide the desired thermal comfort conditions in buildings, especially in outer partition wall sections, up to now, most materials of different origins have been used as thermal insulation materials in buildings. However, it is also often experienced that these thermal insulation materials' expected technical thermal comfort performances cannot be achieved. In particular, to ensure thermal comfort using material derivatives with an excess clearance, a low density, and low moisture content in the structure [3–5].

Global warming and the rapidly increasing climate change are among the top priority issues of the whole world. A series of practices, initiated with the Kyoto Convention and including the measures and precaution packages that should be taken to reduce greenhouse gas emissions in the world, are mainly carried out in many countries of the world. Due to the rapid depletion of primary energy resources in the world, all countries, especially developed countries, have developed methods to control their energy needs and use energy effectively. Today, most of the energy consumed in houses is for heating and cooling purposes. This energy can be effectively used with thermal insulation [2, 6]. Research studies on minimizing energy consumption and increasing energy efficiency have been among the most critical issues today. Producing new-generation thermal insulation construction elements with high performance is a potential method for solving problems such as energy consumption and environmental pollution in new projects in the construction sector. For this, developing new-generation material designs and compositions is necessary. What kind of materials, their properties, and their use in these studies are also a subject of discussion and curiosity.

Vermiculite is a natural, eco-friendly material from a group of foliated hydrous micas. Due to its unique features, it is widely applied in various fields of industry and agriculture. Natural vermiculite is a soft, flexible, and inelastic mineral with cleavages that can be divided into thin sheets characterized by the appearance of mica. Its material structure is essentially very similar to talc. Its hardness is 1.5–2.0 or more, and its density is 2.1–2.8 gr/cm^3; its color is amber, bronze, brown, green, or black. It is similar to talc, especially when wet [1, 7]. When considering the commercial use of vermiculite, hydrobiotite is generally gaining importance. This material derivative is found in commercial deposits together with biotite or phlogopite vermiculite and is defined as hydrobiotite. Vermiculite alone represents the different mineralogical groups. It is also a general term that includes all mica group minerals with industrial expansion properties.

The use of vermiculite material plays an essential role in developing new-generation mortars. Exfoliated vermiculite aggregates generally act as lightweight aggregates and have natural fiber reinforcement properties in mortar mixes. However, vermiculite derivatives are not used as aggregate material in mortar mixtures in their natural state. The heat-treated version of vermiculite exhibits an important and lightweight material characteristic. In this context, all types of vermiculite expand when exposed to high temperatures, their permeability increases, and their volume weight decreases significantly and changes shape. Depending on the high-temperature exposure location, vermiculite derivatives show similar foliation characteristics and take on a shape resembling tiny maggots.

All present technologies of vermiculite exfoliation are based on the principle that water between the layers evaporates, and the crystal layers spread out, pressured by the steam. Due to the mechanical expansion and high-temperature interaction, vermiculite leaves resemble the opening of an accordion. As a result, elongated, curved particles are formed. The material that opens like an accordion turns into a leafy and fibrous shape. This opening phenomenon varies depending on the degree of temperature and the effect time of the temperature. The material obtained in this way is called exfoliated vermiculate.

On the other hand, although vermiculite derivatives differ in their chemical content in origin, their foliar opening characteristics in temperature interaction are similar. In order to get a successful exfoliation, heating must be fast. At slow heating, evaporating water will get enough time to diffuse to the edges of a vermiculite particle and to come out. At slow heating, the steam comes out and does not manage to create enough pressure to spread out the crystal layers. The faster vermiculite is heated, the more pressure water steam creates, and the more efficiently vermiculite is exfoliated.

The advantage of exfoliated vermiculite based on thermal insulation is directly related to time under heat treatment and the amount of expansion under the effect of temperature. Different researchers have conducted alternative experimental studies to investigate the thermal expansion behaviors of vermiculite [8, 9]. Justo et al. [10] emphasized that the expansion of vermiculite with the effect of temperature is not only dependent on the evaporation of water between the layers. The main parameters affecting vermiculite's expansion are the presence of modified mica residue, the number of hydroxide groups, and its chemical composition. Several studies show these parameters can affect expansion with the effect of temperature. Feng et al. [11] analyzed the thermal expandability of vermiculite by a new Na^+ modification method in a series of experimental studies. In particular, they investigated interactions such as expansion rate, heating temperature, and natural raw vermiculite expansion times. In addition to the traditional methods for expanding raw vermiculite, it is possible to see the results of many ongoing studies on mechanical effects, chemical effects, or microwave technology expansion processes. However, in the majority of them, energy consumption during the expansion process is also high, which is also an issue that should be considered. The critical issue to be focused on is to ensure that expansion operations can be performed with minimal energy use.

Table 1. Typical physical and chemical properties of exfoliated vermiculite

Color	:	Light to dark brown	SiO_2	:	39.2
Shape	:	Accordion shaped granules	Al_2O_3	:	18.8
Moh's Hardness	:	1 to 2	TiO_2	:	2.2
pH (in water)	:	6–9	Fe_2O_3	:	11.9
Moisture loss at 110 °C	:	4–12%	CaO	:	3.8
Specific gravity	:	2.5–2.6	MgO	:	17.8
Water holding capacity	:	>180%	Na_2O	:	0.2
Sintering temperature	:	1150–1250 °C	K_2O	:	2.7
Fusion point	:	1200–1320 °C	MnO	:	0.1

New approaches have been developed for various technical parameters and evaluations in the construction industry to determine buildings' thermal comfort and performance with more realistic values. In order to be used in these approaches, numerical values of parameters representing the thermal properties of the material to be used in insulation products should be defined separately. However, it can be seen that the exact technical values for each building material related to these parametric values are not sufficiently reached, or these values are not defined as a whole [12].

In this study, a series of experimental analyses were carried out to examine the expandability of natural vermiculite at different heating temperatures using the Na^+ modification method. Technical comparisons with the values of aggregate samples without Na^+ modification are discussed. Furthermore, the thermal comfort properties of new-generation mortar designs with exfoliated vermiculite aggregates were experimentally analyzed. The thermal properties of prepared test samples are discussed comparatively. The effects of using exfoliated vermiculite on these parameters' values were examined in detail.

2. EXPERIMENTAL STUDY

2.1. Purpose of Assessment

Experimental studies were carried out on using exfoliated vermiculite aggregate in a new generation mortar design for insulation purposes and determining the effects of Na^+ modification on aggregate expansion. It was aimed to evaluate the effects of technical factors affecting the expanding amount of the exfoliated vermiculite aggregate on the thermal performance properties of the mortar combination. It is known that expanded, and lightweight aggregates are used in thermally insulated mortar products and provide insulation benefits. However, thermal comfort is evaluated by the thermal conductivity coefficient and other thermal parameters. This study determined the thermal comfort parameters of cement mortars produced using expanded vermiculite. As a separate series, vermiculite was treated with Na^+ to increase its expansion properties and was used in cement mortar. The thermal comfort properties of this series have also been determined. As a result of the study, thermal comfort parameters obtained from both separate series were compared.

2.2. Materials

2.2.1. Vermiculite and Na^+ Modification

Raw vermiculite is a hydrated magnesium-iron aluminum silicate mineral that is cost-effective and similar to Mica [13]. Vermiculite is generally formed by hydration and oxidation from phlogopite and biotite. It flakes off when exposed to high temperatures. The general appearance characteristic during the expansion process takes a worm-like shape and expands in volume [14, 15]. It takes the shape of an accordion. This property (exfoliation) forms the basis of its commercial use for vermiculite. An internal mechanical force occurs due to the evaporation of water between the layers of raw vermiculite with the effect of temperature and creating internal pressure. With the effect of this force, there is an exfoliation and separation between the layers. This creates the expansion of vermiculite. In exfoliation, the volume of vermiculite can increase by 7–8 to 12 times, while in individual flakes, the expansion rate can reach 20 times. Vermiculite density also changes with the effect of expansion. The bulk density of raw vermiculite can decrease from 640–1200 kg/m^3 to 60–160 kg/m^3 after expansion. The decrease in the unit density value varies according to the structural properties of the raw vermiculite, the time applied in the expansion, the temperature value, and the furnace ambient conditions. In general, as a result of heat treatment, an opening and expansion of approximately 20 to 30 times in volume can be obtained [16]. Vermiculite in exfoliated form is lightweight, non-combustible, layer textured, highly porous, and chemically inert. Exfoliated vermiculite is a new-generation lightweight aggregate suitable for use at temperatures between -200 °C and 1200 °C. In this way, it gains a material feature that allows the production of innovative building elements to contribute to the high-performance sound and heat insulation [1, 4, 5, 7, 17].

The vermiculite used in this study was obtained as raw material from Sivas (Türkiye) quarries under normal market conditions. The grain size of raw vermiculite is 0.5–2 mm on average, and the thickness value varies between 0.18–0.57 mm. Some technical properties are given in Table 1. Raw vermiculite material used in the experimental studies was divided into two groups, one for use in its raw form

and the other for Na^+ modification. Each group was first washed in distilled water, completely free of organic and inorganic substances, until the foreign components on the surface were cleared and dried in a ventilated circulation oven for 72 hours at 70±5 °C. Then, similar to the prescribed methodology by Feng J. et al. [11] in their research, the sample separated for Na^+ modification was placed in a container containing 0.5 mol/liter NaCl solution and subjected to ultrasonic treatment for 45 minutes and then mechanical shaking for 6 hours. This process was repeated three times; each time, the solution was replaced with a new one and left to stand for 8 hours. Then, the samples interacting in this way were washed in distilled water environment completely free of organic and inorganic substances and dried in an oven at 70±5 °C for 72 hours. By such chemical interaction, raw vermiculite aggregate samples were converted into a Na^+ modified material form before the thermal exfoliation.

Each of the raw and Na^+ modified vermiculite material groups prepared for the thermal expansion process was experimentally performed by recording the exfoliation states and times at six different heating temperature values of 350 °C, 450 °C, 530 °C, 620 °C, 710 °C, and 840 °C, respectively, in a laboratory environment. Expansion rates, expansion times, and physical changes for the temperature value of each group of materials in the furnace were determined in detail. During the expansion process with the thermal effect, each temperature and time value at which the aggregate material reaches a stable position while expanding were determined separately. Vermiculite aggregate samples that have exfoliated in an equilibrium stage were grouped to be used as the primary component aggregate in the mortar mixtures to be prepared in the next step of this study.

2.2.2. Cement

CEM 1 52.5R white cement conforming to TS EN 197–1 and TS 21 standards was used to prepare all mortar samples. It was obtained from the local market.

2.2.3. Expanded Clay and Slaked Lime

Expanded clay aggregate is a porous and lightweight aggregate obtained by heating a natural clay with expansion properties to approximately 1200 °C in a rotary kiln. Expanding gas components formed in the clay composition with the effect of temperature by causing thousands of tiny bubbles in the structure of the clay material, and an expanded aggregate material is formed in a honeycomb form. Lightweight expanded aggregate samples were obtained from the production site of a commercial enterprise in the Söğüt region of Eskişehir province of Türkiye, classified in a size range of 0–1 mm. Due to sintering during the production of expanded clay aggregate, it carries a water-impermeable shell form. In this size fraction, the average bulk density was determined as 760 kg/m^3, and the porosity rate is relatively low. It is an aggregate generally suitable for mortar mixtures requiring high strength. It can be used for fine aggregate and filling material in concrete production. Expanded clay is also a well-known lightweight concrete aggregate, and its general use is suitable for products made with dry mixes, such as masonry block construction and lightweight construction elements production.

Lime is a white-colored inorganic-based binder obtained from firing limestone at various temperatures (850–1450 °C), which, when mixed with water, solidifies in air or water, depending on its type. Lime was supplied from normal market conditions in CL 80 standard.

2.2.4. Polymer Materials

In order to facilitate the workability of mortar samples to be prepared for experimental studies, and to make it easier to settle in mold, melamine sulfonate-based superplasticizer in powder form and a small amount of cellulose were added to mixtures. A low rate of adherence-increasing powder additive was used to increase the bond strength of aggregates in mortar composition. Zinc stearate and calcium formate were added as water-repellent agents to offset exfoliated vermiculite's possible high water absorption.

2.2.5. Mixing Design

To analyze the advantages of using Na^+ modified exfoliated vermiculite aggregate and heating temperature values on aggregate expansion on the thermal and comfort properties of cement-based new-generation mortar samples, a control mix (RW0) was designed that did not use exfoliated vermiculite aggregate. A comparative experimental test was conducted. This mixture used throughout the experimental work was obtained only by mixing white cement (CE), slaked lime (LM), expanded clay (EC), and polymer additives (PL). The mix design of RW0 consists of 27% CE, 5.4% powder LM, 67% EC, and 0.67% total PL mixture, respectively. All ratios here are used by weight. RW0 mix design was used as reference test samples throughout comparative experimental analyses.

Furthermore, test samples were prepared in two separate series to evaluate the technical advantages of exfoliated vermiculite aggregate on the thermal properties of composite mortar samples. In the first batch, test specimens were prepared with exfoliated vermiculite aggregates where unmodified raw vermiculite was stabilized in expansion at six different heating temperatures (350 °C, 450 °C, 530 °C, 620 °C, 710 °C, and 840 °C, respectively). Exfoliated vermiculite aggregate was used as a fixed amount of 30% by weight in all of these samples. 27% of CE by weight, 5.4% of powder LM by weight, 37% of EC by weight, and 0.67% of polymer additives were used as remaining components in all the mixtures. In the second series, Na^+ modified exfoliated vermiculite aggregates were used in similar mixture combinations as vermiculite aggregate, provided that the weight usage rates were the same as in the first series. For each batch, test samples were prepared by designing a control mixture without using exfoliated vermiculite aggregate.

Table 2. Mix components

Mix	CE (%)	Unmodified exfoliated vermiculite vunm (%)	Na^+ modified Exfoliated vermiculite $V_{Na}{}^+$ (%)	Slaked lime LM (%)	Expanded clay CA (%)	Polymer PL (%)
RW0	27	0	–	5.4	66.96	0.64
R350	27	30	–	5.4	36.96	0.64
R450	27	30	–	5.4	36.96	0.64
R530	27	30	–	5.4	36.96	0.64
R620	27	30	–	5.4	36.96	0.64
R710	27	30	–	5.4	36.96	0.64
R840	27	30	–	5.4	36.96	0.64
RN0	27	–	0	5.4	66.96	0.64
N350	27	–	30	5.4	36.96	0.64
N450	27	–	30	5.4	36.96	0.64
N530	27	–	30	5.4	36.96	0.64
N620	27	–	30	5.4	36.96	0.64
N710	27	–	30	5.4	36.96	0.64
N840	27	–	30	5.4	36.96	0.64

Fifteen samples were poured into each batch of the exfoliated vermiculite aggregate mix. A total of 210 mortar samples were poured in two series, and the test results were examined. Mixture components are given in Table 2.

Fifteen cubic test specimens of 50 mm dimensions were cast for each mixture to ensure statistically sufficient sample numbers. The samples were kept in the mold for one day and then de-molded from the mold. Test samples were left to cure in a closed environment with a wet towel. However, humidity conditions were kept under control during the curing period. All test samples were dried in an oven at 70±5 °C after 28 days. The properties of test samples were experimentally determined for dry conditions.

2.2.6. Test Methods

The methodology applied within the scope of this study consists of two main stages: The raw vermiculite material expansion process (aggregate material preparation) and the analysis of composite mortar samples prepared with exfoliated vermiculite samples. In the first stage, firstly, raw vermiculite samples were individually exfoliated at six different heating temperatures (of 350 °C, 450 °C, 530 °C, 620 °C, 710 °C, and 840 °C, respectively), and the expansion properties and the effects of the applied temperature value on the expansion were analyzed technically. Afterward, natural vermiculite samples prepared with Na^+ modification were subjected to expansion at equivalent heating temperature values as another series of studies, and the positive effects of Na^+ modification were examined in detail. Samples of both exfoliated vermiculite aggregates were prepared separately for use as aggregate material in composite mortar mixtures according to their expansion temperatures. In the second stage, 14 different batches of cement-based composite mortar samples were prepared with the exfoliated vermiculite samples belonging to two different applications. Different additives and filling materials were used as mixture components with the exfoliated vermiculite aggregate in the mixtures of these mortar samples. The technical findings of these two research stages are discussed comparatively in the following sections.

In order to determine the consistency of the prepared mixtures, a series of flow table tests were analyzed. Flow table tests were followed based on principles stipulated by ASTM C230 standard. In the experiments, the mortar taken from the mixing bowl to the tray was placed in the mold on the flow plate so that it was half filled, and after it was hit 25 times with the mallet, the other part of the mold was filled, and another 25 strokes were applied. After the upper surface of the mold was cleaned and smoothed with a trowel, the mold was pulled out. By turning the arm of the test device five times in 15 seconds, the diameter of the flow sample was measured with the help of calipers in 2 different axes, and the average of the values read was recorded as the consistency value of the mortar.

Compressive strength was analyzed according to EN 1015–11 standard for hardened test samples at 28 days of curing time. 50 mm cube samples prepared for compressive strength tests were used. A compression test device calibrated to a maximum loading force capacity of 303 kN was used in the laboratory environment for crushing all samples. The loading rate was kept at a constant value of 0.1 kN/s in whole samples. In another test study, test samples prepared in the form of plates were analyzed for dry condition conditions after 28 days of curing to determine thermal conductivity.

A calorimeter setup that has defined technical features in experimental analyzes in the literature [18, 19] at different times can be used to analyze specific heat values. This

Table 3. Research findings of EVAM samples

Mixture	Volume weight of fresh mortar (kg/m³)	Unit volume weight (kg/m³)	Consistency (mm)	Compressive strength (N/mm²)	Thermal conductivity (W/mK)	Specific heat (J/kgK)
RW0	1117	926	144	3.47	0.216	833
R350	1070	829	161	3.19	0.136	880
R450	1046	786	157	3.07	0.127	895
R530	818	534	153	2.31	0.084	918
R620	727	443	142	1.74	0.072	964
R710	657	378	136	1.28	0.065	1018
R840	566	306	132	0.82	0.055	1080
RN0	1117	926	144	3.47	0.216	833
N350	1023	774	160	3.13	0.125	918
N450	971	701	155	2.81	0.111	925
N530	710	441	151	1.69	0.072	964
N620	592	340	139	1.11	0.059	1028
N710	516	279	133	0.58	0.052	1105
N840	431	221	130	0.41	0.045	1240

experimental method is based on determining the water temperature that occurs when a certain amount of test sample with a high temperature is added to a certain amount of water at a low temperature. The water takes up the heat, and the vessel can be calculated. The specific heat value can be calculated by balancing this value with the relation of the heat given off by the hot substance. In this study, distilled water was used as the calorimetric liquid. The specific heat value of test samples was determined by measuring with a specific heat calorimeter working as a J/kgK unit.

3. RESULTS AND DISCUSSIONS

Experimental research findings of EVAM samples are summarized in Table 3.

3.1. The Influence of Exfoliation Temperature on Vermiculate Aggregate's Thermal Expansion

Each of the raw and Na^+ modified vermiculite material groups was subjected to thermal expansion in a muffle furnace for specific periods by observing expansion phenomena at six different heating temperatures of 350 °C, 450 °C, 530 °C, 620 °C, 710 °C, and 840 °C, respectively in a laboratory environment. It is worth noting that if vermiculite is heated to a temperature of 1000 °C or higher, it transforms into clinoenstatite, which can include deformation of the material and deterioration of its thermal insulation properties [20, 21]. Therefore, the maximum heating temperature should not exceed 1000–1100 °C. The experimental study determined that the furnace temperature is a direct factor in the exfoliation time and exfoliation rate of the vermiculite aggregate, and the heating time varies between 6 and 550 s. In addition, it has been observed that the exfoliation characteristics of the vermiculite material show variable values in terms of both time and temperature values, depending on whether Na^+ is modified or not. Figure 1 shows the influence of heating temperature and time on exfoliation ratios of raw vermiculite and Na^+ modified vermiculite samples.

The exfoliation ratio increased with the increase in heating temperature. To physically evaluate the expansion characteristics of the materials at each temperature value, the ratio value of the thickness reached by the aggregate after expansion to the aggregate thickness before the expansion was determined as the "exfoliation ratio." This ratio was accepted as the parameter representing how many folds the material opened up. This value was also used as an index comparison value between materials. It was determined that the raw vermiculite exfoliated between 80 s and 540 s at a heating temperature of 350 °C, while the exfoliation ratio of the unmodified vermiculite in 80 s was 1.02; this ratio reached 2.16 at 540 s. Similarly, while the exfoliation ratio of Na^+ modified vermiculite was 1.07 in 80 s, this ratio reached 2.26 in 540 s. In other words, the effect of Na^+ modification on the exfoliation of vermiculite at this equivalent heating temperature value was 21.30% higher.

As evaluating the heating temperature value of 450 °C, it was observed that the exfoliation phenomenon varies between 50 s and 496 s. It is seen that the unmodified vermiculite reached an exfoliation ratio of 1.05 in 50 s, and this value increased to 2.56 in 496 s. It was determined that the exfoliation rate change of the Na^+ modified material was between 1.11 and 3.14 at these equivalent times. In this case, it is understood that the Na^+ modification process is 22.7% more effective in the exfoliation characteristic of vermiculite. The similar exfoliation phenomenon is typical for the other four heating temperature values of 530 °C, 620 °C, 710 °C, and 840

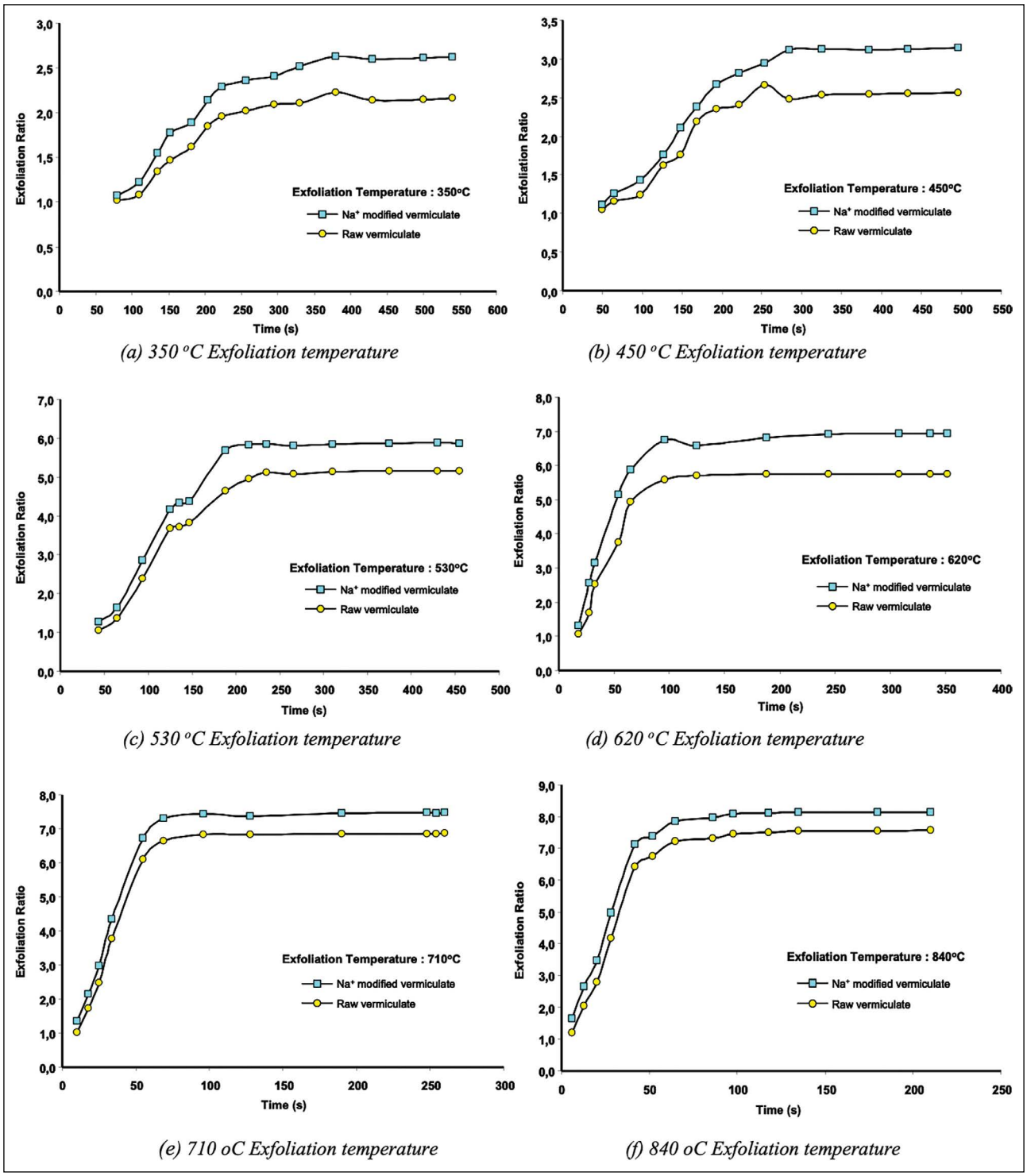

Figure 1. Influence of heating time on exfoliation ratio at different temperatures.

°C. It was observed that the exfoliation times changed as 44 s–455 s, 18 s–352 s, 10 s–260 s, and 6 s–210 s at the heating temperature changes of 530 °C, 620 °C, 710 °C, and 840 °C, respectively. The changes in the exfoliation rates of the unmodified raw vermiculite for each temperature value in these periods are 1.05–5.16, 1.06–5.76, 1.03–6.87, and 1.19–7.56, respectively. The changes in these values for Na^+ modified vermiculite were determined as 1.27–5.87, 1.32–6.94, 1.35–7.47, and 1.64–8.13, respectively. Accordingly, the effect of the Na^+ modification process on the exfoliation characteristic of vermiculite was found to be 13.76%, 20.49%, 8.73%, and 7.54% more effective for these four temperature values, respectively.

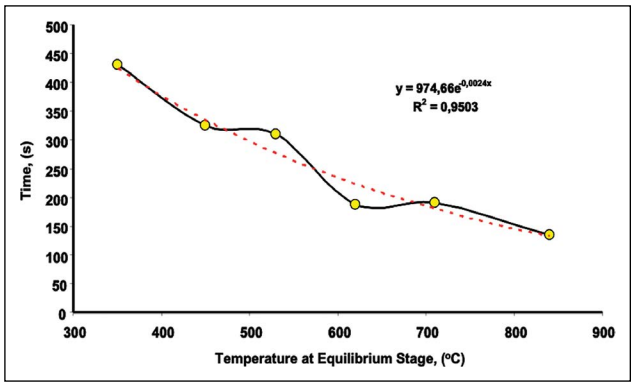

Figure 2. Heating temperature versus time at an equilibrium stage.

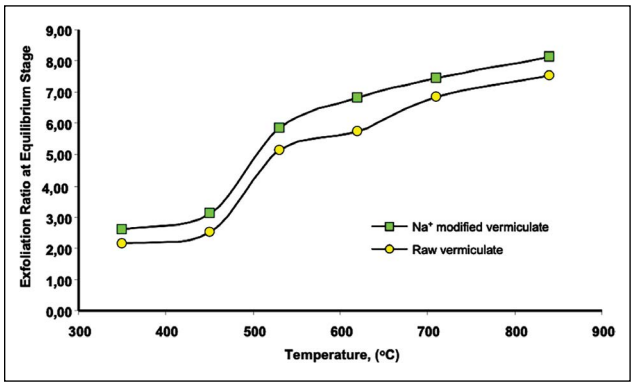

Figure 3. Heating temperature against exfoliation ratio at an equilibrium stage.

Due to the nature of vermiculite, it consists of more than one layer. The vapor pressure formed between the layers during the expansion function directly affects the exfoliation amount of vermiculite. It has been observed that the vapor pressure formed between the layers at low heating temperatures is insufficient to cause the vermiculite to exfoliate. A similar phenomenon has been reported in Feng J. et al. [11] research results, too. The increase in heating temperature shows that the steam pressure formed between the layers is sufficient to exfoliate the vermiculite, but it is seen that this exfoliation rate reaches high levels at high heating temperature values. A similar situation was observed for the modified and unmodified raw vermiculite. However, it was also clear that the effectiveness of Na^+ modification allowed for higher exfoliation. In this context, it has been shown that heating temperature is one of the essential factors for vermiculite exfoliation behavior. Similar to statements belonging to Feng J. et al. [11] and researchers with technical experience in the study of vermiculite exfoliation, the exfoliation characteristic of vermiculite may show more than one trend depending on the heating time. As can be seen, when the time-dependent exfoliation developments at different heating temperatures are examined in Figure 1, this trend can be discussed in two main parts. The first development trend is that there is a sudden exfoliation at the beginning of the expansion due to the rapid evaporation of water contained between layers. This is a general fact. As the water evaporation continues, the amount of exfoliation increases relatively. In the test analysis, it was observed that the Na^+ modification allowed the water vapor pressure between the layers of the material to be formed at a higher rate, and for this reason, it was determined that the Na^+ modification was more effective in the exfoliation amount in an equivalent time.

It has been experienced that when this water evaporation stops, the exfoliation state gains a stable position without any volume change after this process. This new situation can be characterized as the second time-dependent improvement in the exfoliation characteristic. During this

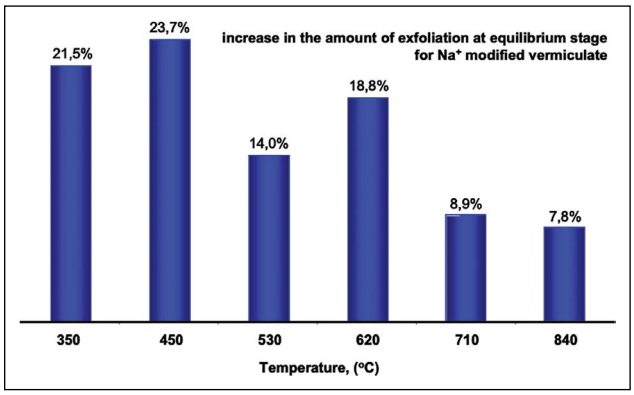

Figure 4. Heating temperature versus exfoliation ratio at the equilibrium stage.

development period, vermiculite may not exhibit an effective exfoliation rate. This trend represents the situation where vermiculite stabilizes in exfoliation. This could also be called the equilibrium stage—a higher heating temperature and shorter time for vermiculite to reach exfoliation equilibrium, depending on its structure.

When the research findings are examined in terms of the equilibrium stage, as the heating temperature value increases, the exfoliation time of vermiculite decreases; this behavior is observed significantly in both groups (Fig. 2).

While the equilibration time in exfoliation at 350 °C heating temperature is 430 s, this time decreases to 135 s at 840 °C heating temperature, depending on the increase in heating temperature. When the amount of exfoliation occurring during these periods is analyzed, it is seen that a higher rate of exfoliation is obtained at high heating temperatures. It was determined that this development showed different values for Na^+ modified and unmodified vermiculite characteristics. This change is illustrated in Figure 3 for research findings.

When Figure 3 is examined, it can be seen that when the equilibrium is reached in expansion, as the heating temperature increases, the exfoliation rates also increase.

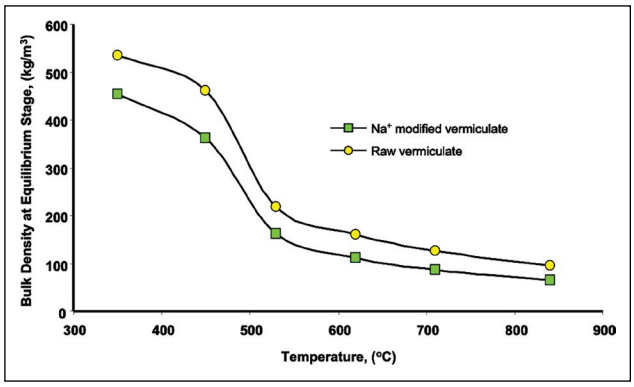

Figure 5. Heating temperature versus bulk density of vermiculites at the equilibrium stage.

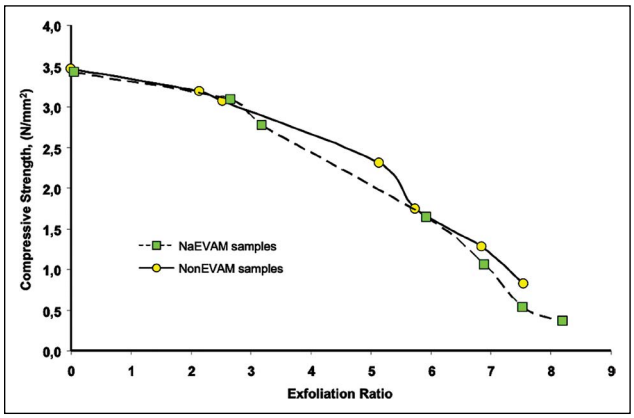

Figure 6. Effects of exfoliation ratio to the compressive strength of EVAM samples at the equilibrium stage.

Na^+ modified vermiculite, as mentioned above, exhibits an effect that significantly increases the exfoliation characteristic. The reflection of the Na^+ modification effect on the exfoliation is examined in Figure 4 as% values in the context of heating temperatures.

After the modification process, some main differences were observed in the findings. The first is that the modified samples achieve a greater exfoliation rate than the raw vermiculite samples under identical conditions. On the other hand, it exhibits lower exfoliation rates with increasing heating temperature. Another is that Na^+ modification reduces the equilibration time. In other words, modified samples need a much lower temperature value to achieve the same exfoliation rate compared to unmodified ones.

3.2. The Influence of Exfoliation Temperature on Vermiculate Aggregate's Bulk Density

The bulk density of vermiculite materials after exfoliation is essential in using this material as an aggregate. Figure 5 shows bulk density values of modified and unmodified aggregate in the exfoliation equilibrium stage at different heating temperatures. In parallel with the increase in heating temperature, it is seen that the bulk density values of the exfoliated vermiculites decrease significantly and reach more lightweight material.

For example, while the bulk density of unmodified raw vermiculite is 530 kg/m^3 after exfoliation at 350 °C, it is seen that this value decreases to 465, 190, 155, 106, and 84 kg/m^3, respectively, in terms of heating temperatures. Similarly, the values of vermiculite after Na^+ modification started from 454 kg/m^3 and changed to 379, 149, 107, 86, and 68 kg/m^3, respectively. As seen here, the Na^+ modification allows obtaining vermiculite aggregate with lower density at each temperature value after exfoliation. This makes its use as a lightweight aggregate in low-density mortar productions on the agenda. On the other hand, vermiculite aggregates with low density and high exfoliation rate become an essential primary and additive material in mortar production with higher performance due to their high pores and interlayer spaces as their thermal comfort properties. Hillier et al. [22] tried to expand raw vermiculite with grain sizes of 1–2 mm at 400 and 900 °C, and they obtained the bulk density of the exfoliated vermiculite in the range of 689–117 kg/m^3. It can also be understood from the literature results that Na^+ treatment is suitable for obtaining aggregates with lower bulk density.

3.3. The Influence of Exfoliation Temperature for Vermiculite on The Consistency of Mortar Samples

Consistency test results for exfoliated vermiculate aggregated fresh mortar are given in Table 3. Flow diameters were 144 mm for RW0 samples. Consistency was changed between 132–161 mm for mortars with whole vermiculite aggregates in the exfoliation equilibrium stage at different heating temperatures. Consistency values were also changed between 130–160 mm for mortars with Na^+ modified vermiculite aggregates in the exfoliation equilibrium stage at different heating temperatures. It has been observed that the Na^+ modification function is not a very effective parameter in the flow value of the mortar. However, aggregate exhibits a lower flow value in stationary mixed water with an increased heating temperature. The main reasons for this include the exfoliation rate, the formation of voids in the matrix structure, and the fact that it reaches low-density values.

The flow value of mortar samples with low heating temperature values is higher than that of the control sample and shows a more helpful mortar consistency feature. When examined in the context of increasing heating temperature values, it was determined that the consistency of the mortar decreased and reached a flow value of 130 mm, which can be considered a lower-limit value in the consistency of the mortar. In this context, it is observed that the flow value of non-modified exfoliated vermiculite aggregated mortar (NonEVAM) samples are, on average, 2.5%, 5%, 11.8%, 15.5%, and 18% at

increasing heating temperatures of 350 °C, 450 °C, 530 °C, 620 °C, 710 °C, and 840 °C, respectively, while the values of Na^+ modified exfoliated vermiculite aggregated mortar (NaEVAM) samples vary between on average 3.1%, 5.5%, 13.1%, 16.9%, and 18.8% respectively. This shows a decrease in the consistency of fresh mortars. Gündüz et al. [12] stated that the flowability of cement mortars is increased up to 0.73 cement-to-exfoliated vermiculite ratio, while higher cement-to-exfoliated ratio values decreased the flowability comparing cement mortars without using exfoliated vermiculite. Koksal et al. [4] concluded an increase in the workability of mortars with exfoliated vermiculite by increasing exfoliated vermiculite to cement ratio from 4/1 to 6/1 and 8/1. In the literature, it is observed that the workability evaluation of exfoliated vermiculite mortars is limited. However, the general opinion is that exfoliated vermiculite can slightly increase workability, according to the literature. However, there is a unique aspect of this study as there is no study showing the effect of vermiculite on the workability of the mortar when used with the classification of vermiculite according to the expansion temperature.

3.4. The Influence of Exfoliation Temperature for Vermiculite on Unit Weight of Mortar Samples

Unit volume weight of hardened NonEVAM and NaEVAM samples are given in Table 3. The effect of Na^+ modification on obtaining lower density values in the exfoliation of vermiculite aggregates appears to have a similar effect on the density values of mortars made with these aggregates. The control samples' density value was 926 kg/m^3. The unit weight values of NonEVAM samples change in the range of 306 kg/m^3–829 kg/m^3. Furthermore, the unit weight values of NaEVAM samples change in the range of 221 kg/m^3–774 kg/m^3. The density values of all samples are lower than those of the control sample and constitute a lighter composition. The increase in the heating temperature applied in vermiculite aggregate exfoliation caused the densities of NonEVAM and NaEVAM samples to decrease. In terms of thermal comfort, it is a general technical advantage that mortar samples have low-density values. The EVAM samples obtained at 710 °C and 840 °C temperature values represent having more good performance in terms of insulation properties. The unit weight reduction of NonEVAM samples prefixes due to the values of the increased change in heating temperature during the exfoliation process is 5.3%, 35.7%, 46.6%, 54.4%, and 63.1% for at increasing heating temperatures of 350 °C, 450 °C, 530 °C, 620 °C, 710 °C, and 840 °C, respectively, This development for NaEVAM examples ranges 9.4%, 43%, 56.1%, 63.9% and 71.4% for the same temperatures, too. Similar results can be found in the literature. Martias et al. [23] concluded that exfoliated vermiculite might reduce the unit weights of plasters up to 23.1–61%.

3.5. The Effect of Exfoliation Rate on Compressive Strength

Compressive strength values of test samples measured at 28 days are given in Table 3. NonEVAM and NaEVAM samples' Compressive strength values remained under the control test samples' values. An increase in the porosity of the matrix structure and a decrease in the unit volume weight of the samples created this result. The porous structure of an exfoliated material negatively affects the strength of the material. Experience has been gained in most research that is directly proportional to unit weight and compressive strength. Similar proportional situations are also shown between the exfoliation ratio and compressive strength of EVAM samples. This change is given graphically in Figure 6 for all sample values.

The compressive strength value for both NonEVAM and NaEVAM samples with an exfoliation ratio of 2.5 is approximately 3.1 N/mm^2. However, when the vermiculite aggregate exfoliation ratio reaches a value of 4 times, the compressive strength of NonEVAM samples is 2.4 N/mm^2, and the compressive strength of NaEVAM samples is 2.7. In other words, although NaEVAM samples had a lower density value, a higher compressive strength value was obtained compared to NonEVAM samples. Furthermore, as the exfoliation rate of the aggregate reached 5.6 times, the compressive strength values of both sample series were found to be equal (1.7 N/mm^2). If the exfoliation rate of the aggregate is more than 5.6 times, lower compressive strengths were obtained in the ratio of the strength value of NaEVAM samples up to 30% compared to NonEVAM samples. In addition, with the increase in the exfoliation rate, the compressive strength decreases. This can be explained by the porosity of the aggregate and the softness of the matrix structure. Similar reductions in compressive strength values can be found in the literature. Abdul Rahman and Babu [24] reported that the compressive strength of concretes is reduced by partially replacing natural sand with 5% and 10% EV, by weight. The seven days compressive strength values reduced to 19.8% and 33.42% with the inclusion of 5% and 10% EV, respectively, whilst the reduction in the 28 days was 5.55% and 13.59%, respectively.

However, in this study, compressive strength values of test samples provided the limit values specified in EN 998–1 [25] standard. According to this standard, mortars for insulation purposes are required to take part in CS-I or CS-II classes. According to the compressive strength of NonEVAM and NaEVAM, samples are located in the range CS-I or CS-II classes. Strength values of samples up to 5.6 times aggregate exfoliation value are included in the CS-II category, and strength values of both NonEVAM and NaEVAM samples above this exfoliation rate remain in the CS-I category. Therefore, these strength values can meet the mechanical limit values stipulated in the EN 998–1 standard [25].

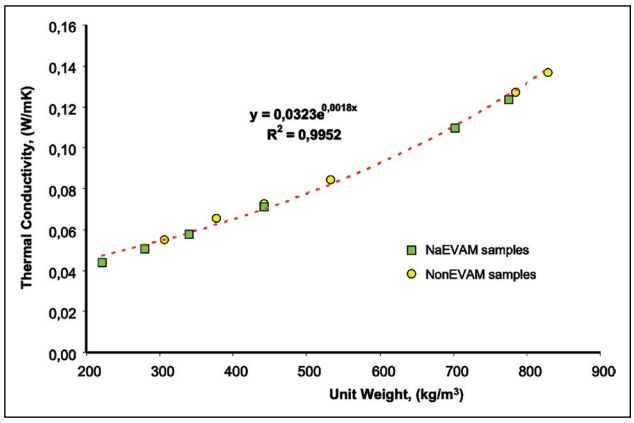

Figure 7. Density and thermal conductivity relationship.

3.6. The Effect of Na^+ Modification on Thermal Comfort Parameters

Thermal comfort properties of NonEVAM and NaEVAM samples in the form of hardened mortar were mainly analyzed in two separate groups of parameters: Parameters measured by experimental analysis and defined with the help of convergent approach calculations. Thermal conductivity (λ) and specific heat values (Cp) for test samples were determined by experimental analyses. The thermal conductivity coefficient values of NonEVAM and NaEVAM samples were determined after 28 days, and the findings are given in Table 3. It is a general technical experience that the thermal conductivity values of mortar materials that contribute to thermal insulation usually change as a function of the density value. NonEVAM and NaEVAM thermal conductivity values are lower than the thermal conductivity value of the control sample. This is also a preliminary indication that the exfoliated vermiculite aggregate mortars will have a higher added value to the thermal insulation. Lower density and lower thermal conductivity coefficient of a material are expected. Thermal conductivity changes due to the density values of NonEVAM and NaEVAM samples are given in Figure 7.

λ value of RW0 was 0.216 W/mK. λ value of NonEVAM samples using non-modified exfoliated vermiculate aggregates ranged between 0.055 W/mK and 0.136 W/mK. As the exfoliation rate for vermiculite aggregate increases due to an increase in heating temperature, λ the value of hardened mortar decreases. Although the amount of aggregate is always used at the same rate in all of these mixtures, the change in the rate of exfoliation of the aggregate has led to the fact that the mortar has acquired a structure that is more resistant to heat transfer. The phenomenon of increased porosity of the aggregate and the air gaps between the opened layers add a feature that makes the matrix structure of the material absorb less heat. A similar effect was also observed for NaEVAM samples. λ value of NaEVAM samples with using Na^+ modified vermiculate aggregates were changed between 0.045 W/mK and 0.125 W/mK. Due to the effect of Na^+ modification, a more porous structure of aggregate ensured that λ the value of mortar was lower. It has been observed that the Na^+ modification creates a more homogeneous gap geometry between the complex layers of vermiculite aggregate, and, accordingly, its thermal property improves compared with NonEVAM samples. With the use of vermiculite treated with Na^+ and expanded at 840 °C in the mortar, the thermal conductivity coefficient of the mortar decreased by 79% compared to the reference mortar. Similarly, Hodhod et al. [26] stated that using exfoliated vermiculite with the size of 0.08–0.5 mm in cement or gypsum plasters exhibited 74.12% and 76.1% reduction in thermal conductivity values compared to that of traditional cement plaster, respectively.

This research finding shows that an increase in exfoliation rates of vermiculate aggregates reduces λ value. There was an excellent linear relationship between λ the value and exfoliation rates of vermiculate aggregates in mixtures. According to the thermal conductivity values of mortars compliant with EN 998–1 standard [25], the cases of contributing to thermal insulation are divided into two separate categories: T1 (*providing thermal insulation*) and T2 (*contributing to thermal insulation*). The T1 category covers mortar samples with λ a value of <0.1 W/mK, and the T2 category covers mortar samples with λ a value of <0.2 W/mK. According to this, λ values of control samples are not included in both categories provided for in EN 998–1 standard [25]. However, it can be seen that both NonEVAM and NaEVAM samples with aggregates exfoliated at a heating temperature of 350 °C and 450 °C are in the T2 category, and the samples with aggregates exfoliated above a heating temperature of 500 °C are in the T1 category. Over the 500 °C heating temperature for exfoliation represents that both NonEVAM and NaEVAM samples have better insulating properties particularly. At lower heating temperatures, the thermal performance of the mortar decreases relatively.

Specific heat capacity (Cp) is evaluated as a measure of the ability of the mortar to absorb heat from the environment where it is applied. Cp value could be generally defined as two different technical parameters; "*Specific heat capacity at constant pressure*" and "*fixed volume-specific heat capacity.*" Fixed volume-specific heat is symbolized by "Cv." Both heat capacities are determined as cal/g°C or J/kgK. When it comes to specific heat capacity for new-generation mortars, "average specific heat capacity value (Cp)" is usually used at constant pressure. Average specific heat is an essential property of a thermal insulation material when used in conditions of temporary or unstable heat flow. Specific heat is an essential parameter of the topic "heat dissipation," which studies the change of thermal insulation throughout the material with an insulating property. Numerical values vary according to the chemical content of the material, its structural form, and the temperature of the material. The origin of the aggregate, the grain size of the aggregate and

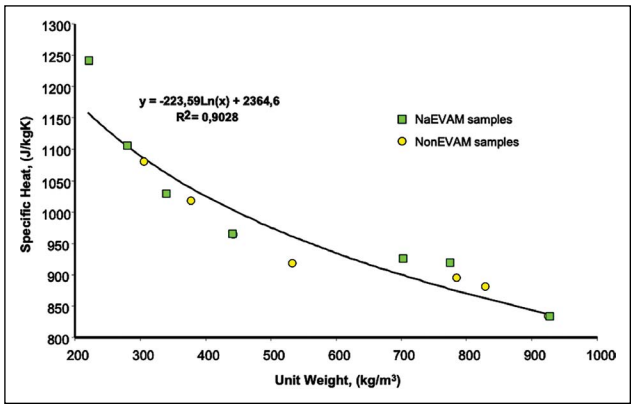

Figure 8. Density versus Cp value of tested samples.

its form of porosity, and the chemical composition of the aggregate used in the mortar combination directly affect to specific heat capacity value of a hardened mortar. However, the matrix structure and porosity that make up the dough part of the mortar are among the parameters directly affecting the specific heat value. In other words, structural form variations in the production of the aggregate also ensure the difference in the Cp value of the mortar.

The Cp value of NonEVAM and NaEVAM samples were determined after 28 days, and the findings are given in Table 3, too. Specific heat of materials could be optionally considered as a function of the density of the material. The higher the density, the lower the specific heat of the material might be expected. All research findings showed the existence of a linear relationship between specific heat and material density. This relationship for NonEVAM and NaEVAM samples is given in Figure 8.

The Cp value of the control mixture without using exfoliated vermiculate aggregates (EXVA) was 833 J/kgK. Cp values for NonEVAM samples were changed between 880 J/kgK and 1080 J/kgK. As the ratio of exfoliation for vermiculite aggregate with the increase of heating temperature increases, the Cp value of the hardened mortar increases, too. A similar effect was also observed for NaEVAM samples. The Cp value of NaEVAM samples using Na^+ modified aggregates was changed between 918 J/kgK and 1240 J/kgK. Due to the effect of Na^+ modification, a more porous structure of the aggregate ensured that the Cp value of the mortar was higher. The Cp value of NonEVAM samples develops by 1.7%, 4.3%, 9.5%, 15.7%, and 22.7% at increasing heating temperatures of 350 °C, 450 °C, 530 °C, 620 °C, 710 °C, and 840 °C, respectively, while the values of Na^+ modified exfoliated vermiculite aggregated mortar (NaEVAM) samples vary between on average 0.8%, 5%, 12%, 20.4%, and 35.5% respectively. This actually shows an improvement in the property of the specific heat capacity of the mortars. It is clearly seen that Na^+ modification on the aggregate is more effective in changing the heat capacity value of the mortar rather than in NonEVAM samples.

If heat is applied to a substance from the outside or heat is received, the temperature of the substance changes. The temperature of mortars is a measure of the energy stored in their molecules. When the temperature of the hardened mortar is increased, the molecules that gain energy generally vibrate at larger amplitudes. This growth in the vibration amplitude of a molecule causes other molecules that are close to this molecule to stay at a greater distance on average. In other words, due to the Kinetic Energy of the substance receiving heat from the outside, the vibration velocity of its particles increases. The forces that hold the particles together are defeated, and they begin to decouple from each other. This is called expansion. Suppose the substance loses heat, the Kinetic Energy of its particles decreases. The substance cools down, and the particles approach each other. When examined in this context, the ability of the mortar to conduct heat varies depending on its atomic structure. Especially in terms of materials that are considered to be used in the design or production of a new generation mortar combination for insulation purposes, it is not desirable that they have electrons moving quite freely in their structure. In a material with a minimum level of electron movement in its structure, the thermal energy transfer from one surface of the material to the other surface is almost negligible [18, 19]. As the rate of time-dependent exfoliation of vermiculite aggregates increases due to the effect of heating temperature, the electron mobility in their bodies tends to decrease. In vermiculite aggregates with Na^+ modification, the electron mobility in the exfoliated aggregate at the equivalent heating temperature is at lower levels compared to that of the whole aggregate. For this reason, the material structure also has the ability to provide higher thermal insulation by having fewer free electrons in the material. Due to increased porosity in the material and increasing exfoliation rates of vermiculite aggregates, mortar absorbs more heat from the environment. Due to the absorbed heat and mechanism mentioned above, the mortar matrix structure becomes more insulated.

Heat storage capability and heat diffusion coefficient were determined by convergent calculations. Industrially used building materials and elements have heat storage properties. During heating, it stores heat, albeit in specific amounts. In the designs of building materials that contribute to insulation, it is desirable not to store heat within the material. During heating, the building element stores the heat acting on it superficially [12, 18]. Heat storage in the structure of building elements varies depending on the unit weight of the material forming matrix structure and specific heat. The numerical value of the ability of mortar applied to the wall surface to store heat in its body gains importance in characterizing heat transfer from the applied mortar layers to contribute to the insulation [18, 19]. Storage of heat by changing the temperature of the substance is called "*sensible heat storage*," and storage by phase change is called "*latent*

Table 4. Calculation results for EVAM samples

Mixture	Heat storage (J/m^3K)	Heat diffusion coefficient ($x10^{-6}$) (m^2/sec)	Required heat for 1 °C temperature rise in 1 cm thickness (cal)
RW0	0.771	0.281	1842
R350	0.730	0.187	1743
R450	0.703	0.181	1679
R530	0.490	0.172	1170
R620	0.427	0.170	1019
R710	0.385	0.169	919
R840	0.331	0.166	790
RN0	0.771	0.281	1842
N350	0.710	0.175	1696
N450	0.649	0.171	1549
N530	0.425	0.170	1015
N620	0.349	0.169	834
N710	0.309	0.168	737
N840	0.274	0.164	655

heat storage." In sensible heat storage, besides the large heat capacity of the substance, it is desirable that it does not have combustion and flammability, that the substance maintains its properties for many years, and that it is not poisonous and corrosive. The heat storage of many materials used as building materials is generally seen as "sensible heat storage." This heat storage could be represented as heat storage capability by the expression of ρ*Cp. The abbreviation ρ indicates the density of the mortar. Heat storage of both hardened NonEVAM and NaEVAM samples is given in Table 4.

Heat storage of NonEVAM and NaEVAM samples were calculated according to the above approach. Heat storage of the control mixture without using EXVA was 0,771 J/m^3K. Heat storage of NonEVAM samples using non-modified EXVA was changed between 0.331 J/m^3K and 0.730 J/m^3K. As the exfoliation rate increases for vermiculite aggregate dependent on heating temperature, NonEVAM samples store less heat. The decrease in heat stored in the mortar represents its advantage for insulation. A similar effect was also observed for NaEVAM samples. Heat storage of NaEVAM samples using Na^+ modified EXVA was changed between 0.274 J/m^3K and 0.710 J/m^3K. Due to the effect of Na^+ modification, the low-density structure of aggregate ensured that the heat storage of mortar was much lower. To understand the effect of using EXVA in composite mortar structures based on aggregate heating temperature for exfoliation, a graphical analysis was derived for research findings. Heat storage for hardened mortar samples based on temperature is given in Figure 9.

Increasing the heating temperature for the exfoliation of the vermiculate aggregate reduces the heat storage capability of the mortar structure. Another important material property that can be taken into consideration for heat transfer in building elements is the "*heat dissipation coefficient*."

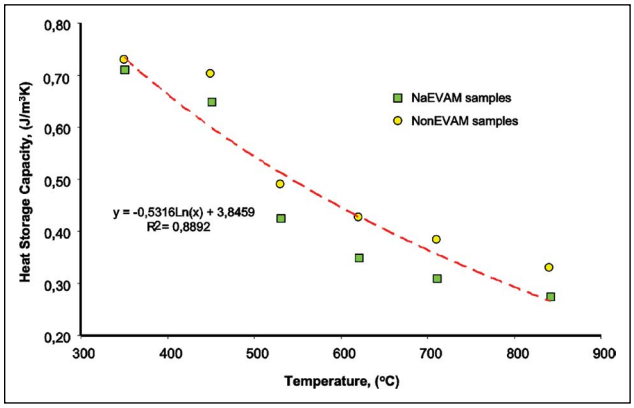

Figure 9. Heating temperature and heat storage capability relationship.

This coefficient shows how quickly heat is emitted on the surface and body of a material. Heat diffusion coefficient can be symbolized by "α, "and its unit is "m^2/sec" [12].α It is the ratio of the amount of heat transmitted in a material to the amount of heat stored in the material. α Values of hardened mortar samples are given in Table 4.

α Values of NonEVAM and NaEVAM samples were calculated based on the above approach. α The value of the control mixture without using EXVA was 0.281 m^2/sec. α of NonEVAM samples are changed between 0.166 m^2/sec and 0.187 m^2/sec. α of NaEVAM samples are also changed between 0.164 m^2/sec and 0.175 m^2/sec, too. Na^+ modification of aggregate affects the heat diffusion characteristic of the material. For example, at a heating temperature of 350 °C for the exfoliation of the aggregate, the heat diffusion property of mortar decreases by 6.42% compared to NonEVAM samples. In addition, at a heating temperature

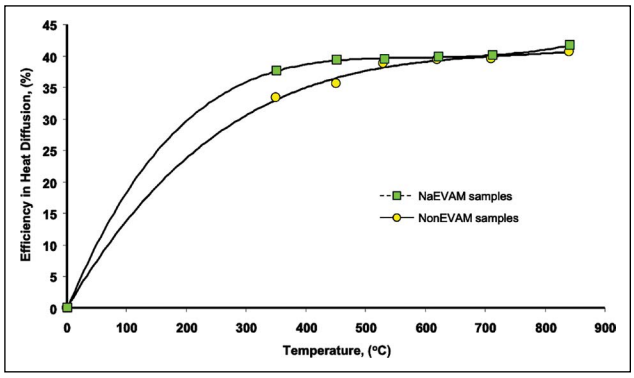

Figure 10. Heat dissipation efficiency against heating temperature.

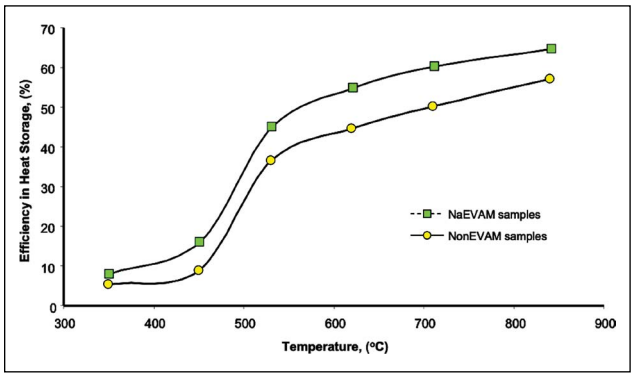

Figure 11. Heating temperature against heat storage efficiency.

of 450 °C, this property decreases by 5.52%. As reaching 710 °C heating temperature, it has been observed that the heat diffusion properties of both NonEVAM and NaEVAM samples approach each other in a convergent value. This development has shown that the effect of Na^+ modification decreases in terms of the heat diffusion property of the mortar at high exfoliation temperature values. This interaction is graphically shown in Figure 10 for NonEVAM and NaEVAM samples after 28 days of curing time.

Increasing the heating temperature for vermiculate exfoliation increases heat diffusion through composite mortar structure in the general sense. As heat dissipation for heating or cooling in the material structure decreases, insulation property improves. To measure this situation at the lowest expansion temperature, the efficiency of NonEVAM samples in heat diffusion is 33.4%, while in NaEVAM samples, this value is 37.5%. The efficiency of NonEVAM samples in heat diffusion at the highest expansion temperature value is 40.7%, while in NaEVAM samples, this value is 41.5%. This shows that materials with high thermal conductivity or low heat capacity have high heat diffusion. High heat diffusion means that heat diffusion from material to the internal environment is high, while low heat diffusion means that heat is absorbed by converting a large amount of heat into heat energy in the material. The amount of heat conduction in such materials is also at low levels. In terms of insulation performance, low heat diffusion values are required for new-generation mortars. The presence of components that will provide low heat dissipation gains importance in the design of a new-generation mortar to contribute to the insulation. While the heat capacity of the mortars using the aggregates obtained by expansion is low, the heat dissipation value of the same material may be higher. This behavior represents that the material will not absorb heat on its surface and inside, but a faster heat flow will be reflected in the indoor environment. This becomes more meaningful when the amount of heat required to increase the temperature of 1 cm thick mortar by 1 °C is determined. This behavior of the cured mortar samples is numerically summarized in Table 4.

The amount of heat required to increase the body temperature by 1 °C decreases significantly in mortar samples prepared with vermiculite aggregates with low density and high exfoliation rate. For example, vermiculite aggregate mortar samples expanded at 710 °C by 1 °C is 919 cal in NonEVAM mixtures. The value of this amount of heat is 737 cal, with a lower heat requirement for NaEVAM mixtures. When these heat requirement amounts are compared with those of the control samples, the NonEVAM mixture combination gives 50% more efficient results, and the NaEVAM mixture combination gives 60% more efficient results, too. In order to evaluate the effect of the use of EXVA on the thermal comfort properties of the mortar, a graphical analysis was made in which the comparison was made with the control mortar values. Analysis of the heat storage efficiency of hardened NonEVAM and NaEVAM samples is given in Figure 11.

Increasing the rate of vermiculate exfoliation in mortar mixes increases efficiency in heat storage. The heat is stored in the mortar and gains a more resistant characteristic against heat flow.

4. CONCLUSIONS

The exfoliation characteristics of natural vermiculate were investigated experimentally in this work. In particular, the effect of Na^+-modification on the natural vermiculate on exfoliation behavior has been revealed. In the second phase of the study, Na^+-modified and non-modified expanded vermiculite were used in lightweight composite mortar mixtures, and physical, mechanical, and especially thermal comfort properties of mortars were determined:

1. The exfoliation ratio increased with the increase in heating temperature.
2. The effect of the Na^+ modification process on the exfoliation characteristic of vermiculite was found to be 21.30%, 22.70%, 13.76%, 20.49%, 8.73%, and 7.54% more effective for 350 °C, 450 °C, 530 °C, 620 °C, 710 °C, and 840 °C, respectively.

3. Since Na^+-modified vermiculite can expand more, aggregate density is lower. Therefore, the density and strength of composite mortars produced with Na^+-modified exfoliated vermiculite were lower than composite mortars produced with non-modified exfoliated vermiculite.
4. Mortar density, which decreased due to the decrease in aggregate unit weight, improved the thermal properties of the mortar.
5. λ The value of NonEVAM samples using non-modified EXVA is changed between 0.055 W/mK and 0.136 W/mK. λ value of NaEVAM samples with using Na^+ modified EXVA are changed between 0.045 W/mK and 0.125 W/mK.
6. The specific heat of the control mixture without using EXVA was 833 J/kgK. The Cp value of NonEVAM samples using non-modified EXVA ranged between 880 J/kgK and 1080 J/kgK. The Cp value of NaEVAM samples using Na^+ modified EXVA was changed between 918 J/kgK and 1240 J/kgK.
7. Heat storage of control samples without using EXVA was 0,771 J/m^3K. Heat storage of NonEVAM samples using non-modified EXVA ranged between 0.331 J/m^3K and 0.730 J/m^3K. Heat storage of NaEVAM samples using Na^+ modified EXVA are between 0.274 J/m^3K and 0.710 J/m^3K.
8. Heat diffusion of the control mixture without EXVA was 0,281 m^2/sec. α of NonEVAM samples were between 0.166 m^2/sec and 0.187 m^2/sec. α of NaEVAM samples were also changed between 0.164 m^2/sec and 0.175 m^2/sec, too.
9. NonEVAM mixture combination gives 50% more efficient results, and NaEVAM mixture combination gives 60% more efficiency compared to reference mortar.

According to the results of the study, Na-modification considerably improves the expansion characteristics of vermiculite samples. Accordingly, the thermal comfort properties of expanded vermiculite aggregate and composite mortars produced with this aggregate have improved considerably.

ETHICS

There are no ethical issues with the publication of this manuscript.

DATA AVAILABILITY STATEMENT

The authors confirm that the data that supports the findings of this study are available within the article. Raw data that support the finding of this study are available from the corresponding author, upon reasonable request.

CONFLICT OF INTEREST

The authors declare that they have no conflict of interest.

FINANCIAL DISCLOSURE

The authors declared that this study has received no financial support.

PEER-REVIEW

Externally peer-reviewed.

REFERENCES

[1] Abidi, S., Nait-Ali, B., Joliff, Y., & Favotto, C. (2015). Impact of perlite, vermiculite and cement on the thermal conductivity of a plaster composite material: Experimental and numerical approaches. *Composites*: Part B, 68, 392–400. [CrossRef]

[2] Claramunt, J., Fernandez-Carrasco, L. J., Ventura, H., & Ardanuy, M. (2016). Natural fiber nonwoven reinforce cement composites as sustainable materials for building envelopes. *Construction and Building Materials*, 115, 230–239. [CrossRef]

[3] Kibert C. J. (2004). Green buildings: an overview of progress. *Journal of Land Use and Environmental Law*, 19(2), 491–502.

[4] Koksal, F., Gencel O., & Kaya M. (2015). Combined effect of silica fume and expanded vermiculite on properties of lightweight mortars at ambient and elevated tempretures. *Construction and Building Materials*, 88, 175–187. [CrossRef]

[5] Shoukry, H., Kotkata, M. F., Abo-El-Enein, S. A., Morsy, M. & Shebl, S. S. (2016). Enhanced physical, mechanical and microstructural properties of lightweight vermiculite cement composites modified with nano metakaolin. *Construction and Building Materials*, 112, 276–283. [CrossRef]

[6] Wu, M. H., Ng, T. S., & Skitmore, M. R. (2016). Sustainable building envelope design by considering energy cost and occupant satisfaction. *Energy for Sustainable Development*, 31, 118–129. [CrossRef]

[7] Gencel, O., del Coaz Diaz, J. J, Sutcu, M., Koksal, F., Rabanal, F. P. A., Martinez-Barrera, G., & Brostow, W. (2014). Properties of gypsum composites containing vermiculite and polypropylene fibers: Numerical and experimental results. *Energy and Buildings*, 70, 135–144. [CrossRef]

[8] Mouzdahir Y. El, Elmchaouri A., Mahboub R., Gil A., & Korili S.A. (2009). Synthesis of nano-layered vermiculite of low density by thermal treatment. *Powder Technology*, 189(1), 2–5. [CrossRef]

[9] Marwa, E. M., Meharg, A. A., & Rice, C. M. (2009). The effect of heating temperature on the properties of vermiculites from Tanzania with respect to potential agronomic applications. *Applied Clay Science*, 43(3–4), 376–382. [CrossRef]

[10] Justo, A., Maqueda, C., Pérez-Rodríguez, J. L., & Morillo, E. (1989). Expansibility of some vermiculites. *Applied Clay Science*, 4(5–6), 509–519. [CrossRef]

[11] Feng, J., Liu, M., Fu, L., Zhang, K., Xie, Z., Shi, D., & Ma, X. (2020). Enhancement and mechanism of vermiculite thermal expansion modified by sodium ions. *RSC Advances*, 10(13), 7635–7642. [CrossRef]

[12] Gündüz, L., Kalkan, Ş. O., & İsker M. (2018). A technical analysis on the effect of exfoliated vermiculite aggregate on thermal comfort parameters of com-

posite mortars for insulation purposes. *3rd International Energy Engineering Congress, UEMK 2018*, 18-19 October 2018, Gaziantep, Turkey.

[13] Patro, T. U., Harikrishnan, G., Misra, A., & Khakhar, D. V. (2008). Formation and characterization of polyurethane—vermiculite clay nanocomposite foams. Polymer Engineering & Science, 48(9), 1778–1784. [CrossRef]

[14] Macheca, A. D., Focke, W. W., Kaci, M., Panampilly, B., & Androsch, R. (2018). Flame retarding polyamide 11 with exfoliated vermiculite nanoflakes. *Polymer Engineering & Science*, 58(10), 1746–1755. [CrossRef]

[15] Binici, H. (2016). The investigation of fire resistance of composites made with waste cardboard, gypsum, pumice, perlite, vermiculite and zeolite. *Çukurova University Journal of the Faculty of Engineering and Architecture*, 31(1), 1–10. [Turkish]

[16] Kaya, A., Kirbaş, İ., & Çifci, A. (2019). Investigation of surface hardness, combustion behavior and electromagnetic shielding properties of wood composite coated with vermiculite-doped rigid polyurethane. *European Journal of Science and Technology*, (17), 206–214. [Turkish]

[17] Chung, O., Jeong, S.G., & Kim, S. (2015). Preparation of energy efficient paraffinic PCMs/expanded vermiculite and perlite composites for energy saving in buildings. *Solar Energy Materials & Solar Cells*, 137, 107–112. [CrossRef]

[18] Incropera, F. P., Dewitt, D. P., & Derbentli, T. (2010). *Isı ve kütle geçişinin temelleri*. Literatür Yayıncılık. [Turkish]

[19] Garbai, L., & Mehes, S. (2006). New analytical solutions to determine the temperature field in unsteady heat conduction. *WSEAS Transactions on Heat and Mass Transfer*, 1(7), 677–685.

[20] Rashad, A. M. (2016). Vermiculite as a construction material–A short guide for civil engineer. *Construction and Building Materials*, 125, 53–62. [CrossRef]

[21] Li, M., Zhao, Y., Ai, Z., Bai, H., Zhang, T., & Song, S. (2021). Preparation and application of expanded and exfoliated vermiculite: A critical review. *Chemical Physics*, 550, Article 111313. [CrossRef]

[22] Hillier, S., Marwa, E. M. M., & Rice, C. M. (2013). On the mechanism of exfoliation of 'Vermiculite'. *Clay Minerals*, 48(4), 563–582. [CrossRef]

[23] Martias, C., Joliff, Y., & Favotto, C. J. C. P. B. E. (2014). Effects of the addition of glass fibers, mica and vermiculite on the mechanical properties of a gypsum-based composite at room temperature and during a fire test. *Composites Part B: Engineering*, 62, 37–53. [CrossRef]

[24] Rahman, S. S. A., & Babu, G. K. (2016). An experimental investigation on light weight cement concrete using vermiculite minerals. *International Journal of Innovative Research in Science, Engineering and Technology*, 5, 2389–2392.

[25] EN 998-1, (2016). *Specification for mortar for masonry - Part 1: Rendering and plastering mortar*, 2016. https://www.en-standard.eu/bs-en-998-1-2016-specification-for-mortar-for-masonry-rendering-and-plastering-mortar/?gclid=Cj0KCQiAyracBhDoARIsACGFcS5f1F50rpz0PoOQmhSFJ2cd87nfiCL-WC6uWuWHoCfMt5FGFr5pm-saAvFjEALw_wcB

[26] Hodhod, O. A., Rashad, A. M., Abdel-Razek, M. M., & Ragab, A. M. (2009). Coating protection of loaded RC columns to resist elevated temperature. *Fire Safety Journal*, 44(2), 241–249. [CrossRef]

Journal of Sustainable Construction Materials and Technologies
Web page info: https://jscmt.yildiz.edu.tr
DOI: 10.47481/jscmt.1197471

JSCMT
Journal of Sustainable Construction Materials and Technologies

Research Article

Production and characterization of heat retardant fiber-reinforced geopolymer plates

Türkan GEZER[1], Gürkan AKARKEN[1], Uğur CENGİZ[*2]

[1]*Department of Energy Resources and Management, Çanakkale Onsekiz Mart University, Çanakkale, Türkiye*
[2]*Department of Chemical Engineering, Çanakkale Onsekiz Mart University, Çanakkale, Türkiye*

ARTICLE INFO

Article history
Received: 01 November 2022
Revised: 21 November 2022
Accepted: 22 November 2022

Key words:
Fiber-reinforced, geopolymer, metakaolin, thermal insulation

ABSTRACT

This paper presents an alternative environment-friendly thermal insulation material for the construction industry. This study aimed to produce this building material with superior heat resistance properties and comparable strength to the concrete produced with Ordinary Portland Cement. The primary purpose of the experimental studies was to produce a basic geopolymeric plate and to add cellubor and polypropylene fibers to the geopolymeric mortar. In the next stage, fiber-reinforced plates were prepared, thermal experiments were carried out, and discussions and conclusions were formed according to the results and findings. This study initially produced different types of fiber-based metakaolin plates with high heat resistance. Then, the flame test examined the heat resistance of the composite plates formed by the mixture of fibers consisting of cellubor, polypropylene, and cellubor + polypropylene fiber mixtures into geopolymeric mortars. It was found that the metakaolin plates containing approximately 6% by weight of Cellubor in the structure, besides their serious resistance to flame, their heat retardancy properties gave 72% better results than Kalekim (cementitious ceramic tile adhesive) plates and 55% better results than non-fiber metakaolin plates.

Cite this article as: Gezer, T., Akarken, G., & Cengiz, U. (2022). Production and characterization of heat retardant fiber-reinforced geopolymer plates. *J Sustain Const Mater Technol*, 7(4), 282–290.

1. INTRODUCTION

Concrete is the most used building material because of its mechanical properties, ease of handling, easy shaping, and availability of its raw materials. Producing and using that tremendous amount of concrete requires its typical constituent, ordinary Portland cement (OPC). OPC needs large amounts of natural resources for its production. 1.5–2.8 tons of raw materials are needed to produce 1 ton of OPC [1–3]. In addition, OPC production requires high temperatures of around 1500 °C, which causes large energy consumption. Thus, 12–15% of the total energy is used worldwide for all OPC production processes [4]. Energy consumption reaches about 40%, considering the construction industry. From the point of view of CO_2 emissions, 5–8% of all CO_2 emissions come from OPC production [5–7], and 1/3 of greenhouse gases emission are contributed by the construction industry [8]. Besides

***Corresponding author.**
*E-mail address: ucengiz@comu.edu.tr

the CO_2 emission, more toxic gases such as Sulfur trioxide (SO_3) and nitrogen oxide (NOx) are released into the atmosphere, which accelerates global warming and causes acid rain [9]. Recently, research has focused on developing alternative materials to OPC due to environmental and energy concerns [10–12]. One promising alternative to OPC is geopolymer material, which uses raw materials rich in aluminosilicate content and an alkaline solution to activate it [13–16]. Most of the geopolymer synthesis methods occur in this process. For example, aluminosilicate substances used in geopolymers may come from natural sources such as metakaolin (from kaolinite) or industrial wastes like fly ash and ground granulated blast furnace slag [2, 17–19]. These precursors are blended with an alkaline solution of silicate with the addition of a base, usually concentrated sodium or potassium hydroxide. The resultant material form looks similar to concrete paste but without Portland cement.

Geopolymers have many environmental and mechanical benefits over OPC [20, 21]. For example, fly ash-based geopolymers cause 80% less CO_2 in the atmosphere and consume 60% less energy during their production processes than OPC [22]. In addition, geopolymers can have better compressive strength and durability [23, 24], adjustable strength and workability [25–27], lower shrinkage and creep [28], better resistance against chlorides, acid attacks [29, 30], superior fire resistance [31], and improved thermal insulation properties [28]. Moreover, geopolymers can reach 90% of their top compressive strength in the first 72 hours [32]. This specialty makes it an ideal choice for early strength applications [33].

Using these alternative products has increased attention in construction due to the critical solution of decarbonization and energy-saving. Integration and formulation of thermal properties have been proven preferable by improving the energy efficiency and durability of the buildings [34]. One of the under research and promising applications of geopolymers are fireproof and fire retardant products [35–37]. In addition, some publications have shown their potential as thermal barriers [38, 39]. These studies proved that geopolymers could be used against fire and show high thermal stability.

One of the properties of the geopolymers, brittle behavior, puts a limitation on the application areas of geopolymer materials [40, 41]. Nowadays, researchers are trying to solve this problem to improve this mechanical property [42, 43]. Fiber-reinforcing is a well-known solution to overcome this problem. For this reason, researchers' studies with different types of fibers focused on reinforcing geopolymer [37], [44]. Polymer fibers are the first preferable for reinforcing the geopolymers [43]. Improving the mechanical properties, especially bending strength, is the main reason for adding fibers into geopolymer. The addition of some chemical fibers into geopolymers can reveal some benefits. Fiber reinforcing can cause better properties, such as higher resistance to fire or a decrease in thermal conductivity, depending on their types [44, 45].

The main objective of this study is to produce an alternative environment-friendly thermal insulation material for the market. Moreover, this study aimed to produce this building material with superior heat resistance properties and comparable strength to the concrete produced with OPC. For this purpose, commercially purchased metakaolin was used as precursor material. Alkaline solutions were prepared with NaOH, KOH, SiO_2, and Na_2O. The geopolymerization was obtained by mixing metakaolin and the alkaline solution at room temperature. Cellubor (CB) and polypropylene (PP) fibers were used as reinforced materials to improve the heat resistance properties of the geopolymer products. The study resulted in a thermal comparison of fiber-reinforced geopolymer plates and plates prepared with OPC. It was found that the heat resistance properties of metakaolin plates containing fibers gave 55% better results than metakaolin plates without fibers.

2. MATERIALS AND METHODS

2.1. Materials

The primary material used in this work, metakaolin, was purchased from AVS Mineral. 100 grams of metakaolin was used for each sample. The activator consists of water, NaOH, and commercial sodium silicate containing 28.7% SiO_2, 8.9% Na_2O, and 62.4% H_2O by weight (Sodel Chemistry, Module: 2). Module for silicate is defined as SiO_2/Na_2O ratio. NaOH was obtained from Interlab. All solutions were prepared with pure water.

This study used PP fibers (Beton Fiber BF06 Polypropylene fibers) obtained from Beton Fiber company. It is preferred to increase concrete strength, abrasion resistance, and toughness and prevent crack formation, manufactured from cold drawn wire according to ASTM A820 standard. Polypropylene fiber homogeneously dispersed in the mortar aims to prevent loading cracks by increasing the toughness of the mortar and its ability to absorb energy. Polypropylene fiber-reinforced concretes have high bending, fracture, and compressive strength. They also have high temperatures, high chemical resistance, and a relatively low-density structure. In addition, they are entirely electronic, heat, and sound insulation products [46].

Another type of fiber used in this study is cellubor fiber. Cellubor fiber, a boron-combined cellulosic insulation material, is a dark green material consisting of a combination of newspaper papers used as waste through various processes using a boron mine. It contains 70–75% by mass of waste paper and 23% boron compounds to increase its flame retardant capability. Since waste paper is used, it has an environmentally friendly structure. It can be used as a heat insulation material on ceilings, attics, floors, and walls [47].

Table 1. The contents of the produced plates

Sample	Metakaolin (g)	Kalekim (g)	Sodium silicate (g)	NaOH (g)	Water (g)	CB-fiber (g)	PP-fiber (g)	Fiber (wt. %)
Fiber free Kalekim	0	200	–	–	50	–	–	0
Fiber free	100	–	82.30	18.30	50	–	–	0
PP1	100	–	82.30	18.30	50	–	0.75	0.74
PP2	100	–	82.30	18.30	50	–	1.13	1.11
PP3	100	–	82.30	18.30	50	–	1.50	1.47
PP4	100	–	82.30	18.30	50	–	1.88	1.84
PP5	100	–	82.30	18.30	50	–	2.25	2.20
CB1	100	–	82.30	18.30	50	2	–	1.96
CB2	100	–	82.30	18.30	50	3	–	2.91
CB3	100	–	82.30	18.30	50	4	–	3.84
CB4	100	–	82.30	18.30	50	5	–	4.76
CB5	100	–	82.27	18.24	50	6	–	5.66
CBPP1	100	–	82.27	18.24	50	2	0.75	2.67
CBPP2	100	–	82.27	18.24	50	3	1.125	3.96
CBPP3	100	–	82.27	18.24	50	4	1.5	5.21
CBPP4	100	–	82.27	18.24	50	5	1.875	6.43
CBPP5	100	–	82.27	18.24	50	6	2.25	7.62

2.2. Methods

2.2.1. Formulation of Geopolymer Prescriptions

The formation and preparation of the geopolymeric plates generally consist of simple steps (Fig. 1). Therefore, the primary purpose of the experimental studies was to produce a basic geopolymeric plate and to add CB and PP fibers into the geopolymeric plate. In the next stage, fiber-reinforced boards were prepared, thermal experiments were carried out, and discussions and conclusions were formed according to results and findings.

In the first stage, studies were carried out using different recipes on the ratios of compounds (Na_2O/NaOH, H_2O/Na_2O) and fibers in different ratios to find the primary geopolymeric plate with the most perfect thermal and structural properties. Initially, sixteen main geopolymeric plates and one Kalekim (Cementitious ceramic tile adhesive) plate sample were produced. Then, the mechanical properties and heat resistance tests of the geopolymeric plates were carried out at the end of seven days. The ratios of substances and fibers that made up the content of the seventeen samples investigated are shown in Table 1.

2.2.2. Preparation of Geopolymers

It is based on the combination of metakaolin used in the production phase of the geopolymeric plate with alumina silicate in an alkaline environment. As the first step, the NaOH compound in the solid phase was measured on a precision balance based on predetermined calculations and transferred to the beaker. In the next step, sodium silicate and distilled water were added to the calculated amount. After, the solution was mixed for 10 minutes until the sodium hydroxide particles melted and became homogeneous in the mixer. After mixing, the solution was left to cool at room temperature and rested until it reached room temperature. If the resting phase is not performed, lumps occur in the mortar, making it more challenging to obtain a homogeneous mortar.

No heat was needed for the solution during the mixing phase because the geopolymerization reaction was exothermic. During the mixing stage, the mixing was covered to ensure minimum water loss so that the water from the solution was not evaporate. After the alkaline solution reached 25 °C, it was added and mixed gently and slowly on the metakaolin, which was prescribed and weighed. At this stage, fibers were added to the paste gradually and mixed in a mechanical mixer to have a homogenous structure. The mixing phase should last for a minimum of 10 minutes. Homogenizing the resulting mortar was an essential factor for the thermal and mechanical quantities of the geopolymer. Mixed and homogenized geopolymer mortars were poured into metal molds measuring 15 cm x 15 cm x 5 cm. After curing for 24 hours at room temperature, they were removed from the molds.

2.2.3. Testing

The flame gun used in the experiments is Integra Flameboy brand. It is a portable, hand-held, and battery-free Bunsen burner that provides piezo-electric ignition at the push of a button. In addition, the size and temperature of the flame can be easily adjusted with an air

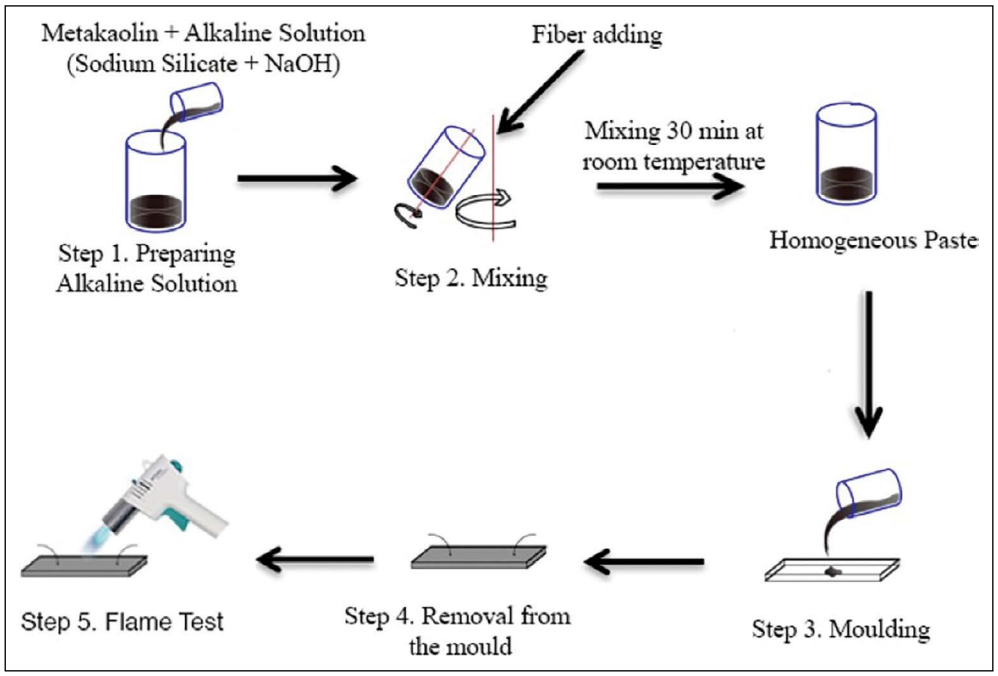

Figure 1. Geopolymer production process.

Figure 2. Flame test.

and gas regulator. The thermocouple thermometer used in this study is UDL 100 brand. It measures the front and back side temperature of the plates. The flame test was applied directly on the panel from a 25 cm distance clamped between the aluminum panel, as seen in Figure 2. The plates' front and back surfaces temperature are recorded at a speed of one-tenth of a second with J-type temperature meters connected to the computer. At this time, the flame-prone plate surface was also measured using an infrared thermometer. Thus, the temperature monitoring of the front surface is measured simultaneously with different measurement techniques.

Table 2. Fiber-free metakaolin and Kalekim plate flame test results

Sample	T_{Front}-Max (°C)	T_{Back} (°C)	t_{Back} (s)	t_{Back} (s) (@50 °C)	Δt_{Back} (s)
Metakaolin plate	909.8	27.9	39	60	21.0
Kalekim plate	880.2	32.2	16	28	12.0

3. RESULTS AND DISCUSSIONS

Fiber-containing geopolymer plates, fiber-free geopolymer, and Kalekim plates were fabricated. The study consists of 2 stages. The first step was to perform flame tests of fiber-free metakaolin and Kalekim plates and to determine the time it takes for the back side temperature to reach 50 °C. The second stage of the study was the flame tests of the fiber plates and the determination of flame retardancy.

A procedure has been developed to compare the study flame test results. Accordingly, the plate's maximum temperature reached by the front side was T_{Front}-Max. When the T_{Front}-Max temperature was determined, the back temperature of the plate was recorded as back-plate temperature "T_{Back}" (24±0.5 °C). In addition, the time elapsed from the start of the flame test to the occurrence of these temperatures (T_{Front}-Max and T_{Back}) was recorded as the "t_{Back}" time. T_{Back} (°C) temperature and

Table 3. Flame test results of metakaolin plates containing different ratios of CB fiber

Sample	Fiber (Wt.%)	T_{Front}-Max (°C)	T_{Back} (°C)	t_{Back} (s)	t_{Back}(s) @50 °C	Δt_{Back} (s)
CB1	1.96	903	24.6	22	52	30.0
CB2	2.91	860.2	20.3	14	44	30.0
CB3	3.84	890.6	24.1	18	48	30.0
CB4	4.76	873.2	24.4	15	50	35.0
CB5	5.66	851.1	24	17	60	43.0

Table 4. Flame test results of metakaolin plates containing PP fiber in different ratios

Sample	Fiber (Wt.%)	T_{Front}-Max (°C)	T_{Back} (°C)	t_{Back} (s)	t_{Back}(s) @50 °C	Δt_{Back} (s)
PP1	0.74	852.7	22.8	20	50	30.0
PP2	1.11	986.7	22.5	15	47	32.0
PP3	1.47	772.2	24.4	20	51	31.0
PP4	1.84	872.2	24.1	19	52	33.0
PP5	2.20	828.5	24.6	18	46	28.0

the t_{Back} (s) time were defined as the initial temperature and time of the back plate. The first time the back plate reaches 50 °C, it was reported as "t_{Back} (s) @ 50 °C" in the test records. This value measures how long after the start of the experiment the backplate reaches 50 °C. The difference between the time of the front and back of the plate to reach the same temperature was expressed as "Δt_{Back} (s)." This period shows how long the plate transmits the heat from the front side to the backside.

Firstly, the flame test of the fiber-free Kalekim plate was performed. The heat delay time of the Kalekim plate was found to be 12 seconds. In the same experiment, when it is made with a metakaolin plate that does not contain any fiber, it is seen that the back side of the plate reaches 50 °C in the 21st second. Therefore, the metakaolin plate provided heat retardancy 9 seconds longer than the Kalekim plate (Table 2).

The back side of the fiber-free metakaolin plates was observed to reach 50 °C 9 seconds later than the Kalekim plate. This heat transfer delay was due to the metakaolin structure [48]. The back plate temperature of metakaolin reached 27.9 °C after 39 s of the start of the experiment at the 909.8 °C of the front plate. Regarding the Kalekim plate, the T_{Back} reached 32.2 °C at 16 s after the experiment at the 880 °C of the front plate. Therefore, when the duration of reaching 50 °C is compared to both plates, the Metakaolin plate was reached after 32 s than the Kalelim plates, which was essential delaying of heat transfer.

Regarding fiber-reinforced plates, CB, PP, and CB+PP mixed fibers were used to obtain fiber-containing metakaolin plates. Flame test analysis results of CB series metakaolin plates containing cellubor fiber in different ratios are shown in Table 3.

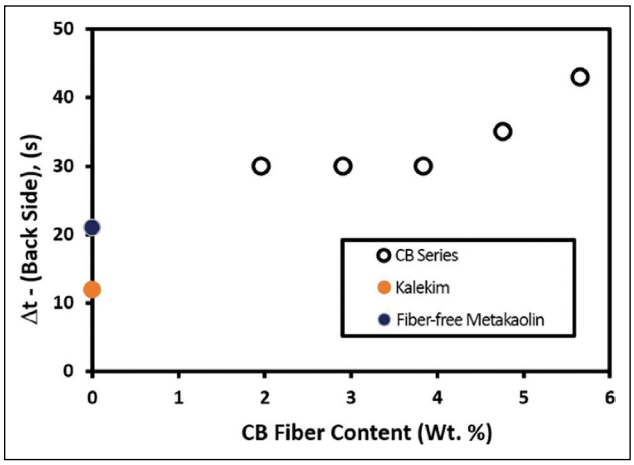

Figure 3. Metakaolin plates flame retardant time variation due to increased CB fiber content.

The t_{back} @50 °C of CB fiber-reinforced metakaolin increased depending on increasing CB fiber content after 3% wt in the metakaolin mortar. The variation of flame retardancy times according to the fiber ratio of metakaolin plates containing different ratios of CB fiber is given in Figure 3. When the CB-fiber content was up to 3% wt, no relation was observed between CB and the t_{back} @50 °C, and heat transfer delaying remained constant. However, a linear trend was observed after 3% wt of fiber content due to the CB fiber heat resistance property. In addition, even with 1.96% wt of CB, the heat transfer delay was observed comparing the fiber-free metakaolin and Kalekim plates (Fig. 3).

Regarding the PP fiber-reinforced metakaolin plates, no relation was observed between the heat transfer delay and fiber content, as shown in Table 4.

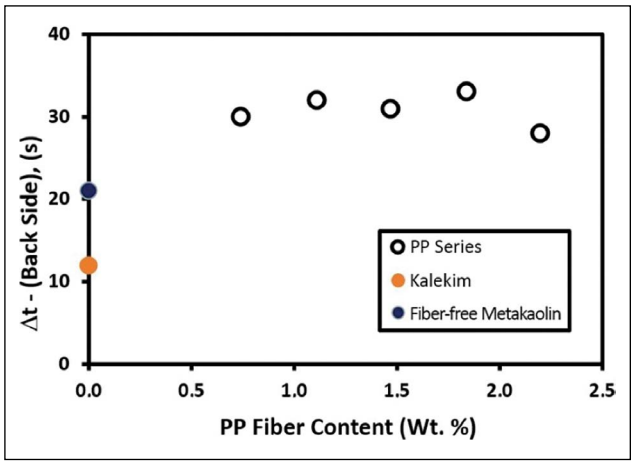

Figure 4. Metakaolin plate flame retardant time change due to increased PP fiber content.

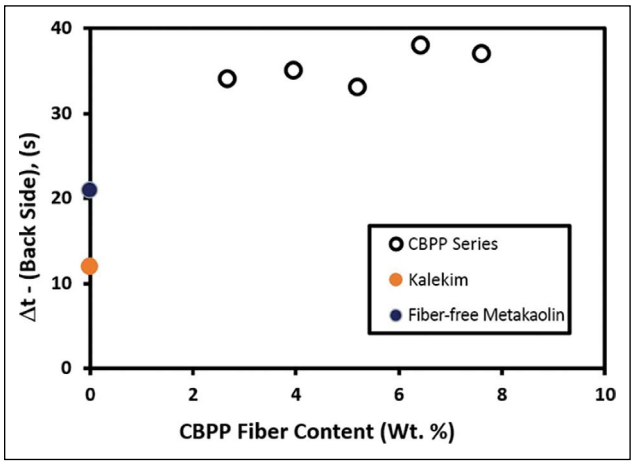

Figure 5. Change of flame-retardant time of metakaolin plate due to increasing CB+PP fiber mixture.

Table 5. Flame test results of metakaolin plates containing different ratios of CB+PP fiber mixture

Sample	Fiber (Wt.%)	T_{Front}-Max (°C)	T_{Back} (°C)	t_{Back} (s)	t_{Back}(s) @50 °C	Δt_{Back} (s)
CBPP1	2.67	878.2	23.1	15	49	34.0
CBPP2	3.96	842.7	23.9	12	47	35.0
CBPP3	5.21	815.8	23.9	10	43	33.0
CBPP4	6.43	907.1	23.9	14	52	38.0
CBPP5	7.62	808.2	24.0	25	62	37.0

The variation in flame retardancy times according to PP fiber content is given in Figure 4. This figure indicated that constant flame retardancy times were observed despite increasing the fiber ratio. It is due to the lower PP fiber melting properties. The PP fiber melts after 120 °C and fills the porous structure of the metakaolin. Thus, the heat-delaying properties are reduced due to the lowering space of the metakaolin. However, PP fiber-reinforced metakaolin plate has better heat retardancy than the fiber-free metakaolin and Kalekim plates.

The CB and PP mixed fibers were also investigated for the thermal performance of metakaolin plates. The flame test results of CBPP series metakaolin plates containing CB+PP fiber mixture in different ratios are given in Table 5.

The variation of flame retardancy times according to the fiber ratio of metakaolin plates containing CBPP fiber in different ratios is seen in Figure 5. This figure indicated that constant flame retardancy times were observed despite increasing the fiber ratio similarly to PP-containing metakaolin plates (Fig. 4). This similarity is due to the melting properties of PP fibers. However, the introduction of CB fiber in PP fiber-reinforced metakaolin plates showed more heat insulation (Fig. 5). In addition, CBPP fibers brought approximately three times stronger fire retardancy to the Kalekim plate and 1.5 times to the metakaolin fiber-free plate (Fig. 5).

4. CONCLUSIONS

This paper produced CB, PP, and CBPP fiber-reinforced geopolymer plates. The flame tests of the plates were carried out. First, according to the flame test results, all the mortars reinforced with fibers showed higher heat retardancy than the fiber-free metakaolin and Kalekim mortars. Depending on the increased CB ratio, it was observed that the temperatures of the back parts of the plates reached 50 °C in between 20 and 43 seconds. Furthermore, it was found that the metakaolin plate containing 5.66% by weight of CB showed approximately 55% more heat retardancy than the fiber-free metakaolin plate and 72% more than the fiber-free Kalekim plate.

On the other hand, the performance of PP-containing metakaolin plates did not change seriously depending on the variation of PP content, and the time to reach 50 °C for the back plate was around 31±2 seconds. This result indicated that a small amount of PP in the building is enough to supply heat resistance. However, heat resistance performance remained stable despite the increasing PP content. It is due to the filling of the gaps with melting PP. Although the flame test results of CBPP series metakaolin plates containing a certain amount of PP and CB blended fibers are relatively good compared to plates containing only PP fibers but not good as CB fibers. The melting PP reduced the gaps between

the CB fibers, so the heat retardancy performance decreased compared with the CB fiber-reinforced metakaolin plates.

As a result of the experiments, it was found that the metakaolin boards containing approximately 6% by weight of CB in the structure showed 72% better heat resistance results than Kalekim boards and 55% better results than non-fiber metakaolin boards. This study is a pioneering study in producing fiber-containing plates, and it is expected that the produced plates will be used as building materials in the construction industry in future studies, as they have both heat resistance and fire retardant properties.

ETHICS

There are no ethical issues with the publication of this manuscript.

DATA AVAILABILITY STATEMENT

The authors confirm that the data that supports the findings of this study are available within the article. Raw data that support the finding of this study are available from the corresponding author, upon reasonable request.

CONFLICT OF INTEREST

The authors declare that they have no conflict of interest.

FINANCIAL DISCLOSURE

This work was supported by Çanakkale Onsekiz Mart University, The Scientific Research Coordination Unit, Project number: FYL-2019-3084.

PEER-REVIEW

Externally peer-reviewed.

REFERENCES

[1] Aly, A. M., El-Feky, M. S., Kohail, M., & Nasr, E. S. A. (2019). Performance of geopolymer concrete containing recycled rubber. *Construction and Building Materials*, 207, 136–144. [CrossRef]

[2] Park, Y., Abolmaali, A., Kim, Y. H., & Ghahremannejad, M. (2016). Compressive strength of fly ash-based geopolymer concrete with crumb rubber partially replacing sand. *Construction and Building Materials*, 118, 43–51. [CrossRef]

[3] Davidovits, J. (1994). Global warming impact on the cement and aggregates industries. *World resource review*, 6(2), 263–278.

[4] Rashad, A. M., & Sadek, D. M. (2020). Behavior of alkali-activated slag pastes blended with waste rubber powder under the effect of freeze/thaw cycles and severe sulfate attack. *Construction and Building Materials*, 265, Article 120716. [CrossRef]

[5] Akbarnezhad, A., Huan, M., Mesgari, S., & Castel, A. (2015). Recycling of geopolymer concrete. *Construction and Building Materials*, 101, 152–158. [CrossRef]

[6] Qiu, J., Ruan, S., Unluer, C., & Yang, E. H. (2019). Autogenous healing of fiber-reinforced reactive magnesia-based tensile strain-hardening composites. *Cement and Concrete Research*, 115, 401–413. [CrossRef]

[7] Teh, S. H., Wiedmann, T., Castel, A., & De Burgh, J. (2017). Hybrid life cycle assessment of greenhouse gas emissions from cement, concrete and geopolymer concrete in Australia. *Journal of Cleaner Production*, 152, 312–320. [CrossRef]

[8] Ruparathna, R., Hewage, K., & Sadiq, R. (2016). Improving the energy efficiency of the existing building stock: A critical review of commercial and institutional buildings. *Renewable and Sustainable Energy Reviews*, 53, 1032–1045. [CrossRef]

[9] Rajendran, M., & Akasi, M. (2020). Performance of crumb rubber and nano fly ash based ferro-geopolymer panels under impact load. *KSCE Journal of Civil Engineering*, 24(6), 1810–1820. [CrossRef]

[10] Tchadjie, L. N., & Ekolu, S. O. (2018). Enhancing the reactivity of aluminosilicate materials toward geopolymer synthesis. *Journal of Materials Science*, 53(7), 4709–4733. [CrossRef]

[11] Turner, L. K., & Collins, F. G. (2013). Carbon dioxide equivalent (CO_2-e) emissions: A comparison between geopolymer and OPC cement concrete. *Construction and Building Materials*, 43(6), 125–130. [CrossRef]

[12] Prakasan, S., Palaniappan, S., & Gettu, R. (2020). Study of energy use and CO_2 emissions in the manufacturing of clinker and cement. *Journal of The Institution of Engineers (India): Series A*, 101(1), 221–232. [CrossRef]

[13] Krivenko, P. (2017). Why alkaline activation–60 years of the theory and practice of alkali-activated materials. *Journal of Ceramic Science and Technology*, 8(3), 323–333.

[14] Yeddula, B. S. R., & Karthiyaini, S. (2020). Experimental investigations and prediction of thermal behaviour of ferrosialate-based geopolymer mortars. *Arabian Journal for Science and Engineering*, 45(5), 3937–3958. [CrossRef]

[15] Davidovits, J. (1988). Geopolymer Chemistry and properties. *Proceedings of the geopolymer '88 first international conference on soft mineralurgy* (pp. 25–48). Geopolymere.

[16] Davidovits, J. (1988) Geopolymers of the first generation: SILIFACE-process. *Proceedings of the geopolymer '88 first international conference on soft mineralurgy* (pp. 49–67). Geopolymere.

[17] Luhar, S., Chaudhary, S., & Luhar, I. (2019). Development of rubberized geopolymer concrete: Strength and durability studies. *Construction and Building Materials*, 204(3), 740–753. [CrossRef]

[18] Amran, Y. M., Alyousef, R., Alabduljabbar, H., & El-Zeadani, M. (2020). Clean production and properties of geopolymer concrete; A review. *Journal of Cleaner Production*, 251, Article 119679. [CrossRef]

[19] Zaetang, Y., Wongsa, A., Chindaprasirt, P., & Sata, V. (2019). Utilization of crumb rubber As aggregate in high calcium fly ash geopolymer mortars. International Journal of Geotechnique, Construction Materials and Environment, 17(64), 158–165. [CrossRef]

[20] Li, Z., Ding, Z., & Zhang, Y. (2004). Development of sustainable cementitious materials. In K. Wang (Ed.), *Proceeding of the International Workshop Sustainable Development Concrete Technology* (pp. 55–76). Center for Transportation Research and Education.

[21] Duxson, P., Provis, J. L., Lukey, G. C., & Van Deventer, J. S. (2007). The role of inorganic polymer technology in the development of 'Green Concrete'. *Cement and Concrete Research*, 37(12), 1590–1597. [CrossRef]

[22] Łach, M., Mikuła, J., Lin, W. T., Bazan, P., Figiela, B., & Korniejenko, K. (2020). Development and characterization of thermal insulation geopolymer foams based on fly ash. *Proceedings of Engineering and Technology Innovation*, 16, 23–29. [CrossRef]

[23] Ding, Y., Dai, J. G., & Shi, C. J. (2016). Mechanical properties of alkali-activated concrete: A state-of-the-art review. *Construction and Building Materials*, 127, 68–79. [CrossRef]

[24] Ding, Y., Dai, J. G., & Shi, C. J. (2018). Fracture properties of alkali-activated slag and ordinary Portland cement concrete and mortar. *Construction and Building Materials*, 165(3), 310–320. [CrossRef]

[25] Wang, Y. S., Provis, J. L., & Dai, J. G. (2018). Role of soluble aluminum species in the activating solution for synthesis of silico-aluminophosphate geopolymers. *Cement and Concrete Composites*, 93, 186–195. [CrossRef]

[26] Wang, Y. S., Alrefaei, Y., & Dai, J. G. (2020). Influence of coal fly ash on the early performance enhancement and formation mechanisms of silico-aluminophosphate geopolymer. *Cement and Concrete Research*, 127, Article 105932. [CrossRef]

[27] Alrefaei, Y., Wang, Y. S., & Dai, J. G. (2019). The effectiveness of different superplasticizers in ambient cured one-part alkali activated pastes. *Cement and Concrete Composites*, 97, 166–174. [CrossRef]

[28] Azmi, A. A., Al Bakri, A. M., Ghazali, C. M. R., Sandu, A. V., Kamarudin, H., & Sumarto, D. A. (2016). A review on fly ash based geopolymer rubberized concrete. *Key Engineering Materials*, 700, 183–196. [CrossRef]

[29] Song, X.J., Marosszeky, M., Brungs, M., & Munn, R. (2005). Durability of fly ash based geopolymer concrete against chloride and sulphuric acid attack. *10DBMC International Conference of Durability of Building Material Components*, Lyon, France, 1507–1510.

[30] Deb, P. S., Sarker, P. K., & Barbhuiya, S. (2016). Sorptivity and acid resistance of ambient-cured geopolymer mortars containing nano-silica. *Cement and Concrete Composites*, 72, 235–245. [CrossRef]

[31] Aziz, I. H., Abdullah, M. M. A. B., Yong, H. C., Ming, L. Y., Hussin, K., Kadir A. A., & Azimi, E. A. (2016). Manufacturing of fire resistance geopolymer: A review. *MATEC Web Conferences*, 78, Article 01023. [CrossRef]

[32] Bakri, A. M., Kamarudin, H., Binhussain, M., Nizar, I. K., Rafiza, A. R., & Zarina, Y. (2013). Comparison of geopolymer fly ash and ordinary portland cement to the strength of concrete. *Advanced Science Letters*, 19(12), 3592–3595. [CrossRef]

[33] Rosenberger, R.K. (2018). Behavior of reinforced crumb rubber ordinary portland cement and geopolymer concrete beams. *UNSW Canberra ADFA, Journal of Undergraduate Engineering Research*, 11, 1–25.

[34] Ahmad, M.R., Chen, B., & Shah, S.F.A. (2019). Investigate the influence of expanded clay aggregate and silica fume on the properties of lightweight concrete. *Construction Building Materials*, 220, 253–266. [CrossRef]

[35] Hýsek, Š., Frydrych, M., Herclík, M., Louda, P., Fridrichová, L., Le Van, S., & Le Chi, H. (2019). Fire-resistant sandwich-structured composite material based on alternative materials and its physical and mechanical properties. *Materials*, 12(9), Article 1432. [CrossRef]

[36] Le, V. S., Louda, P., Tran, H. N., Nguyen, P. D., Bakalova, T., Ewa Buczkowska, K., & Dufkova, I. (2020). Study on temperature-dependent properties and fire resistance of metakaolin-based geopolymer foams. *Polymers*, 12(12), Article 2994. [CrossRef]

[37] Mikuła, J., & Łach, M. (2007). Geopolymers—A new environment friendly alternative to concrete based on portland cement, Part 1— Introduction. In: Mikuła J, (Ed.). *Pro-Ecological Solutions in the Field of Production. Modern Environmentally Friendly Composite Materials*. Cracow University of Technology. (1), pp. 13–179.

[38] Łach, M., Korniejenko, K., & Mikuła, J. (2016). Thermal insulation and thermally resistant materials made of geopolymer foams. *Procedia Engineering*, 151, 410–416. [CrossRef]

[39] Shill, S. K., Al-Deen, S., Ashraf, M., & Hutchison, W. (2020). Resistance of fly ash based geopolymer mortar to both chemicals and high thermal cycles simultaneously. *Construction and Building Materials*, 239, Article 117886. [CrossRef]

[40] Sotelo-Pina, C., Aguilera-Gonzalez, E. N., & Martinez-Luevanos, A. (2019). Geopolymers: Past, Present and Future of Low Carbon Footprint Eco-materials. In L. M. T. Martínez, O. V. Kharissowa, & B. I. Kharisov (Eds.), *Handbook of Ecomaterials* (pp. 2765–2785). Springer. [CrossRef]

[41] Korniejenko, K., Frączek, E., Pytlak, E., & Adamski, M. (2016). Mechanical properties of geopolymer composites reinforced with natural fibers. *Procedia Engineering*, 151, 388–393.

[42] Ranjbar, N., & Zhang, M. (2020). Fiber-reinforced geopolymer composites: A review. *Cement and Concrete Composites*, 107(1), Article 103498. [CrossRef]

[43] Korniejenko, K., Lin, W. T., & Šimonová, H. (2020). Mechanical properties of short polymer fiber-reinforced geopolymer composites. *Journal of Composites Science*, 4(3), Article 128.

[44] Silva, F. J., & Thaumaturgo, C. (2003). Fibre reinforcement and fracture response in geopolymeric mortars. *Fatigue & Fracture of Engineering Materials & Structures*, 26(2), 167–172. [CrossRef]

[45] Nawaz, M., Heitor, A., & Sivakumar, M. (2020). Geopolymers in construction-recent developments. *Construction and Building Materials*, 260(9), Article 120472. [CrossRef]

[46] Branston, J., Das, S., Kenno, S. Y., & Taylor, C. (2016). Mechanical behaviour of basalt fibre reinforced concrete. *Construction and Building Materials*, 124, 878–886. [CrossRef]

[47] Morgul, O. K., and Dal, H. (2016). Using of celluBOR on noise enclosures. *Proceedings of 2016 Fourth International Conference on Advances in Civil, Structural and Mechanical Engineering*, 46–49.

[48] Temuujin, J., Rickard, W., Lee, M., & Van Riessen, A. (2011). Preparation and thermal properties of fire resistant metakaolin-based geopolymer-type coatings. *Journal of non-crystalline solids*, 357(5), 1399–1404. [CrossRef]

Journal of Sustainable Construction Materials and Technologies
Web page info: https://jscmt.yildiz.edu.tr
DOI: 10.47481/jscmt.1165940

JSCMT
Journal of Sustainable Construction Materials and Technologies

Research Article

Influence of porosity on the free vibration response of sandwich functionally graded porous beams

Sura Kareem Abbas AL-ITBI*, Ahmad Reshad NOORI

Department of Civil Engineering, İstanbul Gelişim University, İstanbul, Türkiye

ARTICLE INFO

Article history
Received: 23 August 2022
Revised: 11 September 2022
Accepted: 21 September 2022

Key words:
Dynamic analysis, FGM, finite element method, free vibration, porous materials, sandwich beam

ABSTRACT

Functionally graded materials are composite materials used to build a variety of structures. The porosity made in these materials may negatively affect some behavior aspects like stiffness and strength, but it may provide superior performance in other fields like vibration reduction, thermal isolation, energy absorption, and others. In this paper, we will discuss the effect of porosity on the natural frequencies for functionally graded porous (FGP) sandwich beams. The mechanical properties of the FGP sandwich beams change with the thickness direction's porosity. The free vibration of the beams is examined with the effect of porosity. The analysis is carried out for four different beam supporting types (hinged – hinged, fixed – fixed, free, fixed – hinged). Various porosity ratios are considered with a range from (0.1–0.9). Forty–four samples are analyzed for each type of core material distribution which is the symmetric material constitutive relationships (SMCR) and uniform core material. The results gained from the analysis show that the porosity constant has a significant effect on the natural frequencies of the FGP sandwich beams.

Cite this article as: Al-Itbi, SKA., & Noori, AR. (2022). Influence of porosity on the free vibration response of sandwich functionally graded porous beams. *J Sustain Const Mater Technol*, 7(4), 291–301.

1. INTRODUCTION

Engineering designers are aimed to provide superior structure performance regards various aspects. The structure needs to withstand applied loads in additional requirements that need to be met. Users and designer requirements are continuously developed so that conventional materials cannot give acceptable performance. Damping, strength, stiffness, thermal isolation, lightweight, environmental needs, vibration characteristics, and many more properties may not be met with different materials. For this reason, functionally graded materials (FGMs) should be preferred. Although fabrication technology of FGMs is beginning, they provide various benefits such as high stiffness, lightweight, and thermal isolation. A positive relationship between cross section thickness and natural frequency is explored, in which the beam's maximum frequency can be detected [1]. Functionally graded materials are composite materials that may contain two or more different materials. Cellular materials can be divided into two categories depending on the porosity framework: open or closed cells. In closed cell core type, the porous cannot be interconnected in counter to open cell type. Each type has specific performance and characteristics that give the engineers various choices and solutions [2].

***Corresponding author.**
*E-mail address: surak985@gmail.com

An efficient approach was introduced by [3] to describe the behavior of (SMCR) and monotonic material constitutive relationships (MMCR), which is two types of functionally graded sandwich beams. It reveals a positive relationship between frequency and porosity value in SMCR and MMCR models. It was concluded that the periods of vibration and amplitude are higher when the beam material is MMCR compared with SMCR. When the MMCR porosity modulus rises, more intense vibrations can be predicted. The SMCR material provides the lowest deflection and the highest natural frequencies.

A unified analytical model was established in [4] to study the vibration behavior of functionally graded deep porous beams (straight and curved). The first-order beam theory was used in the formula. The response of forced vibration for FG beams was examined by [5], with the porosity changing in the thickness direction. It was also mentioned that to obtain realistic models, a solid planar continuity model should be used in modeling deep beams. The vibration was categorized depending on vibration characteristics into various categories by [6]. Core materials can alternatively be made of open and closed cell metal foam. Thermoset polymers (unsaturated polyesters, epoxies, etc.) or thermoset polymers (laminates of glass or carbon fiber reinforced thermoplastics) are frequently used as face materials. In rare circumstances, sheet metal is also utilized as a skin material where core and skins are merged [7]. Under various core configurations and core materials, the sandwich beam structure's inherent frequencies and mode shapes were determined by [8]. A finite element (FE) approach was applied to examine the beam.

Ritz approach was used in conjunction with a four-direct iterative algorithm by [9]. The performances of the beam with various porosity distributions were contrasted. In contrast, two non-uniform functionally graded porosity distributions and a uniform distribution were considered. The impacts of the porosity coefficient, slenderness ratio, and thickness ratio were thoroughly examined using numerical data. Porosity effects in vibration analysis of functionally graded beams were studied by using flexible boundary conditions [10]. Based on their study, the most critical factors affecting linear and non-linear frequencies are the percentage of porosity volume, boundary conditions, and the transition and rotational spring constants. A study was made using nanoplates that are FGP and resting on the foundation [11]. Porosity influence was considered by applying two-variable refined plates and Winkler-Pasternak elastic foundations. One of the main goals was to determine the relationship of the free vibration characteristics with elastic foundation stiffness, material properties, boundary conditions, and porosity.

The performance of porous beams with two distinct porosity distributions in terms of elastic buckling and bending was investigated by [12]. Transverse shear deformation's impact was included using the Timoshenko beam theory. The Ritz technique was used to develop and then solve the algebraic governing equations. The modified couple stress theory was used by [13] to examine the FG microplate's forced vibration with porosity effects. Hamilton's principle and Navier type solution method was used to study FG beams with different thermal sinusoidal, loading, non–linear, linear, and uniform temperature field [14].

The modified couple stress theory was used by [13] to examine functionally graded microplates' forced vibration with porosity effects. Hamilton's principle and Navier type solution method was used to study functionally graded beams with a different type of thermal sinusoidal load non–linear, linear, and uniform temperature [14]. The transverse displacement and the non – dimensional frequencies were calculated by [15], and they demonstrated that these parameters increased with the increase of the porosity. Timoshenko beam theory, Lagrange equation method, and Ritz technique were used by [16] for free and forced vibration analysis of FG beam.

The finite element method is one of the most influential and efficient tools used for the numerical solution of a wide range of problems in structural mechanics [17–29]. Besides this, several researchers and engineers examine the dynamic response of structures [30–43]. Also, during the last decades, one of the most trend subjects in the research field is composite and FGP materials. For instance, some recent works [44–57] can be mentioned.

Literature survey shows that the free vibration response of sandwich FGP beam with the aid of ANSYS, which is a finite element package program the free vibration response of sandwich FGP beam with the aid of ANSYS, a finite element package program, has not been reported yet. This study aims to present benchmark free vibration characteristics for FGP sandwich beams. The sandwich beams are assumed to have a porous core and isotropic homogenous face sheets. Results are obtained for different values of porosity coefficients to investigate the impact of porosity on the free vibration characteristics. For the beam boundary conditions, clamped-clamped, clamped-hinged, hinged - hid clamped - free cases are considered four different cases. The shear deformation is taken into consideration in the analysis procedure. For porous material, the symmetric and uniform distributions are employed as two kinds of different distributions. To present this study better, it is ordered as follows: Section 2 gives the type of FGP materials and provides information about the details of the analysis. Section 3 shows the results and discussion, and finally, Section 4 is dedicated to the most important conclusion of this study.

2. MATERIALS AND METHOD

The finite element method is implemented to acquire the natural frequencies of the functionally graded po-

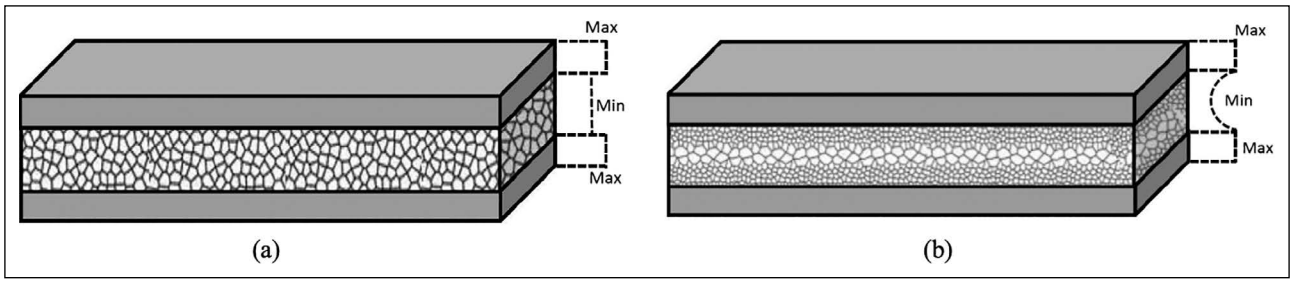

Figure 1. **(a)** FGP sandwich beam with uniform porosity distribution; **(b)** FGP sandwich beam with symmetric porosity distribution.

rous (FGP) sandwich beam shown in Figure 1, which has a length of L, a width of b, and a height of h. The beam has three layers in the thickness direction. The core layer is assumed to be FGP material and the top and the bottom layers are made up of isotropic homogenous material. In this paper two types of different FGP materials are used. The influence of the porosity coefficient for symmetric and uniform porosity distributions is investigated.

In this paper, Poisson's ratio is assumed to be constant. The variation of Young's modulus and mass density for the FGP sandwich beams are presented in this section. The material properties for the sandwich FGP beams are given in Eqs. (1–9) for uniform porosity distribution and in Eqs. (10–18) for symmetric porosity distribution [58].

$$\text{Top Face } \left(+\frac{7h}{18} \le z \le +\frac{h}{2}\right) \begin{cases} E(z) = E_1 & (1) \\ G(z) = G_1 & (2) \\ \rho(z) = \rho_1 & (3) \end{cases}$$

$$\text{Core } \left(-\frac{7h}{18} \le z \le +\frac{7h}{18}\right) \begin{cases} E(z) = E_1\,[\,1 - e_o\varphi] & (4) \\ G(z) = G_1\,[\,1 - e_o\varphi] & (5) \\ \rho(z) = \rho_1\sqrt{1 - e_o\varphi} & (6) \end{cases}$$

$$\text{Bottom Face } \left(-\frac{h}{2} \le z \le -\frac{7h}{18}\right) \begin{cases} E(z) = E_2 & (7) \\ G(z) = G_2 & (8) \\ \rho(z) = \rho_2 & (9) \end{cases}$$

$$\text{Top Face } \left(+\frac{7h}{18} \le z \le +\frac{h}{2}\right) \begin{cases} E(z) = E_1 & (10) \\ G(z) = G_1 & (11) \\ \rho(z) = \rho_1 & (12) \end{cases}$$

$$\text{Core } \left(-\frac{7h}{18} \le z \le +\frac{7h}{18}\right) \begin{cases} E(z) = E_1\left[1 - e_0 \cos\left(\frac{\pi z}{h_c}\right)\right] & (13) \\ G(z) = G_1\left[1 - e_0 \cos\left(\frac{\pi z}{h_c}\right)\right] & (14) \\ \rho(z) = \rho_1\left[1 - e_m \cos\left(\frac{\pi z}{h_c}\right)\right] & (15) \end{cases}$$

$$\text{Bottom Face } \left(-\frac{h}{2} \le z \le -\frac{7h}{18}\right) \begin{cases} E(z) = E_2 & (16) \\ G(z) = G_2 & (17) \\ \rho(z) = \rho_2 & (18) \end{cases}$$

where h_c is the core thickness and constant φ is

$$\varphi = \frac{1}{e_o} - \frac{1}{e_o}\left(\frac{2}{\pi}\sqrt{1 - e_o} - \frac{2}{\pi} + 1\right)^2 \quad (19)$$

In the above equations, e_o is the porosity coefficient, h is the thickness of the cross-section, E_1, G_1 and ρ_1 are the maximum value for the modulus of elasticity, shear modulus, and mass density. The porosity coefficient for the mass density (e_m). Can be obtained by the following equation [3].

$$e_m = 1 - \sqrt{1 - e_0} \quad (20)$$

The solution procedure of the considered problem with the finite element package program ANSYS, BEAM 189, is implemented. This element has three nodes, each with six degrees of freedom. These degrees of freedom are directional displacement in x, y, and z directions and rotations about x, y, and z axes. BEAM189, a 3D element, is based on the first-order shear deformation theory. In this study, the in-plane free vibration characteristics are obtained. For this reason, the displacement in the y direction and rotations about the x and z axes are restrained. More detailed information about the theory of this element can be found in [59].

To generate the FGP sandwich beam model in Ansys Mechanical APDL [60], the material properties, such as mass density and Young's modulus, are first calculated based on the material functions. A data file is created in *.csv format for the calculated values. The section is divided into 36 layers in the thickness direction [3]. The cross-section mesh of the beam consists of 1296 elements, as seen in Figure 2. The first and last four layers are isotropic homogenous, and the middle layers are made up of functionally graded porous materials. Each material is defined to its specific layer using the Edit/ Built-up options of the Custom Sections in Ansys Mechanical APDL. For the mesh size, the beam is divided into 100 elements the longitudinal direction is divided into 100 elements in the longitudinal direction for the mesh size. It is worth to be mentioned that the mesh size is selected to obtain accurate mode shapes.

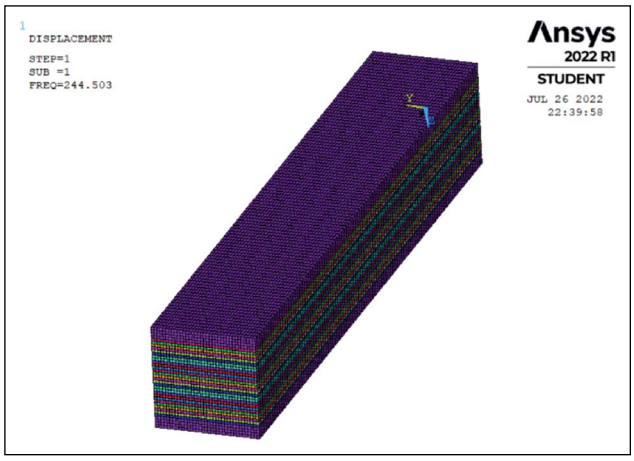

Figure 2. FGP sandwich beam finite element mesh.

3. NUMERICAL RESULTS AND DISCUSSION

The free vibration characteristics of the sandwich FGP beams are obtained for various values of porosity coefficients, two types of FG porosity distributions, and several boundary conditions. For the uniform porosity distribution, the musing modulus of elasticity is calculated using Eqs. (1–9). Eqs acquire the same material properties for the symmetric porosity distribution (10–18). The Poisson's ratio is taken as a constant value of 0.3. In this paper, the value of the maximum mass density (ρ_1=ρ_2) is 7850 kg/m^3, and the value of the maximum modulus of elasticity (E_1=E_2). It is considered 200 GPa for all tables and figures except Table 10. The program automatically calculates the maximum shear modulus with $\left(G_i = \frac{E_i}{2(1+v)}\right)$. The geometric properties of the beam are; h=0.5 m, b=0.5 m, and L=3 m.

The analysis methodology works on eighty-eight different FGP sandwich beams divided equally into two main groups depending on the symmetric and uniform porosity distribution. Each group differs in the type of supports of the beam and the porosity coefficients of FGP materials. All boundary conditions are listed in Table 1 related to rotation and directional displacements. In Table 1, '**i**' denotes the left end of the beam, while '**j**' stands for the right end of the beam.

As the first problem of this section, the symmetric porosity distribution is considered. Ten natural frequencies are calculated for various values of the porosity coefficient (e_0). Four types of boundary conditions are implemented. The free vibration characteristics values for the clamped–clamped supported beams are presented in Table 2.

By the same token, the free vibration characteristics are calculated for the C-H sandwich FGP beam with a core made up of symmetric porosity distribution. These results are determined using eleven different values of the porosity coefficient. Derived results are listed in Table 3.

A third example with the same approach will now be presented. In this part, a sandwich FGP beam of symmetry porosity will be handled with boundary conditions will be H-H. The computed free vibration frequencies are shown in Table 4.

Table 1. Beam boundary conditions

Type of the support	Boundary conditions	
	i	j
Clamped – Clamped (C-C)	Rotz = Roty = Rotx= Uz = Uy = Ux = 0	Rotz = Roty = Rotx= Uz = Uy = Ux = 0
Clamped – Hinged (C-H)	Rotz = Roty = Rotx= Uz = Uy = Ux = 0	Uz = Ux = Uy = 0
Hinged – Hinged (H-H)	Uz = Ux = Uy = 0	Uz = Ux = Uy = 0
Clamped – Free (C-F)	Rotz = Roty = Rotx= Uz = Uy = Ux = 0	-----

Table 2. Natural frequencies of C-C supported FGP sandwich beam with symmetric porosity distribution (Hz)

Mode	e_0										
	0.1	**0.2**	**0.25**	**0.3**	**0.4**	**0.5**	**0.6**	**0.7**	**0.75**	**0.8**	**0.9**
1	244.50	243.56	243.08	242.45	241.16	239.26	236.76	232.84	230.05	226.01	210.86
2	576.28	570.34	567.17	563.46	555.39	544.95	531.75	513.04	500.55	483.83	424.91
3	976.87	820.98	816.18	810.87	801.33	791.39	782.69	775.27	772.89	770.75	669.90
4	1412.10	962.89	955.43	946.93	928.41	905.33	876.86	838.02	812.87	780.16	754.70
5	1868.90	1387.90	1375.00	1360.50	1328.90	1290.00	1242.10	1176.30	1131.50	1065.70	774.01
6	2337.20	1642.00	1632.40	1621.70	1602.70	1582.80	1565.40	1526.10	1378.80	1216.00	955.65
7	2811.10	1833.40	1814.40	1793.30	1747.10	1690.90	1621.80	1537.70	1459.50	1361.40	1001.40
8	3076.50	2288.80	2262.70	2233.50	2167.20	2063.50	1835.30	1550.50	1545.80	1541.50	1247.20
9	3302.80	2462.90	2448.50	2432.60	2399.20	2169.70	2031.70	1858.70	1699.60	1541.60	1285.60
10	3446.80	2748.20	2713.90	2636.90	2404.00	2374.20	2161.30	1902.80	1819.10	1701.20	1542.20

Table 3. Natural frequencies of C-H supported FGP sandwich beam with symmetric porosity distribution (Hz)

Mode	e_0										
	0.1	**0.2**	**0.25**	**0.3**	**0.4**	**0.5**	**0.6**	**0.7**	**0.75**	**0.8**	**0.9**
1	179.65	179.48	179.43	179.29	179.09	178.58	177.85	176.39	175.20	173.23	164.45
2	507.71	503.99	502.03	499.65	494.52	487.62	478.72	465.63	456.67	444.35	399.97
3	916.88	820.98	816.18	810.87	801.33	791.39	782.69	775.27	772.89	752.71	646.50
4	1366.80	905.77	899.83	893.00	878.09	859.18	835.57	802.76	781.21	770.75	694.45
5	1837.50	1345.70	1334.40	1321.70	1294.00	1259.70	1217.60	1160.20	1122.40	1065.60	774.01
6	2318.50	1642.00	1632.40	1621.70	1602.70	1582.80	1565.40	1438.70	1275.90	1105.90	866.61
7	2802.50	1804.90	1787.60	1768.10	1725.70	1673.80	1609.60	1526.10	1454.40	1312.60	958.07
8	2980.30	2273.30	2249.20	2222.20	2162.60	2025.10	1750.60	1550.50	1534.90	1427.40	1139.70
9	3231.70	2462.90	2448.50	2432.60	2289.30	2094.10	1969.00	1683.90	1545.80	1541.50	1248.60
10	3308.70	2737.30	2646.60	2531.50	2404.00	2283.00	2042.40	1902.50	1806.10	1641.10	1431.30

Table 4. Natural frequencies of H-H supported FGP sandwich beam with symmetric porosity distribution (Hz)

Mode	e_0										
	0.1	**0.2**	**0.25**	**0.3**	**0.4**	**0.5**	**0.6**	**0.7**	**0.75**	**0.8**	**0.9**
1	121.88	122.16	122.34	122.49	122.93	123.30	123.73	124.03	124.07	124.25	124.66
2	435.07	433.30	432.39	431.20	428.70	425.01	420.05	412.16	406.48	398.21	366.36
3	852.41	820.98	816.18	810.87	801.33	791.39	782.69	764.77	747.39	724.15	644.76
4	1318.00	844.26	839.91	834.81	823.69	809.21	790.87	775.27	772.89	770.75	650.26
5	1804.30	1300.10	1290.60	1279.80	1256.10	1226.50	1190.10	1140.50	1108.60	1061.30	772.59
6	2298.60	1642.00	1632.40	1621.70	1602.70	1582.80	1565.40	1406.00	1240.40	1067.30	774.01
7	2795.00	1774.90	1759.20	1741.60	1703.30	1656.50	1599.70	1524.30	1371.50	1190.30	933.68
8	2943.40	2256.60	2234.30	2209.40	2155.40	1992.20	1714.20	1538.50	1476.70	1416.40	1021.50
9	3085.10	2462.90	2448.50	2432.60	2252.30	2090.40	1849.20	1550.50	1545.80	1480.20	1226.60
10	3290.80	2725.50	2612.80	2496.20	2390.60	2129.00	2012.30	1851.90	1674.50	1541.50	1306.00

Table 5. Natural frequencies of C-F supported FGP sandwich beam with symmetric porosity distribution (Hz)

Mode	e_0										
	0.1	**0.2**	**0.25**	**0.3**	**0.4**	**0.5**	**0.6**	**0.7**	**0.75**	**0.8**	**0.9**
1	44.48	44.65	44.76	44.87	45.14	45.42	45.79	46.20	46.44	46.63	46.75
2	247.68	246.81	246.36	245.75	244.46	242.46	239.67	235.01	231.52	226.30	204.98
3	604.92	410.49	408.09	405.43	400.66	395.69	391.34	387.63	386.44	385.37	387.00
4	1025.20	599.22	596.14	592.52	584.53	573.97	560.31	540.38	526.80	508.38	443.50
5	1479.10	1010.70	1002.80	993.86	974.02	948.83	916.92	871.79	841.45	800.66	647.33
6	1945.90	1231.50	1224.30	1216.30	1202.00	1187.10	1174.00	1162.90	1159.30	1094.80	808.05
7	2413.00	1453.30	1439.30	1423.60	1388.90	1345.50	1291.10	1214.90	1163.70	1156.10	876.53
8	2846.30	1906.20	1884.70	1860.40	1806.00	1736.30	1639.70	1465.50	1333.30	1177.20	1092.50
9	3095.90	2052.40	2040.40	2027.20	2003.30	1978.50	1862.80	1631.80	1529.50	1414.10	1148.70
10	3239.80	2356.20	2324.80	2289.10	2205.40	2080.20	1956.70	1755.30	1627.50	1486.40	1161.00

In the last case of the symmetry porosity distribution, we seek to determine the natural frequencies of an FGP sandwich beam that is exposed to C-F boundary conditions. The frequencies of the current case are tabled in Table 5.

The same procedure employed for the symmetry porosity distribution will be implemented to acquire the natural frequencies of the FGP sandwich beams with a uniform porosity distribution core. We now turn on to study the ef-

Table 6. Natural frequencies of C-C supported FGP sandwich beam with uniform porosity distribution (Hz)

Mode	e_0										
	0.1	**0.2**	**0.25**	**0.3**	**0.4**	**0.5**	**0.6**	**0.7**	**0.75**	**0.8**	**0.9**
1	243.76	242.11	241.25	240.36	238.49	236.43	234.12	231.40	229.79	227.92	222.62
2	576.21	570.54	567.54	564.39	557.59	549.94	541.06	530.28	523.79	516.19	494.72
3	830.58	819.33	813.46	807.41	794.71	781.06	766.23	749.86	740.93	731.34	709.33
4	978.59	967.07	960.93	954.49	940.54	924.76	906.41	884.18	870.86	855.33	812.27
5	1416.40	1397.80	1387.90	1377.50	1354.90	1329.30	1299.60	1263.60	1242.10	1217.10	1148.00
6	1661.20	1638.70	1626.90	1614.80	1589.40	1562.10	1532.50	1499.70	1481.90	1462.70	1418.70
7	1876.40	1850.00	1835.90	1821.20	1789.10	1752.80	1710.60	1659.60	1629.20	1593.90	1497.00
8	2348.30	2313.50	2294.90	2275.30	2232.80	2184.40	2127.70	2057.70	2013.80	1956.70	1709.50
9	2491.70	2458.00	2440.40	2422.20	2384.10	2343.20	2298.70	2249.60	2181.70	2066.30	1871.00
10	2826.50	2782.70	2759.20	2734.50	2680.50	2618.80	2485.50	2290.80	2222.80	2194.00	2033.10

Table 7. Natural frequencies of C-H supported FGP sandwich beam with uniform porosity distribution (Hz)

Mode	e_0										
	0.1	**0.2**	**0.25**	**0.3**	**0.4**	**0.5**	**0.6**	**0.7**	**0.75**	**0.8**	**0.9**
1	178.87	177.93	177.45	176.96	175.96	174.91	173.78	172.53	171.82	171.03	168.86
2	506.99	502.80	500.59	498.28	493.36	487.87	481.58	474.04	469.53	464.27	449.42
3	830.58	819.33	813.46	807.41	794.71	781.06	766.23	749.86	740.93	731.34	709.33
4	917.62	907.90	902.73	897.32	885.64	872.47	857.21	838.75	827.70	814.80	778.85
5	1370.00	1353.20	1344.30	1334.90	1314.70	1291.70	1265.10	1232.90	1213.70	1191.30	1129.40
6	1661.20	1638.70	1626.90	1614.80	1589.40	1562.10	1532.50	1499.70	1481.90	1462.70	1418.70
7	1843.80	1819.10	1805.90	1792.10	1762.10	1728.20	1688.70	1641.00	1612.60	1579.40	1487.80
8	2328.30	2295.10	2277.30	2258.60	2218.10	2172.20	2118.70	2053.60	2013.20	1937.00	1622.90
9	2491.70	2458.00	2440.40	2422.20	2384.10	2343.20	2298.70	2183.40	2071.40	1975.50	1831.80
10	2816.60	2774.00	2751.20	2727.00	2671.70	2550.90	2381.10	2249.60	2222.80	2193.00	1893.80

Table 8. Natural frequencies of H-H supported FGP sandwich beam with uniform porosity distribution (Hz)

Mode	e_0										
	0.1	**0.2**	**0.25**	**0.3**	**0.4**	**0.5**	**0.6**	**0.7**	**0.75**	**0.8**	**0.9**
1	121.19	120.75	120.53	120.31	119.90	119.52	119.18	118.90	118.80	118.73	118.72
2	433.84	430.98	429.50	427.96	424.74	421.23	417.32	412.77	410.11	407.03	398.47
3	830.58	819.33	813.46	807.41	794.71	781.06	766.23	749.86	740.93	731.34	709.33
4	852.17	844.31	840.14	835.80	826.47	816.03	804.02	789.58	780.95	770.89	742.74
5	1320.00	1305.20	1297.30	1289.10	1271.20	1251.10	1227.80	1199.60	1182.80	1163.10	1108.70
6	1661.20	1638.70	1626.90	1614.80	1589.40	1562.10	1532.50	1499.70	1481.90	1462.70	1418.70
7	1809.40	1786.50	1774.20	1761.40	1733.60	1702.30	1665.80	1621.80	1595.50	1564.90	1480.80
8	2307.10	2275.50	2258.60	2240.80	2202.30	2158.80	2108.30	2047.30	2010.90	1906.00	1586.50
9	2491.70	2458.00	2440.40	2422.20	2384.10	2343.20	2298.70	2146.90	2033.10	1968.70	1722.40
10	2807.10	2766.40	2744.60	2721.70	2668.80	2517.10	2345.70	2249.60	2169.90	2042.50	1853.20

fects of the porosity on the outcomes of the free vibration analysis of these structures. The examples deal with calculating the natural frequencies of C-C, C-H, H-H, and C-F supported FGP sandwich beams. Each case's first to tenth natural frequencies are calculated for several porosity coefficient values and summarized in Tables 6–9.

Table 9. Natural Frequencies of C-F supported FGP sandwich beam with uniform porosity distribution (Hz)

Mode	e_0										
	0.1	**0.2**	**0.25**	**0.3**	**0.4**	**0.5**	**0.6**	**0.7**	**0.75**	**0.8**	**0.9**
1	44.20	44.07	44.00	43.95	43.84	43.76	43.71	43.71	43.74	43.80	44.07
2	246.92	245.37	244.56	243.73	241.99	240.10	238.00	235.55	234.12	232.46	227.75
3	415.29	409.67	406.73	403.71	397.35	390.53	383.11	374.93	370.46	365.67	354.66
4	604.73	599.25	596.35	593.33	586.83	579.55	571.16	561.05	554.99	547.91	527.98
5	1027.20	1015.50	1009.30	1002.80	988.79	972.91	954.43	931.99	918.51	902.73	858.50
6	1245.90	1229.00	1220.20	1211.10	1192.10	1171.60	1149.30	1124.80	1111.40	1097.00	1064.00
7	1484.20	1465.10	1454.80	1444.10	1420.70	1394.30	1363.50	1326.00	1303.40	1277.10	1203.30
8	1955.20	1927.30	1912.30	1896.60	1862.40	1823.30	1777.40	1720.80	1686.20	1645.00	1520.10
9	2076.50	2048.30	2033.70	2018.50	1986.80	1952.60	1915.60	1874.70	1852.30	1828.40	1728.20
10	2427.90	2390.00	2369.60	2348.10	2300.90	2246.40	2181.10	2097.50	2043.20	1972.10	1773.30

Table 10. Natural frequencies of C-C supported FGP unsymmetrical sandwich beam with uniform porosity distribution (Hz)

Mode	e_0										
	0.1	**0.2**	**0.25**	**0.3**	**0.4**	**0.5**	**0.6**	**0.7**	**0.75**	**0.8**	**0.9**
1	232.5	230.51	229.47	228.4	226.15	223.71	221.01	217.94	216.19	214.22	209.06
2	557.66	551.66	548.49	545.19	538.15	530.35	521.49	511.04	504.92	497.9	478.92
3	830.03	817.81	811.4	804.78	790.78	775.6	758.91	740.2	729.83	718.54	691.82
4	956.25	944.53	938.32	931.84	917.93	902.4	884.64	863.57	851.17	836.91	798.43
5	1393.5	1375	1365.1	1354.8	1332.7	1307.9	1279.4	1245.6	1225.7	1202.8	1141
6	1660.1	1635.6	1622.8	1609.6	1581.6	1551.2	1517.8	1480.4	1459.7	1437.1	1383.6
7	1854.8	1828.7	1814.9	1800.4	1769.2	1734.2	1694	1646.1	1618	1585.6	1498.4
8	2330.1	2296	2277.9	2258.9	2217.9	2172	2119.1	2056	2018.7	1975.8	1858.2
9	2490.1	2453.4	2434.2	2414.3	2372.4	2326.8	2276.7	2220.6	2189.5	2155.6	2075.5
10	2813.5	2771	2748.4	2724.7	2673.5	2615.9	2549.6	2470.3	2423.2	2368.6	2078.5

To extend the solutions procedure to unsymmetrical beams as well. The sandwich beam is considered with a steel top face, an FGP core with uniform distribution, and an aluminum bottom face. In this part, the value of the mass density (ρ_2). Are 2700 kg/m^3, and the value of the modulus of elasticity (E_2) It is considered to be 70 GPa. Results are obtained and compared for clamped – clamped supported beam in Table 10. The geometric properties are the same as in the previous example.

The above Tables 2–10 demonstrate some essential ingredients of the free vibration response of FGP sandwich beams. It is visible to see the influence of the porosity coefficient on the natural frequencies from the given comparisons. In each of the above examples, we dealt with 11 different values of e_0. When the uniform distribution was implemented, the natural frequencies showed an apparent decrease, with porosity coefficients increasing for all analyzed beams. Also, for the symmetric porosity distribution, it is carried out that for C-C and C-H, the natural frequencies decrease when the porosity coefficient increases. When H-H and C-F boundary conditions are used, it seems that the first natural frequencies increase while the remaining frequencies decrease. From the general review of analysis, the calculated results demonstrate good compatibility with expected beam behavior. It should also be emphasized that boundary conditions considerably affect the natural frequencies of the FGP sandwich beams. As might well be expected, the highest values of the natural frequencies are in C-C, and the lowest values of the free vibration characteristics are in C-F boundary conditions. To further discuss the finite element procedure for the free vibration response of the problem at hand, PLANE183 is also utilized. Results are obtained for uniform porosity distribution. Calculated results are listed in Table 11 for clamped-clamped supported beams.

When Table 6 and Table 11 are compared, it can be seen that the results of both finite element types are in good agreement. The slight difference is because of differences in the assumptions and theory of the elements.

Table 11. Natural frequencies of C-C supported FGP sandwich beam with uniform porosity distribution obtained with PLANE183 (Hz)

Mode	e_0										
	0.1	**0.2**	**0.25**	**0.3**	**0.4**	**0.5**	**0.6**	**0.7**	**0.75**	**0.8**	**0.9**
1	245.49	243.95	243.15	242.32	240.57	238.67	236.53	234.02	232.54	230.81	225.89
2	582.42	577.2	574.43	571.53	565.31	558.31	550.22	540.43	534.54	527.64	508.13
3	833.3	822.07	816.22	810.18	797.5	783.87	769.05	752.68	743.73	734.12	711.93
4	992.31	981.75	976.13	970.24	957.52	943.17	926.51	906.34	894.25	880.14	840.84
5	1440.3	1423.3	1414.3	1404.8	1384.2	1361	1334.1	1301.4	1281.9	1259.2	1196.2
6	1661.3	1638.6	1626.7	1614.5	1588.8	1561	1530.8	1497.1	1478.5	1458.4	1411.1
7	1912.3	1888.2	1875.4	1861.9	1832.7	1799.6	1761.2	1714.6	1686.8	1654.3	1564.8
8	2397.6	2365.8	2348.8	2331	2292.2	2248.3	2197.2	2135.2	2098	2054.8	1935.6
9	2475	2440.2	2421.9	2403	2363	2319.7	2271.8	2217.7	2187.3	2153.8	2071
10	2889.7	2849.7	2828.3	2805.8	2756.9	2701.5	2636.9	2558.6	2511.8	2427.3	2207

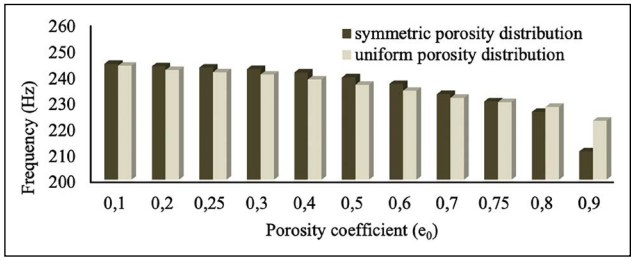

Figure 3. Comparison of the first natural frequencies for C-C sandwich FGP beam.

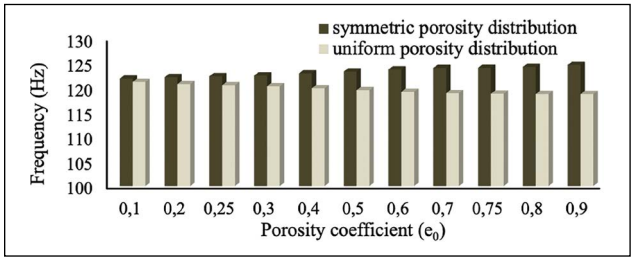

Figure 5. Comparison of the first natural frequencies for H-H sandwich FGP beam.

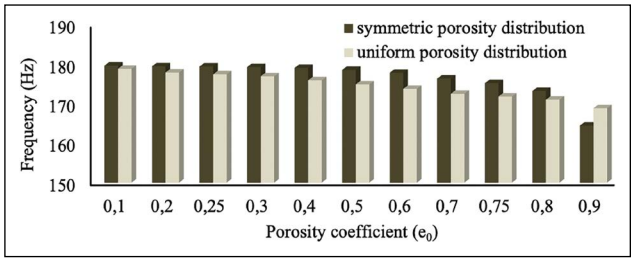

Figure 4. Comparison of the first natural frequencies for C-H sandwich FGP beam.

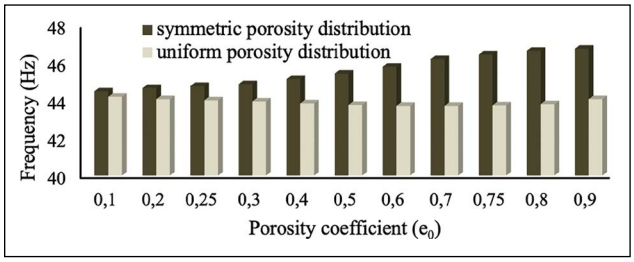

Figure 6. Comparison of the first natural frequencies for C-F sandwich FGP beam.

One of our objectives in this section is to discuss the difference in the influence of the symmetric and uniform distribution on the free vibration sandwich FGP beams. For this reason, the following Figures 3–6 are illustrated to compare the effect of two types of porous distribution on the free vibration response of the considered structures.

As can be seen in Figures 3–6, the material distribution of the core has an essential effect on the structure's natural frequencies. Figure 3 shows that the first natural frequencies are higher in symmetric porosity distribution for values of e_0 less than 0.8 when implementing C-C boundary conditions. Figure 4 demonstrates that when the beam is C-H, the first natural frequencies are higher in uniform porosity distribution for values of e_0 more than 0.9. It is apparent in Figures 5–6 that values of the symmetric porosity distribution are greater than those of the uniform porosity distribution when the beam is H-H and C-F.

4. CONCLUSIONS

In this study, the free vibration response of FGP sandwich beams is investigated with the aid of the finite element method. The first-order shear deformation theory is used. Two kinds of different porous materials are considered for the core of the sandwich structure. The influence of the porosity coefficient and boundary conditions on the natural frequencies is investigated, and the following results can be concluded.

- When the uniform porous material is used in the core of the sandwich beam, an inversely proportional relationship between porosity and frequency is observed, which means higher frequency recorded was for lower porosity coefficients.
- For the symmetric porous material in the core of the beam, it is carried out that C-C and C-H, the free vibration characteristic values decrease when the porosity coefficient increases. When H-H and C-F boundary conditions are used, the first natural frequencies increase, and the other frequencies decrease.
- Higher frequencies were recorded at C-C beams, and lower frequencies were recorded at C-F beams.
- The type of porosity distribution is essential for the value of the free vibration characteristics.
- For H-H and C-F boundary conditions, the natural frequencies of the FGP sandwich beam are greater in symmetric porosity distributions than those of the uniform porosity distribution.
- For C-C and C-H, when the value of e_0 is more than 0.8, the natural frequencies in FGP sandwich beams with uniform porosity distributions start to get higher than those of the symmetric porosity distribution.

ETHICS

There are no ethical issues with the publication of this manuscript.

DATA AVAILABILITY STATEMENT

The authors confirm that the data that supports the findings of this study are available within the article. Raw data that support the finding of this study are available from the corresponding author, upon reasonable request.

CONFLICT OF INTEREST

The authors declare that they have no conflict of interest.

FINANCIAL DISCLOSURE

The authors declared that this study has received no financial support.

PEER-REVIEW

Externally peer-reviewed.

REFERENCES

[1] Prasad, M. S., Reddy, P. S., Manoj, M., & Murthy, N. G. (2014). Analysis of sandwich beam. *International Journal of Science Engineering and Advance Technology*, 2(12), 901–908.

[2] Wu, H., Yang, J., & Kitipornchai, S. (2020). Mechanical analysis of functionally graded porous structures: A review. *International Journal of Structural Stability and Dynamics*, 20(13), Article 2041015. [CrossRef]

[3] Noori, A. R., Aslan, T. A., & Temel, B. (2021). dynamic analysis of functionally graded porous beams using complementary functions method in the Laplace domain. *Composite Structures*, 256, Article 113094. [CrossRef]

[4] Zhao, J., Wang, Q., Deng, X., Choe, K., Xie, F., & Shuai, C. (2018). A modified series solution for free vibration analyses of moderately thick functionally graded porous (FGP) deep curved and straight beams. *Composites Part B: Engineering*, 165, 155–166. [CrossRef]

[5] Akbaş, Ş. D. (2017). Forced vibration analysis of functionally graded porous deep beams.*Composite Structures*, 186, 293–302. [CrossRef]

[6] Rao, S. S. (2007). *Vibration of continuous systems*. John Wiley & Sons.

[7] Wang, Q., & Quek, S. T. (2000). Flexural vibration analysis of sandwich beam coupled with piezoelectric actuator. *Smart Materials and Structures*, 9(1), Article 103. [CrossRef]

[8] Chen, D., Kitipornchai, S., & Yang, J. (2016). Nonlinear free vibration of shear deformable sandwich beam with a functionally graded porous core. *Thin-Walled Structures*, 107, 39–48. [CrossRef]

[9] Yang, Y., Lam, C. C., Kou, K. P., & Iu, V. P. (2014). Free vibration analysis of the functionally graded sandwich beams by a mesh free boundary-domain integral equation method. *Composite Structures*, 117, 32–39. [CrossRef]

[10] Wattanasakulpong, N., & Ungbhakorn, V. (2014). Linear and nonlinear vibration analysis of elastically restrained ends FGM beams with porosities. *Aerospace Science and Technology*, 32(1), 111–120. [CrossRef]

[11] Mechab, I., Mechab, B., Benaissa, S., Serier, B., & Bouiadjra, B. B. (2016). Free vibration analysis of FGM nanoplate with porosities resting on Winkler Pasternak elastic foundations based on two-variable refined plate theories. *Journal of the Brazilian Society of Mechanical Sciences and Engineering*, 38(8), 2193–2211. [CrossRef]

[12] Chen, D., Yang, J., & Kitipornchai, S. (2015). Elastic buckling and static bending of shear deformable functionally graded porous beam. *Composite Structures*, 33, 54–61. [CrossRef]

[13] Şimşek, M., & Aydın, M. (2016). Size-dependent forced vibration of an imperfect functionally graded (FG) microplate with porosities subjected to a moving load using the modified couple stress theory *Composite Structures*, 160, 408–421. [CrossRef]

[14] Ebrahimi, F., & Jafari, A. (2016). A higher-order thermomechanical vibration analysis of temperature-dependent FGM beams with porosities. *Journal of Engineering*, 2016, Article 9561504. [CrossRef]

[15] Ait Atmane, H., Tounsi, A., & Bernard, F. (2015). Effect of thickness stretching and porosity on mechani-

cal response of a functionally graded beams resting on elastic foundations. *International Journal of Mechanics and Materials in Design*, 13(1), 71–84. [CrossRef]

[16] Chen, D., Yang, J., & Kitipornchai, S. (2016). Free and forced vibrations of shear deformable functionally graded porous beams. *International Journal of Mechanical Sciences*, 108, 14–22. [CrossRef]

[17] Dilbas, H. (2021). Application of finite element method on recycled aggregate concrete and reinforced recycled aggregate concrete: A review. *Journal of Sustainable Construction Materials and Technologies*, 4(6), 173–191. [CrossRef]

[18] Doori, S., & Noori, A. R. (2021). Finite element approach for the bending analysis of castellated steel beams with various web openings. *ALKU Journal of Science*, 2(3), 38–49. [CrossRef]

[19] Noori, A. R., Aslan, T. A., & Temel, B. (2019). Dairesel plakların sonlu elemanlar yöntemi ile laplace uzayında dinamik analizi. *Omer Halisdemir University Journal of Engineering Sciences*, 8(1), 193–205. [CrossRef]

[20] Aslan, T. A., & Temel, B. (2022). Finite element analysis of the seepage problem in the dam body and foundation based on the Galerkin's approach. *European Mechanical Science*, 6(2), 143–151. [CrossRef]

[21] Yildirim, S. (2021). Free vibration of axially or transversely graded beams using finite-element and artificial intelligence. *Alexandria Engineering Journal*, 6, 2220–2229. [CrossRef]

[22] Temel, B., & Şahan, M. F. (2013). Transient analysis of orthotropic, viscoelastic thick plates in the Laplace domain. *European Journal of Mechanics A/Solids*, 37, 96–105. [CrossRef]

[23] Aribas, U. N., Ermis, M., Eratli, N., & Omurtag, M. H. (2019). The static and dynamic analyses of warping included composite exact conical helix by mixed FEM. *Composites Part B*, 160, 285–297. [CrossRef]

[24] Chen, J., Shou, Y., & Zhou, X. (2022). Implementation of the novel perfectly matched layer element for elastodynamic problems in time-domain finite element method. *Soil Dynamics and Earthquake Engineering*, 152, Article 107054. [CrossRef]

[25] Hobiny, A. D., & Abbas, I. (2022). The impacts of variable thermal conductivity in a semiconducting medium using finite element method. *Case Studies in Thermal Engineering*, 31, Article 101773. [CrossRef]

[26] Chai, Y., Li, W., & Liu, Z. (2022). Analysis of transient wave propagation dynamics using the enriched finite element method with interpolation cover functions. *Applied Mathematics and Computation*, 412, Article 126564. [CrossRef]

[27] Wu, N., Liang, Z., Zhang, Z., Li, S., & Lang, Y. (2022). Development and verification of three-dimensional equivalent discrete fracture network modelling based on the finite element method. *Engineering Geology*, 306, Article 106759. [CrossRef]

[28] Zhou, L., Wang, J., Liu, M., Li, M., & Chai, Y. (2022). Evaluation of the transient performance of magneto-electro-elastic based structures with the enriched finite element method. *Composite Structures*, 280, Article 114888. [CrossRef]

[29] Noori, A. R., & Temel, B. (2020). On the vibration analysis of laminated composite parabolic arches with variable cross-section of various ply stacking sequences. *Mechanics of Advanced Materials and Structures*, 27(19), 1658–1672. [CrossRef]

[30] Van Vinh, P. (2022). Nonlocal free vibration characteristics of power-law and sigmoid functionally graded nanoplates considering variable nonlocal parameter. *Physica E: Low-dimensional Systems and Nanostructures*, 135, Article 114951. [CrossRef]

[31] Akbari, H., Azadi, M., & Fahham, H. (2022). Free vibration analysis of thick sandwich cylindrical panels with saturated FG-porous core. *Mechanics Based Design of Structures and Machines*, 50(4), 1268–1286. [CrossRef]

[32] Liu, X., Zhao, Y., Zhou, W., & Banerjee, J. R. (2022). Dynamic stiffness method for exact longitudinal free vibration of rods and trusses using simple and advanced theories. *Applied Mathematical Modelling*, 104, 401–420. [CrossRef]

[33] Daikh, A. A., Bachiri, A., Houari, M. S. A., & Tounsi, A. (2022). Size dependent free vibration and buckling of multilayered carbon nanotubes reinforced composite nanoplates in thermal environment. *Mechanics Based Design of Structures and Machines*, 50(4), 1371–1399. [CrossRef]

[34] Chen, W., Luo, W. M., Chen, S. Y., & Peng, L. X. (2022). A FSDT meshfree method for free vibration analysis of arbitrary laminated composite shells and spatial structures. *Composite Structures*, 279, Article 114763. [CrossRef]

[35] Garg, A., Chalak, H. D., Zenkour, A. M., Belarbi, M. O., & Sahoo, R. (2022). Bending and free vibration analysis of symmetric and unsymmetric functionally graded CNT reinforced sandwich beams containing softcore. *Thin-Walled Structures*, 170, Article 108626. [CrossRef]

[36] Rachid, A., Ouinas, D., Lousdad, A., Zaoui, F. Z., Achour, B., Gasmi, H., Butt T.A. & Tounsi, A. (2022). Mechanical behavior and free vibration analysis of FG doubly curved shells on elastic foundation via a new modified displacements field model of 2D and quasi-3D HSDTs. *Thin-Walled Structures*, 172, Article 108783. [CrossRef]

[37] Bozyigit, B., & Acikgoz, S. (2022). Determination of free vibration properties of masonry arch bridges using the dynamic stiffness method. *Engineering Structures*, 250, Article 113417. [CrossRef]

[38] Babuscu Yesil, U., & Yahnioglu, N. (2022). Free vibration of simply supported piezoelectric plates containing a cylindrical cavity. *Archive of Applied Mechanics*, 92, 2665–2678. [CrossRef]

[39] Jin, H., Sui, S., Zhu, C., & Li, C. (2022). Axial free vibration of rotating fg piezoelectric nano rods accounting for nonlocal and strain gradient effects. *Journal of Vibration Engineering & Technologies*, 1–13. [CrossRef]

[40] Zamani, H. A. (2021). Free vibration of functionally graded viscoelastic foam plates using shear- and normal-deformation theories. *Mechanics of Time-Dependent Materials*, 1–22. [CrossRef]

[41] Yildirim, S. (2020). An efficient method for the plane vibration analysis of composite sandwich beam with an orthotropic core. *Cumhuriyet Science Journal*, 41(2), 521–526. [CrossRef]

[42] Temel, B. (2004). Transient analysis of viscoelastic helical rods subject to time-dependent loads. *International Journal of Solids and Structures*, 41(5–6), 1605–1624. [CrossRef]

[43] Calim, F. F. (2016). Free and forced vibration analysis of axially functionally graded Timoshenko beams on two-parameter viscoelastic foundation. *Composites Part B*, 103, 98–112. [CrossRef]

[44] Noori, A. R. , Rasooli, H. , Aslan, T. A. & Temel, B. (2020). Static analysis of functionally graded sandwich beams by the complementary functions method. *Çukurova University Journal of the Faculty of Engineering and Architecture*, 35(4), 1091–1102.

[45] Rasooli, H., Noori, A. R., & Temel, B. (2021). On the static analysis of laminated composite frames having variable cross section. *Journal of the Brazilian Society of Mechanical Sciences and Engineering*, 43, Article 258. [CrossRef]

[46] Humaish, H., Ruet, B., Marmoret, L., & Beji, H. (2016). Assessment of long time approximation equation to determine thermal conductivity of high porous materials with NSS probe. *Journal of Sustainable Construction Materials and Technologies*, 1(1), 1–15. [CrossRef]

[47] Pham, Q. H., Tran, T. T., Tran, V. K., Nguyen, P. C., & Nguyen-Thoi, T. (2022). Free vibration of functionally graded porous non-uniform thickness annular-nanoplates resting on elastic foundation using ES-MITC3 element. *Alexandria Engineering Journal*, 61, 1788–1802. [CrossRef]

[48] Zghal, S., Ataoui, D., & Dammak, F. (2022). Static bending analysis of beams made of functionally graded porous materials. *Mechanics Based Design of Structures and Machines*, 50(3), 1012–1029. [CrossRef]

[49] Chen, D., Rezaei, S., Rosendahl, P. L., Xu, B. X., & Schneider, J. (2022). Multiscale modelling of functionally graded porous beams: Buckling and vibration analyses. *Engineering Structures*, 266, Article 114568. [CrossRef]

[50] Najibi, A., & Shojaeefard, M. H. (2022). Fourier and time-phase-lag heat conduction analysis of the functionally graded porosity media. *International Communications in Heat and Mass Transfer*, 136, Article 106183. [CrossRef]

[51] Ramteke, P. M., Panda, S. K., & Patel, B. (2022). Nonlinear eigenfrequency characteristics of multi-directional functionally graded porous panels. *Composite Structures*, 279, Article 114707. [CrossRef]

[52] Liu, Y., Qin, Z., & Chu, F. (2022). Analytical study of the impact response of shear deformable sandwich cylindrical shell with a functionally graded porous core. *Mechanics of Advanced Materials and Structures*, 29(9), 1338–1347. [CrossRef]

[53] Surmeneva, M. A., Khrapov, D., Prosolov, K., Kozadayeva, M., Koptyug, A., Volkova, A., Paveleva, A. & Surmenev, R. A (2022). The influence of chemical etching on porous structure and mechanical properties of the Ti6AL4V Functionally Graded Porous Scaffolds fabricated by EBM. *Materials Chemistry and Physics*, 275, Article 125217. [CrossRef]

[54] Ansari, R., Oskouie, M. F., & Zargar, M. (2022). Hygrothermally induced vibration analysis of bidirectional functionally graded porous beams. *Transport in Porous Media*, 142, 41–62. [CrossRef]

[55] Teng, M. W., & Wang, Y. Q. (2021). Nonlinear forced vibration of simply supported functionally graded porous nanocomposite thin plates reinforced with graphene platelets. *Thin-Walled Structures*, 164, Article 107799. [CrossRef]

[56] Pham, Q. H., Tran, T. T., Tran, V. K., Nguyen, P. C., Nguyen-Thoi, T., & Zenkour, A. M. (2021). Bending and hygro-thermo-mechanical vibration analysis of a functionally graded porous sandwich nanoshell resting on elastic foundation. *Mechanics of Advanced Materials and Structures*, 1–21. [CrossRef]

[57] Su, J., Qu, Y., Zhang, K., Zhang, Q., & Tian, Y. (2021). Vibration analysis of functionally graded porous piezoelectric deep curved beams resting on discrete elastic supports. *Thin-Walled Structures*, 164, Article 107838. [CrossRef]

[58] Wattanasakulpong, N., & Eiadtrong, S. (2022). Transient responses of sandwich plates with a functionally graded porous core: Jacobi-Ritz method. International *Journal of Structural Stability and Dynamics*, [Epub ahead of print] doi: 10.1142/S0219455423500396 [CrossRef]

[59] ANSYS Mechanical APDL Element Reference. *Mechanical APDL element reference*. Pennsylvania: ANSYS Inc; 2013.

[60] ANSYS Inc. (Oct 10, 2022). *Gain greater engineering and product life cycle perspectives 2022 product releases & updates*. Release Ansys 2022 R2, Canonsburg, PA, 2022. Available at: https://www.ansys.com/products/release-highlights

Journal of Sustainable Construction Materials and Technologies
Web page info: https://jscmt.yildiz.edu.tr
DOI: 10.47481/jscmt.1161504

JSCMT
Journal of Sustainable Construction Materials and Technologies

Research Article

A survey on the relationships between Compression Index, coefficient of consolidation, and atterberg limits

Kaveh DEHGHANIAN*, **Şirin Özkan İPEK**

Department of Civil Engineering, İstanbul Aydın University Faculty of Engineering, İstanbul, Türkiye

ARTICLE INFO

Article history
Received: 12 August 2022
Revised: 22 September 2022
Accepted: 07 November 2022

Key words:
Atterberg limits, coefficient of consolidation, Compression Index

ABSTRACT

Correlations between compression index and Atterberg limits found in the literature are significant for preliminary estimation. These equations are usually interpreted based on the R-square parameter and classified according to the conditions of the data (disturbed, undisturbed, remolded, etc.). Although correlations reliable enough to eliminate oedometer tests are not yet fully available, these correlations can be helpful in local calculations. In this study, correlations obtained from studies conducted after 2000 on the relationship of compression index and consolidation coefficient with Atterberg limits and water content are mentioned and clearly shown. While the compression index equations are pretty high in the literature, the equations produced with the consolidation coefficient are less in number due to the time-consuming consolidation calculations. Using 105 data from research in the literature, two equations were formed between the compression index, liquid limit, and plasticity index. This study does not propose new equations; only relationships are generated using the Linear Regression method with data obtained from independent studies based on the belief that the compression index has a stronger relationship with the liquid limit and plasticity index.

Cite this article as: Dehghanian, K., & İpek, ŞÖ. (2022). A survey on the relationships between Compression Index, coefficient of consolidation, and atterberg limits. *J Sustain Const Mater Technol*, 7(4), 302–315.

1. INTRODUCTION

Maintaining the balance of safety, economy, and aesthetics aimed at engineering studies; requires the design of low-cost, secure structures. Balancing cost and stability is crucial in geotechnical Engineering. Estimating soil parameters by empirical correlation is widely practiced in soil engineering. The main reasons are: that direct measurements are not always applicable and include costly and time-consuming uncertainties. Therefore, empirical correlation can provide a quick and inexpensive way to estimate parameters with a simple test. Most of these correlations are derived from fitting data measurements made under specific site conditions and can cause large deviations when used at other sites. The main research question addressed in this paper is to investigate the applicability of different correlations. The paper is organized as follows. The 'methodology' section presents both the framework of relevant case studies. The following section describes the specifications of the soil samples. A section describes some case studies, linking them with the existing literature. The final section offers a brief discussion and some concluding points. All the research is limited to the year 2000 and later.

***Corresponding author.**
*E-mail address: kavehdehghanian@aydin.edu.tr

2. REVIEW OF THE EXISTING CORRELATIONS

2.1. Compression Index and Liquid Limit Relations

Compression index (C_c) and coefficient of consolidation (C_v) are two soil characteristics that can determine a soil's compressibility: capacity to reduce volume under pressure (C_v). The coefficient of consolidation is used to forecast how long it will take for a given amount of compression to occur, whereas the compression index is used to estimate settlement. Since Atterberg's limits of the soil's liquid limit (LL) and plastic limit (PL) can be determined quickly, cheaply, and quickly using representative soil samples collected during field exploration [1, 2] efforts have been made to predict the value of compression index of fine-grained soils from these limits ever since. Several scientists have studied the Compression Index and Liquid Limit Relations. Hamza Güllü et al. [3] conducted a study in Baghdad and aimed to establish empirical correlations between soil index properties, water content, liquid limit, initial void ratio (e) and the compression index for 69 fine-grained soil samples. The liquid limit values of the samples ranged from 32% to 62%. The relationship between the Cc and the LL was the most reliable among these correlations. The developed correlation in this study is suitable for the Baghdad region.

$$(C_C=0.00454LL - 0.01246, R^2=0.87) \quad (1)$$

Kok Shien Ng et al. [4] showed a correlation between the C_c with the LL. The study was conducted on five remolded cohesive soil samples with different plasticity properties. The liquid limit values of the samples ranged from 29% to 46%. The correlation of the LL with the C_c presented a very high correlation coefficient.

$$(C_C=0.0062LL + 0.0165, R^2=0.9241) \quad (2)$$

The soil samples used in the study by Kumar K [5] were collected from 6 different regions of India. Fine-grained soils (CH) are classified according to the Indian Standard (IS). The liquid limit values of the samples ranged from 63% to 70%. The R^2 value shows a strong linear relationship between the C_c and the LL.

$$(C_C=0.001(LL) - 0.013, R^2=0.865) \quad (3)$$

In the study of Puri et al. [6], soil samples were collected from North India. Geotechnical data were obtained from 1053 different locations in the state of Haryana. They created different relationships between the C_c and the LL using Linear Regression (LR) Analysis, Artificial Neural Network (ANN), Support Vector Machine (SVM), Random Forest (RF), and M5 Tree (M5P) models. According to R^2 values, the accuracy of the M5P model was found to be the highest. Puri proposed three different empirical correlations according to varying liquid limit ranges. These correlations were suitable for use in Haryana and surrounding areas.

$$(C_C=(0.0092LL) - 0.1091, R^2=0.92) \quad LL\leq 29.25 \quad (4)$$

$$(C_C=(0.0017LL) + 0.1235, R^2=0.92) \quad 29.25< LL <37.35 \quad (5)$$

$$(C_C=(0.0064LL) - 0.0523, R^2=0.92) \quad LL \geq 37.35 \quad (6)$$

Solanki [7] aimed to create empirical correlations between C_c and soil index properties with 135 literature data from 10 regions in Gujarat, India. The mineralogy of soil samples was fine-grained montmorillonite and kaolinite. The liquid limit values of the samples ranged from 30% to 60%. The correlation created in the model produced for shallow foundations provides a strong relationship between the LL and the C_c.

$$(C_C=0.0061LL - 0.0024, R^2=0.8435) \quad (7)$$

Other researchers created empirical correlations through the compression index parameter and soil index properties;

Sridharan and Nagaraj [8] performed conventional consolidation tests on ten soil samples. The initial water contents of these samples were kept almost equal to the liquid limits. While applying traditional consolidation tests, the British Standard is taken as a basis. In the study conducted on remolded clay samples, the liquid limit values of the soil samples ranged from 30% to 60%. The study showed a pretty strong relationship between the C_c and the LL as follows:

$$(C_C=0.008\ (LL - 12), R^2=0.8285) \quad (8)$$

Vinod P. and Bindu J. [9] performed studies on remolded marine soil. Eighteen highly plastic soil samples were collected from Kerala in India with gray and black marine clay characteristics. The liquid limit values of the soil samples ranged from 70.8% to 276.3%. The correlation between the C_c and the LL as a result of this study was developed, which had a perfect correlation coefficient.

$$(C_C=0.0055\ (LL - 1.8364), R^2=0.9407) \quad (9)$$

Slamet W. and Abdelazim I. [10] studied 20 samples collected from 10 boreholes in Pontianak, Indonesia. Independent variables associated with the compression index were; void ratio, water content, and liquid limit. The liquid limit values of the soil samples ranged from 17.1% to 62.46%. In the correlation between the C_c and the LL, the R^2 value showed that the relationship between the two parameters is weak.

$$(C_C=0.01706\ LL - 0.02209, R^2=0.349) \quad (10)$$

Zaman et al. [11] used 14 undisturbed clay samples their study collected from Bangladesh. The liquid limit values of the soil samples ranged from 33.73% to 67.097%. The correlation between the C_c and the liquid limit was quite strong. This equation was suitable for use in Bangladesh soils.

$$(C_C=0.01\ (LL - 13.61),\ R^2=0.9805) \quad (11)$$

Binod Tiwari and Beena Ajmera [12] obtained 82 different natural samples by mixing montmorillonite, illite, kaolinite, and quartz in the laboratory. The soil samples in the study were collected from natural disaster areas in Japan. As a consequence of this study, the correlations between C_c and LL were determined as two types. The first of these (12) was for soils having activity less than 1.

$$(C_C=0.0075(LL),\ R^2=0.920) \quad (12)$$

The equation proposed for soils with activity greater than 1 is very efficient with R^2 value.

$$(C_C=0.012(LL),\ R^2=0.943) \quad (13)$$

It was observed that most montmorillonite soil samples have an activity greater than 1. The researchers stated that the empirical equations created with the LL showed the highest performance among the correlations they created between the C_c and other soil index properties.

In the study executed by Amit N. and S.S. DeDalal [13], they used 50 samples mixed with river sand and clay in different proportions. They mainly used bentonite and kaolinite, collected from West Bengal, India. Fourteen of the samples were classified as CH (High-plastic clay), 14 of the samples as CI (Intermediate-plastic clay), 20 samples as CL (Low-plastic clay), Low plastic silty- clayey soil (CL-ML), and a plastic limit of 1 sample could not be determined. In the study, C_c and LL together showed high compliance.

$$(C_C=0.0124LL - 0.1761,\ R^2=0.993) \quad (14)$$

Ayşen Lav and Atilla Ansal [14] suggested correlations between the compression and soil index parameters. For this study, they used 300 soil specimens collected from laboratory data in Türkiye. The liquid limit values of the soil samples ranged from 23% to 166%. They presented an insufficient relationship between C_c and LL for all soils (Eq. 15). They suggested another correlation for Normally-Consolidated clays (NC) with sufficient R^2 value (Eq. 16).

$$(C_C=0.006\ (LL + 1),\ R^2=0.509) \quad (15)$$

$$(C_C=0.007LL - 0.029),\ R^2=0.661) \quad (16)$$

Gil Lim Yoon et al. [15] used 1200 marine clay samples collected from 3 different regions of Korea to establish correlations between C_c and soil index properties. Undisturbed soil samples were classified as CL, CH, Low-Plastic Silt (ML), and High-Plastic Silt (MH). Three hundred fifty-six soil samples were used for the west coast, and their liquid limits ranged from 24.5% to 77.9%. 603 samples were used for the east coast, and liquid limits ranged from 23% to 107%. 278 soil samples were used for the south coast, with liquid limit values ranging from 28.4% to 120.2%. Relatively strong correlations were observed between the C_c and the LL.

$$(C_C=0.012(LL + 16.4),\ R^2=0.64)\ \text{South coast} \quad (17)$$

$$(C_C=0.011(LL - 6.36),\ R^2=0.64)\ \text{East coast} \quad (18)$$

$$(C_C=0.01(LL - 10.9),\ R^2=0.67)\ \text{West coast} \quad (19)$$

Akayuli and Ofosu [16] aimed to produce correlations between C_c and Atterberg limit properties by performing tests on 90 soil samples collected from Kumasi in Ghana. 60 of these samples were used directly in the model, and the other 30 were used to confirm the model in the estimation of the C_c. The samples used in the study were taken from the laboratory and collected under the same conditions. Samples were classified as weathered Brimian phyllites; their liquid limits ranged from 14.6% to 67.6%. As a result of the research, a reasonable correlation has been developed between the C_c and the LL for use in this region.

$$(C_C=0.004LL - 0.03,\ R^2=0.784) \quad (20)$$

Kumar, Jain, et al. [17] created empirical equations in their study using soil samples collected from 16 different regions of Bhopal, India. Soil samples were classified as nine black-cotton soils, four red soils, three yellow soils, two bentonite soils, and five black-cotton soils with different proportions of bentonite. Their liquid limit values ranged from 41.28% to 140.56%. They used ten soil samples under the same conditions to verify their proposed equation. As a result of the study, C_c has a strong relationship with LL.

$$(C_C=0.0067\ (LL) - 0.0364,\ R^2=0.94) \quad (21)$$

Salih [18] worked on soil samples from various Iraq regions. While obtaining this correlation, 76 undisturbed soil samples were used, and their liquid limit values ranged from 30% to 70%. As a result of this study, it was observed that there was a weak correlation between C_c and LL.

$$(C_C=-0.0037LL + 0.352,\ R^2=0.46) \quad (22)$$

Al-Khafaji et al. [19] aimed to generate new empirical equations using 1906 samples from previous studies. They used Robust Bi-Square software in MATLAB to avoid data outliers and obtain more realistic results. First, they produced a correlation (23) for LL >16 using conventional regression analysis. The authors stated that a low Root Mean Square Error (RMSE) value means that the model is 95% reliable. Then an equation (24) was created using Robust Bi-Square. This equation (24) provided higher accuracy with a lower RMSE and was deemed suitable for liquid limit values LL >17. Since most of the mineral soils are evaluated in the 16< LL <100, a reanalysis was performed on the data in this range using Robust Bi-Square. The equation (25) was created as a result of this analysis. The equations (24) and (25) obtained using Robust Bi-Square were almost similar and suitable for use in samples within the specified liquid limit ranges.

$$(C_C=-0.1096 + 0.01049LL, R^2=0.7688) \quad (23)$$

$$(C_C=-0.012\ (LL - 17), R^2=0.8617) \quad (24)$$

$$(C_C=0.0116\ (LL - 16.6), R^2=0.7066) \quad (25)$$

Dway and Thant [20] studied six disturbed samples collected at 3 and 6 feet from 3 locations in Mandalay. Four of the soil samples were classified as CH (High- Plastic Clay) and 2 as CL (Low- Plastic Clay), and their liquid limit values ranged from 41% to 70.1%. Correlations between C_c and soil index properties were established using linear regression. The proposed equation between the LL and the C_c has been found to have a low correlation coefficient and cannot be used to predict the compression index.

$$(C_C=0.0027LL + 0.1994, R^2=0.250) \quad (26)$$

In the study presented by Laskar and Pal [21], they studied three different soil samples collected from different regions of India. The study observed that the correlation between the C_c and the LL was quite reliable.

$$(C_C=0.0046(LL -1.39), R^2=0.994) \quad (27)$$

Abbasi et al. [22] estimated the C_c using 26 soil samples from 5 provinces of Iran. The soil samples used in this study were fine-grained and disturbed. The researchers took care that the liquid limit values of the soil samples were below 75. As a result of the study, the correlation between the C_c and the LL was found to be insufficient.

$$(C_C=0.007LL - 0.043, R^2=0.351) \quad (28)$$

Bartlett and Lee [23] found a weak relationship between the LL and the C_c in their study in Salt Lake Valley.

$$(C_C=0.01LL - 0.026, R^2= 0.3129) \quad (29)$$

McCabe et al. [24] aimed to establish empirical relationships between C_c and soil index properties in fine-grained soils of Ireland. In this study, 61 soil samples were collected from different parts of Ireland, and the liquid limit values ranged between 32% and 199%. The empirical equation formed between the C_c and the LL has been found suitable for local prediction. The R^2 value of the equation was found to be entirely satisfactory.

$$(C_C=0.0118LL - 0.2443, R^2=0.809) \quad (30)$$

Nesamatha and Arumairaj [25] wanted to estimate the C_c by conducting tests on five soil samples collected from different parts of Coimbatore, India. Soil samples were remolded in black cotton soil. The liquid limit values of soils ranged between 66.2% to 77.8%. The R^2 value showed that the LL is very influential in the estimation of the C_c.

$$(C_C=0.002LL - 0.127, R^2=0.9694) \quad (31)$$

Rashed et al. [26] proposed a correlation using 54 undisturbed soil samples from Sulaymaniyah, Iraq. The liquid limit values of the soil samples varied between 35.5% and 65.2%. The equation was found sufficient to be used in preliminary estimating the compression index.

$$(C_C=0.006LL - 0.1, R^2=0.74) \quad (32)$$

In the study of Al-Ameri and Al-Kahdaar [27] soil samples were collected from Ammarah, Iraq. Soil samples obtained from 40 different locations, selected from geotechnical reports, and brought together, were evaluated as low to high-plasticity clays. The LL values of soil samples ranged from 22% to 62%. Linear regression analysis was used to create the empirical correlation. It was observed that there is a strong relationship between the C_c and the LL.

$$(C_C=0.00556LL, R^2=0.868) \quad (33)$$

Shaikh et al. [28] studied soil samples collected from Khulna, Bangladesh. A lot of soil structure is being made on the organic soils of Khulna city with poor bearing capacity; this study was carried out to quickly obtain a preliminary estimate of the C_c in the studies conducted in this region. The LL values of soil samples ranged between 29% to 68%. According to this study, it is seen that there is a powerful relationship between C_c and LL.

$$(C_C=0.011LL - 0.102, R^2= 0.818) \quad (34)$$

Kootahi and Moradi [29] studied approximately 500 marine clay samples from 1000 different locations worldwide from 170 different data sources. These soil samples were obtained from the studies of 40 different researchers.

The intact ones were chosen among these samples for the estimation of the C_c on marine clays. It is stated that most of the marine clays were collected from Southeast and South Asia, Northern Europe, and North and South America. Marine clays had different physical and engineering properties. Researchers classified 70% of marine clays as CH-CL and 30% as MH-ML. The correlation created from this detailed study showed that the C_c has a strong relationship with the LL parameter.

$$(C_C=-0.096 + 0.012LL, R^2=0.87) \quad (35)$$

Ara S et al. [30] used eight undisturbed soil samples collected from Chattagram city. As a result of this study, a strong relationship was established between Cc-LL.

$$(C_C=0.0046LL + 0.2324, R^2=0.9137) \quad (36)$$

2.2. Compression Index and Plasticity Index Relations

Bello et al. [31] studied eight migmatite-gneiss-derived laterite samples collected from Southwest Nigeria. Soils were classified as 37% low-plastic clay (CL), 37% medium-plastic clay (CI), 13% high-plastic clay (CH), and 13% medium-plasticity clay (MI). The plasticity index (PI) values ranged between 8% to 33.65%. Bello established correlations between the C_c and SI (Shrinkage Index), which is the range between liquid limit and shrinkage limit, LS (Linear Shrinkage), which shows a decrease in one dimension of soil expressed as a percentage of its original dimension, when the water content is reduced from its given value up to shrinkage limit, and PI. The most effective of these correlations was found to be the relation between the C_c and the PI.

$$(C_C=0.0028PI - 0.0052, R^2=0.90) \quad (37)$$

Kok Shien Ng et al. [4] also found a correlation between the C_c and the PI. The PI values of soil samples ranged from 8% to 18%. Although this correlation is not very strong, it is usable without other index properties.

$$(C_C=0.0032PI + 0.1817, R^2=0.7186) \quad (38)$$

Solanki [7] also presented a correlation between C_c and PI. PI values of soil samples ranged from 15% to 30%. The R^2 value was satisfactory, although not as good as the liquid limit correlation.

$$(C_C=0.0082PI + 0.0915, R^2=0.7862) \quad (39)$$

The equation proposed by Vinod P. and Bindu J. [9] was created for use in remolded marine soils. PI values ranged from 34.8% to 235.5%. The coefficient of this correlation was found to be relatively high.

$$(C_C=0.0086 (PI + 24.2674), R^2=0.970) \quad (40)$$

The correlation suggested by Zaman et al. [11] also showed a strong relationship between the C_c and the PI. In this study, PI values of soil samples ranged between 12.083% to 44.287%.

$$(C_C=0.0091PI + 0.128, R^2=0.8864) \quad (41)$$

Like other researchers, Sridharan and Nagaraj [8] suggested a strong correlation between C_c and PI. The plasticity indexes of the soil samples ranged from 9.5% to 37.9%.

$$(C_C=0.014 (PI + 3.6), R^2=0.91) \quad (42)$$

In Akayuli and Ofosu [16] study, when they examined the relationship between the C_c and PI, the R^2 value showed a good relationship.

$$(C_C=0.007PI + 0.01, R^2=0.580) \quad (43)$$

Gil Lim Yoon et al. [15] studied marine clay in Korea. Soil samples are divided into three subgroups according to their plasticity characteristics as the east, west, and south coasts. The relationship between C_c and PI was created only for the east coast compared to other soil index properties. This correlation demonstrated a good relationship between the C_c and PI.

$$(C_C=0.014PI + 0.165, R^2=0.61) \quad (44)$$

Salih [18] worked with soil samples he collected from Sulaymaniyah city in Iraq. The correlation he created as a result of this study showed that the PI is unsuitable for finding the C_c.

$$(C_C=-0.0049PI + 0.2882, R^2=0.44) \quad (45)$$

The correlation established by Dway and Thant [20] presented an inadequate relationship. In this study, the PI values of soil samples ranged between 25% and 48.8%.

$$(C_C=0.0038 PI + 0.22, R^2=0.303) \quad (46)$$

In the article they published, Laskar and Pal [21] worked on only three soil samples. Plasticity index values ranged from 5% to 35%, and the correlation presented a relatively high R^2 value.

$$(C_C=0.0058 (PI+13.776), R^2= 0.991) \quad (47)$$

Barlett and Lee [32] presented a relatively low correlation for C_c estimation.

$$(C_C=0.0099PI + 0.2039, R^2=0.1789) \quad (48)$$

Nesamatha and Arumairaj [25] used 5 different remolded stiff clays collected from India in this study. They established a correlation with Regression Analysis in Eq. (49). The R^2 value was relatively high.

(C_C=0.003PI – 0.081, R^2=0.91) (49)

The study of Rashed et al. [26] was conducted using 46 undisturbed fine-grained soil samples collected from Iraq. The plasticity indexes of these soil samples ranged from 15.26% to 28.2%. According to the empirical equation, a strong correlation was found between the C_c and the PI.

(C_C=0.007PI + 0.04, R^2=0.72) (50)

Shaikh et al. [28] derived a robust correlation between the C_c and the PI using organic clays with poor bearing strength from Khulna city, Bangladesh.

(C_C=0.017PI + 0.180, R^2=0.904) (51)

Jain et al. [33] conducted research using 44 soil samples from geotechnical studies in various regions of India. The samples were laboratory data obtained under the same conditions. The empirical equation they produced was found to be reasonably sufficient for the estimation of the C_c. It was stated that the equation in this study is valid for soil samples with PI values between 5 and 35 percent.

(C_C=0.0082PI + 0.0475, R^2=0.8984) (52)

Kootahi and Moradi's [29] study used data from approximately 500 marine clay samples from different researchers' studies. The soil samples used in this study had different plasticity and consolidation properties. As a result, the relationship between the C_c and the PI was found to be entirely satisfactory.

(C_C=0.013 + 0.020PI, R^2=0.85) (53)

2.3. Compression Index and Plastic Limit Relations

Few studies in the literature examined the relationship between C_c and PL. One of these studies is by Kok Shien Ng et al. [4]. As a result of the study, a sufficiently good relationship was observed between these two parameters.

(C_C=0.0133PL – 0.0833, R^2=0.6809) (54)

Akayuli and Ofosu [16] also correlated the C_c and PL. They created an invalid relationship between these two parameters in their study on Brimian phyllites in the Kumasi area.

(C_C=0.003PL + 0.055, R^2=0.43) (55)

Another study that presented a strong correlation between the PL and the C_c was by Rashed et al. [26]. In this study, 45 undisturbed soil samples were used, and these samples were selected from among 60 samples collected from various parts of the Iraqi city of Sulaymaniyah. The PL values of these samples varied between 20 and 37 percent. The empirical correlation they created presented an excellent relationship.

(C_C=0.007PL – 0.005, R^2=0.75) (56)

Ara S et al. [30] proposed a weak correlation between C_c and PL.

(C_C=0.0024PL + 0.3705, R^2=0.3113) (57)

2.4. Compression Index and Water Content Relations

Vinod P. and Bindu J. [9] developed a reasonably strong correlation between C_c and natural water content (w_n). The wn values of these samples varied between 64.7 and 184.3 percent. This correlation is suitable for use for marine clays in India.

(C_C=0.0072 (w_n – 12.625), R^2=0.878) (58)

Solanki [7] also created a correlation between the C_c and water content on soil samples collected from India. The soil samples' water content values ranged from 15% to 30%. The R^2 produced an excellent relationship.

(C_C=0.0091w_n + 0.0522, R^2=0.77) (59)

Slamet W. and Abdelazim I. [10] produced an imperfect correlation between C_c and natural water content.

(C_C= 0.01w_n + 0.12, R^2=0.24) (60)

The correlation suggested by Zaman et al. [11] was strong and suitable for use in Bangladesh soils and similar types of soils.

(C_C=0.0158w_n – 0.179, R^2=0.8997) (61)

Alptekin and Taga [33] performed Atterberg tests on 58 soil samples collected from Türkiye's Mersin city; samples were selected as 18 marine and 40 terrestrials. 4 were not plastic, so Atterberg tests were not performed on these four samples. The soil samples used in this study were undisturbed. For this reason, it is thought that more realistic results are obtained.

(C_C=0.0064w_n – 0.0607, R^2=0.598) (62)

Soil samples used in the study of Lav and Ansal [14] were collected from Türkiye's different regions. Additionally, the authors divided the 300 soil samples into subgroups according to their consolidation properties. Relatively strong correlations were found between the water content and the C_c. The correlation produced for all soil is as seen in Eq. (63). Eq. (64) was produced for normally consolidated clays.

(C_C=0.012w_n – 0.1, R^2=0.758) (63)

(C_C=0.012w_n – 0.098, R^2=0.877) (64)

Soil samples used in the research by Yoon et al. [15] were collected from various regions of Korea. The 1200 data used in this study were characterized as undisturbed marine clay. Correlations were created for soils specific to 3 different regions of Korea. While estimating the C_c, it was understood that the water content would be sufficient for each coast.

(C_C=.013(wn – 3.85), R^2=0.73) South coast (65)

(C_C=0.01(w_n + 2.83), R^2=0.54) East coast (66)

(C_C=0.011(w_n – 11.22), R^2=0.67) West coast (67)

Güllü et al. [3] conducted a study suggesting a correlation between C_c and natural water content. The correlation established on 69 fine-grained soil samples obtained from Baghdad city is suitable for use in the Baghdad region.

(C_C=0.00553w_n + 0.05321, R^2=0.53) (68)

In the study of Akayuli and Ofosu [16], the correlation they formed between the C_c and the moisture content was considered to be weak for the Ghana region.

(C_C=0.002w_n + 0.14, R^2=0.382) (69)

In the research of Sari and Firmansyah [34] 425 of 466 soil samples obtained from 25 different regions in Indonesia were used. This research was carried out to compare the correlations in the literature and check their suitability for use. Samples were divided into subgroups. Correlations were not suitable for use.

(C_C=0.0143w_n – 0.0165, R^2=0.5102)
LL=0 – 100%; PI=0 – 70% (70)

The empirical equation proposed by Dway and Thant [20] between w_n and C_c was found to be moderately usable.

(C_C=0.01w_n + 0.027, R^2=0.491) (71)

In their study, Laskar and Pal [21] used 3 different soil samples, and the water contents varied between 15 and 32 percent.

(C_C=0.0134 (w_n – 7.034), R^2=0.985) (72)

Abbasi et al. [22] correlated the water content and the compression index using 26 fine-grained soil samples collected from different regions of Iran. Most of the soil samples were classified as low-plasticity clay. The correlation coefficient given by this correlation showed a strong relationship between these two parameters.

(C_C=0.008w_n – 0.044, R^2=0.848) (73)

In the study presented by Barlet and Lee [23], it was observed that there is a sufficiently strong correlation between the natural water content and the C_c.

(C_C=0.0163w_n – 0.247, R^2=0.6572) (74)

McCabe et al. [24] examined 61 soil samples in their study on Irish soil. The water contents of these samples ranged from 34.7% to 244.1%. A robust correlation was observed between the C_c and the natural water content. Although this equation is unsuitable for use instead of oedometer tests in Irish soil, it was found to be reasonably sufficient in terms of preliminary prediction.

(C_C=0.014w_n – 0.3175, R^2=0.858) (75)

Al-Ameri and Al-Kahdaar [27] produced an empirical equation using 40 different soil sample data from geotechnical reports in Ammarah, Iraq. The R^2 value of this equation showed that a powerful equation was presented.

(C_C=0.0092w_n, R^2=0.946) (76)

The equation by Kootahi and Moradi [29] is proposed for marine clays. These marine clays were collected from studies in the literature from different parts of the world. The R^2 value of the equation showed that the water content parameter could be used to estimate the C_c.

(C_C=–0.093 + 0.012w_n, R^2=0.91) (77)

2.5. Coefficient of Consolidation Relations

Kassou et al. [35] studied settling and consolidation rates in the High-Speed Rail Project in Morocco. They showed that the elastic method using the pressure-gauge modulus gives more accurate results than the iodometric method. This correlation they produced agrees with the US Navy correlation and the C_v estimate.

(C_V=26.917LL – 2.57) (78)

Asma Y. and Abbas F. [36] tried to estimate and define the relationship between the C_V and LL in their studies in Central and Southern Iraq. The soil samples consisted of 280 undisturbed silty clay. The Casagrande method was used in liquid limit calculations, and Taylor's Square Root of Time Method was used in calculating the consolidation coefficient. Comparing data from Iraqi soil with data from other studies (US Navy study), it was seen that the curves overlap when LL equals 60, and there are deviations when it is less than or greater than 60. The presented curve was compared with the curve formed by the US Navy, and it was observed that the curves agree at one point (LL=60). As a result of the study, a good relationship was established between CV and LL.

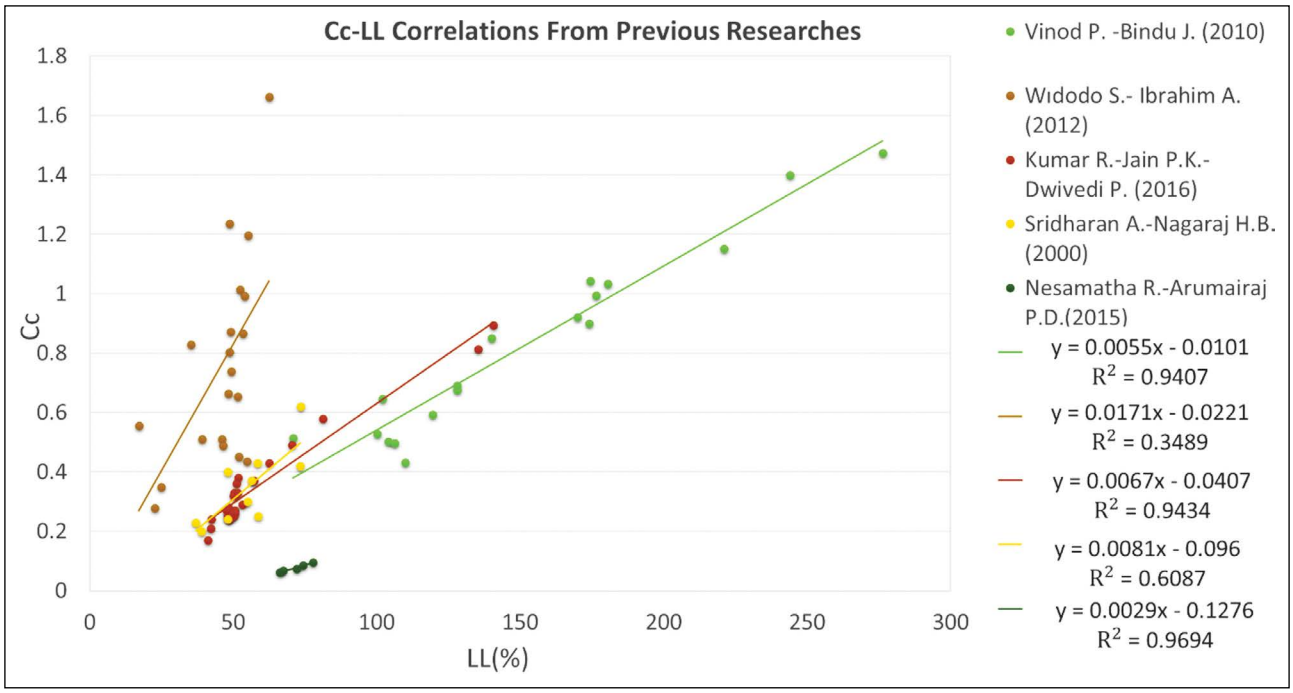

Figure 1. Relationships between C_c and LL.

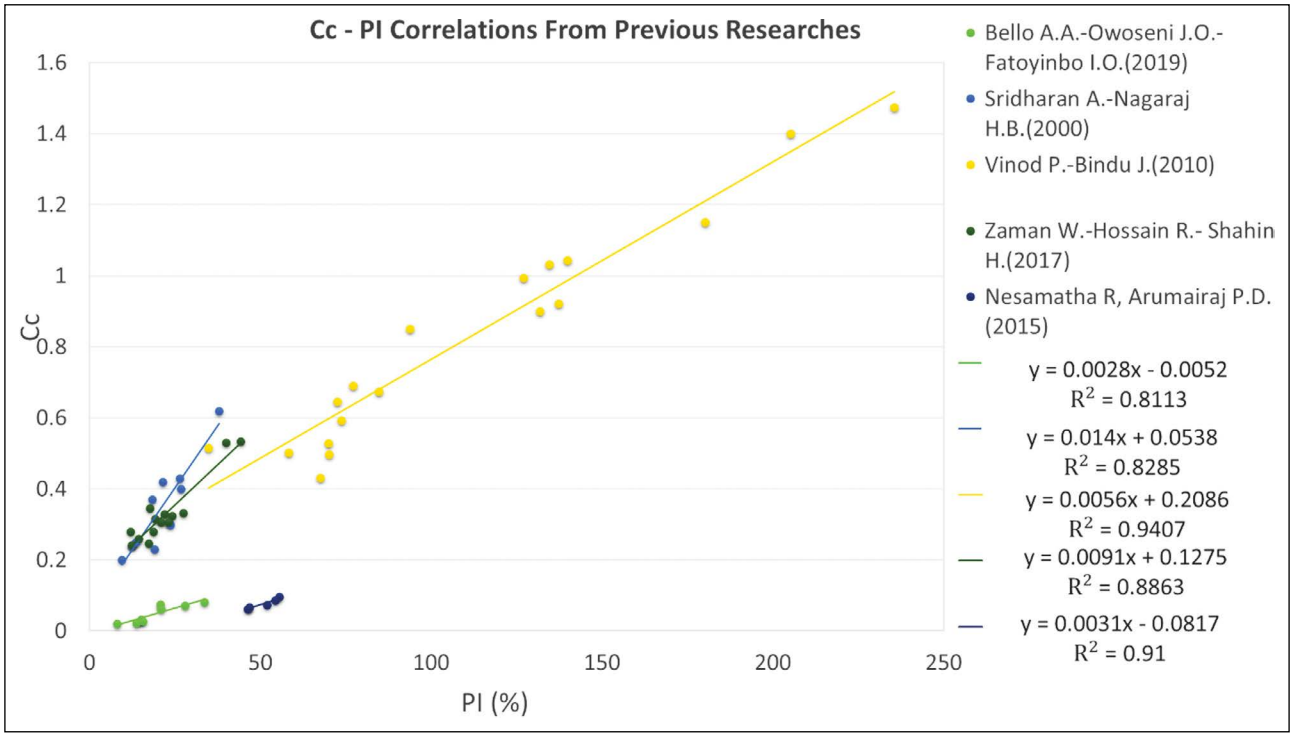

Figure 2. Relationships between C_c and PI.

$$(C_V=4258LL^{-1.758},\ R^2=0.721) \quad (79)$$

Devi et al. [37] produced correlations between the consolidation coefficient and the Atterberg limit properties. Soil samples were collected from different regions in the Manipur Valley (India). The five undisturbed samples included clay, silt, sand, and organic content. C_V values were calculated by the Casagrande method. Among the liquid limit, plasticity index, and shrinkage indices, it was seen that the CV was better associated with the LL.

(C_V=−4x10^{-9} LL + 4x10^{-7}, R^2=0.8298) (80)

(C_V=−1x10^{-7} ln(PI) + 6x10^{-7}, R^2=0.5954) (81)

(C_V=1x10^{-6} e$^{-0.064IS}$, R^2=0.6132) (82)

Solanki's [7] study aimed to predict the consolidation parameters in alluvial deposits as much as possible. This study was conducted with data collected from 10 different regions of Surat (India). Soil samples contained montmorillonite and kaolinite clay. It was studied with 135 test data obtained from the literature. Correlations of C_V with LL and PI were found to be entirely satisfactory.

(C_V=7.7525PI$^{-3.1025}$, R^2=0.9156) (83)

(C_V= 10^8 LL$^{-6.7591}$, R^2=0.7867) (84)

Kok Shien Ng et al. [4] examined the relationships between C_V and Atterberg limits conducted on five cohesive soil samples in Malaysia. Samples were designated as CI, CL, MI, and CI. C_V values were determined by the Taylor method. It was concluded that C_V was best associated with PI. The relationship with LL also gave good results.

(C_V=0.6155 −0.0183PI, R^2=0.9599) (85)

(C_V=0.7519 − 0.0102LL, R^2=0.8608) (86)

(C_V=0.859 − 0.0202PL, R^2=0.6505) (87)

In this experimental study, Sridharan and Nagaraj [38] investigated the relationships between C_V and LL, PI, and Shrinkage Index (SI) on ten disturbed soil samples. Soil samples contained varying proportions of silt, sand, and mainly kaolinite clay. As a result of the study, it was found that C_V had a good relationship with the plasticity index, and the best relationship was with the shrinkage index.

(C_V=4,3x10^7 (PI)$^{-4.7}$, R^2=0.6087) (88)

(C_V=3x10^{-2} (SI)$^{-3,54}$, R^2=0.8836) (89)

Bello et al. [31] studied eight disturbed samples in southwestern Nigeria. The liquid limit values of the samples were almost the same. As a result of the studies, it was observed that the correlation between C_V and PI was more substantial than other parameters.

(C_V=1x10^{-9} PI$^{-0,35}$, R^2=0.62) (90)

Jadhav's experimental work [39] was carried out on 20 different soil samples from different parts of Begaldot district, Karnataka state, India. At the end of the study, it was found that the relationship between the coefficient of consolidation and shrinkage index (SI) was.

(C_V=128.7/ (SI) 3.54 + 0.0002, R^2=0.715) (91)

Shaikh e al. [28] correlated the consolidation coefficient with LL and PI in 2 relationships. The R^2 values of these relations were found to be entirely satisfactory.

(C_V=0.241e$^{-0.08LL}$, R^2=0.818) (92)

(C_V=0.022e$^{-0.12PI}$, R^2=0.790) (93)

In the study of Vinod P. and Bindu J. [9], the slope value of the correlation they created between the compression index and the plasticity index was given as 0.0086 in Eq. (40). However, the slope value was found to be 0.0056 in the equation reconstructed with the help of linear regression as seen in Figure 1. In addition, the R-square value was calculated and found to be 0.9407 in Eq. (94).

(C_C=0.0056PI + 0.2086, R^2=0.9407) (94)

Figure 2 depicts the relationship between CC and PI. Data obtained from several research have been compared with each other. As it can be seen, the correlation factors show a good consistency between the mentioned parameters.

3. MATERIALS AND METHODS

In this part, the studied results are gathered in Table 1. The selected soil types include Low- Plastic soils (L) and High- Plastic Soils (H). Correlations were created with the linear regression method using the data obtained from the literature. The linear correlations between C_c, LL, and PI are shown in Figure 3 and Figure 4.

4. RESULTS

This research studied the published correlations between the plasticity index, compression index, liquid limit, plastic limit, water content, and coefficient of consolidation. The relations were determined based on the coefficient of correlation values. Equations between C_c, LL, and PI variables were created with the help of Linear Regression using independent data from 5 different studies. These soil samples were obtained under different conditions and are from different regions. In C_c and LL correlation, 87 samples were used, and the liquid limit values ranged from 20.5% to 479.9%. The R-Square value of this correlation was found to be 0.925, which indicates a strong relationship between the two parameters. For the correlation between the compression index and the plasticity index, 61 soil samples were used, and these samples were obtained under different conditions. The plasticity index values of these samples varied between

Table 1. List of the used data in the compression index estimation

No.	LL	PI	CC	Location	Author	No.	LL	PI	CC	Location	Author
1	88	40.23	0.747895	Manipur, India	Devi et al.	54	36	–	0.12	New Delhi, India	Kumar Jain et al.
2	58.65	24.09	0.244034	Manipur, India	Devi et al.	55	39.4	–	0.106	New Delhi, India	Kumar Jain et al.
3	76.2	50.65	0.257034	Manipur, India	Devi et al.	56	46	–	0.226	New Delhi, India	Kumar Jain et al.
4	62.1	32.96	0.258915	Manipur, India	Devi et al.	57	37	–	0.2	New Delhi, India	Kumar Jain et al.
5	52.4	22.53	0.14537	Manipur, India	Devi et al.	58	45.5	–	0.32	New Delhi, India	Kumar Jain et al.
6	66	32.3	0.32	Ariake, Japan	Park, Koumoto [40]	59	50	–	0.38	New Delhi, India	Kumar Jain et al.
7	66	32.3	0.35	Ariake, Japan	Park, Koumoto	60	46.5	–	0.35	New Delhi, India	Kumar Jain et al.
8	66	32.3	0.37	Ariake, Japan	Park, Koumoto	61	20.5	–	0.102	New Delhi, India	Ibrahim et al. [40]
9	50.4	32.8	0.23	Ariake, Japan	Park, Koumoto	62	28.7	–	0.092	New Delhi, India	Kumar Jain et al.
10	50.4	32.8	0.27	Ariake, Japan	Park, Koumoto	63	43.4	–	0.17	New Delhi, India	Kumar Jain et al.
11	50.4	32.8	0.31	Ariake, Japan	Park, Koumoto	64	30.7	–	0.16	New Delhi, India	Kumar Jain et al.
12	72.1	34.8	0.28	Ariake, Japan	Park, Koumoto	65	44	–	0.15	New Delhi, India	Kumar Jain et al.
13	72.1	34.8	0.38	Ariake, Japan	Park, Koumoto	66	31.1	–	0.15	New Delhi, India	Kumar Jain et al.
14	72.1	34.8	0.42	Ariake, Japan	Park, Koumoto	67	31.9	–	0.166	New Delhi, India	Kumar Jain et al.
15	81.7	39.7	0.33	Ariake, Japan	Park, Koumoto	68	29.5	–	0.176	New Delhi, India	Kumar Jain et al.
16	81.7	39.7	0.4	Ariake, Japan	Park, Koumoto	69	29.1	–	0.114	New Delhi, India	Kumar Jain et al.
17	81.7	39.7	0.45	Ariake, Japan	Park, Koumoto	70	42.6	–	0.23	New Delhi, India	Kumar Jain et al.
18	86.6	42.3	0.34	Ariake, Japan	Park, Koumoto	71	44.1	–	0.24	New Delhi, India	Kumar Jain et al.
19	86.6	42.3	0.4	Ariake, Japan	Park, Koumoto	72	45.8	–	0.179	New Delhi, India	Kumar Jain et al.
20	86.6	42.3	0.53	Ariake, Japan	Park, Koumoto	73	35.6	–	0.129	New Delhi, India	Kumar Jain et al.
21	78.6	47.5	0.56	Ariake, Japan	Park, Koumoto	74	27.1	–	0.16	New Delhi, India	Kumar Jain et al.
22	138.6	70	0.6	Ariake, Japan	Park, Koumoto	75	28.6	–	0.093	New Delhi, India	Kumar Jain et al.
23	138.6	70	0.72	Ariake, Japan	Park, Koumoto	76	33.9	–	0.126	New Delhi, India	Kumar Jain et al.
24	138.6	70	1	Ariake, Japan	Park, Koumoto	77	34.2	–	0.152	New Delhi, India	Kumar Jain et al.
25	166.2	113.9	0.91	Ariake, Japan	Park, Koumoto	78	34.8	–	0.166	New Delhi, India	Kumar Jain et al.
26	166.2	113.9	1.16	Ariake, Japan	Park, Koumoto	79	24.7	–	0.168	New Delhi, India	Kumar Jain et al.
27	166.2	113.9	1.34	Ariake, Japan	Park, Koumoto	80	34	–	0.124	New Delhi, India	Kumar Jain et al.
28	361.9	317.5	1.62	Ariake, Japan	Park, Koumoto	81	25.3	–	0.182	New Delhi, India	Kumar Jain et al.
29	361.9	317.5	2.27	Ariake, Japan	Park, Koumoto	82	30.6	–	0.135	New Delhi, India	Kumar Jain et al.
30	361.9	317.5	3.02	Ariake, Japan	Park, Koumoto	83	25.5	–	0.13	New Delhi, India	Kumar Jain et al.
31	479.9	443.7	2.87	Ariake, Japan	Park, Koumoto	84	27.8	–	0.13	New Delhi, India	Kumar Jain et al.
32	479.9	443.7	3.65	Ariake, Japan	Park, Koumoto	85	27	–	0.2	New Delhi, India	Kumar Jain et al.
33	479.9	443.7	4.76	Ariake, Japan	Park, Koumoto	86	30.5	–	0.173	New Delhi, India	Kumar Jain et al.

Table 1 (cont.). List of the used data in the compression index estimation

No.	LL	PI	CC	Location	Author	No.	LL	PI	CC	Location	Author
34	50	30	0.184	Southern England	Jones, Hobbs [41]	87	31.3	–	0.114	New Delhi, India	Kumar Jain et al.
35	57	33	0.197	Southern England	Jones, Hobbs	88	–	28.33	0.258	Perlis, Malaysia	Ibrahim et al.[42]
36	46	25	0.212	Southern England	Jones, Hobbs	89	–	29.10	0.265	Perlis, Malaysia	Ibrahim et al.
37	50	30	0.16	Southern England	Jones, Hobbs	90	–	30.14	0.456	Perlis, Malaysia	Ibrahim et al.
38	64	36	0.286	Southern England	Jones, Hobbs	91	–	29.38	0.723	Perlis, Malaysia	Ibrahim et al.
39	49	23	0.18	Southern England	Jones, Hobbs	92	–	30.10	0.764	Perlis, Malaysia	Ibrahim et al.
40	45	24	0.191	Southern England	Jones, Hobbs	93	–	32.75	0.918	Perlis, Malaysia	Ibrahim et al.
41	47	29	0.18	Southern England	Jones, Hobbs	94	–	30.76	0.506	Perlis, Malaysia	Ibrahim et al.
42	48	23	0.171	Southern England	Jones, Hobbs	95	–	30.24	0.270	Perlis, Malaysia	Ibrahim et al.
43	54	34	0.228	Southern England	Jones, Hobbs	96	–	31.70	0.968	Perlis, Malaysia	Ibrahim et al.
44	46.6	–	0.265	New Delhi, India	Kumar Jain et al.	97	–	30.49	0.940	Perlis, Malaysia	Ibrahim et al.
45	45	–	0.169	New Delhi, India	Kumar Jain et al.	98	–	29.07	0.607	Perlis, Malaysia	Ibrahim et al.
46	42.5	–	0.213	New Delhi, India	Kumar Jain et al.	99	–	28.09	0.387	Perlis, Malaysia	Ibrahim et al.
47	43.1	–	0.219	New Delhi, India	Kumar Jain et al.	100	–	28.47	0.101	Perlis, Malaysia	Ibrahim et al.
48	44.7	–	0.133	New Delhi, India	Kumar Jain et al.	101	–	28.80	0.341	Perlis, Malaysia	Ibrahim et al.
49	30	–	0.133	New Delhi, India	Kumar Jain et al.	102	–	30.04	0.723	Perlis, Malaysia	Ibrahim et al.
50	59.7	–	0.259	New Delhi, India	Kumar Jain et al.	103	–	27.49	0.186	Perlis, Malaysia	Ibrahim et al.
51	45.8	–	0.208	New Delhi, India	Kumar Jain et al.	104	–	29.53	0.498	Perlis, Malaysia	Ibrahim et al.
52	53	–	0.27	New Delhi, India	Kumar Jain et al.	105	–	28.19	0.335	Perlis, Malaysia	Ibrahim et al.
53	47.6	–	0.276	New Delhi, India	Kumar Jain et al.						

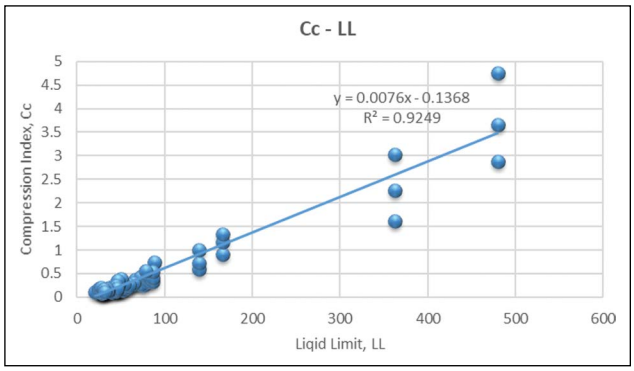

Figure 3. Observed Compression Index (C_c) and Liquid Limit (LL) with Linear Regression Analysis.

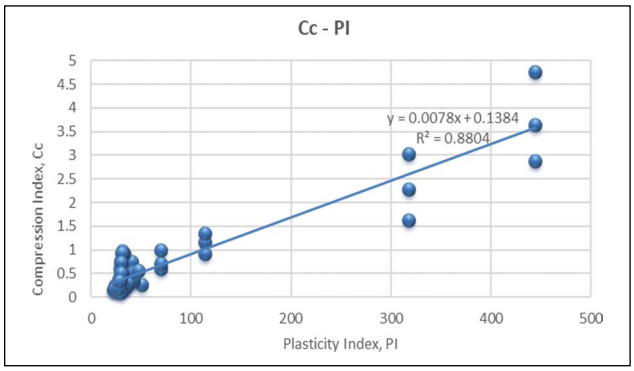

Figure 4. Observed Compression Index (Cc) and Plasticity Index (PI) with Linear Regression Analysis.

Table 2. Regression outputs between compression index, liquid limit, and plasticity index

Regression parameters	C_c-LL	C_c-PI
Multiple R	0.96170497	0.938300725
R Square	0.92487645	0.880408251
Observations	87	61

22.53% and 443.7%. The R-Square value of the correlation is 0.88, representing a solid relationship, as seen in Table 2.

$$(C_C=0.0076LL - 0.1368, R^2=0.9249) \quad (95)$$

$$(C_C=0.0078PI + 0.1384, R^2=0.8804) \quad (96)$$

According to Figures 3 and 4, it can be observed that for LL and PI values greater than 300, the correlation does not predict the Cc value, which can be due to the variable behavior of high plastic clayey soil and their swelling potential so restrictive criteria may be needed to be applied in the correlation. On the other hand, according to the studies presented in the literature, these parameters correlate well for low- plastic soils. Moreover, it can be concluded that the compression index values relate better with plasticity index values than shrinkage index and linear shrinkage values, respectively.

5. CONCLUSION

This study has studied and compared correlations between C_c and LL, C_c and PI, and C_C and w_n. According to the results, as shown in Table 2, the compression index strongly correlates with the liquid limit and plasticity index. As stated in the methodology section, the parameters considered suitable for estimating the compression index can be the primarily liquid limit and plasticity index. The purpose of the regression analysis in this study was to establish strong correlations with samples of various characteristics collected from independent studies. The obtained results presented correlations with strong R-square coefficients that support the studies in the literature. These parameters can support field data estimating the compression index under certain conditions. On the other hand, the coefficient of consolidation best correlates with the plastic index. In the absence of other test data, such as shrinkage limit and shrinkage index, which are not very prevalent tests, these findings can help engineers make predictions of different consolidation parameters with high accuracy without performing conventional oedometer tests.

ETHICS

There are no ethical issues with the publication of this manuscript.

DATA AVAILABILITY STATEMENT

The authors confirm that the data that supports the findings of this study are available within the article. Raw data that support the finding of this study are available from the corresponding author, upon reasonable request.

CONFLICT OF INTEREST

The authors declare that they have no conflict of interest.

FINANCIAL DISCLOSURE

The authors declared that this study has received no financial support.

PEER-REVIEW

Externally peer-reviewed.

REFERENCES

[1] Skempton, A. W., & Jones, O. T. (1944). Notes on the compressibility of clays. *Quarterly Journal of the Geological Society*, 100(1–4), 119–135. [CrossRef]

[2] Terzaghi, K., & Peck R. B. (1967). *Soil mechanics in engineering practice* (2nd ed.). John Wiley & Sons.

[3] Güllü, H., Canakci, H., & Alhashemy, A. (2016). Development of correlations for compression index. *Afyon Kocatepe University Journal of Sciences and Engineering*, 16(2), 344–355. [CrossRef]

[4] Ng, K. S., Chew, Y. M., & Lazim, N. I. A. (2018). Prediction of Consolidation Characteristics from Index Properties. E3S Web of Conferences, 65, 06004. [CrossRef]

[5] Kodicherla, S. P. K., & Kumar, N. D. (2016). Evaluation of coefficient of consolidation in CH soils. *Jordan Journal of Civil Engineering*, 10(4), 515-528.

[6] Puri, N., Prasad, H. D., & Jain, A. (2018). Prediction of geotechnical parameters using machine learning techniques. *Procedia Computer Science*, 125, 509–517. [CrossRef]

[7] Solanki, C. H. (2012). *Quick computation of settlement for shallow foundations of alluvial deposits*. In International Conference on Chemical, Civil and Environment Engineering (ICCEE'2012), Planetary Scientific Research Centre, Dubai.

[8] Sridharan, A., & Nagaraj, H. B. (2000). Compressibility behaviour of remoulded, fine-grained soils and correlation with index properties. *Canadian Geotechnical Journal*, 37(3), 712–722. [CrossRef]

[9] Vinod, P., & Bindu, J. (2010). Compression index of highly plastic clays—an empirical correlation. *Indian Geotechnical Journal*, 40(3), 174–180.

[10] Widodo, S., & Ibrahim, A. (2012). Estimation of primary compression index (Cc) using physical properties of Pontianak soft clay. *International Journal of Engineering Research and Applications*, 2(5), 2231–2235.

[11] Zaman, W, Hossain, R., Shahin, H. (2017). *Correlation studies between consolidation properties and some ındex properties for dhaka-chittagong highway soil.* 1st International Conference on Engineering Research and Practice, 4-5 Feb 2017, Dhaka, Bangladesh.

[12] Tiwari, B., & Ajmera, B. (2012). New correlation equations for compression İndex Of Remolded Clays. *Journal of Geotechnical and Geoenvironmental Engineering*, 138(6), 757–762. [CrossRef]

[13] Nath, A., & DeDalal, S. (2004). The role of plasticity index in predicting compression behaviour of clays. *Electronic Journal of Geotechnical Engineering*, 9, 1–7.

[14] Ansal, M. A., & Lav, M. A. (2001). Regression analysis of soil compressibility. *Turkish Journal of Engineering and Environmental Sciences*, 25(2), 101–109.

[15] Yoon, G. L., Kim, B. T., & Jeon, S. S. (2004). Empirical correlations of compression index for marine clay from regression analysis. *Canadian Geotechnical Journal*, 41(6), 1213–1221. [CrossRef]

[16] Akayuli, C. F. A., & Ofosu, B. (2013). Empirical mod-el for estimating Compression İndex from physical properties of weathered birimian phyllites. *Electron-ic Journal of Geotechnical Engineering* 18, 6135-6144.

[17] Kumar, R., Jain, P. K., & Dwivedi, P. (2016). Prediction of compression index (Cc) of fine grained remolded soils from basic soil properties. *International Journal of Applied Engineering Research*, 11(1), 592–598.

[18] Salih, N. B. (2020). Geotechnical characteristics correlations for fine-grained soils. *IOP Conference Series: Materials Science and Engineering*, 737(1), Article 012099. [CrossRef]

[19] Al-Khafaji, A., Buehler, A., & Druszkowski, E. (2018). Validation of compression index approximations using soil liquid limit. In S. Hemeda, & M. Bouassida (Eds.), *GeoMEast 2018: Contemporary ıissues in soil mechanics* (pp. 31–34). Springer. [CrossRef]

[20] Dway, S. M. M., & Thant, D. A. A. (2014). Soil compression index prediction model for clayey soils. *International Journal of Scientific Engineering and Technology Research*, 3(11), 2458–2462.

[21] Laskar, A., & Pal, S. K. (2012). Geotechnical characteristics of two different soils and their mixture and relationships between parameters. *Electronic Journal of Geotechnical Engineering*, 17, 2821–2832.

[22] Abbasi, N., Javadi, A. A., & Bahramloo, R. (2012). Prediction of compression behaviour of normally consolidated fine-grained soils. *World Applied Sciences Journal*, 18(1), 6–14.

[23] Bartlett, S. F., & Lee, H. S. (2004). *Estimation of compression properties of clayey soils, Salt Lake Valley, Utah*. (Report No: UT-04.28.) Research Division Utah Department of Transportation. https://drive.google.com/file/d/1a6YESbeEfdQJy09wwwAvgH-0aGbCaMvN_/view

[24] McCabe, B. A., Sheil, B. B., Long, M. M., Buggy, F. J., & Farrell, E. R. (2014). Empirical correlations for the compression index of Irish soft soils. *Proceedings of the Institution of Civil Engineers-Geotechnical Engineering*, 167(6), 510–517. [CrossRef]

[25] Nesamatha, R., & Arumairaj, P. D. (2015). Numerical modeling for prediction of compression index from soil index properties. *Electronic Journal of Geotechnical Engineering*, 20, 4369–4378.

[26] Rashed, K. A., Salih, N. B., & Abdalla, T. A. (2017). Correlation of consistency and compressibility properties of soils in Sulaimani city. *Sulaimania Journal for Engineering Sciences*, 4(5), 86–94.

[27] Al-Kahdaar, R. M., & Al-Ameri, A. F. I. (2010). Correlations between physical and mechanical properties of Al-Ammarah soil in Messan Governorate. *Journal of Engineering*, 16(4), 5946–5957.

[28] Shaikh, M., Ahsan, K., & Ali Molla, K. (2014). Development of strength and compressibility correlations of cohesive soils of some regions in Khulna city. *International Journal of Advanced Structures and Geotechnical Engineering*, 3(3), 242–245.

[29] Kootahi, K., & Moradi, G. (2017). Evaluation of compression index of marine fine-grained soils by the use of index tests. *Marine Georesources & Geotechnology*, 35(4), 548–570. [CrossRef]

[30] Ara, S., Uddin, M. S., & Showkat, M. N. H. (2021). Correlation of compression index with index properties of soil samples from several places in Chattogram, Bangladesh. *International Research Journal of Engineering and Technology*, 8(2), 752–755.

[31] Bello, A. A., Owoseni, J. O., & Fatoyinbo, I. O. (2019). Evaluation of plasticity and consolidation characteristics of migmatite–gneiss-derived laterite soils. *SN Applied Sciences*, 1(8), 1–11. [CrossRef]

[32] Jain, V. K., Dixit, M., & Chitra, R. (2015). Correlation of plasticity index and compression index of soil. *International Journal of Innovations in Engineering and Technology*, 5(3), 263–270.

[33] Alptekin, A., & Taga, H. (2019). Prediction of compression and swelling index parameters of quaternary sediments from index tests at Mersin District. *Open Geosciences*, 11(1), 482–491. [CrossRef]

[34] Sari, P. T. K., Firmansyah, Y. K. (2013). The Empirical Correlation Using Linear Regression of Compression Index for Surabaya Soft Soil. World Congress on ASEM13, Jeju, Korea.

[35] Kassou, F., Benbouziyane, J., Ghafiri, A., & Sabihi, A. (2017). Settlements and consolidation rates under embankments in a soft soil with vertical drains. *International Journal of Engineering*, 30(7), 972–980. [CrossRef]

[36] Al-Taeˈe, A. Y., & Al-Ameri, A. F. (2011). Estimation of relationship between coefficient of consolidation and liquid limit of middle and south Iraqi soils. *Journal of Engineering*, 17(3), 430–440.

[37] Devi, S. P., Devi, K. R., Prasad, D. S. V., & Raju, G. V. R. P. (2015). Study on consolidation and correlation with index properties of different soils in Manipur valley. *International Journal of Engineering Research and Development*, 11(5), 57–63.

[38] Sridharan, A., & Nagaraj, H. B. (2004). Coefficient of consolidation and its correlation with index properties of remolded soils. *Geotechnical Testing Journal*, 27(5), 469–474. [CrossRef]

[39] Jadhav, G. (2016). Establishing relationship between coefficient of consolidation and index properties/ indices of remolded soil samples. *International Journal of Advance Research in Science and Engineering*, 5(12), 299–309.

[40] Ibrahim, N. M., Rahim, N. L., Amat, R. C., Salehuddin, S., & Ariffin, N. A. (2012). Determination of Plasticity Index and Compression Index of soil at perlis. *APCBEE Procedia*, 4, 94–98. [CrossRef]

[41] Jones, L. D., Hobbs, P. R. N. (2004). *The shrinkage and swelling behaviour of UK soils: the clays of the Lambeth Group*. (Report No: RR/04/001). British Geological Survey. https://webapps.bgs.ac.uk/data/publications/pubs.cfc?method=viewRecord&publnId=19866440&topic=RP&series=RC&subseries=RR

[42] Park, J. H., & Koumoto, T. (2004). New compression index equation. *Journal of Geotechnical and Geoenvironmental Engineering*, 130(2), 223–226. [CrossRef]

Journal of Sustainable Construction Materials and Technologies
Web page info: https://jscmt.yildiz.edu.tr
DOI: 10.47481/jscmt.1209822

JSCMT
Journal of Sustainable Construction Materials and Technologies

Research Article

Fabrication of superhydrophilic TEOS-lactic acid composite films and investigation of biofouling behaviour

Tuğçe ERVAN[1], Mehmet Ali KÜÇÜKER[2], Uğur CENGİZ[*,3]

[1]*Department of Environmental Engineering, İstanbul Technical University, Faculty of Construction, İstanbul, Türkiye*
[2]*Department of Environmental Engineering, İzmir Institute of Technology, Faculty of Engineering, İzmir, Türkiye*
[3]*Department of Chemical Engineering, Çanakkale Onsekiz Mart University, Faculty of Engineering, Surface Science Research Laboratory, Çanakkale, Türkiye*

ARTICLE INFO

Article history
Received: 25 November 2022
Accepted: 15 December 2022

Key words:
bioadhesion, composite, eco friendly, lactic acid, microalgae, sol-gel

ABSTRACT

Phytoplankton and diatom microalgae species cause biofouling by adhering to the surfaces, especially in closed cultivation systems such as tubular photobioreactors. This biofilm formation blocks the sunlight; after harvesting, it is necessary to clean the reactor. This cleaning process causes loss not only in time and finance but also in terms of environmental pollution due to using toxic chemicals and excess water usage. This study aimed to investigate the reduction of the microorganism cell adhesion on the hybrid surface. To succeed in this, the composite surface of tetraethoxysilane (TEOS) and lactic acid (LA) was prepared by the sol-gel process. Then the hybrid surfaces were coated on glass slides by the dip coating method. The wettability performance of the TEOS-LA hybrid surface was investigated using contact angle measurement and light transmittance. The wettability result showed that the super hydrophilic surface having 54 mJ/m^2 of surface free energy values was obtained. Furthermore, the increased lactic acid content of the composite films increased the surface free energy (SFE) values, decreasing the water contact angle. A pencil hardness test characterized the mechanical strength of the surfaces, and it was determined that the hardness of the composite films was decreased by increasing the LA content of the composite films. Resultantly, it is found that the TEOS-LA superhydrophilic composite film reduces the adhesion of microalgae.

Cite this article as: Ervan, T., Küçüker, MA., & Cengiz, U. (2022). Fabrication of superhydrophilic TEOS-lactic acid composite films and investigation of biofouling behaviour. *J Sustain Const Mater Technol*, 7(4), 316–321.

1. INTRODUCTION

Stepping up day by day after the industrial revolution worldwide, industrialization has caused ecological problems such as environmental pollution, climate change, and various diseases. This situation has led scientists to research how to produce sustainable, eco-friendly, and economical materials. Usage of microalgae to bring down resource consumption has been one of the most common green engineering trends of recent times. Microalgae are unicellular photosynthetic eukaryotic creatures, and there are approximately 40000 defined species worldwide. They

***Corresponding author.**
*E-mail address: ucengiz@comu.edu.tr

are lived in oceans, lakes, surface and ground water. Diatom, phytoplankton, blue-green algae, brown and green flagella, and dinoflagellate are some of the species known as microalgae [1]. According to some investigations, they have been found that microalgae are unicellular; however, some species are multicellular. For example, Heimann and Huerlimann [2] reported that microalgae are multicellular because they possess one plastid and chlorophyll a and b, mucilage sheath. Furthermore, their high nutritional value and organic components are used as feed for aquarium fish, poultry, cats, and dogs, as a natural dye in buildings, biocatalyst in genetic engineering applications [3]. In addition, they are utilized as the raw material of the bioplastic to decrease the petroleum-based plastics' adverse environmental impact [4].

Adhesion consists of three stages: primary adhesion, irreversible adhesion, and biofilm density. Depending upon the negative or positive surface charges of all microorganisms are affected by the adhesion strength between the cell and surface via physicochemical interactions [5]. Microalgae harvesting occurs in closed and open systems, flat panels, stirred tanks, hybrid type, helical type, airlift, bubble column photobioreactors (PBRs), and raceway ponds [6]. Some optimum conditions are required for microalgae harvesting to take place. These can be listed as the light, CO_2, and PBR designs. As a result of limited scattering of light, biofilm layer and microalgae adhesion inside the PBR [7]. Besides little light, cell-surface interaction, microalgae surface free energy, and hydrophilicity or hydrophobicity of microalgae caused adhesion on any surface [8, 9]. Microalgae adhesion formation is decreased by altering the thin films' wettability properties [10–12].

Superhydrophilic surfaces were defined as water contact angles lower than 10° and showed antifogging, self-cleaning, and antireflective properties [12, 13]. However, microalgae behavior on superhydrophilic surfaces is also exciting [14]. Koschitzli et al. [14] reported that the superhydrophilic surface successfully results against the microalgae adhesion, especially the pure culture of microalgae harvesting, due to the absence of the silt. In this study, the TEOS-LA super hydrophilic composite thin films were fabricated containing different LA content having high light transmittance. The super hydrophilic TEOS-LA composite surfaces were also tested in pure microalgae cultures of *Chlorella sorokiniana* (*C. sorokiniana*), *Nannochloropsis* sp., and *Chlorella vulgaris* (*C. vulgaris*). Increasing the composite surface's LA content decreased the water contact angle from 79 to 8°. In addition, the surface hardness values of the composite surface changed from 9H hardness to 6B softness with increasing the LA content. The microalgae adhesion test indicated that the biofilm formation is decreased on superhydrophilic TEOS-LA surfaces.

Table 1. The weight contents of the composite solutions

Code	M_{TEOS}(g)	M_{LA}(g)	M_{MeOH}(g)	M_{water}(g)
TLA_{0}	5.00	0	25.50	2.65
$TLA_{3.7}$	5.00	1.06	25.50	2.65
$TLA_{7.1}$	5.00	2.12	25.50	2.65
$TLA_{8.8}$	5.00	2.65	25.50	2.65
$TLA_{10.3}$	5.00	3.18	25.50	2.65
$TLA_{13.3}$	5.00	4.24	25.50	2.65
$TLA_{15.0}$	5.00	4.88	25.50	2.65
$TLA_{18.7}$	5.00	6.36	25.50	2.65
$TLA_{23.5}$	5.00	8.48	25.50	2.65

2. MATERIALS AND METHODS

2.1. Materials

Methanol (MeOH), Tetraethoxysilane (TEOS), and Lactic acid (LA) were purchased from Aldrich. The test liquids of ultra-pure water, Diiodomethane (MeI_2), α–Bromonaphthalene (α-BN), and Formamide (F) were purchased from Merc.

2.2. Fabrication of Transparent TEOS-LA Surfaces

The TEOS-LA solution was prepared with different ratios of LA content, as given in Table 1. Firstly, the TEOS, LA, MeOH, and water were mixed in 100 ml of the reactor, and then the reaction was heated from 60 °C. Next, the sol-gel reaction was stirred for 3 h at 60 °C, and 0.1 mL of NH4F (0.1 M) was added to the reaction medium to catalyze. The sol-gel reaction lasted 4 h at 60 °C in reflux.

The TEOS-LA composite thin films were fabricated with the dip coating method. First, the glass slide was cleared sequentially in ethanol and water and dried in an oven at 85 °C for 1 h. Next, the glass slides were stood for 2 minutes dipping with a vertically moving mechanical immersion at a speed of 6.53 mm/sec. Finally, the coated glass slide was kept in an oven at 85 °C.

2.3. The Surface Characterization of Composite Films

The water contact angle (WCA) of the composite films was determined by the Attention Theta contact angle meter. The static WCA values were determined after removing the needle from 5 μL droplets [13]. Five different CA measurements were done on each copolymer film surface, and average CA values were reported with standard deviations of ±1°. The Van-Oss Good method calculated the composite films' surface free energy (SFE) using test liquid contact angle values [15, 16]. Light transmittance of the composite films was measured by Analytical-Jena model ultraviolet-visible spectroscopy (UV–VIS). Finally, the scratch resistance of the composite surface was characterized by a pencil hardness tester (Model 291, Erichsen) [13]. The scratch test was made using different hardness pencils having 6 mm lengths and flat tips. Another mechanical test is the peeling tape

Table 2. The contact angle values of the test liquids and SFE values calculated by the Van Oss-Good Method

	Contact angle results of test liquids (°)				The SFE results of composite films (mJ/m²)				
Code	**Water**	**MeI_2**	**α-BN**	**F**	γ^{LW}	γ^{+}	γ^{-}	γ^{AB}	γ^{Tot}
TLA_0	38	48	34	26	36.4	1.7	35.8	15.7	52.1
$TLA_{3.7}$	79	61	48	69	29.3	0.0	12.8	0.2	29.5
$TLA_{7.1}$	45	56	33	19	34.4	3.6	25.3	19.1	53.5
$TLA_{8.8}$	34	52	32	25	35.4	1.7	41.0	16.5	52.0
$TLA_{10.3}$	13	50	27	17	36.9	1.4	55.6	17.3	54.3
$TLA_{13.3}$	9	44	18	19	39.8	0.7	56.9	12.9	52.7
$TLA_{15.0}$	12	48	24	15	38.0	1.2	55.4	16.6	54.5
$TLA_{18.7}$	8	49	19	17	38.5	1.0	56.1	15.3	53.8
$TLA_{23.5}$	14	45	22	16	39.2	1.0	54.9	14.9	54.2

Figure 1. Microalgae adhesion test of the composite coating.

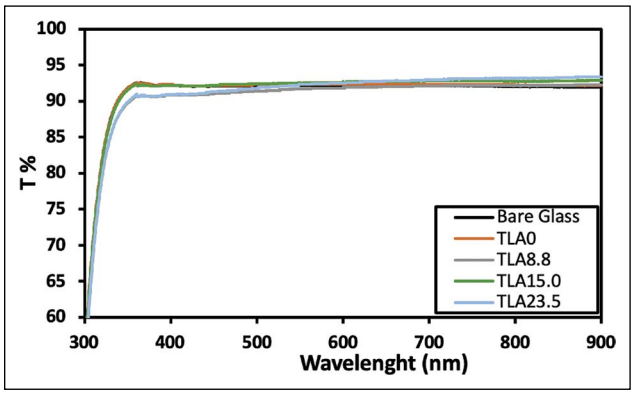

Figure 2. Optical transmission of the TEOS-LA composite films.

test of the coating surface. In this test, 3M-scotch tape (1x2 cm) was adhered to the composite surface. Then, 10 Pa pressure was applied to the tape for strong adhesion. Next, the bant was removed from the surface, and the tested surface was characterized by light transmittance compared to the untested region. The abrasion test of the composite coating was determined using H_2SO_4 (1M), NaCl (3.5%), and NaOH (2.5 M) solutions. The composite coatings were immersed in test liquids for 2–3 weeks, and it was checked whether there was abrasion against test liquids on the coating surfaces [17]. Finally, the adhesion behavior of microalgae species (*C. vulgaris, C. sorokiniana, and Nannochloropsis sp.*) on the superhydrophilic $TLA_{18.7}$ composite film was determined to keep with microalgae medium for 14 days (Fig. 1).

3. RESULTS AND DISCUSSIONS

The light transmittance of the composite surfaces is given in Figure 2. This figure indicated the optical transmission of the TEOS-LA composite films with a bare glass slide. All composite films have exhibited higher optical transmittance, almost as bare glass.

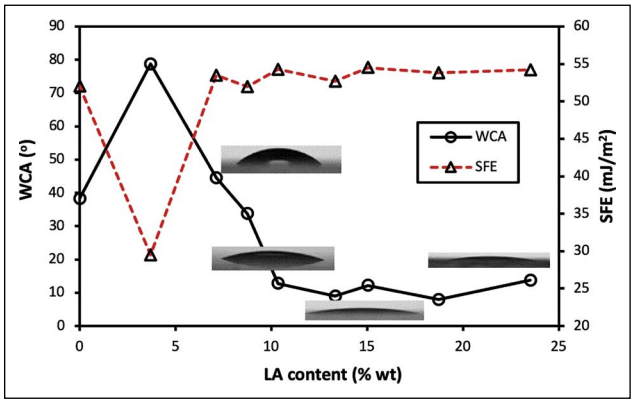

Figure 3. Changed with WCA and SFE values depending on the LA content of the composite films.

The contact angle of the water, MeI2, α-BN and F result on the composite surface, and the SFE of the composite films are given in Table 2. This table indicated no linear connection with the rising LA content of the composite films. The lactic acid molecular structure has two –OH groups, so the LA surface tends to be hydrophilic. However, the number of the –OH group decreased with the sol-gel reaction's progression,

Table 3. Hardness degree of synthesized composite surfaces

Code	9H	H	F	B	2B	3B	5B	6B
$T_{0.0}$	✖	✖	✖	✖	✖	✖	✖	✖
$TLA_{3.7}$	✖	✖	✖	✖	✖	✖	✖	✖
$TLA_{7.1}$	✓	✓	✖	✖	✖	✖	✖	✖
$TLA_{8.8}$	✓	✓	✖	✖	✖	✖	✖	✖
$TLA_{10.3}$	✓	✓	✓	✖	✖	✖	✖	✖
$TLA_{13.3}$	✓	✓	✓	✓	✓	✖	✖	✖
$TLA_{15.0}$	✓	✓	✓	✓	✓	✓	✓	✖
$TLA_{18.7}$	✓	✓	✓	✓	✓	✓	✓	✓
$TLA_{23.5}$	✓	✓	✓	✓	✓	✓	✓	✓

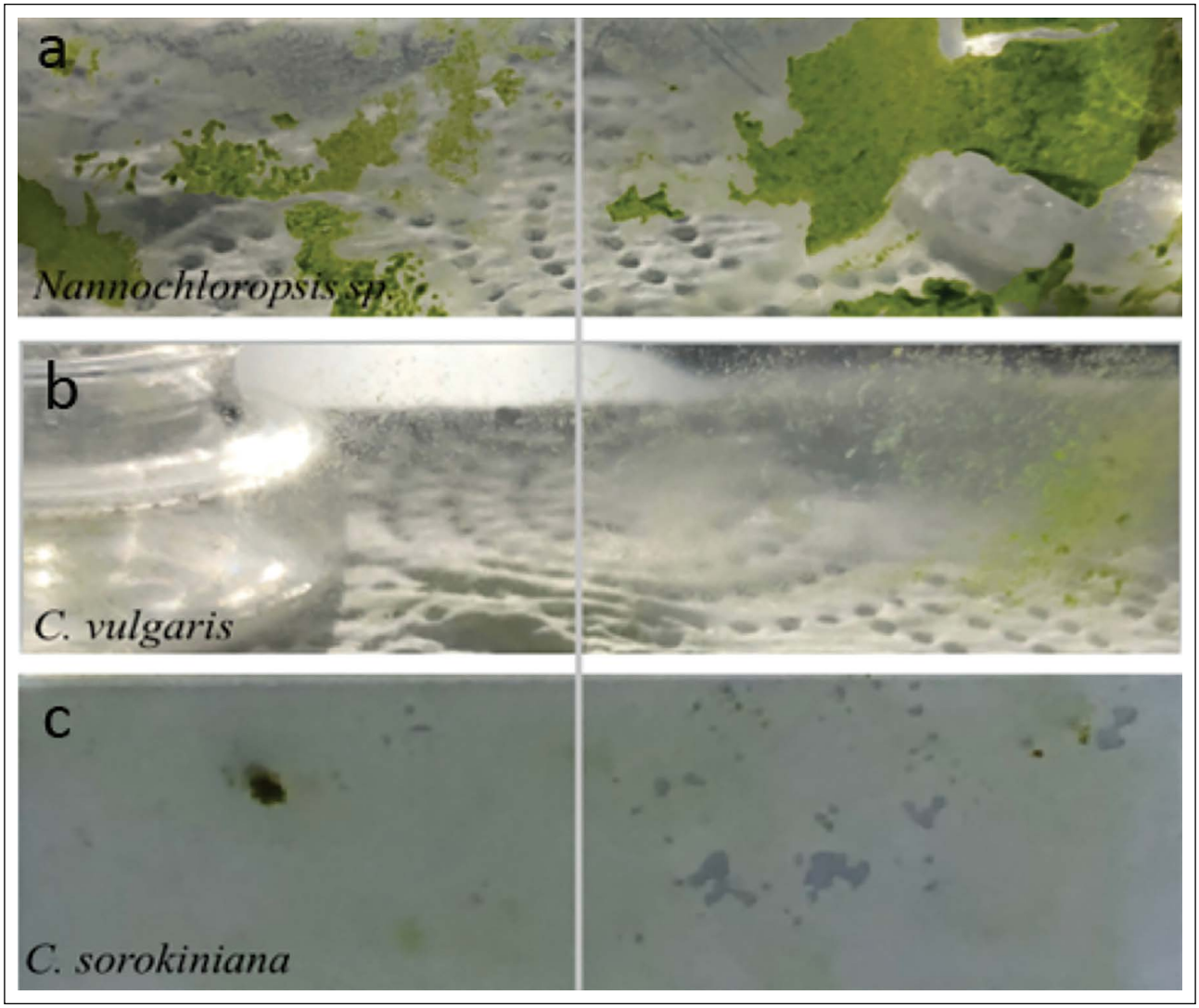

Figure 4. The biofouling performance of $TLA_{18.7}$ interaction with microalgae species. The left side is coated, and the right side is uncoated on images a) *Nannochloropsis sp*. b) *C. vulgaris*, and c) *C. sorokiniana*, respectively.

especially the LA's lower content. Because the sol-gel reaction between TEOS and LA continues with the attack silanol structure of TEOS on the –OH group of LA. While the water contact angle value is high at low LA content, the water contact angle values decrease at high LA content due to the free –OH group, and superhydrophilic surfaces were obtained in Table 2.

The variation of WCA depending on LA content decreased sharply up to 10% (wt) LA content. However, a constant WCA plateau was obtained despite increasing the LA content from 10 to 25% (wt) as given in Figure 3. In addition, total SFE values (γ^{Tot}) of the composite films were calculated by the Van-Oss Good method using the test liquids tabulated in Table 2.

Usually, the variation of SFE values changes opposite the contact angle values of the test liquids. An increasing contact angle results in a decreasing SFE value, as given in Figure 3. The mechanical stability of the composite film was tested by scratching [13], and the hardness test results are shown in Table 3.

The findings showed that while the hardest coating is $T_{0.0}$ having a 9H value, the softest coating is $TLA_{23.5}$ having 6B due to the rising organic part of the composite surface depending on LA content. An increasing organic amount of the composite layer resulted in a decrease in the hardness [18]. Miller et al. [18] reported that higher PLA content results in softer films.

The $TLA_{18.7}$ surface was selected to investigate microalgae adhesion due to the lowest contact angle values. The test was carried on for 14 days in 3 types of microalgae. The microalgae concentration on day 14 is measured as 3.2 g/L for *C. vulgaris*, 2.8 g/L for *C. sorokiniana*, and 3.5 g/L for *Nannochloropsis sp*. The $TLA_{18.7}$ coated and uncoated glass slides were taken out in the microalgae medium after a harvesting period of 14 days, as shown in Figure 4. This figure showed that biofouling occurred on both surfaces. However, the biofouling of *C. vulgaris* is less than other microalgae. In addition, it is shown in Figure 4 that the $TLA_{18.7}$ coated surface showed partial success on biofouling.

4. CONCLUSIONS

The dip coating method successfully fabricated superhydrophilic TEOS-LA composite films in this study. The sol-gel reaction between TEOS and LA was prepared at constant TEOS content with increasing LA. The superhydrophilic composite films having 8° of the contact angle were obtained without nanoparticle adding. This point of view is important in terms of environmental sustainability for developing biocompatible materials with reduced chemical content. The Van-Oss Good method calculated the SFE values of the composite films. The SFE results increased from 28.5 to 54.5 by increasing the LA content due to the rising OH unit on the composite films. However, a decrease in the WCA and an increase in the SFE did not have a linear relationship to LA content. The hardness test indicated that an increase in the organic part of the composite films resulted in a decreasing hardness. As a result of the bioadhesion test showed that the superhydrophilic $TLA_{18.7}$ thin film reduced the biofouling formation in the microalgae.

ETHICS

There are no ethical issues with the publication of this manuscript.

DATA AVAILABILITY STATEMENT

The authors confirm that the data that supports the findings of this study are available within the article. Raw data that support the finding of this study are available from the corresponding author, upon reasonable request.

CONFLICT OF INTEREST

The authors declare that they have no conflict of interest.

FINANCIAL DISCLOSURE

This research was financially supported by Çanakkale Onsekiz Mart University The Scientific Research Coordination Unit, Project number: FYL-2020-3256.

PEER-REVIEW

Externally peer-reviewed.

REFERENCES

[1] Verna D., Fortunati, E., Jain, S., & Zhang, X. (2019). *Biomass, biopolymer-based materials, and bioenergy: Construction, biomedical, and other industrial applications*. Elseiver.

[2] Heimann, K., & Huerlimann, R. (2015). Microalgal Classification: Major Classes and Genera of Commercial Microalgal Species. In S-K. Kim, (Ed.), *Handbook of marine microalgae: Biotechnology advances* (pp. 25–41). Elseiver. [CrossRef]

[3] García J. L., de Vicente M., & Galán B. (2017). Microalgae, old sustainable food and fashion nutraceuticals. *Microb Biotechnol*, 10(5), 979–1274. [CrossRef]

[4] Onen Cinar, S., Chong, Z. K., Kucuker, M. A., Wieczorek, N., Cengiz, U., & Kuchta, K. (2020). Bioplastic production from microalgae: A review. *International Journal of Environmental Research and Public Health*, 17(11), Article 3842. [CrossRef]

[5] Gottenbos, B., Grijpma, D. W., Van Der Mei, H. C., Feijen, J., & Busscher, H. J. (2001). Antimicrobial effects of positively charged surfaces on adhering Gram-positive and Gram-negative bacteria. *Journal of Antimicrobial Chemotherapy*, 48(1), 7–13. [CrossRef]

[6] Singh, V., & Mishra, V. (2020). Enhanced biomass production and nutrient removal efficiency from urban wastewater by Chlorella pyrenoidosa in batch bioreactor system: optimization and model simulation. *Desalination and Water Treatment*, 197, 52–66. [CrossRef]

[7] Talluri, S. N. L., Winter, R. M., & Salem, D. R. (2020). Conditioning film formation and its influence on the initial adhesion and biofilm formation by a cyanobacterium on photobioreactor materials. *Biofouling*, 36(2), 183–199. [CrossRef]

[8] Ozkan, A., & Berberoglu, H. (2013). Physico-chemical surface properties of microalgae. *Colloids and Surfaces B: Biointerfaces*, 112, 287–293. [CrossRef]

[9] Yu, L., Schlaich, C., Hou, Y., Zhang, J., Michael Noeske, P-L., & Haag, R. (2018). Photoregulating antifouling and bioadhesion functional coating surface based on spiropyran. *Chemistry*, 24(30) 7531–7780. [CrossRef]

[10] Stafslien S. J., Bahr, J. B., Daniels, J., Christianson, D. A., Chisholm, B. J. (2011). High-throughput screening of fouling-release properties: An overview. *Journal of Adhesion Science and Technology*, 25(17), 2239–2253. [CrossRef]

[11] Majumdar, P. (2011). Combinatorial materials research applied to the development of new surface coatings XV: An investigation of polysiloxane anti-fouling/fouling-release coatings containing tethered quaternary ammonium salt groups. *ACS Combinatorial Science*, 13, 298–309. [CrossRef]

[12] Wu, Z., Zhai, L., Cohen, R.E., Rubner, M. F. (2006). Nanoporosity-driven superhydrophilicity: A means to create multifunctional antifogging coatings. *Langmuir*, 22, 2856–2862. [CrossRef]

[13] Topcu Kaya, A. S., Cengiz, U. (2019). Progress in Organic Coatings Fabrication and application of superhydrophilic antifog surface by sol-gel method. *Progress in Organic Coatings*, 126, 75–82. [CrossRef]

[14] Koschitzki, F., Wanka, R., Sobota, L., Koc, J., Gardner, H., Hunsucker, K. Z., Swain, G. W., & Rosenhahn, A. (2020). Amphiphilic dicyclopentenyl/carboxybetaine-containing copolymers for marine fouling-release applications. *ACS Applied Materials and Interfaces*, 12, 34148–34160. [CrossRef]

[15] Erbil, H. Y. (2006). *Surface chemistry of solid and liquid interfaces*. Blackwell Publishing. [CrossRef]

[16] Rudawska, A., & Jacniacka, E. (2018). Evaluating uncertainty of surface free energy measurement by the van Oss-Chaudhury- Good method. *International Journal of Adhesion and Adhesives*, 82, 139–145. [CrossRef]

[17] Panja, B., Das, S. K., Sahoo, P. (2016). Tribological behavior of electroless Ni-P coatings in various corrosive Environments. *Surface Review and Letters*, 23(5), 1–18. [CrossRef]

[18] Miller, K. R., & Soucek, M. D. (2012). Photopolymerization of biocompatible films containing poly (lactic acid). *European Polymer Journal*, 48(12), 2107–2116. [CrossRef]

Journal of Sustainable Construction Materials and Technologies
Web page info: https://jscmt.yildiz.edu.tr
DOI: 10.47481/jscmt.1193891

JSCMT
Journal of Sustainable Construction Materials and Technologies

Research Article

The influence of anhydrite III as cement replacement material in production of lightweight masonry blocks for unreinforced non-load bearing walls

Şevket Onur KALKAN, Lütfullah GÜNDÜZ

Department of Civil Engineering, İzmir Katip Çelebi University, İzmir, Türkiye

ARTICLE INFO

Article history
Received: 24 October 2022
Revised: 04 December 2022
Accepted: 08 December 2022

Key words:
Anhydrite III, calcium sulfate, cement replacement, compressive strength of masonry, lightweight concrete, masonry block, thermal conductivity

ABSTRACT

Lightweight cellular hollow concrete (LCHC) block is a masonry unit with excellent thermal and acoustic performance, fire resistance, and high weathering resistance manufactured by precast technique. This work presents an experimental study that investigates the effects of partial volumetric replacement of Portland cement by calcium sulfate anhydrite on precast properties, especially the hardening time of the products, thermal insulation properties, and mechanical properties of the LCHCs. LCHC block is produced by the mixing of Portland cement (PC), anhydrite III (ANH), expanded perlite (EP), pumice (PU), and calcite (CA) for building applications. Experimental studies were carried out on both 10x10x10 cm^3 cube specimens and 19x19x39 cm^3 block specimens with 16 different mixture batches. The unit weights and compressive strengths of the cube specimens decreased as the ANH replacement level increased, depending on the decrease in the cement ratio. However, it was observed that the compressive strength of the block specimens increased up to the volumetric replacement level of 1.86%. As expected, the specimens' thermal conductivity values decreased with the unit weight. The most notable change in the specimens occurred during the hardening time. The hardening process of the specimens can be completed up to 90 times faster than the control mixture. In addition, within the scope of the study, three formulations are presented in which the compressive strength and the elastic modulus of the wall sections made with LCHC blocks can be calculated, and the thermal conductivity value of the masonry block unit can be calculated.

Cite this article as: Kalkana, ŞO., & Gündüz, L. (2022). The influence of anhydrite III as cement replacement material in production of lightweight masonry blocks for unreinforced non-load bearing walls. *J Sustain Const Mater Technol*, 7(4), 322–338.

1. INTRODUCTION

Lightweight concrete masonry units are mainly used to construct walls as a building material. To produce normal-weight concrete masonry units, a fresh concrete mixture is commonly used: Portland cement, water, sand, and gravel. This practice produces a light grey colored concrete block with a fine surface texture and a sufficiently high compressive strength. Load-bearing walls and partitions are generally built with these types of blocks. The mass of these types of concrete blocks generally ranges from 16 kg to 27 kg [1]. While the amount of sand in the concrete mixture

*Corresponding author.
*E-mail address: onur_kalkan@hotmail.com

prepared for concrete blocks is higher than the typical concrete mixture, the amount of gravel and water is less. The resulting concrete block is commonly called a lightweight masonry block when lightweight aggregates are used instead of normal-weight sand and gravel in the fresh mixture. This process achieves more porous and lighter concrete blocks with a medium-to-coarse surface texture, good strength, good sound-deadening properties, and a higher thermal insulating value than a normal-weight concrete block. LCHC blocks can be produced by mixing lightweight aggregates, cement, and water to construct non-load-bearing infill walls and slabs. Lightweight concrete blocks can be manufactured with densities ranging from 400 kg/m^3 to 1100 kg/m^3, affecting an average reduction in dead load of 40% to 50% compared to buildings with conventional concrete walls [2–4]. The mass of a typical lightweight concrete block is usually between 5 and 14 kg, depending on the aggregate type, shape, and grading [1].

Lightweight aggregates generally have maximum dry loose bulk densities of about 880 kg/m^3 for the coarse fractions and 1040 kg/m^3 for all-in aggregates [5]. Depending on their final source, lightweight aggregates are also classified as natural and artificial. The primary natural lightweight aggregates are diatomite, pumice, scoria, volcanic slug, and volcanic tuff. Except for diatomite, all are volcanic in origin. Pumice and scoria are more widely used for hollow and solid concrete block production in Türkiye [6, 7]. Also, using the expanded perlite in lightweight concrete productions and hollow block cavities is involved in studies mostly for thermal insulation [8–11]. On the other hand, most of the studies only investigate the use of cement as a binding material. There are not enough studies on cement and gypsum as dual-binder systems.

Gypsum is one of the most common mineral binders for building materials. The use of chemical additives, the use of mineral additives, the addition of cement, the addition of lime, and the use of reinforcement materials allow for obtaining various properties for gypsum binders [12]. The main component of this material is calcium sulfate, which can be found in hydrous and non-hydrous compounds: dihydrate ($CaSO_4.2H_2O$), hemihydrate ($CaSO_4.0.5H_2O$), and anhydrite ($CaSO_4$). Gypsum has many advantages thanks to its unique performance. These advantages can generally be evaluated as recyclability, non-toxicity, high sound and heat insulation ability, easy application, and rapid hardening. However, its most important feature is that it is the material with the least CO_2 emission during its production, among the most used binding materials in building materials, which are gypsum, lime, and cement. Hemihydrate production from mineral gypsum requires about 150 °C heating and about 350 °C heating for anhydrite, while that of Portland cement requires about 1450 °C calcination heat and lime requires 900 °C calcination heat. Compared to lime and cement, the total CO_2 emission of gypsum is relatively low.

Gypsum binders are produced by heating the gypsum mineral ($CaSO_4.2H_2O$) at specific temperatures. As the temperature increases, the gypsum mineral begins to dehydrate, and gypsum with lower H_2O content begins to be produced. Calcium sulfate hemihydrate ($CaSO_4.0.5H_2O$) is formed when 1.5 mol of H_2O is lost. The hemihydrate is formed under ambient conditions from 45 °C to 200 °C temperature range [13]. Further heating of calcium sulfate hemihydrate leads to soluble anhydrite (anhydrite III, $CaSO_4$) [14]. By heating the gypsum mineral at a sufficient temperature, two types of hemihydrate or anhydrite binders can be produced depending on the equipment applied and technological parameters: α- and β-hemihydrate or anhydrite. Compared to the α-modification, the specific surface area of the β-modification is larger and more porous. Therefore, the β-modification has a higher water requirement and lower strength [15, 16]. After the formation of anhydrite III, continued heating leads to less soluble anhydrite (anhydrite II). Under ambient conditions, $CaSO_4$.II reacts very slowly with water; hence, the name dead burnt gypsum is also given to this mineral [17]. Anhydrite I is formed at temperatures above 1180 °C [14].

Due to the high CO_2 emission values originating from cement production, reducing the cement ratio by cement replacement in cement-binding building materials is among the research topics that have been given importance in recent years from ecological points of view [18, 19]. Therefore, using other binders or cement replacement materials has been the subject of many publications [20]. Cement-based materials should offer economic and environmental benefits besides physical and mechanical properties. For this reason, many studies have been made in the literature to reduce the cement amount of concrete derivative materials by cement replacement method [20–22].

Gypsum is widely used in cement production as a calcium sulfate activator. However, the usage level is currently limited to about 5% of cementitious material because of its high sulfate content. It is mainly considered that large amounts of sulfate in cement-based materials would cause excessive expansion and cracking [23, 24]. Therefore, the number of studies with gypsum replacement for cement in cement-based building materials is very few. Researchers supported cement-gypsum combination with pozzolans to eliminate the harmful effect of ettringite minerals formed in the microstructure due to using cement and gypsum-derived materials and obtained positive results [25–27].

Concrete masonry units are manufactured with very dry, stiff concrete mixtures. The "no-slump" or "low-slump" material is placed into molds, vibrated, compacted, and demolded quickly. The demolded units are stiff enough to hold their shape as they enter the curing chamber. Afterward, they are palletized and readied for shipping [11]. However, since the products are immediately removed from the mold due to the production method, LCHC blocks that have not gained enough strength may suffer wastage due to breakage.

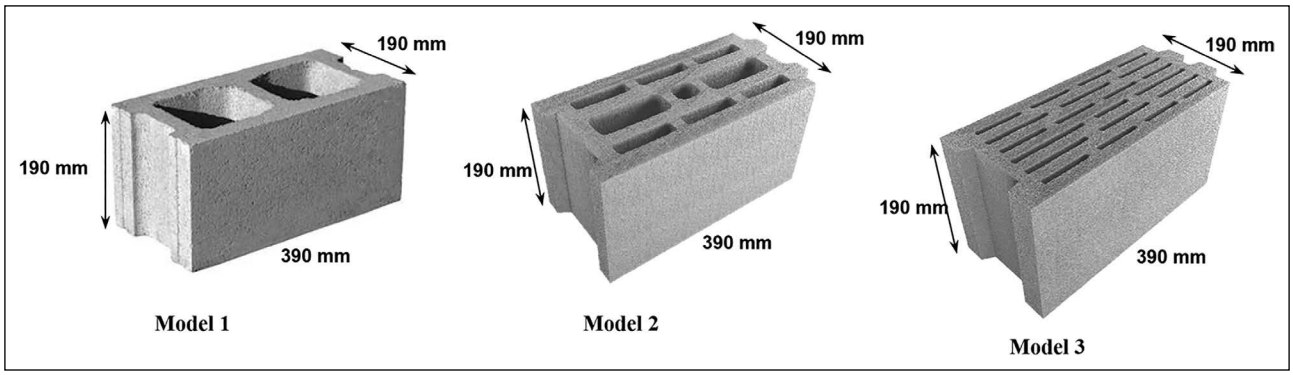

Figure 1. The three different models of masonry units.

For this reason, in this study, cement binder and anhydrite gypsum binder were used together with the replacement method in order to gain rapid strength to the products and to bring the products out of production into use quickly. In addition, it is thought that with less cement, the impact on the environment resulting from cement production will decrease, and sustainable building materials can be produced. The present experimental work evaluated the cementitious matrix modified by partial volumetric replacement of the ordinary Portland cement by anhydrite III to produce LCHC blocks as a building material. The effects of anhydrite III on precast properties, the incredibly initial hardening time of the products, thermal insulation properties, mechanical properties, and water absorption of the blocks were investigated. In light of previous literature studies, micronized pumice with high pozzolanic activity was also used in the design of the mixture in order to eliminate the adverse effects of ettringite formation. Pumice and expanded perlite were used as lightweight aggregates for the blocks to be included in the lightweight block category. Also, within the scope of the study, three formulations are presented in which the compressive strength and modulus of elasticity of the walls made with LCHC blocks and the thermal conductivity value of the masonry block unit can be calculated.

2. EXPERIMENTAL STUDY

2.1. Materials Used in the Research

In this study, three block designs with different cavity geometry are used, provided their outer dimensions are the same. The lightweight concrete masonry hollow blocks with dimensions of 185 mm height, 390 mm length, and 190 mm width, which are generally used for Türkiye, were used throughout the experimental work. The three models of masonry units are shown in Figure 1. Some physical properties of the three models are given in Table 1.

CEM I 42.5N Portland cement was used as a binder.

The β-modification anhydrite III binder was used as a partial replacement material for cement in the test batches. Anhydrite was obtained from a production facility in Türkiye.

Table 1. Geometrical properties of the block models

Model number	Cellular holes	ψ(cm²)	η(dm³)
1	2	321	7.97
2	9	462	10.11
3	21	567	10.78

ψ: Filled surface area of masonry units; η: Net fullness ratio of masonry units by volume.

Two different aggregates, relatively light in terms of density, were used to produce lightweight concrete mix and lightweight blocks. These are expanded perlite (EP) and pumice (PU). The grain size of the expanded perlite was 0/3 mm, and the grain size of the pumice was 0/4 mm. In addition, calcite (CA) with 0/1 mm grain size distribution was used as filling material in the mixture designs.

As mentioned earlier, although the inclusion of extra sulfate in the cement matrix is seen as a disadvantage, with the experience gained from the literature studies, micronized pumice material with a strong pozzolanic effect was used to eliminate the effect of this disadvantage. Natural pozzolans constitute a part of the lightweight aggregate group that could increase the strength and durability of concrete in the production of block-making mixtures. Pumice aggregate in powder form is one of the well-known pozzolans used in concrete applications. 4% by weight of the pumice aggregate used in this study, which has a particle size distribution of 0/4 mm, consists of micronized pumices with a smaller size than 45 μm and high pozzolanic activity. The pozzolanic material minimizes the deleterious effect of the extra sulfate in the cement matrix.

The chemical composition of the cement, anhydrite, EP, PU, and CA used in this research are given in Table 2.

Specific gravity, dry bulk density, and water absorption values of EP, PU, and CA are given in Table 3 and were determined according to the BS 812:P2 [28], BS 812:P110 [29], ASTM C127 [30] and ASTM C128 [31].

Table 2. Chemical compositions of CEM I, ANH, EP, PU, and CA (mass %)

Major element	CEM I	ANH	EP	PU	CA
SiO_2	20.92	2.35	74.14	74.16	0.15
Al_2O_3	5.18	0.74	12.35	13.47	0.14
Fe_2O_3	3.87	0.31	0.79	1.46	0.10
CaO	62.44	43.35	1.87	1.22	55.09
Na_2O	0.19	–	3.45	2.76	–
K_2O	0.78	0.11	4.66	3.13	–
MgO	2.45	2.64	0.48	0.41	1.12
SO_3	2.48	45.45	–	–	–
LOI	1.51		1.16	3.08	42.86

Table 3. Physical properties of EP, PU, and CA

Material	Particle size (mm)	Specific gravity	Dry bulk density (kg/m³)	Water absorption (wt %)
P	0/1	2.30	105	41.4
PU	0/4	2.32	780	28.9
CA	0.1/0.8	2.70	1400	1.80

2.2. Mix Design and Specimen Preparation

In order to analyze the use of ANH to produce LCHC blocks for walls and partitions, 16 different mixture proportions (B0–B15) adopted for the concrete mixture batches. The mix proportion of test specimens are presented in Table 4.

B0 coded mixture was considered a control mixture, and anhydride III binding material was not used in this mixture. In the specimens named from B1 to B15, anhydrite III binder has been replaced by volume instead of cement. Also, Table 4 shows weight replacement ratios corresponding to volume replacement ratios are given. The ratios of EP, PU, and CA entering the fresh mixture were kept constant in all batches. The concrete design methodology was constructed according to TS EN 771-3 standard [32].

In the first stage of this experimental study, 10x10x10 cm³ cube specimens were produced (Fig. 2) using the mixture design given in Table 4. Compressive strength, unit weight, water absorption, and initial hardening time tests were carried out on cube specimens. For each batch of mixtures, three specimens were produced to be used in compressive strength and unit weight tests, three were produced in initial hardening time tests, and three were produced to be used in water absorption tests; in total, nine specimens for each batch. A total of 144 cube specimens were produced for 16 different mixtures.

In this study, the value defined as the *initial hardening time* was evaluated as the time required for the cube specimens to reach a strength value of 1 MPa from when they were removed from the mold. The value of 1 MPa has been experienced as the appropriate strength value predicted in real applications regarding the transport of the specimens to the area to be applied, the required strength, and permanence during the application. For this reason, it has been accepted, based on the author's experience, that the blocks produced from specimens reaching a compressive strength of 1 MPa are suitable for real applications.

Figure 2. Cubic specimen production process.

In the second stage of the experimental study, using the mixture design in Table 4, the 16 different mix designs were adapted to each of the three-block models. The second stage was carried out on 19x19x39 cm³ block specimens. Block geometry for each model is given in Table 1. Unit weight,

Table 4. Proportions of trial mixtures (% by volume)

Mix	Binder		ANH (wt% in total binder)	EP	PU	CA
	CEM I	ANH				
0	0.00	10.35	0.00	35.00	45.00	9.65
1	0.31	10.04	3.00	35.00	45.00	9.65
2	0.83	9.52	8.00	35.00	45.00	9.65
3	1.24	9.11	12.00	35.00	45.00	9.65
4	1.86	8.49	18.00	35.00	45.00	9.65
5	2.59	7.76	25.00	35.00	45.00	9.65
6	3.42	6.93	33.00	35.00	45.00	9.65
7	3.93	6.42	38.00	35.00	45.00	9.65
8	4.35	6.00	42.00	35.00	45.00	9.65
9	4.66	5.69	45.00	35.00	45.00	9.65
10	4.97	5.38	48.00	35.00	45.00	9.65
11	5.38	4.97	52.00	35.00	45.00	9.65
12	5.69	4.66	55.00	35.00	45.00	9.65
13	6.00	4.35	58.00	35.00	45.00	9.65
14	6.73	3.62	65.00	35.00	45.00	9.65
15	7.76	2.59	75.00	35.00	45.00	9.65

compressive strength, water absorption, and thermal conductivity tests were carried out on LCHC block specimens. In addition, a formula has been proposed in which the thermal conductivity of the blocks can be calculated based on the compressive strength and the block net fullness ratio without performing a thermal conductivity test. BS 1881: Part 125 [33] was followed for mixing and sampling the fresh concrete in the laboratory, and BS 1881: Part 114 [34] was followed for measuring the density of hardened concrete. A cellular hollow block form confirming the specifications of BS 6073: Part 1 [35] standard was used for the preparation of LCHC specimens.

For each mixture and each block model, nine specimens were produced, a total of 27 blocks for one mixture design. 144 LCHC blocks were produced and tested for 16 different mix designs. The specimens were then air cured at 22±3°C and 50±5% relative humidity for up to 28 days until testing. The specimens were tested in air-dry conditions for compressive strength by BS 6073: Part 1 [35]. A measurement setup was used for the thermal conductivity test in which the hot box device methodology developed under laboratory conditions was applied. In the Hot Box method, thermal conductivity measurement can be made for the test sample, optionally for temperature environments ranging from 0 ˚C to +55 ˚C. The temperature value on each sample surface was measured from at least 9 points to form a grid on the surface. The thermal conductivity device consists of an electrical heater called the hot room, the section where the sample is placed, and the cold room. The temperature sensors in both the cold and hot chambers were fully contacted with the sample surface without damage, and the sample surface temperature values were measured with an accuracy of 0.1 ˚C. The given heat can be controlled with a continuously variable (20–400 watt) current. Since the heat transfer is three-dimensional, the test device is designed to minimize errors. Before recording the temperature data, the sample was stabilized, and data recording was started after reaching the steady state. The desired temperature difference on both surfaces of the test sample placed in the apparatus was provided by the electrical power (QT, Watt) applied to the heater, and the temperature difference between the surfaces was determined as the average value (ΔT, °C) from the measurement values. The thermal conductivity value (λ, W/mK) of the test sample was calculated using the following equation:

$$\lambda = \frac{Q_T \times d}{A \times \Delta T} \quad (1)$$

Here;
λ, thermal conductivity value of the test sample, (W/mK),
Q_T, electrical power applied to the heater (Watts),
D, sample thickness, (m),
A heated area in the heating section (m^2),
ΔT = temperature difference between surfaces, (˚C),

In the last stage of the study, the compressive strength value and elasticity modulus value of the non-load bearing wall, which is built with these block elements and unreinforced, using 0.7 mm thick masonry mortar only in a

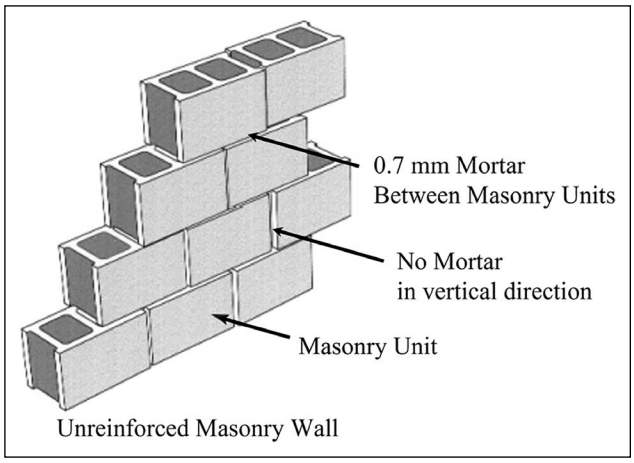

Figure 3. Wall section model.

horizontal position, has been examined. The wall section is presented in Figure 3. By comparing the obtained wall strength values with the technical values predicted in Eurocode 6, the effects of the use of anhydrite in the production of masonry blocks on the mechanical performance of the wall section were tried to be analyzed.

3. RESULTS AND DISCUSSIONS

3.1. Cube Specimens

In the first stage of the study, cube specimens were produced, and these specimens' physical and mechanical properties were determined. The physical and mechanical properties of the cube specimens are summarized in Table 5.

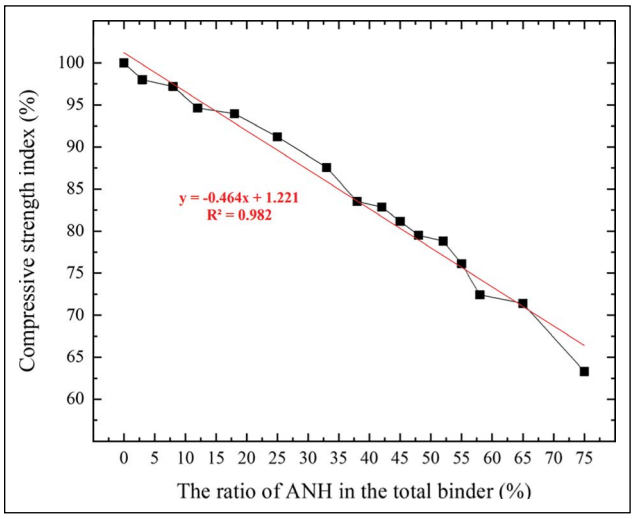

Figure 4. Compressive strength indices of cube specimens versus ANH as a percentage of binder.

The mixtures were coded according to the ANH replacement level, where "C" defines the cubic specimens, and the numbers 0 to 75 define the replacement level of ANH by cement by weight. The water/total binder ratio was kept constant in all mixtures, and the W/B ratio was used as 0.21.

3.1.1 Compressive Strength

Figure 4 shows the compressive strength results for the fifteen trial mixtures at 28 days of curing. The compressive strength of the control batch was 2.97 MPa (i.e., 100%). The compressive strength indices of cube specimens were linearly decreased with increasing ANH replacement levels.

Table 5. Physical characteristics of the 100 mm-cube specimens

Mix	Dry density (kg/m^3)	Compressive strength (N/mm^2)	Water absorption (% by weight)	A/B
C0	762	2.97	21.1	3.73
C3	758	2.91	21.3	3.75
C8	757	2.89	21.7	3.77
C12	756	2.81	21.8	3.80
C18	756	2.79	22.2	3.83
C25	754	2.71	22.4	3.87
C33	751	2.60	22.7	3.92
C38	750	2.48	23.3	3.95
C42	749	2.46	23.4	3.98
C45	747	2.41	23.8	4.00
C48	745	2.36	24.1	4.01
C52	744	2.34	24.2	4.04
C55	740	2.26	24.4	4.06
C58	738	2.15	24.7	4.08
C65	737	2.12	24.9	4.13
C75	732	1.88	25.4	4.20

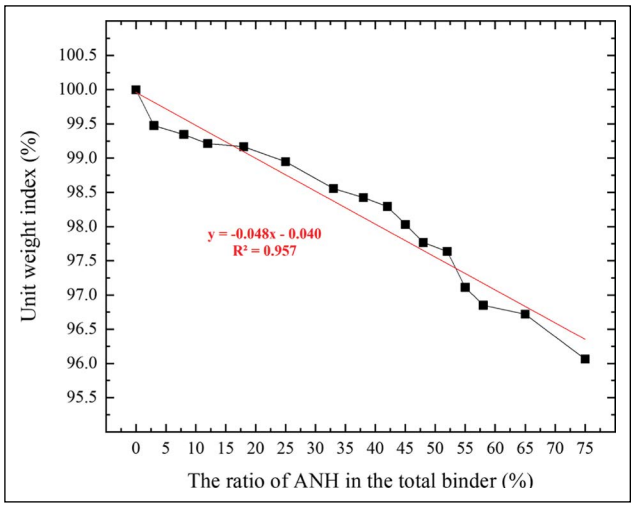

Figure 5. Unit weight indices of cube specimens versus ANH as a percentage of binder.

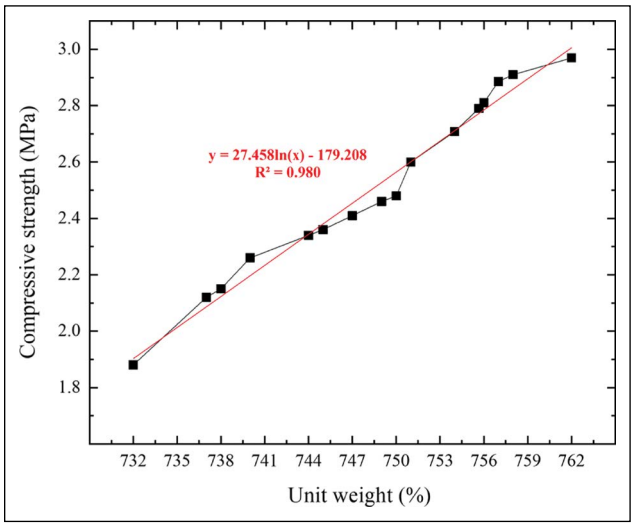

Figure 6. Relation between unit weight and compressive strength of cube specimens.

In cube specimens, test samples (C3–C75) lost compressive strength from 2% to 37% compared to the control sample.

The reduction in the compressive strength as the number of ANH increases in the total binder amount can be explained by the binding abilities of these two binders. It is known that the strength and binding ability of cement are higher than gypsum derivative binders. As the gypsum replacement level for cement increased, the compressive strength of the cube specimens decreased as expected because the cement ratio decreased. In addition, the increase in the use of gypsum together with cement also increases the pore volume [27], resulting in a loss in compressive strength.

3.1.2. Unit Weight

Figure 5 shows the unit weight values for the fifteen trial mixtures at 28 days of curing. The unit weight value of the reference batch was 762 kg/m^3 (i.e., 100%). The unit weight indices of cube specimens were linearly decreased with increasing ANH replacement levels. In cube specimens, unit weights of test specimens (C3–C75) decreased from 0.52% to 3.94% compared to the control specimen. The main reason for this decrease in unit weight is the increase in the use of gypsum derivative anhydrite III in the matrix structure.

Filling and partitioning, non-load bearing walls seem to be the top building domain of application of lightweight concrete masonry units made of LCHC. Therefore, lightness, material integrity, adequate durability, good thermal and acoustic insulation ability, cost, and sustainability are some expected material properties [36]. LCHC blocks are a non-structural element that can be used for non-load-bearing applications. However, this type of masonry unit must present a particular compressive strength [37]. It is well-known that, in general, strength increases with an increase in density. For instance, the cube specimens' unit weights and compressive strengths were compared and shown in Figure 6.

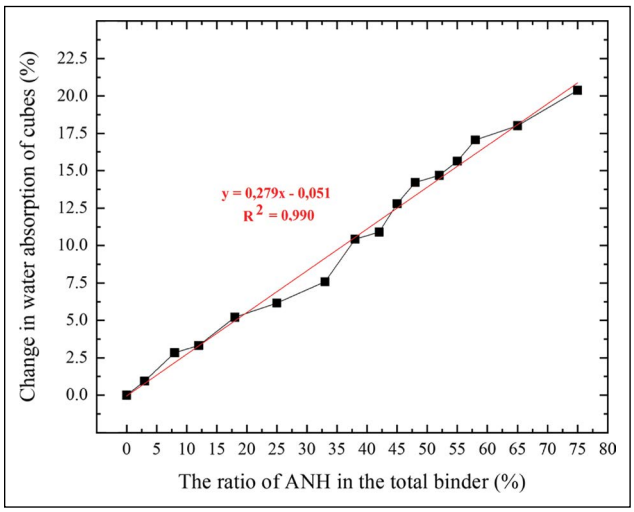

Figure 7. The effect of ANH replacement level on water absorption of cube specimens.

3.1.3. Water absorption

Cement-based products can be widely used in industrial applications in the external atmosphere or outdoor conditions. For this reason, the resistance of such building materials to the effect of water and their resistance to water rising as capillaries or absorbed into the material is very important. In other words, as with all material derivatives, the basic principle of cementitious materials absorbing water at the minimum level possible and impermeable to water when water affects should be sought. In this context, the capillary water permeability assessment of mortar materials is also essential. Thus, a water absorption test was performed on cube samples as the easiest and most common durability parameter. However, in light concrete derivative materials, the products are produced from highly porous

aggregates, and also the structure of the product's structure is also designed with a porous structure for the material to have light characteristics.

For this reason, it is expected that this type of product will have a very high water absorption characteristic. At this point, the importance of water absorption characteristics of lightweight concrete derivative products becomes more critical in determining mechanical and transport properties as with other building products [38]. The water absorption properties of the cube samples are shown in Figure 7.

Results indicate that as the amount of ANH increases in the total binder amount, the water absorption of the specimens increases considerably, as seen in Figure 7. When the water absorption of the reference cube specimen is assumed to be zero (0%) as a starting point, the water absorption rate of the samples increases as the ANH replacement level for cement increases. When it is evaluated with the lowest replacement level of 3% (C3), these test specimens absorbed approximately 1% by mass more water compared to the reference specimen, and when it is evaluated with the highest displacement ratio of 75% (C75), these test specimens absorbed approximately 20% more water by mass compared to the reference specimen. It has been determined that the ANH replacement level and the water absorption characteristic of the cube specimens are directly proportional. As the ANH replacement level increased, the water absorption rate of the samples increased. The possible reason is that, like other gypsum derivatives, the anhydrite III increases the cement matrix's total pore volume and causes an expansion in pore sizes. Similar results were reported by Khatib et al. [27]. In the final product, which already has high porosity due to its light structure, the different porosity of the matrix structure strengthens essential features such as heat and sound insulation.

3.1.4 Initial Hardening Time

LCHC blocks are cast into molds with Vibro-compacting, de-molded immediately, and transferred to a storage area for curing for up to 28 days in normal air conditions. Since LCHC blocks are removed from the mold immediately after pouring in a new concrete state, they can be deformed before they reach sufficient hardening due to casting errors or effects from the external environment. These errors can cause different products to be produced, increasing costs. By accelerating the hardening times of the products, different factors can prevent them from being quickly deformed.

Another handicap regarding the hardening times of the fully cementitious LCHC specimens is the curing time of final products for 28-day final strength. In other words, the block products' storage cost incurred during the curing period to reach their final strength. Before the block products reach the user, they are cured for 28 days for the cement to gain its real strength. This creates a storage cost.

For these two reasons, the early strength of block products is considered advantageous. Anhydride III binder was used in this study to give early strength to the products. It is advantageous to give products early strength to increase the speed and capacity of production and reduce storage time.

In this study, the value defined as the *initial hardening time* was evaluated as the time required for the cube specimens to reach a strength value of 1 MPa from when they were removed from the mold. The value of 1 MPa has been experienced as the appropriate strength value predicted in real applications regarding the transport of the specimens to the area to be applied, the required strength, and permanence during the application. For this reason, it has been accepted, based on the author's experience, that the blocks produced from specimens reaching a compressive strength of 1 MPa are suitable for real applications. The examination of the time taken for the cube specimens to reach a compressive strength value of 1 MPa after being removed from the mold is represented in Figure 8.

When Figure 8 is examined, the initial hardening time of the control batch is 443 min. For cube specimens with ANH replacement levels up to 45% for cement, the initial hardening time rapidly decreased to 89%. Although there is a reduction in initial hardening time after 45% replacement (C45), this reduction has a slowing trend. The initial hardening time of the B15 specimen with the highest replacement level of 75% (C75) is 94.6% quicker than the control specimen. This increase in the setting time is associated with the fact that anhydride III reacts very quickly with the mixing water and provides a very fast hardening of the total binder. The setting starts when the anhydrite III in the test mixture reacts quickly with water and turns into calcium sulfate dihydrate. Kovler [39] studied the triple mixture of gypsum, cement, and silica fume. Similarly, the researcher determined that the setting of this triple mixture started in 5 minutes with the conversion of calcium sulfate hemihydrate into calcium sulfate dihydrate. This experimental study determined that early strength was gained rapidly when ANH was added to the mixtures.

3.2. LCHC Block Specimens

In the second stage of the study, LCHC block specimens were produced, and these specimens' physical and mechanical properties were determined. The physical and mechanical properties of the LCHC block specimens are summarized in Table 5.

The mixtures were coded according to the ANH material addition, where "B" defines the LCHC block specimens, "M1, M2, M3" defines the model of LCHC block, and the numbers 0 to 75 define the replacement level of ANH by cement by weight.

3.2.1. Block Mass

The block mass of a lightweight concrete masonry block is expressed as the oven-dry mass of the block in kg. In production, the density of a given concrete masonry unit is

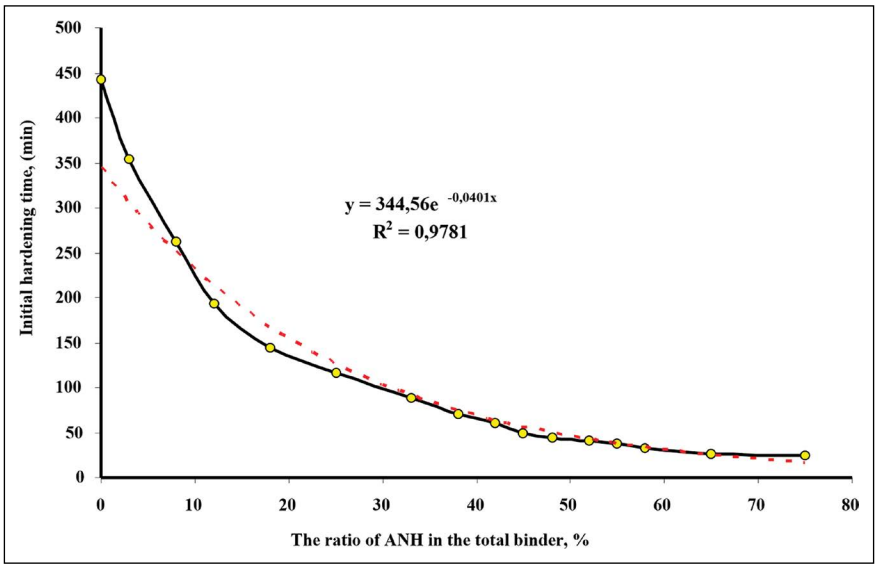

Figure 8. Effect of ANH replacement on initial hardening time of cube specimens.

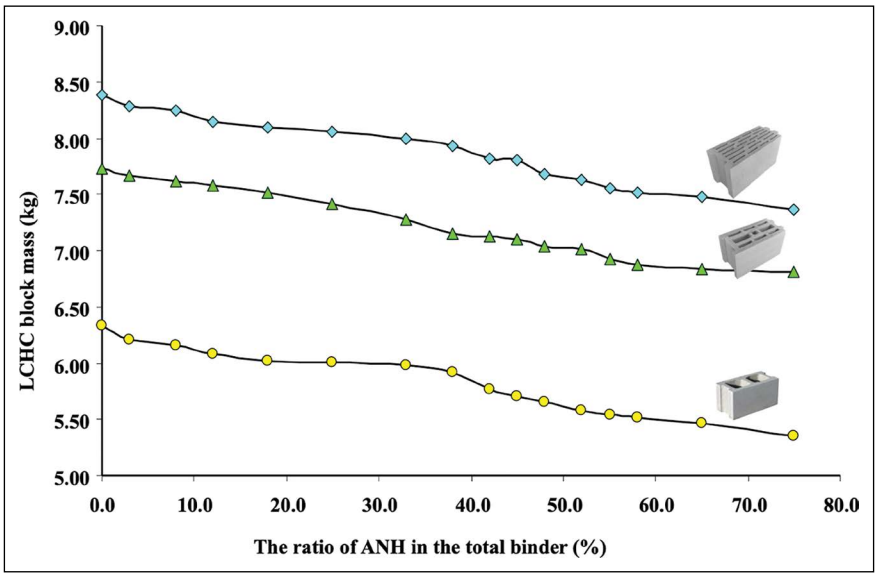

Figure 9. Effect of ANH replacement level on the mass of LCHC block specimens.

partly controlled by the methods used to manufacture the unit but mainly by the type of aggregate used in production [40]. Through the use of lightweight aggregates, the resulting density of lightweight concrete masonry units can be varied by the producer to achieve one or more desired physical properties. Block dry density or dry mass, however, can influence other structural design considerations aside from compressive strength. Reducing the density of a concrete masonry unit can reduce the overall weight of a structure and potentially reduce the required size of the supporting foundation and the structural members. Reducing the mass of a structure or element also reduces the seismic load a structure or element must be designed to resist because the magnitude of seismic loading is a direct function of dead load [40]. In this context, the oven-dry masses of the blocks were measured, and the results are represented in Figure 9.

The mass of LCHC blocks decreases as the percentage of ANH replacement increases. This is due to the lower specific gravity of ANH (2.30) compared to fine aggregate (3.15). Also, entrapped air caused by the use of anhydrite III may contribute to the reduction in mass of the LCHC blocks. Masses of the hollow blocks varied between 5.35 kg and 6.33 kg for M1, 6.81 kg and 7.73 kg for M2, and 7.36 kg and 8.38 kg for M3. In general, the experience for this reduction for the hollow blocks used in this research was approximately 1% block mass reduction versus a 5.70% increase in ANH replacement level for cement. Assuming the mass of normal-weight aggregate concrete masonry for

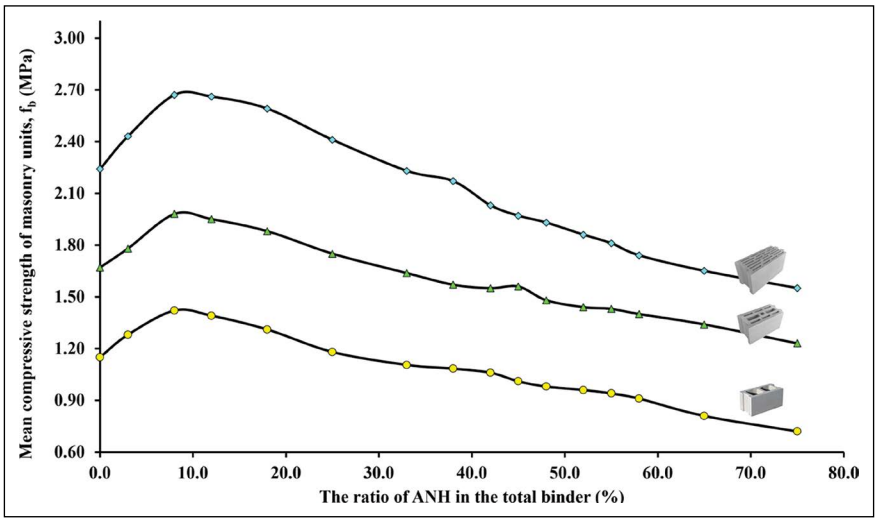

Figure 10. Effect of ANH replacement level on compressive strength of LCHC blocks.

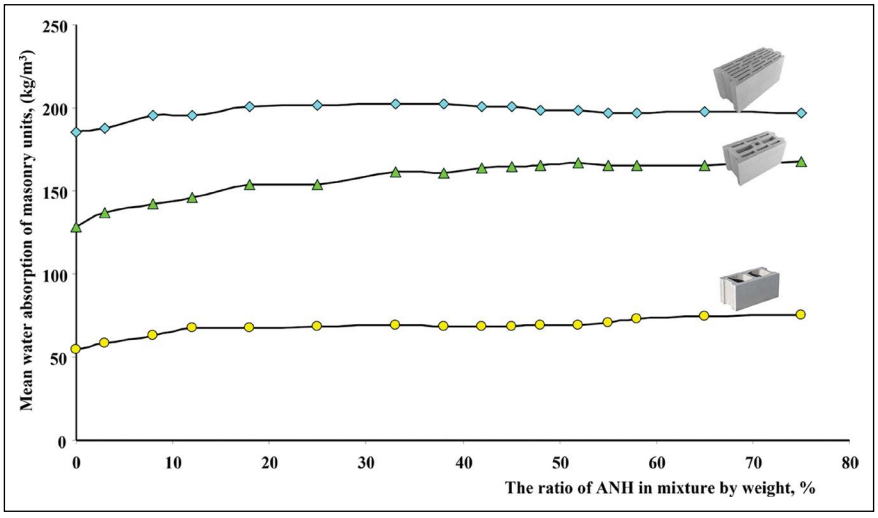

Figure 11. Effect of ANH replacement level on water absorption of LCHC blocks.

non-load bearing walls and partitions vary between 14 kg and 27 kg depending on their unit design geometry, the research showed that LCHC blocks are 61% to 80% lighter than normal-weight concrete masonry units.

3.2.2. Compressive Strength

The compressive strengths of the LCHC blocks, made from cement, ANH, and lightweight aggregates containing 16 mixtures, are shown in Figure 10.

It can be seen from Figure 10 that non-load-bearing LCHC blocks can be produced by using ANH replacement for cement. Generally, it can be noticed that the compressive strength of LCHC decreased as the percentage of ANH replacement level increased. The strength reduction is due to the weaker bonding ability of gypsum-based binders compared to Portland cement. Furthermore, the air-entraining property (when used with cement) of ANH binder reduces the bonding area within the concrete matrix. This phenomenon also causes a reduction in compressive strength. However, compressive strength reduction starts with an 8% ANH replacement level (B8). Above the 8% ANH replacement level, the compressive strengths of the LCHC block decreased continuously. On the contrary, utilization of 3% (C3) and 8% (C8) ANH replacement levels resulted in an increase in compressive strength as 11.30% and 23.5% for M1, 6.60% and 18.50% for M2, and 8.50% and 19.20% for M3, respectively.

There has been observed to be an increase in cement replacement rates up to 8% of the ANH ratio in mixtures in block production, which can be considered linear in block compressive strength values. It has been experienced that this increase in the strength value causes the mineral formations in the matrix structure that form strength earlier to develop more rapidly due to the anhydride ratio and the amount of cement contained in the mixture composition, and the edge and angular units in the geometric form of the block to form in a more compact structure, which has

a strength-enhancing effect. Furthermore, up to a 25% replacement level, all test specimens' compressive strength values were higher than the compressive strength value of the reference block specimen. However, it has been experienced that minerals formed as a result of hydration at anhydride utilization rates higher than 8% cause the matrix structure to acquire a more brittle form, which leads to a decrease in strength values.

3.2.3. Water Absorption

Lightweight hollow concrete masonry unit specifications typically establish upper limits on the amount of water permitted to be absorbed. Expressed in a kilogram of water per cubic meter of concrete, these limits vary with the density classification of the unit. Although no limit value for water absorption has been stated in BS 6073: Part 1 for the concrete masonry units, US National Concrete Masonry Association proposes that the maximum water absorption should be lower than 288 kg/m^3 for lightweight concrete masonry units [40]. The mean values for water absorption of LCHC blocks are given in Table 6. This table clearly shows that all absorption values are 54.4 kg/m^3 and 201.7 kg/m^3, within the acceptable water absorption values according to the US National Concrete Masonry Association recommendation. The research findings are represented in Figure 11.

While the absorption values are not directly related to masonry units' physical and geometrical properties such as dimension, pore size, and mechanisms of deterioration such as freeze-thaw, they provide a measure of the void structure within the lightweight concrete of the masonry unit. Several production variables can affect the void structure, including the plastic mix's degree of compaction, binder and water content, aggregate gradation, and the parameters of the mixing operation. Due to the vesicular structure of lower-density units, there is a potential for higher measured absorption than is typical for higher-density units [40]. This effect is observed in LCHC blocks almost for all mixes. Besides, the ANH replacement level increase appeared as a slight increase in the water absorption characteristics in all three block designs. LCHC blocks, already porous products by nature, are expected to have higher water absorption properties. Furthermore, the amount of water absorption increased more with the enlargement of the pore sizes in the cement matrix by adding ANH.

Table 6. Physical characteristics of the LCHC block specimens

Mix	A/B	Block mass (kg)			Compressive strength (N/mm^2)			Water absorption (kg/m^3)			Thermal Conductivity (W/mK)		
		M1	M2	M3	M1	M2	M3	M1	M2	M3	M1	M2	M3
B0	3.73	6.33	7.73	8.38	1.15	1.67	2.24	54.4	128.1	185.1	0.267	0.196	0.155
B3	3.75	6.21	7.66	8.28	1.28	1.78	2.43	58.3	137.1	187.6	0.263	0.195	0.157
B8	3.77	6.16	7.62	8.25	1.42	1.98	2.67	62.7	142.3	195.7	0.263	0.194	0.157
B12	3.80	6.08	7.58	8.15	1.39	1.95	2.66	67.4	146.4	195.1	0.255	0.194	0.155
B18	3.83	6.02	7.52	8.10	1.31	1.88	2.59	67.5	154.1	200.5	0.252	0.193	0.154
B25	3.87	6.01	7.41	8.06	1.18	1.75	2.41	68.2	153.5	201.7	0.251	0.191	0.154
B33	3.92	5.98	7.28	8.00	1.11	1.64	2.23	68.9	161.8	202.6	0.250	0.188	0.153
B38	3.95	5.92	7.15	7.93	1.08	1.57	2.17	68.7	160.5	202.3	0.246	0.186	0.152
B42	3.98	5.77	7.13	7.82	1.06	1.55	2.03	68.4	164.1	200.6	0.238	0.185	0.150
B45	4.00	5.71	7.10	7.80	1.01	1.56	1.97	68.5	164.9	201.0	0.235	0.185	0.150
B48	4.01	5.65	7.04	7.68	0.98	1.48	1.93	69.4	165.5	198.7	0.232	0.184	0.148
B52	4.04	5.58	7.01	7.63	0.96	1.44	1.86	69.4	166.8	198.5	0.228	0.183	0.148
B55	4.06	5.54	6.92	7.55	0.94	1.43	1.81	70.8	165.1	197.2	0.225	0.181	0.146
B58	4.08	5.51	6.87	7.51	0.91	1.40	1.74	72.8	165.4	196.9	0.224	0.180	0.146
B65	4.13	5.46	6.84	7.48	0.81	1.34	1.65	74.5	165.7	198.0	0.221	0.180	0.145
B75	4.20	5.35	6.81	7.36	0.72	1.23	1.55	75.2	167.4	197.3	0.215	0.179	0.143

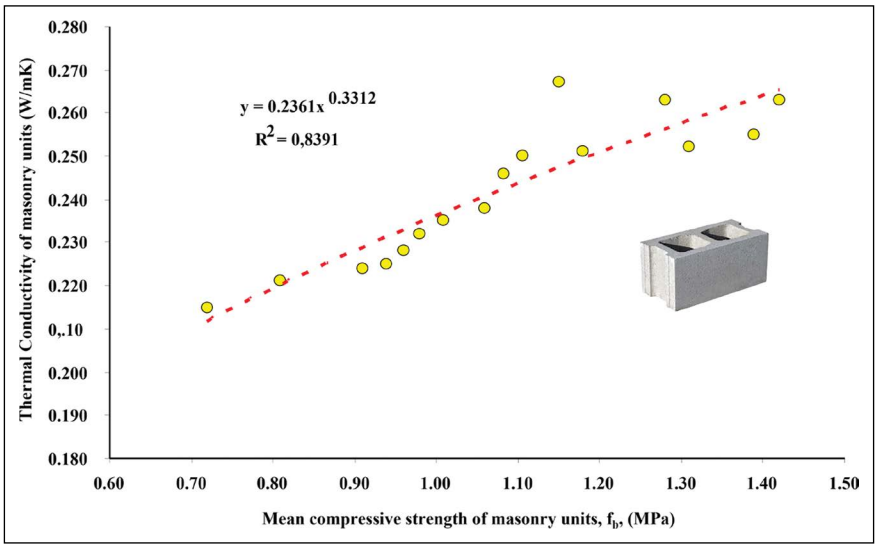

Figure 12. Compressive strength versus thermal conductivity values of LCHC model 1 blocks.

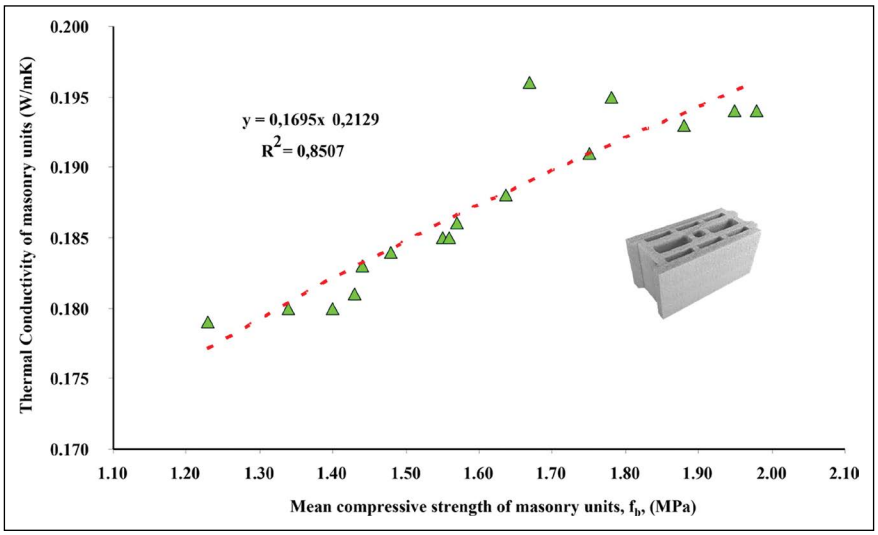

Figure 13. Compressive strength versus thermal conductivity values of LCHC model 2 blocks.

3.2.4. Thermal Conductivity

The thermal properties of the masonry blocks analyzed are given in Table 6 for three different LCHC block models. Each block type can be produced from lightweight concrete of different densities and black masses. The different mass values directly influence the thermal properties of lightweight concrete masonry blocks. It can be easily noticed from Table 6 that the thermal conductivity coefficients of the blocks decrease depending on the decrease in the mass of the blocks. The thermal conductivity values of model 1 blocks vary between 0.215 W/mK and 0.267 W/mK, the thermal conductivity values of model 2 blocks vary between 0.179 W/mK and 0.196 W/mK, and the thermal conductivity values of model 3 blocks vary between 0.143 W/mK and 0.155 W/mK. For all three types of block products, it was determined that as the ANH replacement level for cement increased, the thermal conductivity values of the block products decreased. From this, it is concluded that using cement and anhydrite III binder together harms the overall compressive strength but significantly improves the thermal insulation performance of the block products. In order to both compare the thermal performances and compressive strengths of all three models of block samples and to approximately determine the thermal conductivity (λ) value of a block product whose compressive strength is determined; in Figure 12, Figure 13, and Figure 14, the compressive strength values versus the thermal conductivity values of the model 1, model 2 and model 3 block specimens, respectively, are represented.

According to Figures 12–14, as the compressive strength values of all three model block samples decrease, the thermal conductivity values also decrease. In other

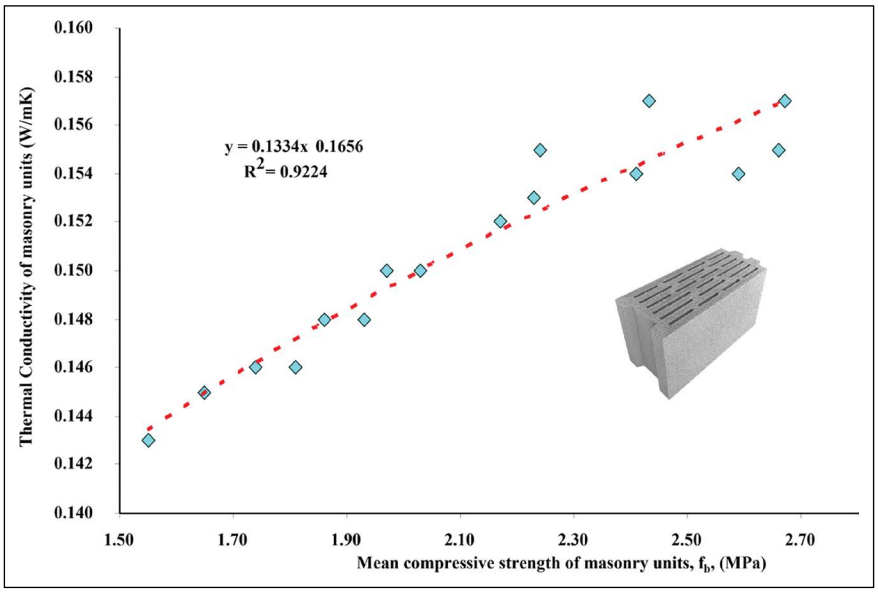

Figure 14. Compressive strength versus thermal conductivity values of LCHC model 3 blocks.

words, as the ANH displacement rate increases, the unit weights of the specimens decrease, and accordingly, the compressive strength values and thermal conductivity values decrease. Thus, their performance in terms of thermal insulation is improved. It has been determined that model 3 block specimens perform better than the other two model block samples in terms of compressive strength and thermal conductivity.

The compressive strength of the blocks can be determined in a shorter time and more efficiently than the determination of the thermal conductivity coefficient. In addition, a relationship was determined between the compressive strength and thermal conductivity values of the block samples produced for all three models tested within the scope of the study. Therefore, a formula has been proposed by which the thermal conductivity coefficient of the blocks can be determined by using the compressive strength of the blocks, which is determined relatively quickly, and the net fullness ratio, covering all three block models (Eq. 1).

$$\lambda_b = \frac{1.101}{e^{0.191\times\eta}} \times f_b^{\left(\frac{2.212}{e^{0.237\times\eta}}\right)} \quad (1)$$

Where λ_b Is the thermal conductivity coefficient of a single block, f_b It is the compressive strength of a single block, and η is the net fullness ratio of the single block.

3.3. Wall Section Model

The scope of the masonry tests on the wall section model is to determine the wall's characteristic compressive strength (f_k) and modulus of elasticity (Ek). The wall model is represented in Figure 3. In this wall section, there was no mortar in the vertical direction between the LCHC blocks, but 0.7 mm masonry mortar was applied in the horizontal direction between the LCHC blocks.

Eurocode 6 [41] gives a relation between the mean compressive strength of a masonry unit and the characteristic compressive strength of masonry (fk): $f_k = 0.5 \times f_b^{0.85}$. The results obtained from this study and the Eurocode 6 estimation is represented in Figure 15.

According to Eurocode 6 [41], the thickness of bed joints of 0.5 mm to 3 mm ensures that the thin layer mortar has been applied, and thin layer mortar applications are not taken into account when calculating the compressive strength of the wall. In Figure 15, the results of the masonry model's characteristic compressive strength (f_k) and the normalized mean compressive strength of the masonry units (f_b) are shown, and the comparison of Eurocode 6 and the results of this work is given.

Test results show that the characteristic compressive strength of the tested thin joint hollow concrete masonry with lightweight aggregates could be estimated by the equation given by Eurocode 6. When the compressive strength of the wall model obtained with LCHC blocks with relatively low compressive strengths is calculated, the results are more suitable for Eurocode 6, but as the compressive strength of the block increases, higher wall compressive strengths (f_k) are obtained than the formula values defined by Eurocode 6. Thus, an alternative formulation is proposed that includes the results of all three models in order to make a more precise inference (Eq. 2):

$$f_k = 0.526 \times f_b^{0.985} \quad (2)$$

In Figure 16, the elasticity modulus of the masonry section is given.

When Figure 16 is examined, as expected, the elastic modulus of the wall section increases as the compressive strength of the LCHC blocks forming the wall section increases. Using the results of the compressive strengths of three different models of LCHC blocks, the modulus of elasticity formula of the wall section was determined (Eq. 3).

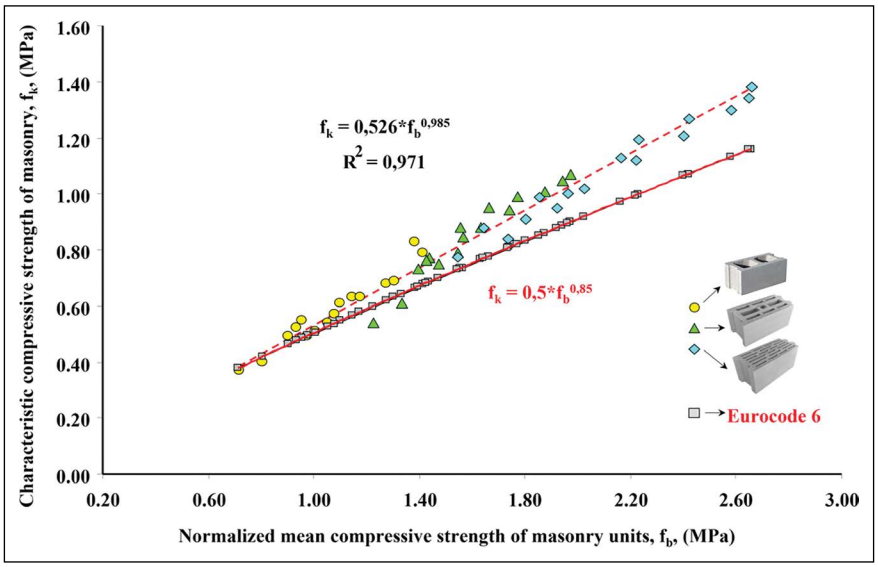

Figure 15. Characteristic compressive strength of the masonry section and comparison with Eurocode 6.

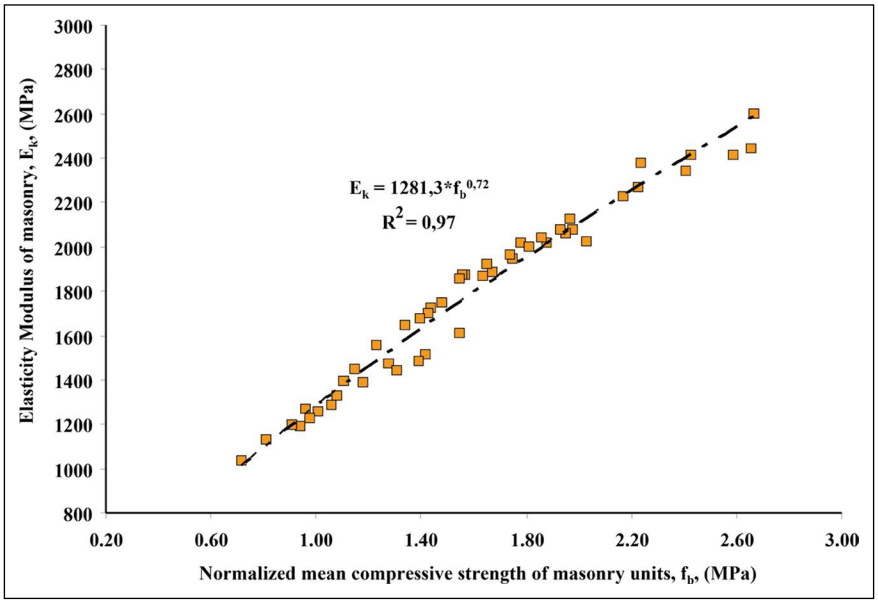

Figure 16. The elasticity modulus of the masonry section.

$$E_k = 1281.3 \times f_b^{0.72} \quad (3)$$

4. CONCLUSIONS

The properties of lightweight hollow concrete masonry units made of CEM I, anhydrite III, expanded perlite, pumice, and calcite were investigated in this research work. In particular, the changes in the physical and mechanical properties of lightweight concrete and lightweight masonry block products resulting from replacing anhydrite III with cement in specific proportions were investigated. It was possible to manufacture standard shape and size LCHC blocks using dry, too-stiff consistency mixtures to keep their shape and size during the demolding, curing, and hardening processes. The dry densities of the LCHC blocks complied with the standard acceptable limits for lightweight hollow concrete masonry units (i.e., less than 880 kg/m^3).

The research findings show that the higher the ANH replacement level for cement in the mixture, the lesser the dry density and block mass of LCHC blocks. In cube specimens, unit weights of test specimens decreased from 0.52% to 3.94% compared to the control specimen, when the ANH replacement level started from 3% to 75% for cement, respectively. Similarly, the increase in the ANH displacement ratio in masonry block products caused a decrease in the weight of the block products.

In cube specimens, test specimens (C3–C75) lost compressive strength from 2% to 37% compared to the control specimen. However, it has been observed that there is an increase in compressive strength values of LCHC block products with ANH replacement levels of up to 8% in mixtures. Furthermore, up to a 25% replacement level, all test specimens' compressive strength values were higher than the compressive strength value of the reference block specimen. However, the 8% ANH replacement ratio was determined as the optimum value.

When it is evaluated with the lowest replacement level of 3% (C3), these cubic test specimens absorbed approximately 1% by mass more water compared to the reference specimen, and when it is evaluated with the highest displacement ratio of 75% (C75), these cubic test specimens absorbed approximately 20% more water by mass compared to the reference specimen. Similarly, the ANH replacement level increase appeared as a slight increase in the water absorption characteristics in all three block designs (M1, M2, M3).

For cube specimens with ANH replacement levels up to 45% for cement, the initial hardening time rapidly decreased to 89%. Although there is a reduction in initial hardening time after 45% replacement (C45), this reduction has a slowing trend. The initial hardening time of the B15 specimen with the highest replacement level of 75% (C75) is 94.6% quicker than the control specimen.

The thermal conductivity values of Model 1 blocks vary between 0.215 W/mK and 0.267 W/mK, the thermal conductivity values of Model 2 blocks vary between 0.179 W/mK and 0.196 W/mK, and the thermal conductivity values of Model 3 blocks vary between 0.143 W/mK and 0.155 W/mK. For all types of block products, it was determined that as the ANH replacement level for cement increased, the thermal conductivity values of the block products decreased. Furthermore, a formula has been proposed by which the thermal conductivity coefficient of the blocks can be determined by using the compressive strength of the blocks and the net fullness ratio, which are determined relatively easily, covering all three block models (Eq. 1).

When the compressive strength of the wall model obtained with LCHC blocks with relatively low compressive strengths is calculated, the results are more suitable for Eurocode 6, but as the compressive strength of the block increases, higher wall compressive strengths (fk) are obtained than the formula values defined by Eurocode 6. Thus, an alternative formulation is proposed that includes the results of all three models in order to make a more precise inference (Eq. 2). Also, by using the results of the compressive strengths of three different models of LCHC blocks, the modulus of elasticity formula of the wall section was determined (Eq. 3).

ETHICS

There are no ethical issues with the publication of this manuscript.

DATA AVAILABILITY STATEMENT

The authors confirm that the data that supports the findings of this study are available within the article. Raw data that support the finding of this study are available from the corresponding author, upon reasonable request.

CONFLICT OF INTEREST

The authors declare that they have no conflict of interest.

FINANCIAL DISCLOSURE

The authors declared that this study has received no financial support.

PEER-REVIEW

Externally peer-reviewed.

REFERENCES

[1] Gündüz, L., & Kalkan, Ş. O. (2020). Lightweight cellular hollow concrete blocks containing volcanic tuff powder, expanded clay, and diatomite for non-load bearing walls. *Teknik Dergi*, 31(6), 10291–10313. [CrossRef]

[2] Gündüz, L. (2008). Use of quartet blends containing fly ash, scoria, perlitic pumice and cement to produce cellular hollow lightweight masonry blocks for non-load bearing walls. *Construction and Building Materials*, 22(5), 747–754. [CrossRef]

[3] Türkmenoğlu, A. G., & Tankut, A. (2002). Use of tuffs from central Turkey as admixture in pozzolanic cements: Assessment of their petrographical properties. *Cement and Concrete Research*, 32(4), 629–637. [CrossRef]

[4] Faella, G., Manfredi, G., & Realfonzo, R. (1992). Cyclic behaviour of tuff masonry walls under horizontal loadings. *In Proc. 6th Can. Masonry Symp.*, Canada, 317–328.

[5] ASTM. (2005). *Annual book of ASTM standards, book of standards section 4 – construction, Volume 04.02 and 04.03*. ASTM International.

[6] Gündüz, L. (2005). A technical report on lightweight aggregate masonry block manufacturing in Turkey. *Suleyman Demirel University*, 1, 110.

[7] Şapcı, N., Gündüz, L., & Yağmurlu, F. (2014). Usage of Aksaray ignimbrites as natural lighweight aggregate and evaluation of the production for lightweight hollow masonry units. *Pamukkale University Journal of Engineering Sciences*, 20(3), 63–69. [CrossRef]

[8] Al-Tamimi, A. S., Al-Amoudi, O. S. B., Al-Osta, M. A., Ali, M. R., & Ahmad, A. (2020). Effect of insulation materials and cavity layout on heat transfer of concrete masonry hollow blocks. *Construction and Building Materials*, 254, Article 119300. [CrossRef]

[9] Al-Hadhrami, L. M., & Ahmad, A. (2009). Assessment of thermal performance of different types of masonry bricks used in Saudi Arabia. *Applied Thermal Engineering*, 29(5-6), 1123–1130. [CrossRef]

[10] Sengul, O., Azizi, S., Karaosmanoglu, F., & Tasdemir, M. A. (2011). Effect of expanded perlite on the mechanical properties and thermal conductivity of lightweight concrete. *Energy and Buildings*, 43(2-3), 671–676. [CrossRef]

[11] The Portland Cement Association. (2016). (Dec 09, 2022). *Concrete masonry units*. https://www.cement.org/cement-concrete/products/concrete-masonry-units

[12] Lushnikova, N., & Dvorkin, L. (2016). Sustainability of gypsum products as a construction material. In *Sustainability of Construction Materials* (pp. 643–681). Woodhead Publishing. [CrossRef]

[13] Powell, D. A. (1958). Transformation of the α-and β-forms of calcium sulphate hemihydrate to insoluble anhydrite. *Nature*, 182(4638), Article 792. [CrossRef]

[14] Bensted, J., & Prakash, S. (1968). Investigation of the calcium sulphate-water system by infrared spectroscopy. *Nature*, 219(5149), 60–61. [CrossRef]

[15] Odler, I. (2000). *Special inorganic cements*. Taylor & Francis.

[16] Macia, E., Dubois, J-M., & Thiel, P. A. (1985). *Ullmann's encyclopedia of industrial chemistry*. Wiley.

[17] Sievert, T., Wolter, A., & Singh, N. B. (2005). Hydration of anhydrite of gypsum ($CaSO_4$. II) in a ball mill. *Cement and Concrete Research*, 35(4), 623–630. [CrossRef]

[18] Binici, H., Kapur, S., Arocena, J., & Kaplan, H. (2012). The sulphate resistance of cements containing red brick dust and ground basaltic pumice with sub-microscopic evidence of intra-pore gypsum and ettringite as strengtheners. *Cement and Concrete Composites*, 34(2), 279–287. [CrossRef]

[19] Hossain, K. M. A. (2003). Blended cement using volcanic ash and pumice. *Cement and Concrete Research*, 33(10), 1601–1605. [CrossRef]

[20] Kabay, N., Tufekci, M. M., Kizilkanat, A. B., & Oktay, D. (2015). Properties of concrete with pumice powder and fly ash as cement replacement materials. *Construction and Building Materials*, 85, 1–8. [CrossRef]

[21] Torkaman, J., Ashori, A., & Momtazi, A. S. (2014). Using wood fiber waste, rice husk ash, and limestone powder waste as cement replacement materials for lightweight concrete blocks. *Construction and Building Materials*, 50, 432–436. [CrossRef]

[22] Duan, P., Shui, Z., Chen, W., & Shen, C. (2013). Enhancing microstructure and durability of concrete from ground granulated blast furnace slag and metakaolin as cement replacement materials. *Journal of Materials Research and Technology*, 2(1), 52–59. [CrossRef]

[23] Mehta, P. K., & Monteiro, P. J. (2014). *Concrete: Microstructure, properties, and materials*. McGraw-Hill Education.

[24] Naik, T. R., Kumar, R., Chun, Y. M., & Kraus, R. N. (2010). *Utilization of Powdered gypsum-wallboard in concrete*. In Procedding International Conference Sustainable Constructions Materials Technologies.

[25] Escalante-Garcia, J. I., Martínez-Aguilar, O. A., & Gomez-Zamorano, L. Y. (2017). Calcium sulphate anhydrite based composite binders; effect of Portland cement and four pozzolans on the hydration and strength. *Cement and Concrete Composites*, 82, 227–233. [CrossRef]

[26] Hansen, S., & Sadeghian, P. (2020). Recycled gypsum powder from waste drywalls combined with fly ash for partial cement replacement in concrete. *Journal of Cleaner Production*, 274, Article 122785. [CrossRef]

[27] Khatib, J. M., Wright, L., & Mangat, P. S. (2013). Effect of fly ash–gypsum blend on porosity and pore size distribution of cement pastes. *Advances in Applied Ceramics*, 112(4), 197–201. [CrossRef]

[28] British Standards Institution. (1995). *BS 812: Part 2, Testing aggregates. Methods for determination of density*. British Standards Institution.

[29] British Standards Institution. (1990). *BS 812: Part 110, Testing aggregates. Methods for determination of aggregate crushing value (ACV)*. British Standards Institution.

[30] ASTM. (2004). *ASTM C127-04, Standard test method for density, relative density (specific gravity), and absorption of coarse aggregate*. ASTM International.

[31] ASTM. (2004) *ASTM C128-04, Standard test method for density, relative density (specific gravity), and absorption of fine aggregate*. ASTM International, West Conshohocken, PA," 2004.

[32] Turkish Standards Institution. (2015). *TS EN 771-3+A1, Specification for masonry units - Part 3: Aggregate concrete masonry units (Dense and lightweight aggregates)*. Turkish Standards Institution.

[33] British Standards Institution. (1986). *BS 1881: Part 125, Testing concrete. Methods for mixing and sampling fresh concrete in the laboratory*. British Standards Institution.

[34] British Standards Institution. (1983). *BS 1881: Part 114, Testing concrete. Methods for determination of density of hardened concrete*. British Standards Institution.

[35] British Standards Institution. (1981*). BS 6073: Part 1, Precast concrete masonry units. Specification for precast concrete masonry units*. British Standards Institution.

[36] Faustino, J., Silva, E., Pinto, J., Soares, E., Cunha, V. M., & Soares, S. (2015). Lightweight concrete masonry units based on processed granulate of

corn cob as aggregate. *Materiales de Construcción*, 65(318), Article e055. [CrossRef]

[37] British Standards Institution. (2011). (Dec 09, 2022). *BS EN 771-3, Specification for masonry units. Aggregate concrete masonry units (dense and lightweight aggregates)*. British Standards Institution. https://www.en-standard.eu/bs-en-771-3-2011-a1-2015-specification-for-masonry-units-aggregate-concrete-masonry-units-dense-and-lightweight-aggregates/?gclid=Cj0KCQiA1sucBhDgARIsAFoytUtgPd8N-5WkaafFDB_VaHfY0o90I4baU43G9DQ-I862y2Sv-J0296GRgaAra9EALw_wcB Accessed on Dec 16, 2022.

[38] Yan, S., Sagoe-Crentsil, K., & Shapiro, G. (2012). Properties of cement mortar incorporating de-inking waste-water from waste paper recycling. *Construction and Building Materials*, 29, 51–55. [CrossRef]

[39] Kovler, K. (1998). Setting and hardening of gypsum-portland cement-silica fume blends, Part 1: temperature and setting expansion. *Cement and Concrete Research*, 28(3), 423–437. [CrossRef]

[40] Masonry Advisory Council, (2007). Density-related properties of concrete masonry. *Building Construction & Design Viewpoint*, 1(1), 1–4.

[41] Turkish Standards Institution. (2013). (Dec 09, 2022). *TS EN 1996-1-1:2005+A1, Eurocode 6 - Design of masonry structures - Part 1-1: General rules for reinforced and unreinforced masonry structures*. Turkish Standart Institutions. https://www.en-standard.eu/bs-en-1996-1-1-2005-a1-2012-eurocode-6-design-of-masonry-structures-general-rules-for-reinforced-and-unreinforced-masonry-structures/?gclid=Cj0KCQiA1sucBhDgARIsAFoytUs_2bX5SS1dUwRNNbQfhG7cuoT5cVhZW-IxC4B8omVbaOcUVlLl2b4aAuPhEALw_wcB Accessed on Dec 16, 2022.

Journal of Sustainable Construction Materials and Technologies
Web page info: https://jscmt.yildiz.edu.tr
DOI: 10.47481/jscmt.1144427

JSCMT
Journal of Sustainable Construction Materials and Technologies

Review Article

Structural performance of concrete reinforced with banana and orange peel fibers - a review

Abiodun KILANI[1], Ademilade OLUBAMBI[*2], Bolanle IKOTUN[3], Oluwatobi ADELEKE[4], Oluwaseun ADETAYO[1]

[1]*Department of Civil Engineering, Federal University Faculty of Engineering, Ekiti State, Nigeria*
[2]*Department of Civil Engineering Science, University of Johannesburg, Johannesburg, South Africa*
[3]*Department of Civil Engineering, University of South Africa, Florida Campus, South Africa*
[4]*Department of Mechanical Engineering Science, University of Johannesburg, Johannesburg, South Africa*

ARTICLE INFO

Article history
Received: 21 July 2022
Revised: 23 August 2022
Accepted: 02 September 2022

Key words:
Banana peel fiber, concrete reinforcement, orange peel fiber, structural properties, supplementary materials

ABSTRACT

In recent years, there has been a surge in interest in developing novel materials for sustainable building construction made from renewable resources. Using natural fibers in concrete reinforcement, as opposed to agricultural waste, has significant environmental benefits in reducing the environmental repercussions of the continuous dumping and land filling of massive amounts of agricultural waste in overburdened landfill sites. Banana peel fiber (BPF) and orange peel fiber (OPF) are common agro-wastes with a long history of use in concrete as an additive or a cement substitute. However, their efficiency and performance in terms of reinforcement must be assessed. Based on recent findings, the characteristics, fresh and hardened state structural performance of BPF and OPF as composite materials in sustainable concrete manufacturing are reviewed in this study. For quality concrete reinforcing, it was discovered that OPF and BPF have good surface areas and low specific gravity. For quality concrete reinforcing, it was discovered that OPF and BPF have good surface areas and low specific gravity. BPF and OPF, on the other hand, have significant pozzolanic binding properties of up to 97.3%. This allows them to act as binders and supplement the high strength yielding in concrete. Furthermore, using BPF in concrete enhanced workability, consistency, compressive and tensile strengths, and setting times by 21.1%, 48.64%, 46%, 52.5%, and 47.37%, respectively, whereas the use of OPF raised concrete density by 5.34%. This indicated that both BPF and OPF had much potential for producing high-quality concrete. Using BPF and OPF to reinforce concrete and composites against flexural deflection, heat transmission, and modulus of elasticity significantly increase concrete strength in terms of cracking, deflection, creep, and shrinkage. The inclusion of orange and banana peels in concrete was found to improve the structural qualities of the concrete significantly; thus, they can be employed as supplementary materials in manufacturing concrete. Finally, this study identifies new approaches for achieving the much-anticipated biodegradability and sustainability of natural fiber-reinforced composites for use in various concrete reinforcing applications.

Cite this article as: Kilani, A., Olubambi, A., Ikotun, B., Adeleke, O., & Adetayo, O. (2022). Structural performance of concrete reinforced with banana and orange peel fibers - a review. *J Sustain Const Mater Technol*, 7(4), 339–357.

***Corresponding author.**
*E-mail address: ajoeolubambi@gmail.com

1. INTRODUCTION

Concrete is a composite material generally produced from coarse and fine aggregates, cement, and water proportionally with or without admixture [1, 2]. Concrete is considered a globally acceptable construction material because of its low production cost, global availability for use, setting times, hardening, and strength generation rate that can be achieved at ambient temperature. Some structures were constructed using concrete materials such as bridges and roads, parking structures, buildings, pavements, poles, and fences [3]. Concrete is the second most used material globally; from his estimation, the rate at which an individual yearly consumes concrete globally is up to 3 tonnes. Comparing this to other construction materials such as clay, metals, and wood, the number of concrete materials used for structural construction in building industries was twice that of other construction materials Gopal [4–6]. Almost 19,000 concrete bathtubs are produced every second globally, both in engineering firms and construction industries. It was recorded that up to sixteen million cubic meters of concrete were used for constructing three Gorges dams in China. It was also recorded that up to 4.2 billion cubic meters (about 10 billion tonnes) of concrete were produced globally in a year [7].

As the world population is increasing, the concrete production and construction rate is also increasing, especially in China and Asia. The estimation conducted by the global concrete and cement association showed that up to 4.65 billion tonnes of cement were produced yearly, and about ten billion tonnes of concrete were produced in the construction industries globally in a year. It was also recorded that about one billion meters of cubic water were used for concrete production around the globe yearly [8]. Presented in Table 1 is the rate of cement production in the twelve selected countries of the world from 2010 to 2020. China is considered the largest producer of cement around the globe. Because the amount of concrete produced by concrete industries in China is 2.2 billion metric tonnes greater than that of concrete produced in the other countries of the world in 2020. India is the next country to China in the production of a large quantity of concrete. It was estimated that about 340 million metric tonnes of concrete were produced in India in the year 2020 [9].

Consequent to the generation of cement in China, about 823 million metric tonnes of carbon dioxide were emitted, causing atmospheric pollution [10]. Up to 5.8% of greenhouse gases were emitted from the use of cement for concrete production. Supposed cement is a country, it would have been referred to as a third of the largest carbon dioxide emitter in the world. Among the large concrete-producing countries in the world, the United States and China were generating about 2.8 billion tonnes of concrete than other countries like India, Russia, and the UK, this has been causing their high rate of releasing

Table 1. Categories of Artificial and Natural wastes generation in the globe [78, 79]

Categories of global wastes generation	Types of wastes generated
Synthetic	Polyamide (nylon), Polyethylene (fibre, mesh, strip), Polypropylene (Crimpled fibre fibrillated fibre, monofilament fibre, mesh, pulp, tape)
Metallic	Aluminum (foil, rod), Copper (wire), Steel (rod wire), Galvanized steel
Natural	Bhabar, Human hair, coconut (shell), oil palm fibers, Cotton, hemp, pineapple peel, orange peel, banana peel, mango peel

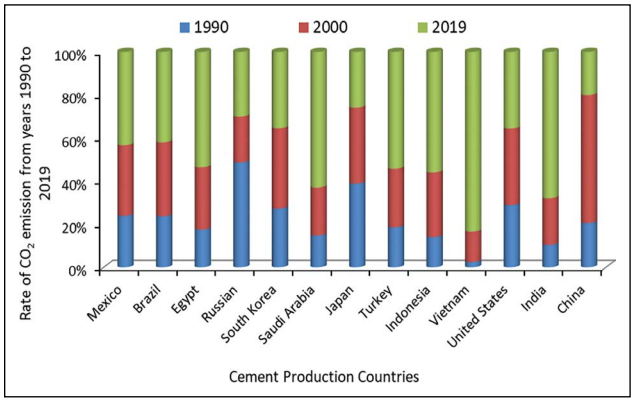

Figure 1. Rate of carbon dioxide emissions from cement manufacturing companies [10].

carbon dioxide into the atmosphere, affecting the ozone layers [11, 12]. The United States, India, and China were observed to have emitted higher percentages of CO_2 into the atmosphere from the year 1990 to 2019 than the other selected countries as presented in Figure 1.

In the construction industry, producing environmentally friendly cement has played a vital part in reducing carbon dioxide emissions from cement production, which is a prerequisite for climatic changes near factory locations around the world. The use of new kiln clinker technology for cement production has reduced the average CO_2 emission from the clinker to about 840 kg, which is also expected to be reduced to about 400 kg for the production of one tonne of cement. For instance, the types of cement produced in Spanish cement factories reduced the rate of emitting carbon dioxide by 21%, with a target for cement production from 2010 to 2050. Following the target, the sectors will be able to attain 550 kg of CO_2 emission suggested for one tonne of cement produced if the manufactured cement from the companies were made with low emission of CO_2 and good cement aggregate intensity is used for the pro-

duction of concrete and mortar come the year 2050. The burden placed on the environment by the generation and consumption of this large quantity of cement has resulted in an increased quest and interest in more sustainable and green composite materials as suitable replacements for cement in building industries [13, 14].

It was observed that, the rates of global generation of agricultural wastes such as banana and orange peels, especially in the developing nations these days were very high. In a recent report, it was observed that many researchers have been applying agricultural wastes as admixtures in concrete for its sustainability. The effectiveness of these wastes (banana and orange peels) in concrete need evaluation, most especially on concrete structural properties. Thus, this study provides a comprehensive review of the significant properties of concrete structure, its durability characteristics, and structural performance at the application of banana and orange peel fibers as admixtures or aggregates in concrete. It also focuses on evaluating the critical concrete mechanical properties such as compressive strength, tensile strength, flexural strength, density and microstructure, and durability properties such as slump, workability, setting time, and consistency with banana and orange peel fibers. Furthermore, the significant effect of the physical and chemical properties of bananas and oranges - peels on concrete structural enhancement were evaluated. Also, the potential for enhancement of concrete properties with the inclusion of agricultural wastes like banana and orange peels is intensively reviewed in this study. The aim is to determine the level of structural enhancement made by applying the wastes (peels) from banana and orange fruits to concrete in order to improve its structural properties. This evaluation is based on discovery of gaps yet to cover by research scholars, and to recommend them for appropriate improvement. The aim was achieved through the following objectives: (i) to evaluate the physical and chemical sustainable properties of banana and orange peels for concrete structural enhancement (ii) to evaluate the level of structural efficiency of using agricultural wastes (banana and orange peels) to improve the concrete fresh properties (iii) To determine the level of reinforcement contribution made by using agro-wastes (banana and orange peels) to improve the concrete mechanical properties (iv) To evaluate the level of durability capacity of concrete reinforced with banana and orange peels using the reliable experimental data from researchers, and (v) to discover some properties of concrete yet to be efficiently reinforced with the application of banana and orange peel – fibres for its sustainability.These areas, where reinforcement of concrete was not covered were explored for future development. The present study will spotlight new ideas toward realizing the much-anticipated biodegradability and sustainability of these natural fiber-reinforced composites for wide applications in concrete reinforcement.

2. LITERATURE REVIEW

The surge in waste generation rate has been a global threat to environmental sustainability. The World Bank report has estimated that about 2.01 billion tons of waste were generated in 2016, and it is projected to have a 70% increase (3.01 billion tons) by 2050, owing to the growing population and urbanization. This amount to 0.74 kg of waste generation by one person in a day; however, this waste is poorly managed, especially in developing countries. About 90% of the wastes generated from low-income nations of the globe are burned, incessantly dumped, or disposed of irregularly. This consequently impacts the environment negatively, resulting in diseases, climatic changes, and urban violence, especially in developing nations where these wastes are mainly generated [15–17]. Currently, waste disposal cost is high; a method of using them should be developed. Thus, sustainable recycling and reuse of this waste in suitable applications is a sustainable approach to managing this waste. This has led to the inclusion of generated wastes in concrete materials to improve their structural properties. Most of wastes generated global were from industrial and environmental products which were classified as artificial (synthetic, metallic) and natural waste – products. The series of products from these waste categories were commonly used for concrete reinforcement to improve its sustainability and durability were presented as shown in Table 1.

As shown in Table 1, most of the wastes generated from the industrial products ((synthetic and metallic) are too expensive to be afforded because of their cost of treatment for the suitability of concrete reinforcement. Researchers have discovered that, the use of wastes from agricultural products is the best alternative to substitute for the high cost of synthetic and metallic fibres for better sustainability of concrete structure. As reviewed, several research works have been conducted on the use of natural fibres (wastes), most expecially on oil palm fibers, Cotton, hemp, pineapple peel, mango peel, orange peel, and banana peel. The effect of orange, and banana peels have to be properly evaluated so as to encourage the more use of it the construction industries for more structural stability.

Banana is a fruit from the herbaceous plant of Musa species produced in several firmness, colors, and sizes. It has a curved and elongated shape. Its cover can be in deferent colors such as brown (ripe one), purple, red, yellow and green. It is rich in starch and soft in the flesh [18–20]. Plantains were the sorts of bananas used for cooking in several parts of the world. Musa paradisiaca, Musa balbisiana, and Musa acuminata are the scientific names for it. Australia is one of the essential banana-growing countries in the world. Although bananas are grown in up to 135 countries worldwide, Papua New Guinea is dominated by them due to their value for ornamental plants, banana beer and wine, and fiber manufacture [21–27]. Figure 2 shows the image of bananas with their different cover colors. At the same time,

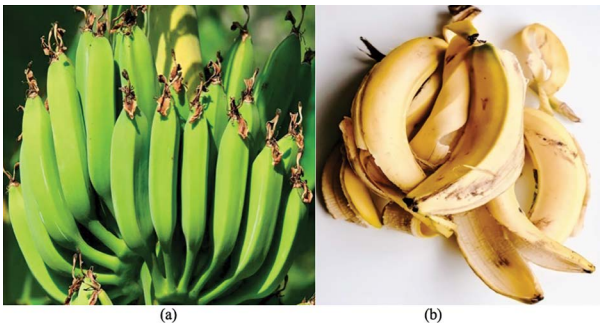

Figure 2. The image of bananas with their different colors **(a)** Banana fruits with green and yellow colors **(b)** Yellow bananas' peels scaled [24]

orange is a fruit from the citrus species. Sinensis citrus orange is known as sweet orange. Other oranges are referred to as Citrus aurantium, especially bitter orange, which originated from an area surrounded by Myanmar, Northeast India, and Southern China [28–30]. Orange trees are the most cultivated fruit trees around the globe. They have grown adequately in subtropical and tropical climates. Orange fruit can be eaten fresh after peeling its cover. Juice can also be squeezed from it. About 70% of sweet citrus oranges were produced globally in 2012 [31]. In Brazil only, about 22% of 79 million tonnes of citrus oranges were produced globally in 2019. With this estimation, Brazil is the highest producer of oranges in the world. China and India are next to Brazil in high orange production [27, 31]. Figure 3, 4 show the picture of fresh oranges, squeezed oranges, peeled oranges, and processed orange peels in different sizes.

Based on the available statistics from the United Nations, the global production of bananas was estimated at 115.74 million metric tonnes in 2018. Banana fruits generate about 30–40% peels, an equivalent of about 34.72–46.29 million metric tonnes of peels produced from bananas in 2018, which is a significant burden to the environment [33, 34]. According to Sasha [35], up to 60% of biomass from banana produce in the world is left as waste after harvest. Likewise, juice fruit markets and manufactory industries were generating many waste peels from bananas that can be used to produce other materials instead of allowing them to waste away [36]. Without proper treatment, banana peels will become an environmental problem and lead to a high rate of GHGs emissions. The peel waste from citrus is the highest volume of waste generated from the citrus fruit industries. As estimated, orange peels occupy about 20% of global oranges production. In 2011, estimation showed that up to 15.10 Mt of peels from oranges were produced globally [37]. According to Grohmann [38], about 50–60% of generated wastes around the globe were from the orange fruit. Wastes like segment membrane, peel, and seed. These wastes range from 15 to 25 million tonnes annually [39].

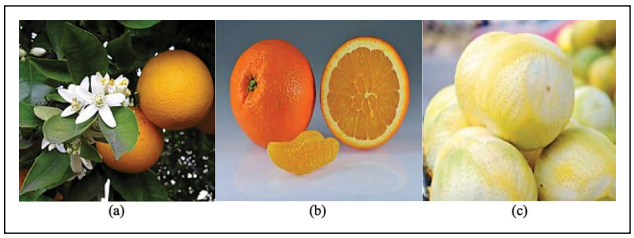

Figure 3. **(a)** Bloss oranges **(b)** Half segment of a whole orange **(c)** Peeled oranges [28].

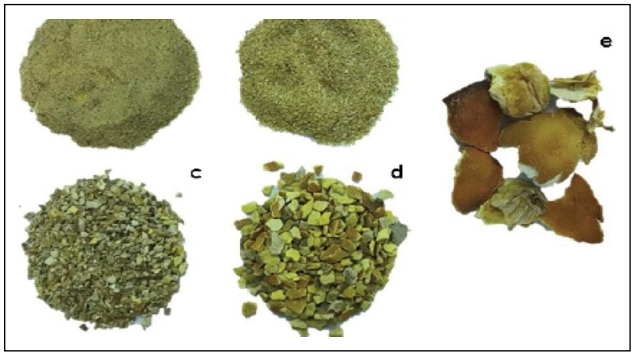

Figure 4. Oranges' peels were processed into different particles after oven-dried at hamper temperature [32].

The principal constituent of fruit weight mass is the citrus peel. It occupies up to 44% of waste mass-generated in the world. In 2016, up to 50–60% of global citrus produced 124 million tonnes were eaten raw after cover peeling. Also, about 40 to 50% of these amounts were for industrial purposes [40, 41]. In up to 135 countries, where the production of banana fruits was in large quantities, the skin peels of bananas were collected in urge quantities from government agricultural farms, where the plantation of banana fruits many. Also, banana peels could be serene in bulky at a famous dumping hill in a country, waste disposing locations that belong to banana juice production firms, huge plantain production sites, and global agricultural research centers. As reviewed, mainly all the wastes collected from the dumping locations were treated with chemicals to remove gems and impurities, after which they were sun-dried and oven-dried before turning them into ashes or used as a pure admixture in concrete [23, 42]. Likewise, the peels from citrus fruits were mainly collected from different waste dumping locations, especially from orange production farms around the globe [75].

The review observed that the most significant percentage of orange peels could be composed of juice processing factories in developing countries where agriculture is the primary occupation for economic sustainability. From the other observation, the most significant quantities of citrus peeled skins could be obtained from pastries, hotels, and restaurants waste dumping locations [76]. There is an upsurge in the generation rate of agro-wastes such as banana and orange peels worldwide. Thus, recycling and reusing

Table 2. Mechanical and physical properties of Nendran and Dwarf Scavendish banana (Peels) [42, 70]

Properties	Value	
	Nendran peels	Dwarf Scavendish peels
Average pulp's moisture content (%)	153.39	264.17
Average peel's moisture content (%)	516.41	666.28
Average pulp to peel ratios	2.32	1.39
Peel's thickness (mm)	2.95	3.65
Max. diameter of a banana fruit without peel (mm)	37.08	23.34
Average pulp's specific gravity	1.110	0.993
Max. effective length of banana pulp (mm)	194.5	137.0
Max. effective width of banana pulp (mm)	50.0	66.5
Max. load requirement to cut cross-section of pulp (N)	28.2	22.4
Maximum energy (J/m^2)	724.46	686.81

them as composite materials in building materials is a sustainable approach to managing waste and its attendant environmental consequences. Applying these agricultural wastes as admixtures in structural concrete has recently gained traction. However, to further enhance its performance in concrete manufacturing, it is essential to evaluate its properties and structural performance.

2.1. Mechanical, Chemical, and Physical Properties of Banana Peels

Investigation of the relevant properties of banana peels is critical to evaluating their binding effect and performance in concrete reinforcement. This section examines the banana peels' physical, mechanical and chemical properties. The literature is replete with intensive studies on banana peels' mechanical and physical properties. Kachru et al. [42] and Soltani et al. [69] indicated that the mechanical and physical properties of two different varieties of banana peels, namely Nendran and Dwarf Scavendish, were investigated, as presented in Table 2. As revealed in the table, the average moisture content of Nendran banana peels is 516.41%, which is less than that of Dwarf Scavendish banana peels, which are 66.28%. This implies that peels from the Nendran banana specie have a higher potential for reinforcement of concrete's structural properties than peels from Dwarf Scavendish species of banana. Similarly, the thickness of Dwarf Scavendish banana peels which is 3.65 mm each, had a better quality than that of Nendran banana peels (2.95 mm each).

Sequel to this, the peels from Dwarf Scavendish of banana species will improve the concrete reinforcement qualities than that of the concrete reinforced with peels from Nendran specie of banana by 23.7%. However, on the contrary, the maximum diameter and specific gravity of a peel of a banana fruit from Dwarf Scavendish banana species which were 23.34 mm and 0.993, had a good surface characteristic for concrete strength enhancement than the peel of a banana fruit from Nendran banana (37.08 mm and 1.110) due to their low surface properties.

As investigated by Benjamin et al. [43], the chemical composition and properties of banana peels were presented as shown in Table 2. The types of banana peels observed were from Musa sepientum species. Banana peels from Musa sepientum species are rich in calcium and potassium, making them perform better as accurate binders in structural concrete during the geopolymerization process. The combination of potassium (78.10±6.58 mg/g) and calcium (19.20±0.00 mg/g) from Musa Sepientum banana peels, which up to 97.3% (Table 3a), shows that concrete reinforcement with banana peels will pass through smooth geopolymerization. The pozzolanic properties of banana peels observed by Lakhiar et al. [44] and Mohammad et al. [45] are 63.34% and 60.05%, respectively. These values were obtained from the combination of some essential elements such as Silica dioxide (SiO_2), Aluminium oxide (Al_2O_3), and Iron oxide (Fe_2O_3) (Table 3a).

The properties possessed good binding elements for concrete reinforcement up to 63.34% [44] (Table 3b), but less than that of the specified standard for a material to be used as binding material in concrete stated by ASTM C618 [46] for quality concrete production. The use of peels from bananas can be appreciated for standard concrete production when another admixture, like oil palm fiber, is blended with it.

2.2. Mechanical, Chemical, and Physical Properties of Orange Peels

Exploring the full benefits of orange fruit peels as composite materials in concrete application and evaluating their structural performance is contingent on proper knowledge of their physical, mechanical, and chemical properties. The properties of orange peels are discussed as follows; the properties of the peels from the sweet species of orange are presented in Table 4.

As indicated in Table 4, the sweet orange's bulk density, which ranges from 0.085 to 2.24, possesses a good surface area for producing lightweight concrete with

Table 3a. Mechanical and physical properties of Nendran and Dwarf Scavendish banana (Peels) [42, 70]

Chemical composition of banana peels		Chemical properties of banana peels	
Element	**Concentration (mg/g)**	**Parameter**	**Concentration**
Niobium	0.02±0.00	Saponins (mg/g)	24.00±0.27
Zirconium	0.02±0.00	Phytate (mg/g)	0.28±0.06
Strontium	0.03±0.01	Oxalate (mg/g)	0.51±0.14
Rubidium	0.21±0.05	Hydrogen cyanide (mg/g)	1.33±0.10
Bromine	0.04±0.00	Crude fiber (%)	31.70±0.25
Manganese	76.20±0.00	Carbohydrate (%)	59.00±1.36
Iron	0.61±0.22	Crude liquid (%)	1.70±0.10
Sodium	24.30±0.12	Protein (%)	0.90±0.25
Calcium	19.20±0.00	Organic matter (%)	91.50±0.05
Potassium	78.10±6.58	Ash (%)	8.50±1.52
		Moisture (%)	6.70±02.22

Table 3b. Chemical composition of banana peels [44, 45]

Chemical composition	**CaO**	**SiO_2**	**Al_2O_3**	**Fe_2O_3**	**MgO**	**K_2O**	**C**	**SO_3**	**Lol**
Banana peels (%)	8.95	55.98	2.71	4.65	1.08	17.20	1.69	2.18	5.56
Banana peels (%)	8.95	55.98	2.71	1.36	1.08	28.72	–	0.10	–

Table 4. Physical and mechanical properties of peels from sweet oranges [47]

Properties	**Sweet orange**		
	Minimum	**Maximum**	**Deviation**
Relative density of dried peels (gcm^{-3})			0.4007±0.0023
Bulk density of peels (gcm^{-3})	0.085	2.24	0.99±0.38
The volume of peels (cm^3)	12	65	37.18±13.88
The volume of fruit (cm^3)	64	190	112.25±31.56
Total volume (cm^3)	85	240	149.43±39.30
Mass of peel (g)	73.96	55.23	32.69±7.90
Mass of fruit (g)	177.26	280.18	213.10±22.26
Total mass (g)	202.72	313	250.05±27.10

high-density quality. Likewise, the average Volume of the peels generated from the sweet orange (38.5 cm^3) was up to 30.3% of the average Volume of its fruit. This implies that with 30.3% of peels generated from citrus specie, the structural properties of concrete can be improved using orange peels in concrete production composite. Also, considering the significant rate of wastes (peels) generated from citrus species (especially sweet orange), up to 28.2% mass of lightweight concrete can be substituted with the wastes (peels) from citrus specie. With this, the hygienic condition of our environment can be increased, and there will be excellent availability of construction material, especially for concreting operations [47].

The investigation conducted by Jose et al. [48] determined the chemical composition of orange peels, as shown in Table 5. As presented in Table 5, the orange peel's composition is chemically made up of hemicelluloses, lignin, and cellulose. Among the three, hemicelluloses are the least, with 5.933%, followed by lignin and cellulose, with 19.801% and 69.096% constituent, respectively, as indicated in Table 5. The best component of plant fiber is cellulose, which is a suitable property for concrete structural reinforcement [49]. 69.096% of cellulose from orange peels has excellent potential for concrete reinforcement. All the data in Table 4 showed that orange peels are chemically fit and suitable for concreting operation.

Table 5. Analysis of citrus peels' chemical and proximate composition [48]

Analysis	Composition (% in weight)	Standard deviation
Hemi-cellulose	5.433	5.433
Cellulose	69.096	9.015
Holocellulose	78.110	4.404
Lignin	19.801	3.595
Extractable hot water	40.399	2.595
Acetone extractable	6.821	0.604
Fixed Carbon	0.680	0.078
Ash	0.052	0.004
Volatiles	99.261	0.074
Moisture	73.530	0.477

3. RESULTS

3.1. Performance of Banana Peels Fiber on Concrete Structural Properties

Several studies have unveiled the significant influence of banana peel fiber on the durability performance, fresh and hardened state properties, and structural characteristics of reinforced concrete. Critical insights into the influence of some banana peels' properties on the reinforced concrete's characteristics, such as workability, water absorption, compressive strength, and flexural strength, are provided.

3.1.1. Workability of Concrete with Fiber from Banana Peels

The workability of concrete reinforced with banana skill ash (BSA) is presented in Table 6. According to Teh-Sanariah et al. [50], specific volumes of ordinary Portland cement (OPC) were substituted with 1 and 2% of banana skin ash (BSA). In the investigation, it was observed that as the percentages of BSA in concrete were increasing, the slump values of the freshly mixed concrete were decreasing (from 19±1.0 to 15±0.0 mm), which is equivalent to a 21.1% reduction in the workability of the mixed concrete. Including BSA in the concrete led to a reduction in concrete workability by more than 21%. Contrary to the findings of Teh-Sanariah et al. [50], the experimental results of Aliyu et al. [51] investigation show that the replacement of concrete (OPC) with specific percentages of plantain peel ash (PPA) increased the concrete workability. According to the authors, replacing OPC with 5 to 25% (with an increased interval of 5%) of PPA has improved the quality of concrete slump produced. The results of the concrete slump tests fell within the limit of the specification stated for true concrete slumps by [52].

As presented in Figure 5, the increase in the workability of concrete was attached to high slump values. Likewise, the result shows that the inclusion of PPA in concrete aggregate should not exceed 10% to prevent unnecessary

Table 6. Percentage of BSA, slump, and type of slump formed with concrete reinforced with BSA [50]

Percentage of BSA (%)	0	1	2
Slump (mm)	>100	19±1.0	15±0.0
Type of slumps	Collapse	True slump	True slump

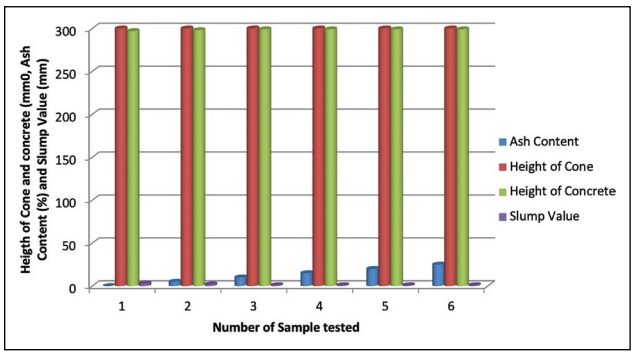

Figure 5. Cement – PPA concrete slump test result [51].

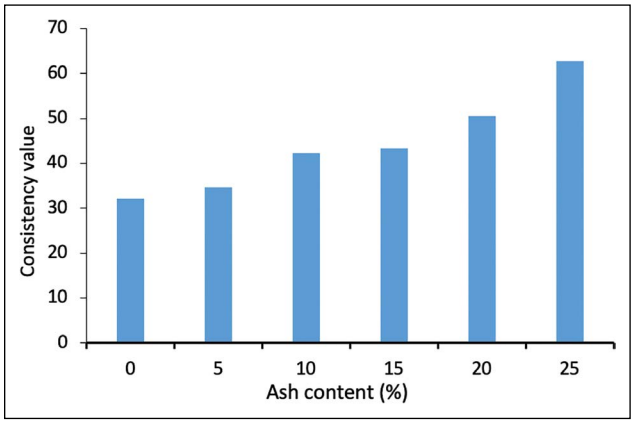

Figure 6. Consistency of cement paste at different percentages of PPA included [51].

constant in concrete fresh–slump values (1 mm). If the PPA inclusion in concrete is beyond 10%, there will be a reduction in concrete moisture during the hydration of cement-concrete, leading to breakage in the hydration process due to moisture loss (Table 7).

3.1.2. Consistency of Cement Paste with Banana Peels

The consistency of the paste's PPA investigated by Aliyu et al. [51] is presented as shown in Figure 6. The consistency value of the cement paste with PPA showed a gradual increment up to 48.64% more than that of the paste with OPC (Table 7). As shown in Figure 5, the values of paste consistency observed were within the specified limit stated by BSEN-196-3 [53]. At the inclusion of treated banana fiber in the cement paste for the modification of cement mortar composite performance, Banjo [54] observed that the cement mortar reinforced with banana fiber developed

Table 7. Concrete temperature transmission and its time reduction with banana peel fibre [60]

Concrete grade	Temperature transmission/days					Time reduction/days				
	1	7	14	21	28	1	7	14	21	28
M20(plain)	3.34	2.14	1.91	1.82	1.37	49.18	44.15	41.54	39.16	34.13
M20 (with BPP)	2.89	1.62	1.51	1.64	1.20	48.29	43.11	39.45	37.06	33.29
M30 (plain)	3.56	2.32	2.13	1.89	1.39	51.49	45.22	43.08	41.08	38.48
M30 (with BPP)	3.29	2.21	1.88	1.73	1.17	50.23	43.17	42.09	39.32	37.04

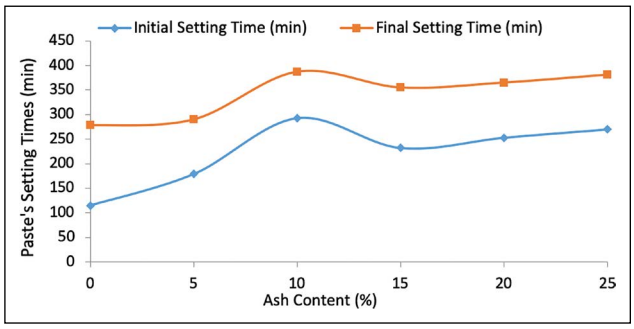

Figure 7. Final and initial setting time of cement paste with PPA [51].

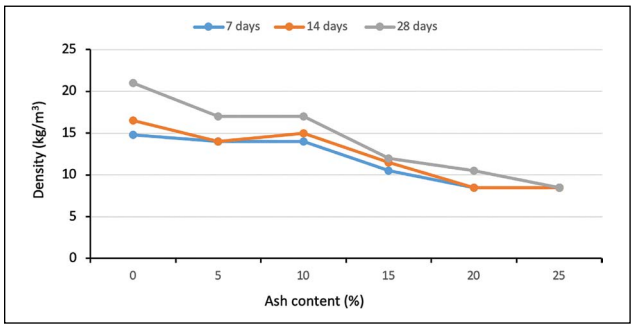

Figure 8. Density of concrete reinforced with plantain peels ash (PPA) [51].

optimum consistency, especially with the addition of 1.5% of banana fiber. It was concluded that including banana fiber in concrete will enrich its paste consistency.

3.1.3. Setting Time of Cement Paste with Banana Peel Fiber

In construction settings, the concrete setting time is defined as when the water is mixed with cement to form a paste, and this paste can be molded into any form until it loses its plasticity and begins to harden [55]. The time when a paste formed from the mixture of water and cement begins to gain hardening is referred to as concrete's initial setting time. While the time when a paste formed from the mixture of cement and water has sufficiently hardened in a way that an impression can be made on it by a 1mm needle but would not if a 5mm needle is impressed on it is referred to as concrete's final setting time [56, 71–74]. As conducted in the experiment, the setting times of cement pastes reinforced with banana peel ashes are presented in Figure 7. As presented in Figure 7, the increase in the percentage of PPA included in the concrete cement paste led to an increase in the initial setting time of the paste.

Contrary to this, the initial setting time decreased when the percentage of PPA included in the paste was beyond 10% until a 15% constituent of PPA in the paste was reached. The time of the paste setting at the initial stage later rose when 20% and 25% of PPA were added to the paste. The final setting of the concrete paste followed the same pattern as its initial one.

The paste setting time was increased up to 5%, including PPA in the mix. Likewise, the decrease in the setting time also took place with the inclusion of 10% and 15% of PPA in the paste. With the inclusion of 20% and 25% of PPA in concrete paste, the final setting time of the paste increased from 355min to 365 and 381mins respectively [51]. Including PPA in concrete paste improved the structural properties of the concrete paste.

3.1.4. Density of Concrete Reinforced with Banana Peel Fiber

The density of concrete reinforced by substituting some proportion of cement with plantain peel ash (PPA) is presented as shown in Figure 8. The increase in the percentage of PPA present in cement – PPA concrete has contributed to the decrease in the densities of concrete produced, especially at its 14th and 28th days of curing. It was observed that concrete with 10% of PPA has a higher density value than that concrete without PPA. The substitution of some percentage of sand aggregate with 1.0, 0.75, 0.5, and 0.25% of plantain fiber has decreased the density of the concrete produced. The data presented by the author shows that the average concrete density of the specimens with 0% of plantain fiber which ranges from 2167–2190 kg/m^3, was less than that of concrete with 0.25 to 1.0% of plantain fiber which is within the range of 2051 to 2066 kg/m^3. The average concrete weight density reduction was 65.2%. This implies that the addition of plantain fiber to concrete could yield the production of light weight concrete. With this, the weight of materials used for structural concrete construction can be reduced, thus improving the concrete's flexibility properties [51, 57].

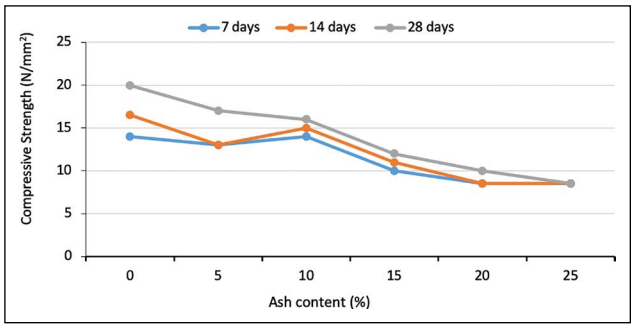

Figure 9a. Concrete compressive strength with specific percentages of PPA [51].

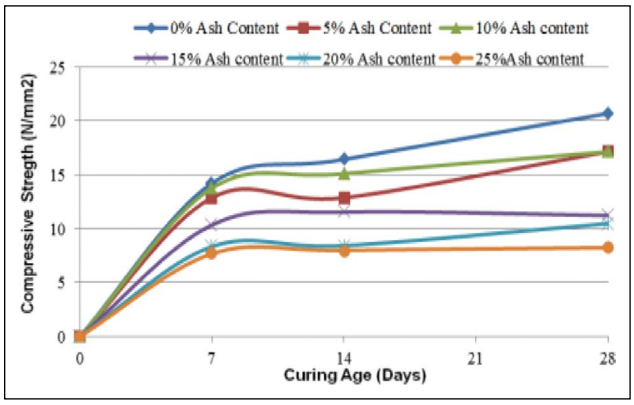

Figure 9b. Cement-PPA concrete compressive strength [51].

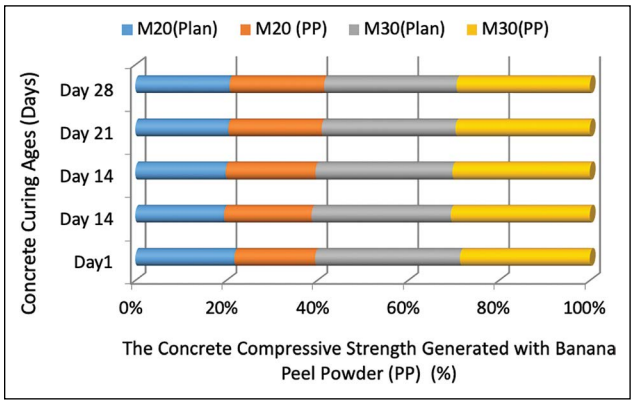

Figure 10. Concrete compressive strength with banana peel powder and its curing ages [60].

3.1.5. Compressive Strength of Concrete Reinforced with Banana Peel Fiber

The concrete compressive strength is an essential property needed by a concrete structure to carry its intending loads [58]. High compressive strength of concrete with banana skin powder (BSP) was recorded in the experiment carried out by Mohamed et al [45]. According to the authors, the replacement of certain concrete sand aggregate with BSP has caused the increment in concrete compressive strength from 18.9 to 27.6 MPa which was about 46%. With this output, it was deduced that BSP has the great potential for concrete reinforcement and it will be useful in concrete industries in terms of replacing some aggregate to lengthen the existed construction materials. Though, the use of plantain peel ash (PPA) as a supplement of cement in concrete does not have positive effect towards the reinforcement of concrete compressive strength like that of BSP used as aggregate substitutes in concrete. According to Aliyu et al [51], the inclusion of plantain peel ash (PPA) as cement substitute has contributed to the formation of low concrete compressive strength which is bad for construction purposes. As shown in figure 9(a), all the compressive strengths of concrete with PPA observed were less to that of concrete with 0% of PPA at 7, 14 and 28 days of curing in water. This implies that, the application of PPA in concrete as a cement supplement material could reduced the concrete strength unlike when the banana peel powder (BPP) is applied as aggregate substitute in concrete which really increase the strength of concrete at compressive zone. According to these findings, it is advisable to make use of banana peels as aggregate supplement in concrete or as concrete additive than to use them as cement substitute in order to increase the concrete compressive strength greatly.

From another perspective, the cement – PPA concrete compressive strength was appreciated by increasing its curing ages presented in Figure 9b. It could be deduced from Figure 9b that fiber from PPA could function as binder or pozzolan in replacement of structural concrete. Its curing age is prolonged till 28, 180, and beyond. Likewise, the findings of Gangadhar et al. [59] also support the latest strength increment of concrete reinforced with banana fiber. According to the authors, the compressive strength of concrete with banana fiber increased up to 4% inclusion of the fiber. This grade 30 concrete with banana fiber performed excellently in loading than the ordinary concrete. Also, concrete began to increase in its compressive strength at 21 curing days when M20 grade was used together with banana peel powder for its production. At the same time, its strength increment with grade M30 was appreciated from 14 days of curing [60].

With the findings presented in Figure 10, it could be observed that the compressive strength of the concrete reinforced with banana peel fiber will increase strength if the high grades of concrete cement are used and cured for long days. The higher the curing days of concrete with banana peel fiber, the better the strength [60].

3.1.6. Tensile Strength of Concrete with Banana Peel Fiber

Concrete tensile strength is defined as concrete's ability to resist breaking or cracking when suggested to tension. This strength is usually within the range of 300–700 psi, equivalent to 2–5 MPa. Averagely, the tensile strength of standard concrete is about 10% of its compressive strength [61]. The result of incorporating some percentage of banana fiber in a concrete mix of grade 30 was indicated by Gan-

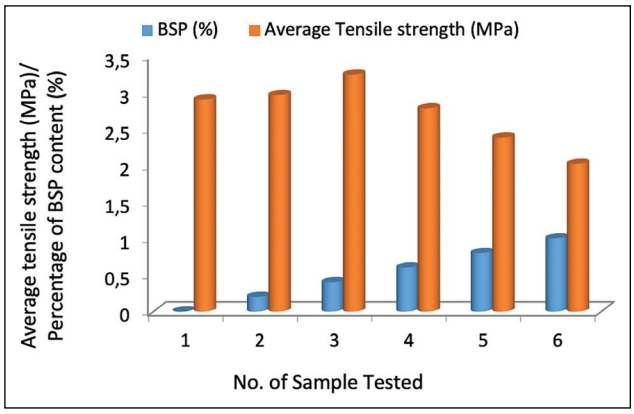

Figure 11. Average tensile properties of concrete with banana skin powder [62].

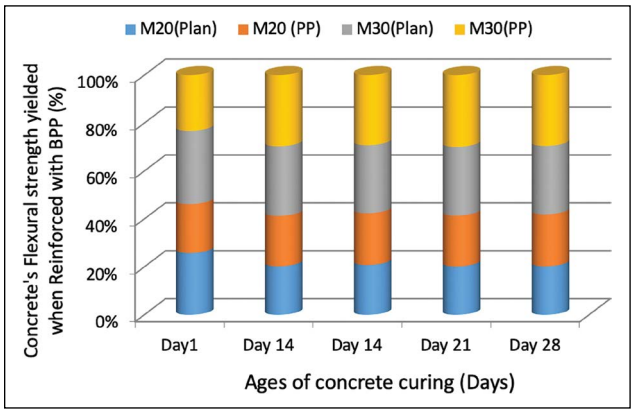

Figure 12. Flexural strength of concrete reinforced with BPP versus curing ages [60].

gadhar et al. [59]. It proved that banana fiber has a greater resistance capacity against cracking during tension. As conducted by the authors, the strengths of the concrete specimens cast with banana fiber were far greater than that of concrete with Ordinary Portland Cement (OPC). Also, replacing some sand aggregate percentages with banana peel powder (BPP) has increased the concrete tensile strength against cracking from 1.54 MPa to 3.24 MPa. This increment was about 52.5%. Thus, BPP can double the strength of concrete against cracks [45]. The findings of Humphrey [57] also support the above report. According to the author, as the concrete's curing ages with banana fiber increased, the concrete tensile strength was also increasing rapidly. The three best strengths yielded were 1.58, 1.6, and

1.65 MPa at the inclusion of 0.25, 0.5, and 1.0% of banana fiber. These values are 12.1% more than the control's (1.45 MPa). When reinforced with banana fiber, the concrete's tensile capacity can be increased by 12%. The result of the investigation conducted by Muhammad [62] also complied with previous results of the scholars presented earlier. As shown in Figure 11, including banana skin powder (BSP) in concrete has contributed to the high increase in the concrete's tensile strength. The highest tensile strength was recorded at the inclusion of 0.4% of BSP in concrete (3.24 MPa), which is 10.5% greater than the tensile strength of standard concrete (2.90MPa). With these reinforcement achievements of using BSP in concrete, it was clearly shown that BSP is a great potential material for controlling cracks in concrete which is one of the significant problems in construction industries nowadays.

3.1.7. Flexural Strength of Concrete with Banana Peel Fiber

As presented in Figure 12, the flexural strength of concrete with banana peel powder (BPP) was significantly increased in both concrete produced with grades M20 and M30 compared with that of control. According to Gadgidhalli et al. [60], the bending resistance capacity of grade M20 concrete reinforced with BPP was 85.2% greater than

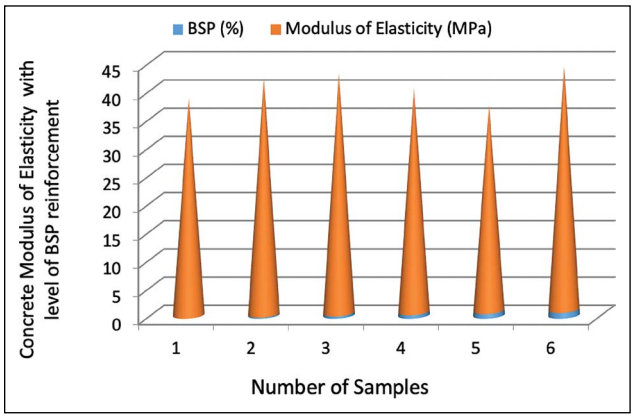

Figure 13. Concrete modulus of elasticity with the level of BSP reinforcement [62].

that of plain concrete. Likewise, the tensile strength of M30 grade concrete was increased by 87.1% over its control specimen. This implied that BPP is a tremendous potential material for concrete reinforcement against bending. Mohamad et al. [45] also confirmed that banana skin powder (BSP) has excellent potential for concrete flexural strength increment up to 1.0% inclusion of BSP compared with control.

3.1.8. Modulus of Concrete Elasticity with Banana Peel Fiber

The process of a concrete structure contracting and expanding due to climatic variations is known as concrete elasticity. If the issue is frequent and not adequately addressed, it may result in cracks [49]. As a result, quality design is required to expand cracks of concrete composites or materials to prevent cracks. The result shows that the concrete's expansion and contraction rate was reduced by replacing a certain percentage of sand aggregates with banana skin powder in concrete. This reduction was achievable because some of the developed pores and holes within the concrete might have been blocked by BSP, thus restricting their movement during contraction and expansion. As indicated in Figure

Table 8. Optimized model validations [50]

	Concrete curing ages (day)								
	7 days			14 days			28 days		
BSA (%)	0	1	2	0	1	2	0	1	2
Experimental	20.76	21.19	21.51	23.86	21.97	24.00	31.61	28.77	29.50
Predicted	19.90	21.70	27.00	23.30	25.10	30.50	32.30	34.10	39.40
Error percentage (%)	4.1	2.4	25.50	2.4	14.3	27.1	2.2	18.5	33.6

13, the reduction rate in concrete's elasticity (MOE) was higher than that of concrete with OPC. All the concrete specimens reinforced with 0.2%–1.0% of BSP (with a 0.2% increase interval) showed an increase in concrete stiffening strengths against expansion due to its modulus of elasticity.

3.1.9. Effect of Banana Peel Fiber on Concrete Temperature Transmission

One of the significant climatic conditions that are usually causing cracks in concrete is the change in concrete temperature. The effect of expansion and contraction of concrete structures in high temperatures can be developed into forming pores, cracks, and holes within the concrete structure. Including peels from banana fiber as concrete's admixture has caused much reduction in its heat transmission and high temperature that could increase the concrete's elasticity. The concrete's strength developed against high temperatures rising was 2.5 to 3.5% greater than regular concrete [63]. However, banana peel powders (BPP) were added to the concrete as an admixture, and the BPP included has increased the strength capacity of concrete significantly against deformation, cracking, and shrinkage, thus, reducing the rate of concrete temperature and time transmissions [60].

As presented in Table 7, the rates of reduction in concrete's temperature's transmission were reduced by 24.3 and 11.7% (Maximum) on the 7th and 14th days of concrete curing of grades M20 and M30, respectively. Likewise, the concrete temperature transmitting time rates were reduced by 5.4 and 4.5% on the 21st and 7th days of curing grades M20 and M30, respectively. Therefore, it was concluded that dried BPP has excellent potential for reduction of exothermal reaction in concrete. Also, the increase in concrete curing age will significantly develop the high resisting capacities of concrete against thermal transmission.

3.1.10. Modeling and Analysis of Concrete's Strength Response Reinforced with Banana Peel Fiber

The interrelation between banana skin ash (BSA) in concrete, concrete's curing days, and its compressive strength were predicted by Teh-Sabariah et al. [50] during experimental laboratory work. The modeling activity involved Expert design software using the surface response method (SRM) for the central design of concrete composites (CDC). Its statistical prediction involved the use of analysis of variance (ANOVA). It was discovered that adding BSA to concrete composite has excellent potential for concrete strength increment. From the validity of the model result recorded, the optimum BSA adopted by the authors for concrete strength reinforcement was 1.25%. At this optimum (1.25%), from 7 to 28 days of curing concrete, all the concrete compressive strengths were at maximum. As presented in Table 8, the minimum errors observed were 18.5, 14.3, and 2.4% for 28, 14, and 7 days of curing concrete. With the use of Pearson's proximity matrices device, it was observed that there was a correlation between concrete compressive strength and its curing ages (both predicted and experimental). Looking at the validation of the model, it can be applied for the prediction of concrete reinforced with BSA as an admixture in industries.

3.2. Performance of Orange Peels Fiber on Concrete Structural Properties

3.2.1. Workability of Concrete Reinforced with Orange Peels Fiber

As it has been known, concrete workability depends on the materials' quality, the proportion of mixed aggregates, the percentage of water applied to the concrete mixing, and its production methods. If these were not adequately catered for, it could result in segregation, production of tick concrete that cannot flow easily, wet concrete, formation of pores and holes within the concrete, shrinkage, and creeping [49]. Apart from proper production methods, applying admixture in concrete will improve the quality of concrete produced. From the literature review, no proper workability test was conducted on concrete with orange peel fiber.

3.2.2. Consistency of Cement Paste with Orange Peel Fiber

One of the standard methods of calculating the precise amount of water needed for normal concrete paste formation is the consistency of the paste. Olumide et al. [64] replaced 2.5 to 10.0% of ordinary Portland cement with burnt ashes from orange peels. The replacement of concrete cement aggregate with orange peel ash (OPA) has caused an increase in the water demand rate for the formation of OPA cement to paste from 89.4 to 127.2 mm. The more the increase in the content of OPA in the cement paste, the higher the consistency of OPA- paste (Figure

Table 9. The rate of demand for water, settings times, and consistency of OPA – cement pastes [64]

OPA content (%)	0.0	2.5	5.0	7.5	10.0
Water consistency (%)	28.5	29.80	34.20	38.60	42.40
Water demand (mm)	85.8	89.4	102.6	115.8	127.2
Initial setting time (min)	120	126	136	148	152
Final setting time (min)	148	152	162	198	224

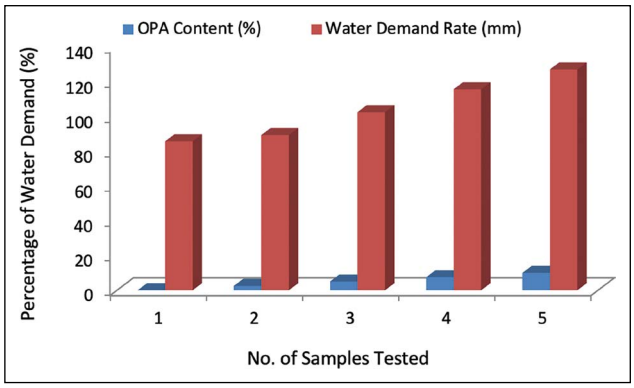

Figure 14. Effect of OPA content on the rate of water demanding binary cement blend [64].

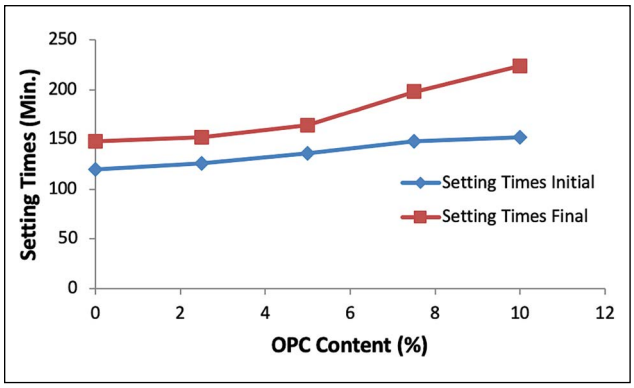

Figure 15. Effect of blending some percentages of cement with OPA on concrete setting times [64].

14). The high level of water demand in the OPA-cement paste was attributed to the presence of unburnt carbon in the OPA produced. Hence, a higher water-cement ratio is required to form a consistency of OPA-cement paste.

3.2.3. Setting Time of OPA-Cement Paste

A setting time of cement paste or concrete is defined as the assigned time needed for the mortar or concrete to change to a plastic state from liquid state, and solid state from plastic state until its surface becomes adequately rigid in withstanding a certain amount of pressure [77]. According to [77], the time at which the cement – paste starts to loss its plasticity is called initial setting time of cement. While the time at which a cement paste has completely loses its plasticity is known as cement final setting time. These times are important for the accurate setting of concrete paste for standard building concrete inner strengths for structural stability. The setting times of concrete with OPA were evaluated, and some of the data were presented in Figure 15 as shown below.

As presented in Figure 15, the increase in Orange Peel Ash (OPA) content of OPA-cement paste has lead to the increase in the both initial and final setting times of concrete pastes by 20.64% and 47.37% than that of paste with Ordinary Portland Cement (OPC). These increments were within the range of including 7.5–10.0% of OPA in the concrete's paste. This might be attributed to the clinker content diminution in the OPA included in the concrete –cement - paste. Since the normal consistence of concrete required high content of water to attain a standard paste' consistence, hence, the higher water cement ratio is required to achieve the consistence of cement paste with OPA (Olumide et al. [64]). Table 9 gives the compressive information on the rate of demanding for water by OPA – Cement pastes, settings times and Consistence of OPA – Cement pastes.

3.2.4. Composite/Concrete Density Reinforced with Orange Peel Fiber

All construction industries require the use of concrete with high-yielding strength to construct structural members. The suitability of the materials used will determine the weight of the concrete produced against deformations during loading [49]. Applying orange peel fiber in composite or concrete improved the quantity of concrete structural properties. Katla and Chetty [65] and [77] on the reinforcement of epoxy composite with fiber from orange peel indicated that the percentage of orange peel powder (OPP) used ranges from 5–30% with an increased interval of 5%. As observed from the result, the 20, 30, and 10% composite samples showed a high rise in composites' density by 5.34%, 5.07%, and 2.79%, respectively, as presented in Figure 16.

From their experimental output, it was observed that an increase in the content of OPP in the composite had caused an increase in the density of the composite. On the contrary, the composite bulk density developed by using certain percentages of dried orange peels (DOP) for the production of building insulating material decreased as the DOP content increased. The decrease rate was from168.63±12 kg/m^3 (W75) to 558.46±13 kg/m^3 (W100). This is equivalent to about a 16% reduction. Hence, DOP is good for lightweight concrete production [32].

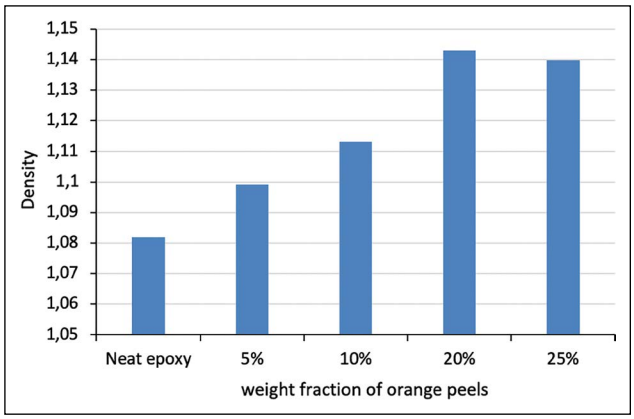

Figure 16. Density of epoxy composite reinforced with orange peel fiber [65].

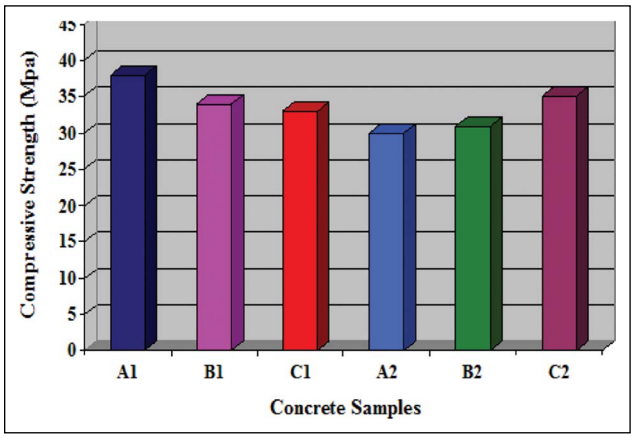

Figure 17. Compressive strength of concrete samples after immersion in tap water [66].

3.2.5. Compressive Strength of Concrete Reinforced with Orange Peel Fiber

Shaymaa and Tamas [66] indicate that orange peel fiber (green inhibitor) was incorporated in concrete material to mitigate its sulfate and chloride attack. According to the authors, the inclusions of inhibitors were by 1 and 3% of the weight of cement. The output of the investigation was presented as shown in Figure 17. From Figure 17. The concrete reinforced with corrosion inhibitor (orange peel extract) was observed to reduce strength by 10.5 and 13% when 1 and 3% of inhibitors were included, respectively. Therefore, to use orange peel in concrete as an inhibitor, proper treatment should be adopted to prevent causing a reduction in concrete strength.

Also, concrete mortar reinforced with orange peel ash (OPA) developed low strength compared to concrete with only OPC (control). The reduction could result from the high demand for water by OPA – paste to attain consistency or diminution because of its clinker content [64] (Fig. 18). It is observed that the mortar's compressive strength was significantly increased from 28.88 to 44.41 MPa, which is equivalent to 80% of strength increment at 28 days of curing. The inclusion of OPA in concrete mortar should not exceed 5% to avoid strength reduction. Besides, the increase in mortar's curing ages from 2 to 60 days has increased mortar compressive strength. Therefore, the concrete reinforced with OPA requires long curing age to develop high strength. Considering the effect of orange peels on composite, the investigation by Mahato et al. [32] showed that blending orange peel with epoxy to form composite has developed maximum hardness (strength) at the point of blending 20% of orange peels with epoxy to form composites.

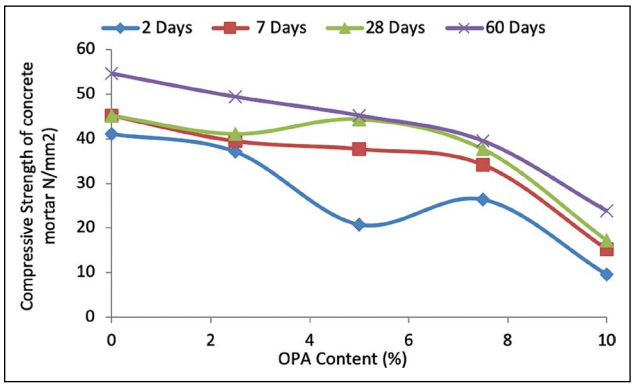

Figure 18. Effect of OPA on mortar compressive strength [64].

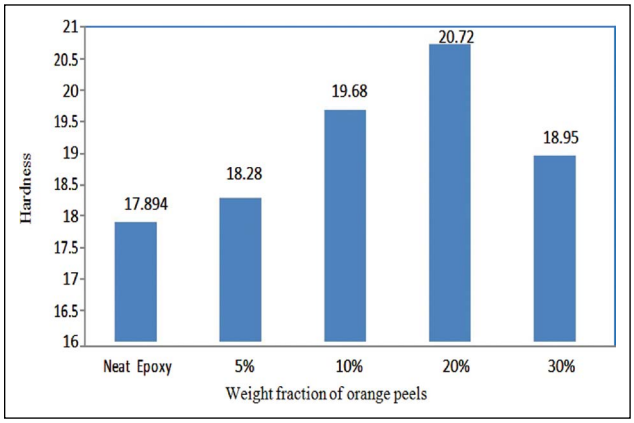

Figure 19. Variation of tensile strength with different percentages of orange peels content [65].

3.2.6. Tensile Properties of Composite/Concrete Reinforced with Orange Peel Fiber

The reinforcement of epoxy with 20% of orange peel powder (OPP) to form composite has developed high strength against cracking than the other two samples observed together with the control. According to Katla and Chetty [65], the level of strength increment was about 30.25% more than that of the control, as shown in Figure 19.

This shows that orange peels can increase concrete strength by 30% when applied as an admixture in concrete or composite. Thus, orange peel could be an excellent substitute for concrete aggregate or cement in the concrete industries. Likewise

3.2.7. Concrete/Composite Flexural Strength Reinforced with Orange Peel Fiber

The investigation conducted by Olumide et al. [64] shows that concrete flexural strength was mostly appreciated when 2.5% of OPA was included in its mix and cured for 60 days, as illustrated in Figure 20. The bending resisting capacity of OPA – concrete declined when its OPA content was increased beyond 2.5%. From another perspective, the increase in curing ages of OPA-concrete mortar leads to an increase in the mortar's strength to withstand bending and deflections during loading. In support of this, an output of blending orange peels as an insulator for building applications shows that orange peels have great potential for concrete and composite improvement [32].

The investigation highlight revealed that the W75 sample developed higher strength to withstand deflection than the other samples tested. The samples from W80 to W100 displayed a high level of deflection when suggested to stress. With critical consideration of the above results, it was observed that applying orange peels in composite or concrete as admixture or as a substitute material for cement will contribute an excellent strength increment to concrete strength against deflection or bending.

3.2.8. Modulus of Elasticity of Composite Reinforced with Orange Peel Fiber

The composite modulus of elasticity without orange peels (W100) is higher by ten times than that of W75 samples. The performance was associated with the mixed composite's homogeneity and porosity. Also, there might be the reaction of pyrolysis, caramelization, and Maillard of organic components within the compacted aggregates. This implied that, with the inclusion of orange peel fibers in concrete or composite, the pores and holes within the concrete or composite aggregate would have been blocked and acts as fillers in concrete to prevent cracks due to constant elasticity [32].

3.2.9. Effect of Orange Peel Fiber on Concrete Thermal Conductivity

The strength of an orange peel-reinforced composite against thermal expansion was conducted and observed by Mahato et al. [32]. The samples used were allowed to pass through the thermal conductivity test, and the results were recorded. AW75 sample was observed to show a higher level of thermal conductivity. The mean thermal conductivity of the W100 sample, with 0.66W/mk capacity, is 1.2 times more than that of the W75 sample with 0.77 W/mk capacity [67]. Also, the authors stated that the composite produced with 4 to 12% orange peels could generate high thermal conductivity with the increase in the temperature of the composite. This is in line with the findings of Ochs et al. [68]. Therefore, orange peel is excellent potential for composite and concrete reinforcement.

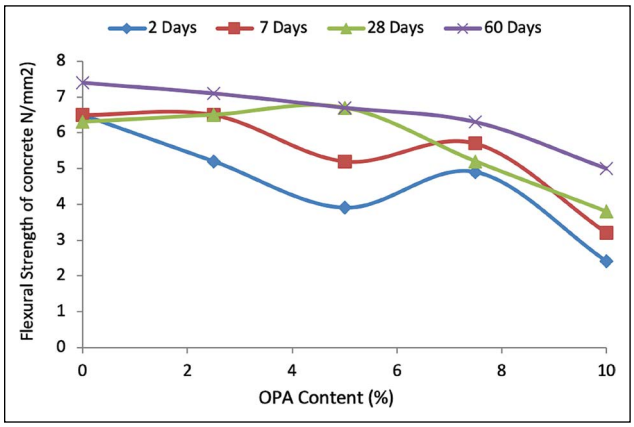

Figure 20. Flexural strength of concrete blended OPA [64].

4. DISCUSSION

The previous estimation showed that up to 4.2 billion meters and 3 tonnes of cement and concrete were consumed globally in a year [5, 8]. Likewise, the carbon dioxide emission rate from cement production companies globally is very high. China only was emitting about 823 million metric tonnes of carbon dioxide yearly from its cement production companies, causing harm to human health, destroying the ozone layers, and increasing the rate of global warming. Also, the study showed that about 34.72 to 46.29 million metric tonnes of peels were generated from bananas, and up to 15.10Mt of peels were generated from oranges globally [33, 37]. These wastes have become environmental problems, hazardous to humans' health, and have emitted a high volume of carbon dioxides into the atmosphere. With the outcome of this review, the application of treated orange and banana waste peels for cement and concrete production will go a long way in enhancing the rate of cement and concrete production around the globe. It will be a strategic method of eradicating the large Volume of piled wastes from banana and orange peels that have been causing environmental pollution, likewise, as global warming.

Also, their application will serve as a substitute for cement and concrete materials, making the two materials cheaply available for global citizens at affordable prices. Then, many concrete structures could be raised due to the availability and low cost of cement and concrete materials. Furthermore, applying these peels in concrete will prolong the use of non-renewable natural materials (sand, granite), which can be exhausted in years to come if supplementary materials are not provided [38, 67]. The results of the experiments conducted by the scholars show that banana and orange peel fibers were physically fit for concrete reinforcement. As reviewed, both wastes have good surface areas for quality concreting, low specific gravity for stability, and exact lengths and breadths for concrete reinforcement.

The review has shown that the pozzolanic components of banana peels' essential elements: potassium (78.10±6.58 mg/g) and calcium (19.20±0.00 mg/g), are made up of 97.3% of pozzolanic binding properties for quality concrete reinforcement. This percentage (97.3%) is more than that of specified properties of any material used as pozzolan in concrete, as stated by ASTM C618 [46], which is 70%. While orange peels have three important chemical properties that could significantly enhance the quality of concrete produced, that is, hemicelluloses - 5.933%, lignin – 19.801%, and cellulose – 69.096%. These qualities made both orange and banana peels suitable for concrete. The application of banana peels in concrete increased its workability properties by 21.1% [50]. This negates the results of other studies that indicate that banana peels decrease concrete workability. With the critical consideration of these results, it was observed that banana peels have great potential for improving concrete workability, but proper care should be taken on the water-cement ratio used for its production. As observed in the review, the concrete paste with banana and orange peels was discovered to increase by 48.64% more than that of the control. As the percentage of banana peel fiber (BPF) substantially increases, the BPF – the concrete paste will also increase. Likewise, the more the percentage of OPF in concrete, the more the consistency of OPF-cement pastes. So, a high water-cement ratio is required to attain the consistency of BPF and OPF-cement concrete paste. The increase in the percentage of BPF in concrete has brought about an increase in concrete's final and initial setting time.

This time increment was achievable up to 5% of BPF in concrete, while the decrease in concrete setting times occurred within 10 to 15% of including BPF in concrete. Likewise, the addition of OPF to concrete increased OPF – cement concrete setting times by 47.37%. It requires the use of a higher water-cement ratio to control this. Also, to achieve the typical setting of concrete with BPF, a not-too-high water-cement ratio should be adopted. Application of OPF in concrete leads to an increase in concrete density by 5.34%. Therefore, orange peels have great potential for the production of lightweight concrete. The review shows an increase in the concrete compressive strength with the increase in the percentage of banana peels included in the concrete up to 46% than that of the control. This shows that the relationship between the concrete and banana peel fiber is linear. Concrete with BPF should be suspended for long curing days (Up to 180 days) to gain maximum compressive strength. Since applying orange peels in concrete as a green inhibitor was to mitigate the effect of sulfate and chlorine attack in concrete, proper treatment should be applied to OPF before use in concrete as an inhibitor. The BPF-concrete's tensile properties developed maximum strength increment up to 52.5%.

Therefore, banana peels have an excellent potential for concrete strength reinforcement against cracks due to stress on concrete. The study's flexural strength tests show that BPF has contributed about 87.1% to the concrete strength against bending and deflection. So, BPF is suitable for producing concrete for residential house slabs, beams, and columns. The concrete stiffness capacities against expansion due to elasticity were greatly enhanced than that of control with the application of BPF. The concrete elasticity effect in concrete due to stress could be eradicated using BPF. The capacity of BPF-concrete was developed to withstand temperature transmission by 2.5 to 3.5% more than regular concrete [63–65]. It was found that BPF reduced the concrete transmission temperature by 24.3%. The review output deduced that applying BPF in concrete will reduce deformation, crack, and shrinkage. The prediction observed from Expert design model software shows that 1.25% is the optimum for reinforcing concrete with BPF [66–71].

Though, according to the review, the high concrete strength yielding was observed when the processed banana and orange peels were included in concrete, notwithstanding, the proper treatment is required on banana and orange peels biomass in order to prevent them from chemical attack and acidic reaction during the hydration process which can reduce the rate of concrete strength yielding at the formation stage. The production of banana and orange peels" ashes require adequate supervision so as to allow the burning of peels to produce pure ashes (without impurity) for supplementary of concrete pozzolanic materials. Ashes with impurity can reduce the strength, durability, sustainability and stability of concrete, thus, reducing the quality of concrete needed for accurate construction purposes.

5. CONCLUSION AND RECOMMENDATIONS

It was observed that banana and orange peels have great potential for concrete reinforcement. The authors suggested that an accurate water-cement ratio should be used to avoid reducing concrete workability. Based on the information provided by this review, using banana peels in concrete requires a higher water-cement ratio to attain stable consistency. To avoid too quick setting and too late setting of concrete with BPF, the author suggested that the medium (not too high) water-cement ratio should be adopted. Also, a higher water-cement ratio should be adopted for OPF-cement concrete to normalize their high setting time. With the observed 46% strength increment on the concrete compressive capacity, BPF is recommended for twice the reinforcement of concrete strength to carry the intending loads. More research work should be done on BPF-concrete compressive strength. Since the researchers on the use of BPF in concrete were very few, more investigation is needed on the concrete compressive strength using banana peels as an admixture or as a material substitute. Also, it was suggested that concrete with BPF should be suspended for long curing days (Up to 180 days) to gain maximum compressive strength.

It was suggested that BPF should be adopted for concrete tensile cracking and deflection control. It was recom-

mended that the use of OPF in concrete should not exceed 2.5% to avoid a decrease in its flexural strength. Authors suggested that banana and orange peels should be incorporated into concrete that will be used to construct residential houses' slabs and for frame beam construction to prevent them from being saved against deflection. Also, the inclusion of OPF in concrete should not exceed 20% to avoid reducing concrete flexural strength. Concrete with orange peels should be allowed to be a cure for long days to improve its strength against deflection. BPF is recommended for thermal reaction reduction in concrete. Also, proper treatment should be applied to OPF before use in concrete as a green inhibitor. It was recommended that software like artificial intelligence model, finite element structural model software, and civil engineering simulation be used to predict the optimum strength of concrete with BPF and OPF for industrial use.

Likewise, this software should be used to show the correlation between concrete compressive strength and its curing age to increase its industrial values. In conclusion, using orange and banana peels in concrete has contributed significantly to enhancing concrete's structural properties; hence, they can be used as supplementary materials for concrete production. More rigorous studies which investigate the OPF-cement concrete consistency are required. More slump and impact factors tests were needed to predict the effect of OPF in concrete. Few research tests were conducted on using banana peel fibers in concrete. More experimental investigations are needed on concrete compressive strength, the accurate water-cement ratio for BPF –cement concrete, and more test is required in the area of concrete elasticity with BPF. Predictability of the critical structural materials of these natural fibers in concrete reinforcement is significant to ensuring accurate building design prior to construction.

This study recommends an intelligent predictive model and process optimization for natural-fibers-based concrete. Owing to the limitations of the classical linear model involving the use of Expert design and Pearson's proximity metrics device for statistical analysis, artificial intelligence model, finite element structural model software, and civil engineering simulation software is recommended to predict the concrete strengths to ascertain the standard and accurate strength prediction of using BPF and OPF in concrete. The use of OPF for tensile reinforcement of concrete properties needs more investigation using a not too high water-cement ratio. The application of OPF for concrete tensile strength reinforcement requires more investigation. The concrete thermal conductivity with orange peel fiber needs quick investigation. Future studies could focus on this to determine the capacity of the OPF against thermal defects.

Further, the application of orange peel to improve the elasticity capacity of concrete due to modulus effects needs to be researched. This will reduce cracks in the concrete due to the modulus of elasticity. Finally, different software applications are needed to accurately predict concrete strength on all its mechanical properties, which requires quick action.

ETHICS

There are no ethical issues with the publication of this manuscript.

DATA AVAILABILITY STATEMENT

The authors confirm that the data that supports the findings of this study are available within the article. Raw data that support the finding of this study are available from the corresponding author, upon reasonable request.

CONFLICT OF INTEREST

The authors declare that they have no conflict of interest.

FINANCIAL DISCLOSURE

The authors declared that this study has received no financial support.

PEER-REVIEW

Externally peer-reviewed.

REFERENCES

[1] Demissew, A. (2022). Comparative analysis of selected concrete mix design methods based on cost-effectiveness. *Advances in Civil Engineering*, 2022, Article 4240774. [CrossRef]

[2] Pacheco, J. De Brito, J. (2021). Recycled aggregates produced from construction and demolition waste for structural concrete: constituents, properties, and production. *Materials*, 14, Article 5748. [CrossRef]

[3] Mohammed, S. I., Collette, C., & Sean, M. (2012). Trend and development in green cement and concrete technology. Int. *J. Sustainable Built Environment*, 1,194–216. [CrossRef]

[4] Pro-crew. (Apr 9, 2020). *Concrete in construction: Uses, advantages, and types. Concrete construction*. www.crewschedule.com

[5] Colin, G. R. (2012). Cement and concrete as an engineering material: An historic appraisal and case study analysis. *Engineering Failure Analysis*, 40, 114–140. [CrossRef]

[6] Gopal, M. (Oct 25, 2021). *Fiber-reinforced concrete: Types, properties, and advantages of fiber reinforced concrete*. theconstructor.or.

[7] Chang J. (Apr 9, 2020). *Britannica, The Editors of Encyclopedia. 'Three Gorges Dam'. Encyclopedia Britannica*. https://www.britannica.com/topic/Three-Gorges-Dam

[8] Gareth B. (Sep 20, 2022). *Improving the world through better use of concrete. Materials, Resources, and Sustainability Series*. https://irp-cdn.multiscreensite.com/8bbcaf75/files/uploaded/190805_MRS-1_concrete.pdf

[9] Garside M. (Sep 1, 2021). *Major Countries worldwide, cement production 2010-2020. Chemical and resource mining, metals and materials*. www.statista.com

[10] Lan T. (Jun 7, 2021). *Global Cement Manufacturing CO_2 emissions 1990-2019, by country energy and environment, Emissions*. https://www.statista.com/statistics/1091672/carbon-dioxide-emissions-global-cement-manufacturing/

[11] The European Cement Association. (Sep 20, 2022). *Activity report*. (1st ed). CEMBUREAU: Brussels, Belgium, (2017), 1–42. https://cembureau/media/1716/activity-report-2017.Pdt

[12] World Business Council for Sustainable Development (WBCSD). (Sep 10, 2019). *Cement sustainability initiative (CSI). Cement industry energy and CO2performance. Getting the Numbers Right (GNR) Project*. (1st ed). World Business Council for Sustainable Development: Geneva, Switzerland, 2018. http://www.wbcsdcement.org/index.php/key-issue/climate-protection-database

[13] Elzinga, D. J. (2015). *Energy Agency Perspectives 2015: Mobilizing innovation to accelerate climate action*. (1st ed). International Energy Agency (IEA) Publications Paris, France, 1–412.

[14] Garcia-Gusano, D., Hemera, I., Garrain, D., Lechon, Y., & Cabal, H. (2014). Life cycle assessment of the Spanish cement industries implementation environment–friendly solutions. *Clean Technology &Environmental Policy*, 17, 59–73. [CrossRef]

[15] Ibrd-Ida (Sep 20, 2022). *The World Bank Group at COP 26. Cop26 climate action*. https://www.worldbank.org/en/topic/urbandevelopment/brief/solid-waste management.

[16] Kaza, S., Yao, L. C., Bhada-Tata, P., & Van Woerden F. *What a waste 2.0: A Global Snapshot of Solid Waste Management to 2050. Urban Development*. World Bank.

[17] Obi, F., Ugwuishiwu, B., & Nwakaire. J. (2016). Agricultural waste concept, generation, utilization, and Management. *Nigerian Journal of Technology*, 35, 957–964. [CrossRef]

[18] Purdue. (Apr 16, 2019). Banana from the fruit of warm climate. Julia Morton. Hort.pursue.edu. Archived from the original. https://hort.purdue.edu/newcrop/morton/author.htmlArmstrong, P. (Aug 17, 2013). *Wayne. Identification of major fruit types. Wayne's word: An online Textbook of natural history*. https://www2.palomar.edu/users/warmstrong/

[19] Armstrong, P. (Aug 17, 2013). Wayne. Identification of major fruit types. Wayne's word: An online Textbook of natural history. https://www2.palomar.edu/users/warmstrong/

[20] Merriam-Webster. (Jan 4, 2013). Bananas. https://www.merriam-webster.com/dictionary/bananas

[21] Tracing Antiquity of Banana Cultivation in Papua New Guinea. (Aug 29, 2017). *The Australia and pacific science foundation*. ttps://cembureu/media/1716/activity-report-2017

[22] Nelson, S. C., Randy, P., & Angela, K. K. (2006). Musa Species (Banana and Plantain). Species profiles for Pacific Island Agroforestry. https://www.researchgate.net/publication/267362931_Musa_species_banana_and_plantain

[23] Pro-Musa. (Oct 25, 2016). Where bananas were grown. https://www.promusa.org/Turkey

[24] Merymol. (Feb 11, 2022). *5 ways you need to know about how to use banana peel to benefit your skin*. https://merymoi.com/5-ways-you-need-to-know-about-how-to-use-banana-peel-to-benefit-your-skin/

[25] United States Department of Agriculture (USDA). (2022). *Citrus – sinensis. Germplasm Resources Information Network* (GRIN). Agricultural research service (ARS), https://data.nal.usda.gov/dataset/germplasm-resources-information-network-grin

[26] Franck, C., Frederique, O., Andres, G., Navarro, L. F., & Patrick, L. (2016). Phylogenetic origin of limes and lemons revealed by cytoplasmic and nuclear markers. *Annals of Botany*, 117(4), 565–583. [CrossRef]

[27] U.N. Food and Agricultural Organization, Corporate Statistical Database (FAOSTAT). (2020). *Production of Orange in 2019 Crop/ Regions? World List? Production Quantity (pick lists)*. Retrieved 21 March 2021. https://www.fao.org/faostat/en/#data/QCL

[28] Xu, Q., Chen, J. W., Ge X. J, Lei Y, Hu Q., Miao Y., Wang L., Xiao S., Biswas M. K, Zeng W, Guo F, Cao H, Yang X, Xu X. W, Cheng Y. J, Xu J, Liu J. H, Luo O. J, Tang Z, Guo W. W, Kuang H., Zhang H. Y, Roose M. L, Nagarajan N, Deng X. X., & Ruan Y. (2013). The draft genome of sweet orange (citrus genesis). *Nature Genetics*, 45(1), 59–66. [CrossRef]

[29] Morton, J. F. (1987). *Fruits of warm climates*. Creative Resources Systems, pp. (134–142).

[30] Manuel, T., Marco, C., & Fred, G. G. (2020). *The genus citrus*. Woodhead Publishing.

[31] United States Department of Agriculture (USDA). (Dec 10, 2017). *Citrus Sinesis Germplasm Resources Information Network (GRIN). Agricultural Research Service* (ARS). https://data.nal.usda.gov/dataset/germplasm-resources-information-network-grin

[32] Mahato, N., Sharma, K., Sinha, M., & Cho, M. H. (2018). Citrus waste-derived Nutra-/pharmaceuticals for health benefits: Current trends and future perspectives. *Journal of Functional Foods*, 40, 307–316. [CrossRef]

[33] Albarelli, J. Q., Rabelo, R.B., Santos, D. T., M.M. Beppu, M. M., & Meireless, M. A. (2011). Effects of supercritical carbon dioxide on waste banana peels for heavy metal removal. *Journal of Supercritical Fluids*, 58, 343–351. [CrossRef]

[34] Zema, D. A., Calabro, P. S., Folino, A., Tamburino, V., Zappia, G., & Zimbone, S. M. (2018). Valorisation of Citrus processing waste: A review. *Wastes Management*, 80, 252–273. [CrossRef]

[35] Sasha, A. A., Diaz-Carrillo, A. J., Florez-Lopez, E., & Tovar, D. G. (2021). Recovery of Banana wastes – loss from production and processing: A contribution to a circular economy. *MDPI Journal Molecules*, 26, 17, Article 5282. [CrossRef]

[36] Ali Sial, T., Khan, N., Lan, Z., & Kumbhar, F. (2019). Contrasting effect of banana peel waste and its biochar on greenhouse gas emissions and soil biochemical properties. *Process, Safetyand Environmental Protection*, 122, 366–377. [CrossRef]

[37] Graind, S. (2016). Exploitation of orange peel for fungal solubilization of rock phosphate by solid-state fermentation. *Waste Biomass Valorization*, 8, 1351–1360. [CrossRef]

[38] Grohmann, K., & Baldein, E. A. (1992). Hydrolysis of orange peel with pectinase and cellulose enzymes. *Biotechnology Letters*, 14(12), 1169–1174. [CrossRef]

[39] Marin, F. R., Solar-Rivas, C., Benaverite-Garcia, O., Castillo, J., & Perez-Alvarez, J. A. (2007). By-products from different citrus processes as a source of customized functional fibers. *Food Chemistry*, 100(2), 736–741. [CrossRef]

[40] Widner, K., Zhou, W., & Grohman, K. (2010). Pre-treatment effect on orange processing waste for making ethanol by simultaneous saccharification and fermentation. *Bioresource Technology*, 101(14), 5242–5249. [CrossRef]

[41] FAO. (2017). *Citrus fruit fresh and processed statistical bulletin* 2016. FAO.

[42] Kachru, R. P., Kotwaliwale, N., & Balasubramanian D. (2000). Physical and Mechanical Properties of green banana (Musa paradisiacal) fruit. *Journal of Food Engineering*, 26(3), 369–378.

[43] Anchwang, B., Torshian, J., & Nyiatagher, T. D.(2009). Chemical composition of musa sepientum (banana) Peels. *Electronic Journal of Environmental, Agricultural and Food Chemistry*, 8(6), 437–442.

[44] Muhammed, L. T., Mohamad, N., Abdul Samad, A., Muthusamy, K., Mydin, O., Goh, W. I., & George S. (2021). Effect of banana skin powder and coir-fibre on properties and flexural behavior of precast SCC beam. *International Journal of Sustainable Engineering*, 14(5), 1193–1206. [CrossRef]

[45] Mohamad, N., Abdul Samad, A. A., Lakhiar, M. T., Othuman, M. A., Jusoh, S., Sofia, A. E., & Fendi, S. A. (2018). Effects of incorporating banana skin pow-der (BSP) and palm oil fuel ash (POFA) on mechan-ical properties of lightweight foamed concrete. *In-ternational Journal of Integrated Engineering*, 10(9), 69–76. [CrossRef]

[46] ASTM C 618-05 (2006). *Specification for coal fly ash and raw or calcined natural pozzolan for use in concrete*. Annual Book of ASTM, Standard, Section 04 Construction, Volume 04.02 Concrete and Ag-gregate, ASTM International, West Conshohocken. https://www.astm.org.

[47] Oyebola, O. O., Agboola, S.O, Olabode, O. A., & Ayoola, P. O. (2017). Analysis of the physical and chemical composition of sweet orange (Citrus sinensis) peels. *International Journal of Environment Agriculture and Biotechnology*, 2(4), 2201–2206. [CrossRef]

[48] Jose, R. A., Gisela, M., Marcos, A. C., Conrado, G., Mario, A. C., Jose, A. L., Carlos, A. S., & Daniela G. M. (2021). Characterization of orange peels waste and valorization to obtain reducing sugars. *MDPI Molecules*, 26, Article 1348. [CrossRef]

[49] Kilani, A., Fapohunda, C., Adeleke, O., & Metiboba, C. (2021). Evaluating the effects of agricultural wastes on concrete and composite mechanical properties: A Review. *Research on Engineering Structures and Materials*, 8(2), 307–336. [CrossRef]

[50] Teh-Sanariah, B. A., Nur, L. M., Salmia, B., Taimur, K., Daud, M., Agustril, S., Zarina, I., Hisyam, J., Nur, A. N., Wan, H. M., Mohamed, H. I., Nasir, S., Amirrudin, A., & Nadiah, W. R. (2021). Strength enhancement of concrete using Incinerated agricultural wastes as supplementary cement materials. *Science Reports*, 11, Article 12722. [CrossRef]

[51] Aliyu, U., Nura, B., & Moshudi, B. (2018). Effect of plantain peel ash (PPA) on the mechanical properties of concrete. *Noble International Journal of Scientific Research*, 2(3), 11–18.

[52] British Standard (BS)-1881: *Part 102: Method for determination of slump 1983*. British Standard)

[53] British Standard Institute. BS EN 196 – 3:(1995). *Methods of testing cement. Determination of setting time and soundness*. British Standard)

[54] Akinyemi, B. (2020). Development of banana fibres and wood botton ash modified cement mortars. *Journal of Construction and Building Materials*, 241, Article 118041. [CrossRef]

[55] Krishna (2017). *Initial and final setting time of cement. civil read home Structure*. Available online: https://civilread.com/cement-initial-final-setting-time/#:~:text=The%20time%20at%20which%20cement%20completely%20loses%20its%20plasticity%20and,final%20setting%20time%-20of%20cement.&text=The%20time%20taken%20by%20cement,is%20600%20minutes%20(10hrs).

[56] Ur-Rahman, F. (2018). *Initial Setting Time and Final Setting Time of Concrete*. The Constructor. https://theconstructor.org/concrete/initial-final-setting-time-concrete/25819/

[57] Danso, H. (2020). Influence of plantain pseudostem fibers and lime on the properties of cement mortar. *Advances in Materials Science and Engineering*, 2020, Article 4698603. [CrossRef]

[58] Jamal, H. (2017). *Properties of Harden Concrete. Notes Mixture, Material Properties*. https://www.coursehero.com.

[59] Gangadhar, N., Krishna, P. C., Vinod Kumar, C., Madhuri, R., & Parthiban, A. (2020). Fiber-reinforced pervious concrete by using banana fiber. *Global Journal of Current Research*, Vol. 7(2), 66–67.

[60] Gadgihalli, V., Meenay, R., Sindhu, S., Raghavendra, P., & Havanje, D. (2017). Analysis of properties of concrete using dried banana peel powder as admixture. *International Journal of Research*, 5(11), 351–354. [CrossRef]

[61] Prasad (Feb 5, 2022). *What is tensile strength of concrete Structural Guide Manual?* https://www.structuralguide.com.

[62] Muhammad, T. L., Noridah, M., Abdul Aziz, A., Samad, K., Muthusamy, K., Mydin, A. O., Goh, W. I. & George, S. (2021). Effect of banana skin powder and coir fiber on properties and flexural behavior of precast SCC beam. *International Journal of Sustainable Engineering*, 14(5), 1193–1206. [CrossRef]

[63] Mohabe, M. R. (2021). Utilization of banana peel powder in concrete: A result. *International Journal of Creative Research Thoughts*, 9(6), 153–156.

[64] Olumide, O. O., Basiru, A., & Osha, A. O. (2019). Potential of orange peel ash as a cement replacement material. Path of Science: *International Electronic Scientific Journal*, 5(7), 2009–2019. [CrossRef]

[65] Katla, P. K., Chetty, N. (2010). An investigation of Mechanical characterization of Orange Peel Reinforced Epoxy Composite. *IOSR Journal of Mechanical and Civil Engineering*, 33–41.

[66] Shaymaa, A. A., & Tamas, T. I. (2019). Studying the effect of addition of green inhibitor on compression strength of reinforced concrete. *IOP Conference Series: Materials Science and Engineering*, Volume 613, 5th International Conference on Competitive Materials and Technology Processes 8–12 October 2018, Miskolc-Lillafüred, Hungary.

[67] Schiavoni, S., D'Alessandro, F., Bianchi, F., & Asdrubali, F. (2016). Insulation materials for the building sector: A review and comparative analysis. *Renewable and Sustainable Energy Reviews*, 62, 988–1011. [CrossRef]

[68] Ochs, F., Heidemann, W., & Müller-Steinhagen, H. (2008). Effective thermal conductivity of moistened insulation materials as a function of temperature. *International Journal of Heat Mass Transfer*, 51, 539–552. [CrossRef]

[69] Soltani, M., Alimardanil, R., & Omid, M. (2011). Some physical properties of full-ripe banana fruit (Cavendish variety). *International Journal of Agricultural Science, Research and Technology*, 1(1), 1–5.

[70] Syukriani, L., Febjislami, S., Lubis, D. S., Hidayati, R, Asben, A., Suliansyah, I., & Jamsari, J. Physicochemical characterization of peel, flesh, and banana fruit cv. Raja [Musa paradisiaca]. *IOP Conference Series: Earth and Environmental Science*, Volume 741, 2nd International Conference of Bio-Based Economy for Application and Utilization 16th December 2020, Padang West Sumatera, Indonesia. [CrossRef]

[71] Tirkey, N., & Ramesh, G. B. (2018). Experimental study on the banana fiber reinforced concrete. *International Journal of Pure and Applied Mathematics*, 119(18), 2053–2056.

[72] Lakhiar, M. T., Mohamad, N., Abdul Samad, A., Muthusamy, K., Mydin, M. A., Goh, W. I., & George, S. (2021). Effect of banana skin powder and coir fibre on properties and flexural behavior of precast SCC beam. *International Journal of Sustainable Engineering*, 14(5), 1193–1206. [CrossRef]

[73] Hussein, H. S., Shaarawy, H. H., Hussien, N. H., & Hawash. S. I. (2019). Preparation of nano-fertilizer blend from banana peels. *Bulletin of the National Research Centre*, 43, 26. [CrossRef]

[74] Jonca, Z., & Lewandowski, W. (2004). Verification of measurement capabilities of flam atomic spectrometry for the determination of sodium, potassium, magnesium, and calcium in natural fresh water WW part 1. Comparism of recommended methods. *Polish Journal of Environmental Studies*, 13, 275–280.

[75] Golmohammadi, M., Borghei, A., Zenouzi, A., Ashrafi, N., & Taherzadeh, M. J. (2018). Optimization of essential oil extraction from orange peels using steam explosion. *Heliyon*, 4(11), e00893. [CrossRef]

[76] Alamineh, E. A. (2018). Extraction of pectin from orange peels and characterizing its physical and chemical properties. *American Journal of Applied Chemistry*, 6(2), 51–56. [CrossRef]

[77] Tanvi Lad (2016). What is setting time of cement? Materials. Cimc-rjst.com Accessed on Oct 03, 2022.

[78] Kaniraj, S. R., & Fung, Y. C. (2018). Influence of discrete fibers and mesh elements on the behaviour of lime stabilized soil. *Pertanika Journal of Science and Technology*, 26(4), 1547–1570.

[79] Fapohunda, C. A., & Kilani A. (2021). Study of Structural Performance Evaluation of Concrete Reinforced with oil palm empty fruit bunch fibre. Proceedings of the 3rd International Conference on Engineering Innovations as a Catalyst for Rapid Economic Growth tagged COLENG, Federal University of Agriculture, Abeokuta, Nigeria, May 24–26, 2021.

Journal of Sustainable Construction Materials and Technologies
Web page info: https://jscmt.yildiz.edu.tr
DOI: 10.47481/jscmt.1211086

JSCMT
Journal of Sustainable Construction Materials and Technologies

Review Article

FRP strengthening of RC structures: Sustainable, environmental and structural evaluations

Ali Cem YAĞAR*[1], Ceren İNCE[2], Shahram DEROGAR[3]

[1]*Sustainable Environment and Energy Systems, Middle East Technical University, Northern Cyprus Campus, North Cyprus*
[2]*Civil Engineering Program, Center for Sustainability, Middle East Technical University, Northern Cyprus Campus, North Cyprus*
[3]*Line Consulting Engineers, 392 Jockey Road, Sutton Coldfield, UK*

ARTICLE INFO

Article history
Received: 28 November 2022
Accepted: 19 December 2022

Key words:
Fibre reinforced polymers, modifications, strengthening, sustainability, TS 500

ABSTRACT

Strengthening and rehabilitation have been widely implemented for many years to extend the service life of reinforced concrete structures. The paper begins with a comprehensive review of the fiber-reinforced polymers (FRP) utilization on strengthening, particularly over the traditional materials formerly used in practice with respect to materials, manufacturing, operation, Construction, and maintenance phases as the engineering and environmental performance of such materials. Carbon and Glass FRP, the most frequently used strengthening materials, are particularly designated in the study and are employed to conduct an environmental performance evaluation using the previously published data in the literature. The paper then investigates the punching shear strength of flat slab-column connections strengthened with externally bonded FRP using a nominated database comprising 57 data points harvested from the recent literature. The database is used to evaluate the test data with TS 500 code equations and the recent modification of Chen and Li. The study enabled the key factors affecting the punching shear strength of such connections to be emphasized and highlighted that the TS 500 code equations fall conservative in predicting the punching shear strength of slab-column connections strengthened with FRP. The study is novel as it provides a comprehensive review of the FRP as a strengthening material regarding environmental sustainability. It also provides insight into the structural implications of this material by evaluating the current TS 500 code provisions and recent modifications.

Cite this article as: Yağar, AC., İnce, C., & Derogar, S. (2022). FRP strengthening of RC structures: Sustainable, environmental and structural evaluations. *J Sustain Const Mater Technol*, 7(4), 358–374.

1. INTRODUCTION

Strengthening refers to converting a non-damaged structure or structural element to a higher level of performance than its existing condition [1]. Inadequate maintenance, overloading, changes in the standards of application, or exposure to severe environmental conditions often necessitates strengthening reinforced concrete structures [2].

***Corresponding author.**
*E-mail address: yagar.ali@metu.edu.tr

Steel plate bonding, external pretension addition, cross-sectional enhancement, and reinforced concrete coating are some of the strengthening techniques that have been developed in the past and have gained significant popularity over the last decades. Although the methods mentioned above can successfully increase the load-bearing capacity of such components, they are often prone to corrosion [3]. This feature causes the strengthening system to lose its function both in the medium and long term. Consequently, the traditional strengthening methods have mainly been replaced with new non-corrosion strengthening systems such as fiber-reinforced polymers (FRPs). Hence, the potential to extend reinforced concrete structures' service life has been considerably expanded with reduced maintenance costs [4].

Strengthening materials can be investigated in two categories as traditional and advanced strengthening materials [5]. Steel and concrete are the most utilized traditional strengthening materials [2, 6]. The traditional materials' strengthening methods comprise cross-sectional enlargement, external prestressing and steel plate bonding, and Ferro-cement coating methods. FRP composite materials, the so-called advanced material, are successfully used to construct new structures and repair and strengthen existing structures [7]. The most commonly used FRP reinforcement methods are external bonding and near-surface mounting [8, 9].

The cement industry is an essential source of greenhouse gas (GHG) emissions, particularly CO_2 emissions. The cement industry, for instance, accounts for about 7% of global CO_2 emissions [10]. This is mainly due to the calcination process of raw materials necessary for producing cement and fossil fuels burned to maintain the high temperatures needed during production. This process requires about 3.2–6.3 GJ of energy and 1.7 tons of raw materials (mainly limestone) per ton of clinker produced [11]. In addition, it is devastating, particularly from an environmental perspective, to note that approximately one kilogram of CO_2 is released while producing one kilogram of cement [12]. Steel production processes account for about 9% of total CO_2 emissions worldwide. Since the construction industry consumes about half of all steel produced worldwide, the impact of this material is critical in determining the carbon footprint of the construction industry [13]. The traditional primary steel manufacturing method is essential oxygen furnace steel production. This process is divided into two main parts: iron production in a blast furnace (BF) and steel production in a basic oxygen furnace. 70% of CO_2 emissions are produced during the BF processes [14]. Approximately 65% of the total steel produced in the world is produced using this method. CO_2 corresponds to 82% of all GHG emissions. Industries are responsible for 21% of all CO_2 emissions, which includes cement and steel production. 30% and 26% of all carbon emissions are released in steel and cement production processes, respectively, which means that more than half of the CO_2 emissions of all industrial activities are caused by steel and cement production [14]. High temperatures, 1,400 °C for glass; 1,200–2,400 °C for carbon, are required during producing (FRP) [15]. This indicates that a significant amount of energy is spent during their production. The epoxy resin, the most commonly used adhesive in FRP utilization, and FRP have the highest unit carbon dioxide emissions (~5 and 6 kg/kg, respectively). These emission rates are approximately 0.2 kg/kg for concrete and 1.8 kg/kg for reinforcing steel [16]. It must be emphasized, however, that the production of FRP causes much lower water and air pollution rates compared to that of structural steel, aluminum, and concrete, indicating its environmentally friendly features [17].

Due to their widespread availability, cost-effectiveness, and well-defined material properties, steel and concrete were widely used in reinforcement applications. However, the labor and cost-intensive phases of repair and maintenance, the low corrosion resistance of steel, and the limited lifespan of these traditional strengthening materials have encouraged exploring new strengthening materials. Considering the above-mentioned features, FRP have a longer service life and high corrosion resistance and stand out as an optimum alternative material. [7, 9, 18]. Moreover, FRPs are available in more considerable lengths than steel plates, usually limited to 6 m, which avoids the need for joints [19]. The frequency of maintenance required for FRP material is almost two times less than for traditional materials. Considering the main phases of Construction, maintenance, or demolition, it can be concluded that the carbon emissions of these processes can be substantially reduced using FRPs compared to traditional materials [20]. On the other hand, FRP composites have almost eight times higher environmental impact when used to strengthen reinforced concrete structures than conventional steel [21–24].

It is well documented in the literature that the reinforced concrete flat slabs suffer from brittle punching shear failure due to the shear stresses and the imbalanced moment conveyance between the slabs and columns [25–31]. When the existing flat slab-column connections become incapable of meeting the punching shear strength requirement primarily as a result of the structural deficiencies, either the structure will be demolished to rebuild, or the structure will be strengthened [32]. Rebuilding the structure not only results in an expensive solution but also is not consistent with the sustainable development goals of the United Nations Foundation [33]. The strengthening strategy thus is often executed utilizing FRPs, a composite material composed of a polymer matrix packed with fibers. The precedence of the FRP strengthening, previously aforementioned, comprises high tensile strength, lightweight, and simplicity of installation [6, 34–37]. Although the FRP strengthening techniques can widely range, it is worth noting that the externally bonded (E.B.) FRP is the most commonly implemented strengthening method for enhancing the strength and energy dissipation of inadequately detailed members.

Although the utilization of FRP on flat slab-column connections is widely recognized and implemented in practice frequently, especially over the last decade, a unified formula that systematically addresses the FRP utilization on such connections does not exist in the literature. Even though the literature comprises several studies concerning the FRP strengthening of flat slab-column connections, TS 500 [38] code provisions, for instance, do not constitute the influence of FRP strengthening on the punching shear strength of slab-column connections. It is widely documented in the literature that FRP strengthening significantly influences the punching shear capacity of flat slab-column connections [39–44]. Therefore, its impact on such structural performance cannot be neglected. Individual researchers such as Chen and Li [45] introduced modifications to reflect the influence of FRP strengthening on punching shear strength by modifying the adequate depth and reinforcement ratio parameters with the equivalent effective depth and equivalent reinforcement ratio. Although the influence of these modifications on punching shear strength, examined by Chen and Li [45], improved the expertise in this context, these studies mainly utilized their specific experiments. They hence failed to provide adequate preciseness into the diverse implementation of FRP strengthening on connections. This feature necessitated further investigations to achieve a comprehensive assessment of the aforementioned modifications, particularly concerning the preciseness of the TS 500 [38] code provisions.

The paper, therefore, aims to provide a comprehensive review of the FRP utilization on strengthening, particularly concerning the traditional materials formerly used in practice. The utilization of FRP and traditional strengthening materials and methods have been reviewed concerning the materials, manufacturing, operation, Construction, and maintenance phases, as well as the engineering and environmental performance of such materials. Carbon and Glass FRP, the most frequently used strengthening materials, are particularly designated in the study and are employed to conduct an environmental performance evaluation using the previously published data in the literature. The environmental performance evaluations comprised elastic modulus, energy input, average yield strength, the temperature needed for the production, and cost and cost efficiency of Carbon and Glass FRP. The second phase of the paper investigates the punching shear strength of flat slab-column connections strengthened with externally bonded FRP using a nominated database comprising 57 data points harvested from the recent literature. The database is used to evaluate the test data with TS 500 [38] code equations and the recent modification of Chen and Li [45]. The study's second phase enabled the key factors affecting the punching shear strength of such connections to be emphasized and highlighted that the TS 500 [38] code equations fall conservative in predicting the punching shear strength of slab-column connections strengthened with FRP.

2. DATABASE DEVELOPMENT

The database used in the study is on the punching shear strength of the flat slab-column connections. The analysis is focused on the externally bonded FRP use without shear reinforcement. The inner columns strengthened with FRP are considered only. The database is developed using specimens with concrete compressive strength higher than 10 MPa, slab depth of at least 50 mm, and a slenderness ratio higher than 5.0. The database principally encompasses the geometrical information of the concrete section, steel yield strength, reinforcement ratio of both internal steel reinforcement and the external FRP strengthening, and measured failure load. The selected articles used in the database development and the associated parameters are presented in Appendix A. The data summarised in the database are converted to the S.I. unit system. Data with incomplete information were omitted from the database. It is worth noting that initially, more than 100 data points were harvested from the literature; however, nearly one-third of this could not be included in the database due to the inconsistency attained with respect to the set criteria, such as determined for concrete compressive strength, slab depth, span to depth ratio and FRP strengthening technique.

3. THEORETICAL BACKGROUND

This section includes the theoretical basis of the TS 500 [38] code provisions and the modifications introduced by Chen and Li [45] on the use of FRP in flat slab-column connections. According to TS 500 [38], the punching shear capacity is calculated using the following equations:

$$V_{pr} = \Upsilon f_{ct} u_p d \quad \text{Eq. 1}$$

$$f_{ct} = 0.35\sqrt{f_{ck}} \quad \text{Eq. 2}$$

Υ=1.0 (in the case of axial loading) Eq. 3

V_{pr} is the punching shear strength, f_{ct} is the concrete tensile strength (MPa), u_p is the critical perimeter which is $\frac{d}{2}$ away from the column face, and the d is the adequate depth. The unbalanced moment's effects are reflected by the coefficient Υ, which is 1.0 for the axial loading case. The punching shear strength design equation provided in TS500 [38] is moderately similar to the code provisions of ACI 318 [46]. The main drawback of TS500 [38] is the disregard of the effect of the reinforcement ratio in predicting the punching shear strength of slab-column connections, even though it is one of the most influential parameters affecting the punching shear capacity of such connections [47–49]. Additionally, the size effect is not included in the code equations in relation to the punching shear strength despite its strong impact on the punching shear capacity of such connections [50]. Considering that the minimum re-

inforcement ratio is now defined, and the size effect parameter is included in the code equations about the punching shear strength of flat slab-column connections calculation in ACI 318 [46], the code equations provided in TS500 are practically similar to the code provisions provided in the former version of ACI 318 [51].

Consequently, further computations were performed using the Chen and Li [45] modification to reflect the effect of FRP strengthening in the punching shear calculations. The adequate depth and reinforcement ratio parameters were replaced with equivalent effective depth, $d$eq, $_{Chen}$, and equivalent reinforcement ratio, ρeq, $_{Chen}$, respectively. Because TS500 [38] does not consider the reinforcement ratio, only the effective depth could be replaced with an equivalent effective depth herein. Modified equations by Chen and Li [45] are as follows:

$$\rho_{eq,Chen} = \frac{T_s+T_f}{b d_{eq,Chen} f_y} \quad \text{Eq. 4}$$

$$d_{eq,Chen} = \frac{M_{nf}}{T_s+T_f} + \frac{a}{2} \quad \text{Eq. 5}$$

where the T_s is the tension force of the steel; T_f is the tension force of the FRP; b is the unit width of the slab section; a is the depth of the rectangular stress block; and M_{nf} is the flexural strength of strengthened R.C. slab, which is the moment taken about the tension steel reinforcement and is determined as:

$$M_{nf} = C_C \left(d - \frac{a}{2}\right) + T_f(h-d) \quad \text{Eq. 6}$$

in which, C_C is the neutral axis depth and can be calculated iteratively from internal force equilibrium until the following equation is achieved:

$$C_C = T_s + T_f \quad \text{Eq. 7}$$

It is investigated in section 4.2 that the measured ultimate punching shear strength over TS 500 [38] and TS 500 with Chen and Li [45] modification predictions ratio versus key parameters such as tensile reinforcement ratio, concrete compressive strength, and FRP reinforcement ratio to evaluate the accuracy of these predictions depending on influencing parameters.

4. RESULTS AND DISCUSSIONS

4.1. The Overview of the FRP as a Strengthening Material

4.1.1. Materials and Methods

Fiber materials and the matrix from the two primary components of FRPs. The most commonly used fibers are carbon, glass, basalt, and aramid, whereas resins comprise the majority of matrix materials. These two materials, combined in an appropriate proportion prior to a multifarious procedure to constitute the innovative high-performance FRP material, are used in reinforced concrete structures in the form of laminates, rods, grids, and sheets. Externally bonded FRP sheets and strips (EBR) and near-surface mounting FRP strips (NSM) are the two most commonly used strengthening techniques [52, 53]. Due to the ease of application, externally bonded reinforcement (EBR) is the most widely used strengthening method. Externally bonded FRPs, divided into two main categories: "wet laying" (or "cured in place") systems and "prefabricated" (or "precured") systems [52], can be applied in different configurations such as orthogonal, skewed, radial, and whole-layer configurations. The number of FRPs used in each direction and the distance between the FRP and the column face have an important role in the effectiveness of the strengthening. For instance, the skewed FRP reinforcement with orthogonal internal steel reinforcement is more effective in preventing crack propagation since cracks caused by the punching shear force propagate in several different directions [54]. Moreover, since the FRPs in the critical punching shear area are evenly distributed in all directions, the radially located strengthening performs even better than the diagonal orientation [55].

The near-surface mounted (NSM) technique, developed to strengthen reinforced concrete structures, is an effective alternative to the external bonding of FRPs. Cutting a series of shallow grooves in the concrete surface is the first step in the process. The depth of the groove is suggested to be less than the concrete cover to prevent any damage to the existing reinforcement. Following this aspect, the carbon fiber composite rods or strips are then placed into grooves partially filled with epoxy resin. The rest of the groove is filled with epoxy resin, and the surface is leveled then [56]. The most imperative advantage of this implementation is the soundness of the reinforcement compared to that of the external bonding method, which often experiences premature debonding between the concrete surface and the FRP.

4.1.2. Manufacturing Process of FRPs

Pultrusion and wet laying (manual method) are the manufacturing procedures for FRPs used as construction materials. FRP reinforcement, FRP strips for external strengthening, and FRP profiles are produced by pultrusion. The wet laying method is used more frequently for FRP sheets to strengthen the existing buildings [57, 58]. Pultrusion is the most cost-effective method for producing FRP rods, profiles, and strips. The energy required for the pultrusion process is approximately 3.1 MJ / kilogram [58]. This method automatically produces FRP forms with a fixed cross-section. I-beam, channel, and multi-cellular profiles are all made by pultrusion. Pultrusion consists of a fiber and a matrix system. Pultrusion consists of six stages: (1) a series of spools piled on creels for fiber reinforcement handling; (2) performing guides; (3) resin impregnation bath; (4) forming and curing die; (5) a pulling system; and (6) cutting system [58].

Hand layup, a manual procedure of stacking fiber layers in a resin system, is commonly used to reinforce FRP sheets and textiles. After hardening, the solid FRP compo-

Table 1. Energy required for extraction and production of the main constituents of FRP composite [18]

Materials	Energy input (M.J./kg)
Polyester	63–78
Epoxy	76–80
Glass	13–32
Carbon	183–286
Steel	30–60

nent takes the shape of the mold. This method is known as laminating or wet layup. Hand layup can be done on-site or off-site; however, on-site manufacturing is essential for strengthening applications. In this case, an appropriate connection between FRP elements and the newly strengthened structural section is essential; hence, resins with strong adhesive capabilities are used in connection with carbon or glass fibers [58–60].

The first step of the manufacturing process is extracting the essential components of FRPs from their sources as raw materials. Glass, the most commonly used fiber type in FRP composites, has the lowest energy density when considering the production stages because of the ease of extraction and production. The carbon fibers in FRP composites, however, require the highest energy for the extraction and production of all fibers and hence are recognized as the least cost-effective options. This factor poses a severe obstacle to the widespread use of carbon FRPs, despite their superior mechanical properties compared to other fibers or traditional engineering materials [18].

Table 1 demonstrates the energy required for the extraction and production of the main constituents of FRP composite. The energy required to extract and produce glass is, on average, twelve times less than the energy required for carbon (13–32 M.J./kg for glass and 183–286 MJ/kg for carbon). Approximately the same amount of energy is required for the extraction and production of polyester and epoxy, the two most commonly used matrix components (63–78 M.J./kg for polyester, 76–80 M.J./kg for epoxy). The energy consumed on the matrix components corresponds to one-third of the energy consumed on carbon. In addition, the energy required to extract and produce steel as a raw material (30–60 M.J./kg) is about twice the energy required for glass (13–32 M.J./kg); however, the energy required for steel is lower than carbon, polyester, and epoxy.

Glass fibers (G.F.) have a minor diameter among all fibers, ranging from 1 to 4 microns. Glass fibers are formed by several oxides, mainly silicon oxide [59]. The components are combined and melted at temperatures above 1400 °C during the manufacture of glass fibers, and a large amount of non-renewable energy is used for this production [61]. The production of 1 kilogram of glass fiber consumes approximately 54.7 MJ of energy [12, 20].

Two leading processes often used in manufacturing carbon fibers are the petroleum-based pitch and the polyacrylonitrile (PAN) [57, 59]. The pitch technique removes graphite strands from hot liquid pitch using an injector. The PAN method involves heating and oxidation to remove a chain of carbon atoms from polyacrylonitrile (PAN). The polymer is stretched in a straight line parallel to the axis of the fiber. The polymer is then converted into a non-melting precursor fiber following the oxidation process between 200–300 °C in air. The precursor fiber is then heated in a nitrogen-rich atmosphere. The temperature continues to rise until the carbon fiber reaches a minimum 92% of carbon ratio. As the production process reaches temperatures ranging from 2500–3000 °C, carbon fibers have one of the highest environmental impacts compared to other types of fibers used for strengthening in composite applications considering that a significant amount of non-renewable energy is consumed to reach such temperatures required during this stage. It must be noted that the superior mechanical properties result in a considerable reduction of carbon fibers used for the strengthening and hence yields an overall reduced environmental impact [57, 61].

Polyester resins are widely used in strengthening applications due to their mechanical properties and low cost; however, the main drawback of this material is its negative impact on human health [12]. Peroxide and styrene substances are known to cause the sources of adverse effects of polyester resin. While these compounds can cause severe damage to the eyes and skin, they can also potentially negatively affect the brain [62]. It is widely noted in the literature that polyester resins have the highest environmental impact compared to epoxy and vinyl ester resins [18]. Epoxy resin is a popular choice for strengthening reinforced concrete structures with FRPs due to their superior mechanical qualities and easy adaptability [12]. The hardening process of epoxy mixtures also causes significant effects on human health [62]. However, it must be noted that epoxy resins are pretty challenging to recycle [12]. Vinyl ester resin is a composite material comprising mainly polyester and epoxy resins, and vinyl esters can be made using a mixture of epoxy and polyester resins. This attributes that the vinyl ester resin comprises all the harmful effects of the two inclusive resins observed in the mixture [12].

4.1.3. The Operation, Construction, and Maintenance Phases of FRPs

The production of FRP creates a higher unit quantity of carbon emissions compared to other traditional materials such as concrete or steel. Despite the high unit amount of carbon emissions during the manufacturing phase, several life-cycle evaluations have shown that carbon emissions may decrease when other factors like Construction, maintenance, and disposal are considered. Garg et al. [63] compared the CO_2 emissions and energy consumption of steel rebars with FRP rebars such as CFRP, GFRP, and BFRP. The

results revealed that replacing FRP with steel rebars reduced CO_2 emissions and energy consumption by 39%, 43%, and 40% when CFRP, GFRP, and BFRP reinforcement were used, respectively, instead of steel. Furthermore, the energy consumption of FRP-reinforced beams was lower than that of steel-reinforced beams by 30%, 47%, and 50% for CFRP, GFRP, and BFRP, respectively. Inman et al. [64] conducted a similar study where the basalt FRP rebars were compared to steel rebars using crucial indicators such as CO_2 emissions, ozone depletion, and human toxicity. The results revealed that replacing steel rebars with BFRP reduced CO_2 emissions by 38%, human toxicity by 79%, and ozone depletion by 40% for the best scenario in each case. Although the life cycle assessment does not address the strengthening method's structural efficiency, it demonstrates the environmental and ecological advances of such material compared to that of steel, taking the operation, construction, and maintenance phases into account [65].

The resins used in the FRP components are known to create the highest ozone depletion, one of the environmental impacts of such implications. Maxineasa et al. [66] studied the strengthening of a structural element using carbon FRPs and epoxy resin by the external bonding method. It has been shown in the study that epoxy resin causes 98% of ozone depletion throughout the whole process of FRP strengthening. The study also stated that half of the human toxicity effect occurs at the stages of transportation, Construction, and maintenance.

4.1.4. Engineering Performance of FRP Application

The most commonly used FRP strengthening materials are carbon (CFRP) and glass (GFRP) based FRPs. Carbon fibers are often used for strengthening due to their high strength, high creep levels, chemical resistance, low conductivity, low density, and high elastic modulus. The disadvantages of carbon fibers are their high cost and anisotropic nature [67]. Glass fibers are the most widely used type of fiber. E-Glass, S-Glass, and C-Glass are the three common glass fiber varieties. The main characteristics of glass fibers are their high strength, low cost, and superior water and chemical resistance [68].

The method of external bonding under axial load is considered a successful approach. Ten square-section columns were strengthened using near-surface mounting (NSM), external bonding (E.B.), and hybrid strengthening methods by Challapandian et al. [69]. While the NSM system increased the axial capacity by 8%, the E.B. system increased the axial capacity by 42% in the same column. It was reported in the study that the most effective method of strengthening the columns is the combination of NSM strips and the E.B. system. It is known that strengthening a rectangular section with externally glued FRP usually results in a relatively low bending rigidity along its flat side and an uneven axial stress distribution under compression while significantly increasing the rigidity in circular sections [70].

As structural elements can be subjected to repeated bending movements, it is necessary to strengthen their bending strength. The type of strengthening method used, the qualities of FRP and adhesives, and the additional anchors used considerably affect the performance of the strengthened structural element. It is known that the externally utilized FRP strengthening applied along the stretched face of the structural elements significantly increases the bending performance. In order to enhance the performance to a maximum level, it is recommended to apply FRP along the surface of the structural element [71]. In addition, the near-surface mounting (NSM) method is a more effective method compared to the external bonding (E.B.) method due to its potential to increase the strength by 200% under bending. [69, 72]. Attari et al. [73] conducted experiments to strengthen reinforced concrete structures using carbon, glass, and carbon-glass fiber hybrid sheets. Experimental results have shown that the bending strength of a beam strengthened using a carbon-glass fiber sheet increased by 114%. Carbon-glass hybrid FRP strengthening was found to be more effective in bending compared to that of carbon FRP.

Externally bonded FRP shear strengthening can strengthen shear-weak R.C. beams in vertical, inclined, side-bonded, U-wrapped, or anchored designs. The performance of strengthened structures are affected by the fibers' quality and amount, the FRP's orientation and distribution, and the interaction between internal steel bars and FRPs [74]. The inclined wrapping system was shown to be the most effective strategy for increasing the shear capacity of all wrapping systems investigated. According to Singh et al. [75], wrapping a concrete beam with a 45° angled CFRP sheet, and bidirectional CFRP sheets increased the load capacity against shear force by 11.9% and 7.7%, respectively. In addition, in 2013, Hussein et al. [76] achieved a 57% improvement in the load-bearing capacity by strengthening a damaged beam with a U-wound CFRP system along with the external prestressed force in this study.

In addition, Chen and Li [45] conducted experiments on slab-column connections with relatively low and medium reinforcement ratios (0.31% and 0.62%, respectively) to investigate the effect of glass fiber reinforced strengthening on punching shear strength. The results showed that the FRP strengthening attachment to the slab's tension surface increases the bending strength of the slab-column connection considerably. However, after the shear strength was increased to the point where the bending shear strength of the plate was less than the ultimate shear strength, increasing the FRP strengthening area did not significantly improve the shear strength or stiffness of the plate. Harajli et al. [77] conducted experiments using sixteen samples with different plate depths and reinforcement ratios. The same carbon FRP configuration was tested using FRPs with different widths. The results showed that using CFRP significantly increased the sheets' bending stiffness and

punching strength. It is also stated that the increase in the two-way shear force can be between 17–45%, depending on the area, the thickness of the applied CFRP sheets, and the reinforcement ratio of the slab. Esfahani et al. [48] experimented with eleven slab-column systems with two different reinforcement ratios (0.84% and 1.59%) with CFRP sheets with different widths (100–300 mm). The results showed that the punching shear strength of the floors was improved when using CFRP sheets in addition to steel reinforcement bars. It is stated that this application is more effective in slabs consisting of high-strength concrete with a low steel reinforcement ratio.

Farghaly et al. [78] conducted experiments using three flat slab-column connection specimens. Carbon FRP sheets of two different widths are bonded to the tension face of the slab in two perpendicular directions parallel to the internal reinforcement. In order to prevent FRP from debonding, CFRP sheets were applied in a single layer and extended from one end of the slab to the other. Experimental results have shown that the stiffness and punching shear strength of sheets are improved using FRP. In addition, the behavior of externally connected slab-column connections strengthened with different CFRP arrangements was investigated by Silva et al. [79].

In some cases, anchoring was used at the end of the FRP. The results showed that skewed placement of CFRP is more effective than orthogonal configurations. It has been shown that the appropriate strengthening arrangement makes it possible to increase the punching capacity for slab-column connections by 46%. In addition, FRP debonding without end anchors was also observed, while anchored samples did not have the same premature failure, indicating the failure can be prevented by end anchors.

Kim et al. [80] studied the effectiveness of prestressed and non-prestressed externally bonded FRP strengthening on the punching shear of slab-column connections. A total of four different samples were used in this study. While one Sample was left non-strengthened, the other was strengthened with non-prestressed externally bonded FRP, and the other two were strengthened by adding different prestresses. It was found that the prestressed FRP sheets did not significantly improve the system at the punching shear. Abdullah et al. [81] studied the effectiveness of prestressed externally bonded FRP strengthening on the punching shear in flat slab-interior column connections. This study was then re-evaluated by Abdullah and Bailey [82]. In the study, five slabs with dimensions of 1800×1800×150 mm and columns with dimensions of 250×250×150 mm were used. While one Sample was not strengthened, one other was left without prestress, and the remaining three were strengthened using prestress. The study suggests that prestressed externally applied FRP strengthening reduces crack openings, while its effect on the ultimate load was not as significant as in the case of the non-prestressed externally applied FRP strengthening.

4.1.5. Environmental Performance of FRP Applications

The life cycle assessment (LCA) technique, widely used and accepted, is also utilized to measure the environmental impact of the activities of the construction industry in general. Maxineasa et al. [66] used LCA to compare the environmental impact of strengthening an existing reinforced concrete beam with FRP with the environmental impact of building a new reinforced concrete beam. The research includes FRP strengthening techniques such as externally bonded (EB) FRP and near-surface mounted (NSM) techniques. This study considered global warming, human toxicity, and ozone depletion. The results showed that building a new beam has the highest adverse environmental impact. According to the results, the most environmentally friendly solution is the application of the CFRP strip, which is glued on a cross-section of 1.4×36 mm and a length of 2600 mm to the lower base of the beam.

The total CO_2 emissions of the strengthening process are 69% lower than those from the Construction of a new reinforced concrete beam. It has also been stated that the near-surface mounted technique increases the load capacity the most, which could go up to a 207% increase (from 60KN to 184KN). It has also been noted that strengthening the existing beam instead of building a new beam reduces human toxicity by 73% and the effect of ozone depletion by 48%. The parameters of ozone depletion and human toxicity are highly related to the production process of materials. The amount of cement and rebar production required to build a new beam is much more than the amount of FRP required to strengthen the existing beam. Therefore, when the existing beam is strengthened instead of building a new beam, the damage caused to the thinning of the ozone layer and human health is reduced. Palacios-Munoz et al. [83] research findings align with the study by Maxinease et al. [66]. Palacios-Munoz et al. [83] conducted a LCA on the environmental impacts of strengthening an existing beam with CFRP or steel plates and demolishing and rebuilding the existing beam. The results showed that the demolition and reconstruction of the existing beam caused two times higher CO_2 emissions than strengthening the existing beam with CFRP. In addition, it has been determined that demolishing the existing beam and building a new one will increase energy consumption by up to 60%.

Vitiello et al. [84] conducted a LCA on a building located in Naples. The building was constructed in the 70s using old standards and without considering the area's seismic conditions. In this case study, four different strengthening techniques were used. The first strengthening technique was EB FRPs to prevent brittle failure, the second technique was concrete coating to increase the bending and shear capacity, the third technique was adding two shear walls to enhance the building against seismic movements, and the fourth one was to integrate a horizontally flexible and dissipative interface on the building's first floor to minimize

demand rather than increase structural capacity. The results showed that FRP sheets and concrete coating have almost the same effect on human health, while shear wall strengthening significantly affects human health.

Moreover, considering the effects on ecosystem quality and climate change, it has been observed that FRP sheets have a less negative impact than the shear wall and concrete coating techniques. Maxineasa et al. [12] evaluated strengthening methods by conducting experiments on six beams. While one beam remains as a control specimen, two beams strengthened with different sizes (1.4×36×2600 mm and 1.4×72×2600 mm) of EB CFRP; the other three beams strengthened with different sizes (1.4×18×2600, 1.4×12×2600 1.4×24×2600 mm) of CFRP using the near-surface mounting technique. The results showed that the near-surface mounting technique could increase the load capacity up to three times that of the control specimen and is the best strengthening method in this sense. In addition, it was concluded in the study that strengthening the existing beam in place of rebuilding could reduce the effect of ozone depletion by 87.5%.

Moreover, all other cases compared to building a new beam achieved approximately 74% reduction of CO_2 emission. Shi et al. [85] studied a supported reinforced concrete beam as a case study. The concrete beam represents the beam on a bridge spanning 20 meters. CFRP fabrics and CFRP plates were used as strengthening materials. The results showed that the environmental effects of the CFRP fabric strengthening technique are greater than those of CFRP plates. CFRP fabric strengthening materials have consumed more CFRP materials and epoxy resin adhesives, resulting in increased environmental effects. In addition, the environmental impact of CFRP plates is also considerably less, mainly when the maintenance during the service life is considered.

4.1.6. The Environmental Evaluations of the FRP Utilization

This section addresses the environmental evaluations of FRP utilization as a strengthening material. Carbon and glass FRPs, the most commonly used strengthening materials, are chosen for this evaluation. Structural performance is often plotted versus an environmental parameter to provide insight into implementing such materials in a more holistic approach.

Figure 1 demonstrates the elastic modulus and energy input of carbon and glass FRPs. The elastic modulus of glass FRP is between 35–51 GPa, while this value ranges from 120 to 500 GPa for carbon FRPs [21]. As the resistance of a material to elastic deformation, when subjected to stress, is governed by its elastic modulus, the carbon FRP offers a higher deformation capacity than the glass FRP and has superior structural properties over glass FRP. On the other hand, it must be emphasized that glass FRP consumes much lower energy than carbon FRP during the production stage, which comprises raw material extraction and manufacturing of FRP. The low energy consumption of glass FRP indicates these materials' sustainable and environmental advances over carbon FRP. The energy required to extract one kilogram of glass FRP as raw material along its complete production process is approximately 20 M.J., while the same process necessitates about 200 MJ for carbon FRP. The studies by Dong et al. [86] and Zhang et al. [87], published in the literature, agree greatly with the findings in Figure 1.

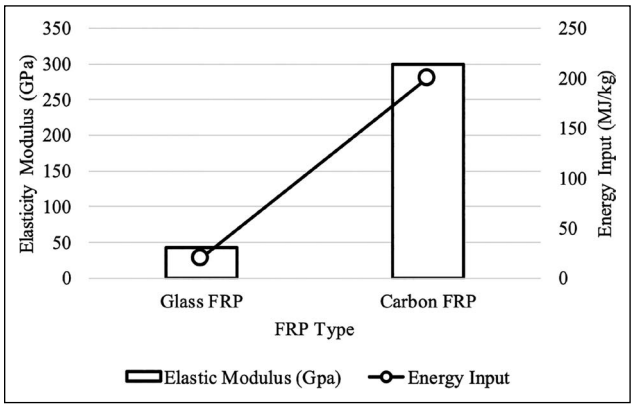

Figure 1. Average elastic modulus versus energy input of carbon and glass FRPs [18, 21].

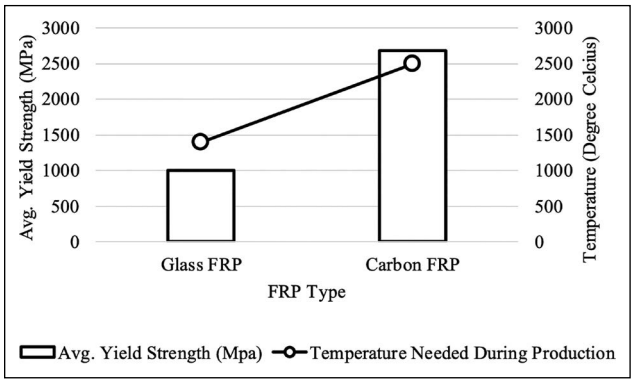

Figure 2. Average yield strength versus temperature needed during the production of carbon and glass FRPs [21, 57].

Figure 2 exhibits the average yield strength and temperature required while producing carbon and glass FRPs. The average yield strength of carbon FRP is around 2700 MPa, while the average yield strength of glass FRP is around 1000 MPa. Yield strength is an essential parameter in evaluating structural performance, as it is the stress point at which materials begin to deform permanently. The required temperature for production is closely associated with environmental sustainability, mainly due to fossil fuel consumption during this process [88]. The increase in the temperature required for the production also necessitates higher energy consumption that implicates higher fossil fuels consumptions for this phase. The maximum temperature required for producing glass FRPs is around 1400 °C, which is around 2500 °C for carbon FRPs [57]. The results

Table 2. Classification system for distribution of V_{test}/V_{pred}

Vtest/Vpred	Classification
<0.5	Extremely dangerous
0.5–0.65	Dangerous
0.65–0.85	Low safety
0.85–1.30	Appropriate safety
1.30–2.00	Conservative
>2.00	Extremely conservative

Table 3. Comparison of prediction by TS500 [38] and TS500 modified by Chen and Li [45] code equations

Code	TS500 [38]	TS500 modified by Chen and Li [45]
Mean	1.61	1.42
SD	0.377	0.346
COV	0.23	0.24

SD: Standard deviation; COV: Coefficient of variation.

shown in Figure 2 indicate that although carbon FRPs have structurally superior properties, glass FRPs have more outstanding environmental advances. The studies by Sen et al. [89], and Preinstorfer et al. [90], published in the literature, agree greatly with the findings in Figure 2.

Figure 3 demonstrates the cost efficiency and the cost of glass and carbon FRPs. In addition to structural and environmental factors, the cost of materials is also a decisive factor that is taken into account before implementation. The unit price of glass FRPs is approximately 5.5$, while the price of one kilogram of carbon FRPs is about 38$ [91]. Despite their structurally superior properties, carbon FRPs are about seven times more expensive than thass FRPs, which at first sight could restrict the frequency of use of carbon FRP. Cost efficiency incorporates the FRP implementation's cost and structural aspects. It, therefore, provides a more holistic approach to evaluating the authentic performance of such utilization cost efficiency, demonstrated in Figure 3, which is determined by dividing the average yield strength by the unit price of the material. The cost efficiency value of glass fiber reinforced polymers is 182MPa/kg, while the cost efficiency of carbon fiber reinforced polymers is around 70.5MPa/kg. These results indicate that the cost efficiency of glass FRPs is nearly two and a half times higher than the cost efficiency of carbon FRPs.

4.2. The Evaluation of the TS 500 Code Equation

This section evaluates the TS 500 code equation in predicting the punching shear strength of flat slab-column connections strengthened with FRP laminates. The selected database is used to conduct the Ratio of the measured ultimate punching shear strength, $V_{u,\,test}$, to the calculated value from TS 500 Code Equation, $V_{u,\,pred}$. This is then utilized to compare and nominate the safety factor, γ. The safety factor, γ, is provided in Eq. (8).

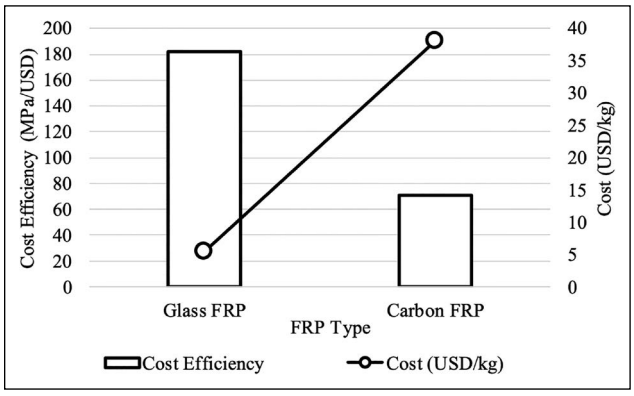

Figure 3. Cost efficiency versus the cost of carbon and glass FRPs [21, 91].

$$\gamma = \frac{V_{u,test}}{V_{u,pred}} \qquad \text{Eq. 8}$$

A given test's predicted value is considered conservative when γ>1. The material properties introduced in the formula were the average values obtained from the test reports.

It should be noted that all strength reduction factors, and material strength reduction factors are equal to unity when assessing the performance of the code equations in predicting the experimental results. Mean, Standard Deviation (SD), and coefficient of variation (COV) of the strength ratio V_{test}/V_{pred} are used to examine the performance of the code provisions. In addition, the classification system proposed by Collins [92] is used to assess the distribution of V_{test}/V_{pred}, summarised in Table 2.

4.2.1. Evaluation of the Performance of TS 500 Code and Modified TS 500 Code Provisions

Table 3 shows the means, standard deviation (S.D.), and coefficient of variation (COV) for the Ratio V_{test}=V_{pred} for the code provisions examined in this study.

TS 500 [38] performed more conservative predictions than the TS 500 modified by Chen and Li [45], as the modifications considered the effect of the FRP contribution on the strength of slab-column connections subjected to FRP strengthening. When the TS 500 [38] code provision is computed, it was determined that 72% of the data had γ>1.4, while with TS 500 [38] modified by Chen and Li [45], this is reduced to 54%. 15% of the predictions are categorized as highly conservative for TS 500, while this value is reduced to 6% with TS 500 modifications. It is well recognized that TS 500 [38] is not taking the reinforcement ratio and size effect into account, leading to conservative predictions resulting in a mean value of 1.61, a standard deviation of 0.377, and a covariance of 0.23. However, the modifications provided by Chen and Li [45] include the contribution of FRP that yields a substantial improvement on the aforementioned parameters and therefore results in considerably improved predictions.

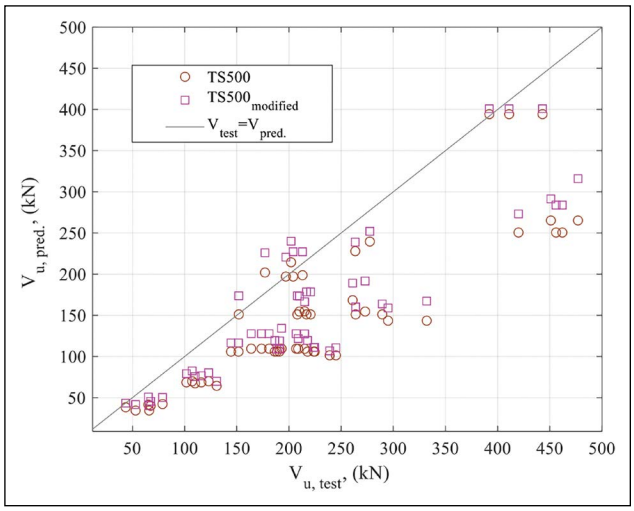

Figure 4. Comparison of predictions of TS 500 and TS 500 modified with the experimental test results .

4.2.2 Comparisons with the TS 500 Design Equation

Figure 4 demonstrates the predictions of punching shear strength of slab-column connections strengthened with FRP using TS 500 [38] and T.S. 500-modified with the experimental results harvested for the paper using the V_u, pred data plotted versus the V_u, test. It is eminently demonstrated in Figure 4 that the predictions show a large scatter for both models. Predictions by T.S. 500-modified lead to less conservative results, mainly as a result of the inclusion of the FRP in computing the strength of such connections.

The safety factor, γ, is plotted versus concrete compressive strength in Figure 5. It must be underlined that the concrete compressive strength is the only parameter considered in TS500 [38]. According to the distribution of the test data shown in Figure 5-a, the TS-500 [38] code equation appears conservative when the concrete compressive strength is less than 30 MPa. It is shown that when the concrete compressive strength is between 30 and 35 MPa, TS 500 [38] code equation provides approximately safe predictions. It was evident that the modified equation of TS 500 that adopted the equivalent adequate depth (proposed by Chen and Li [45]) in the code equation leads to less conservative predictions for all ranges of concrete compressive strength in this study.

The safety factor, γ, is plotted versus the flexural reinforcement ratio $\rho=As/bd$ in Figure 6. It must be noted that the flexural reinforcement ratio is not considered in TS500 [38]. Results shown in Figure 6 indicate that the safety factor is increasing with the increase in flexural reinforcement ratio. It can be seen in Figure 6 that the overall safety of TS-500 for slabs with ρ_{flex}<0.8% is 1.25, which is categorized as approximately safe, while for slabs with ρ_{flex}>0.8% is 1.69, which makes conservative predictions. The results in Figure 6 demonstrate that the safety factors increase gradually with the increase in reinforcement ratios, which validates the pronounced influence of the reinforcement ratio on the punching shear strength of slabs without shear reinforcement. Figure 6-b shows that the mean value of the safety factor for the modified version of TS 500 on predicting the punching shear strength of

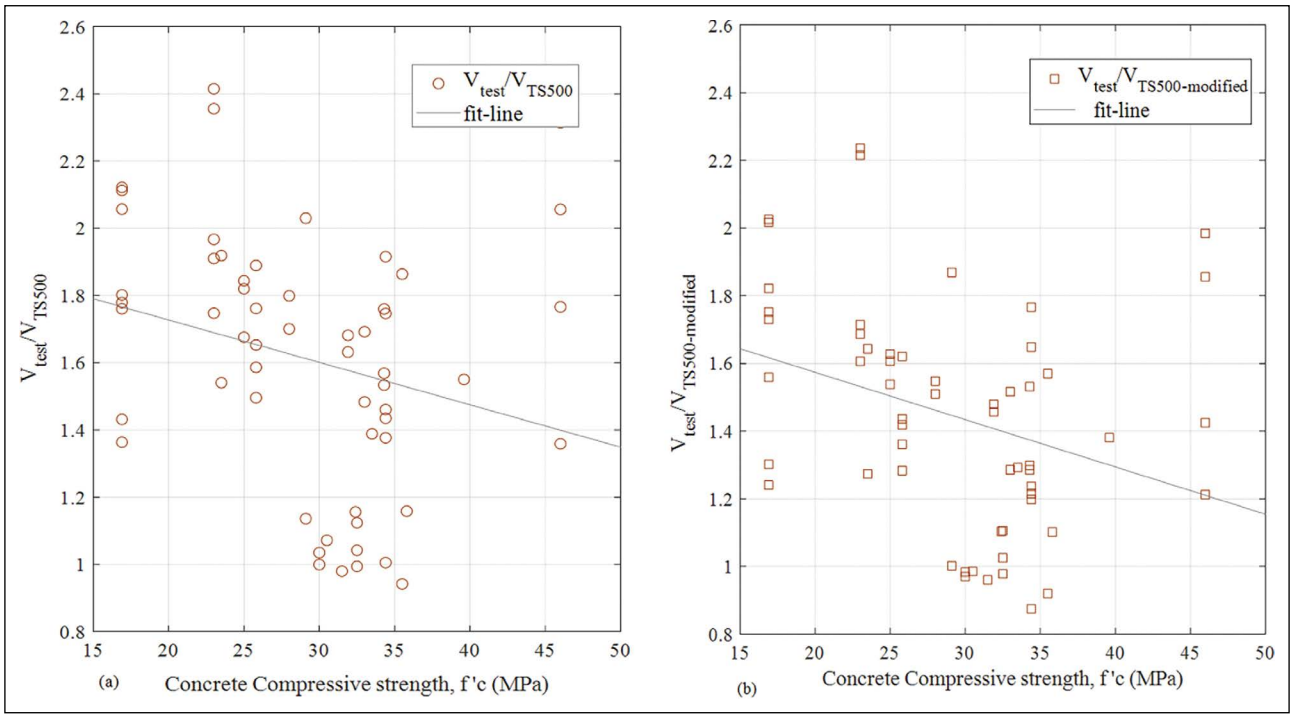

Figure 5. Safety factor $\gamma=V_{u,test}/V_{u,cal}$ for TS500 plotted versus concrete compressive strength.

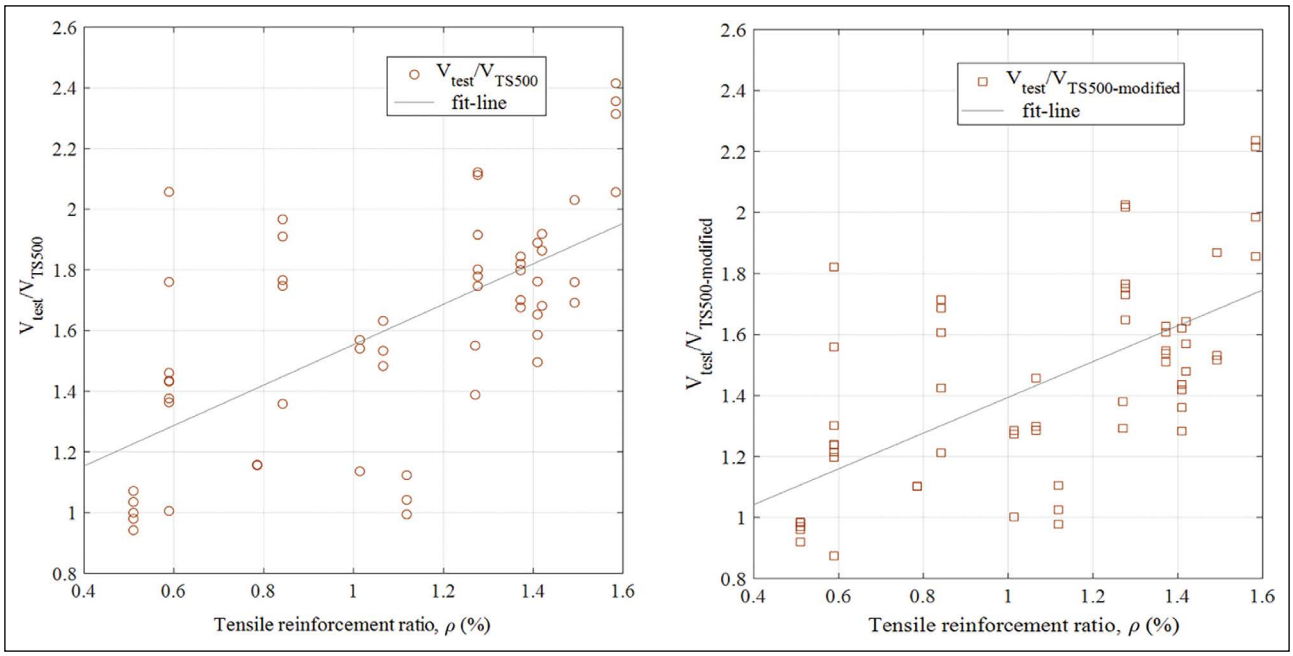

Figure 6. Safety factor $\gamma=V_{u,\,test}/V_{u,\,cal}$ for TS500 plotted versus Tensile Reinforcement ratio.

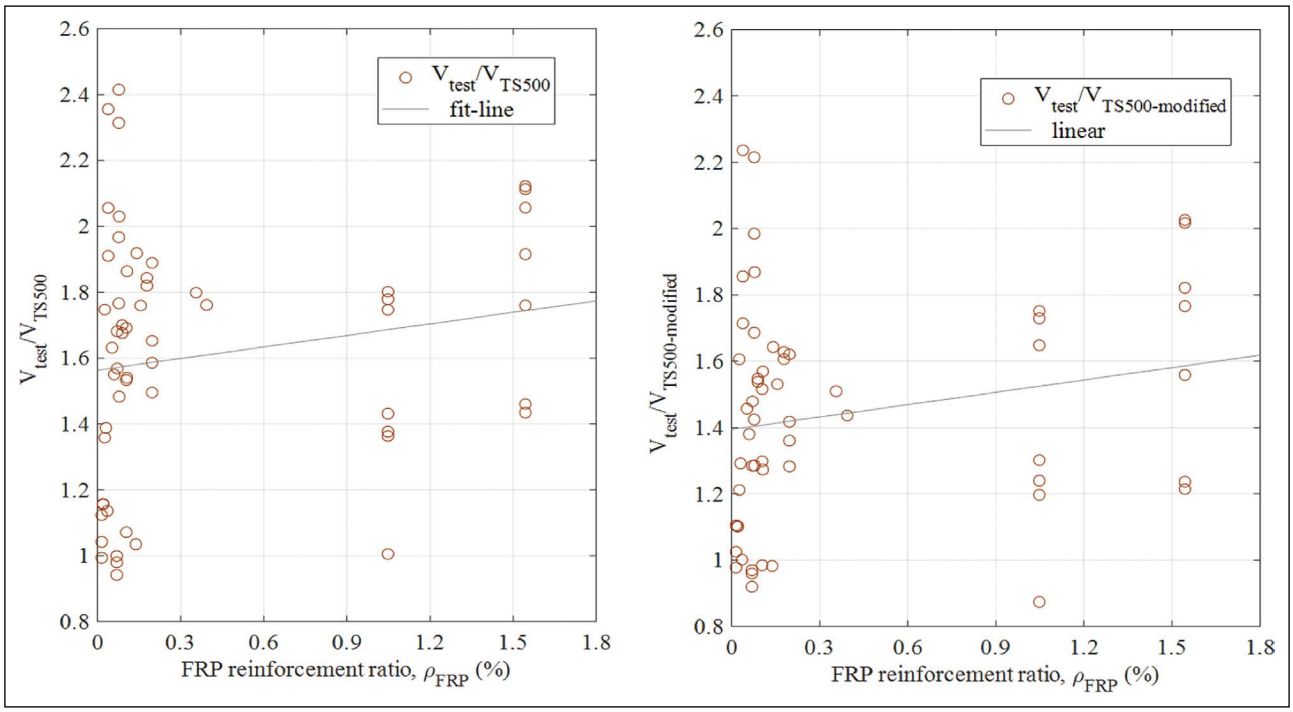

Figure 7. Safety factor $\gamma=V_{u,\,test}/V_{u,\,cal}$ for TS500 plotted versus concrete compressive strength.

such connections with ρf_{lex}<0.8% is 1.12 and for slabs with ρ_{flex}>0.8% is 1.51. This implies that the modified TS500 equation leads to less conservative predictions.

The safety factor, γ, is plotted versus the FRP reinforcement ratio $\rho_{FRP}=A_{FRP}/bd$ in Figure 7. It must be noted that TS500 does not include the contribution of FRP laminates in increasing the punching shear strength of such connections. The flexural reinforcement ratio is not a parameter in TS500. Results shown in Figure 7 indicate that the safety factor is increasing with the increase in FRP reinforcement ratio. It can be seen in Figure 7 that the overall best-fit line safety of TS 500 for all types of slabs is categorized as conservative for both TS500 and T.S. 500-Modified.

5. CONCLUSION

The paper reports a comprehensive review of the FRPs utilization on strengthening, particularly over the traditional materials formerly used in practice with respect to materials, manufacturing, operation, Construction, and maintenance phases as the engineering and environmental performance of such materials. The results provided in the paper suggest that carbon FRP requires a higher temperature during manufacturing, resulting in a higher energy input than the glass FRP. Although its superior structural properties, such as higher elastic modulus and higher yield strength, carbon FRP has lower cost efficiency as a result of the higher cost of production. Glass FRP, on the other hand, has weaker structural properties, lower environmental impact, and cheaper production costs compared to that of the carbon FRP. The results are paramount as they offer a comprehensive review of the structural performance of such materials by considering the environmental and sustainable implications.

The paper also investigates the punching shear strength of flat slab-column connections strengthened with EB FRP using a nominated database comprising 57 data points harvested from the recent literature. The database is used to evaluate the test data with TS 500 code equations and the recent modification of Chen and Li. The results have shown that TS 500 code equation does not consider the contribution of flexural reinforcement and size effect in the calculation of punching shear strength of slab-column connections; moreover, the code does not include the contribution of FRP laminates in enhancing the strength of such connections. The results have also shown that TS 500 often provides conservative predictions for the cases examined in the paper. However, the modifications by Chen and Li that replace adequate depth with the equivalent effective depth improve the strength predictions of such connections and hence result in less conservative approximations.

The study is novel as it provides a comprehensive review of the FRP as a strengthening material regarding environmental sustainability and provides insight into the structural implications of this material by evaluating the current TS 500 code provisions and recent modifications. The authors encourage the researchers to conduct further studies in this context to suggest modifications to improve further the TS 500 code equation in predicting the punching shear strength of flat slab-column connections.

ETHICS

There are no ethical issues with the publication of this manuscript.

DATA AVAILABILITY STATEMENT

The authors confirm that the data that supports the findings of this study are available within the article. Raw data that support the finding of this study are available from the corresponding author, upon reasonable request.

CONFLICT OF INTEREST

The authors declare that they have no conflict of interest.

FINANCIAL DISCLOSURE

The authors declared that this study has received no financial support.

PEER-REVIEW

Externally peer-reviewed.

REFERENCES

[1] Ersoy U., & Tankut T. (1992). Current research at METU on repair and strengthening of R/C structures. *Technical University of Istanbul Bulletin*, 45(1-3), 209–240.

[2] Banu, D., & Taranu, N. (2010). Traditional solutions for strengthening reinforced concrete slabs. *Bulletin of the Polytechnic Institute of Jassy*, 3(3), 54–62.

[3] Yooprasertchai, E., Piamkulvanit, M., Srithong, C., Sukcharoen, T., & Sahamitmongkol, R. (2022). A comparison of punching shear strengthening of RC flat plates with FRP bars and steel bolts. *Case Studies in Construction Materials*, 16, Article e00828. [CrossRef]

[4] Saadatmanesh, H. (1997). Extending service life of concrete and masonry structures with fiber composites. *Construction and Building Materials*, 11(5-6), 327–335. [CrossRef]

[5] Gkournelos, P. D., Triantafillou, T. C., & Bournas, D. A. (2021). Seismic upgrading of existing reinforced concrete buildings: A state-of-the-art review. *Engineering Structures*, 240, Article 112273. [CrossRef]

[6] Heiza, K., Nabil, A., Meleka, N., & Tayel, M. (2014). State-of-the art review: Strengthening of reinforced concrete structures–different strengthening techniques. *In Sixth International Conference on Na-no-Technology in Construction*, 6, 12–24.

[7] Naser, M. Z., Hawileh, R. A., & Abdalla, J. A. (2019). Fiber-reinforced polymer composites in strengthening reinforced concrete structures: A critical review. *Engineering Structures*, 198, Article 109542. [CrossRef]

[8] Yuhazri, M. Y., Zulfikar, A. J., & Ginting, A. (2020). Fiber reinforced polymer composite as a strengthening of concrete structures: A Review. *IOP Conference Series: Materials Science and Engineering 2nd International Conference on Industrial and Manufacturing Engineering (ICIE&ME 2020)*, 1003(1), Article 012135. [CrossRef]

[9] Zaman, A., Gutub, S. A., & Wafa, M. A. (2013). A review on FRP composites applications and durability concerns in the construction sector. *Journal of Reinforced Plastics and Composites*, 32(24), 1966–1988. [CrossRef]

[10] Ali, M. B., Saidur, R., & Hossain, M. S. (2011). A review on emission analysis in cement industries. *Renewable and Sustainable Energy Reviews*, 15(5), 2252–2261. [CrossRef]

[11] Rahman, A., Rasul, M. G., Khan, M. M. K., & Sharma, S. (2015). Recent development on the uses of alternative fuels in cement manufacturing process. *Fuel*, 145, 84–99. [CrossRef]

[12] Maxineasa, S. G., & Taranu, N. (2018). Life cycle analysis of strengthening concrete beams with FRP. In F. Pacheco-Torgal, R. E. Melchers, X. Shi, N. De Belie, K. V. Tittelboom, & A. Sáez (Eds.), *Eco-efficient repair and rehabilitation of concrete infrastructures* (pp. 673–721). Woodhead Publishing. [CrossRef]

[13] Moynihan, M. C., & Allwood, J. M. (2012). The flow of steel into the construction sector. *Resources, Conservation and Recycling*, 68, 88–95. [CrossRef]

[14] Baena-Moreno, F. M., Cid-Castillo, N., Arellano-García, H., & Reina, T. R. (2021). Towards emission free steel manufacturing – exploring the advantages of a CO_2 methanation unit to minimize CO_2 emissions. *Science of The Total Environment*, 781, Article 146776. [CrossRef]

[15] Lee, L. S., & Jain, R. (2009). The role of FRP composites in a sustainable world. *Clean Technologies and Environmental Policy*, 11(3), 247–249. [CrossRef]

[16] Siddika, A., Mamun, M. A. A., Ferdous, W., & Alyousef, R. (2020). Performances, challenges and opportunities in strengthening reinforced concrete structures by using FRPs – A state-of-the-art review. *Engineering Failure Analysis*, 111, Article 104480. [CrossRef]

[17] Daniel, R. A. (2010). A composite bridge is favoured by quantifying ecological impact. *Structural Engineering International*, 20(4), 385–391. [CrossRef]

[18] Belarbi, A., Dawood, M., & Acun, B. (2016). Sustainability of fiber-reinforced polymers (FRPs) as a construction material. In J. M. Khatib (Ed.), *Sustainability of construction materials* (2nd ed., pp. 521–538). Woodhead Publishing. [CrossRef]

[19] Thacker, M. H., & Vora, T. P. (2015). State-of-the-art review of FRP strengthened RC slabs. *International Journal for Scientific Research & Development*, 3(10), 78–85.

[20] Mara, V., Haghani, R., & Harryson, P. (2014). Bridge decks of fibre reinforced polymer (FRP): A sustainable solution. *Construction and Building Materials*, 50, 190–199. [CrossRef]

[21] Mugahed Amran, Y. H., Alyousef, R., Rashid, R. S. M., Alabduljabbar, H., & Hung, C. C. (2018). Properties and applications of FRP in strengthening RC structures: A review. *Structures*, 16, 208–238. [CrossRef]

[22] Smith, S. T., & Teng, J. G. (2002). FRP-strengthened RC beams. I: review of debonding strength models. *Engineering Structures*, 24, 385–395. [CrossRef]

[23] Al-Salloum, Y. A., & Almusallam, T. H. (2002). Rehabilitation of the infrastructure using composite materials: Overview and applications. *Journal of King Saud University - Engineering Sciences*, 16(1), 1–21. [CrossRef]

[24] Zhou, A., Qin, R., Chow, C. L., & Lau, D. (2019). Structural performance of FRP confined seawater concrete columns under chloride environment. *Composite Structures*, 216, 12–19. [CrossRef]

[25] Binici, B., & Bayrak, O. (2003). Punching shear strengthening of reinforced concrete flat plates using carbon fiber reinforced polymers. *Journal of Structural Engineering*, 129(9), 1173–1182. [CrossRef]

[26] Durucan, C., & Anil, O. (2015). Effect of opening size and location on the punching shear behavior of interior slab–column connections strengthened with CFRP STRIPS. *Engineering Structures*, 105, 22–36. [CrossRef]

[27] Derogar, S., Ince, C., & Mandal, P. (2018). Development and evaluation of punching shear database for flat slab-column connections without shear reinforcement. *Structural Engineering and Mechanics*, 66(2), 203–215.

[28] Abdulrahman, B. Q., & Aziz, O. Q. (2021). Strengthening RC flat slab-column connections with FRP composites: A review and comparative study. *Journal of King Saud University - Engineering Sciences*, 33(7), 471–481. [CrossRef]

[29] Derogar, S., Ince, C., Yatbaz, H. Y., & Ever, E. (2022). Prediction of punching shear strength of slab-column connections: A comprehensive evaluation of machine learning and deep learning based approaches. *Mechanics of Advanced Materials and Structures*, 1–19. [CrossRef]

[30] Saleh, H., Kalfat, R., Abdouka, K., & Al-Mahaidi, R. (2018). Experimental and numerical study into the punching shear strengthening of RC flat slabs using post-installed steel bolts. *Construction and Building Materials*, 188, 28–39. [CrossRef]

[31] Georgewill, V. A., Ngekpe, B. E., Akobo, I. Z. S., & Jaja, G. W. T. (2019). Punching shear failure of reinforced concrete flat slab system- A review. *European Journal of Advances in Engineering and Technology*, 6(2), 10–16.

[32] Wittocx, L., Buyle, M., Audenaert, A., Seuntjens, O., Renne, N., & Craeye, B. (2022). Revamping corrosion damaged reinforced concrete balconies: Life cycle assessment and life cycle cost of life-extending repair methods. *Journal of Building Engineering*, 52, Article 104436. [CrossRef]

[33] Talentino, A. K. (2004). The two faces of nation-building: Developing function and identity. *Cambridge Review of International Affairs*, 17(3), 557–575. [CrossRef]

[34] Kamis, H. E. H. (2012). *Three dimensional analysis of fibre reinforced polymer laminated composites* [Unpublished doctoral dissertation]. University of Manchester.

[35] Qian, K., & Li, B. (2013). Strengthening and retrofitting of RC flat slabs to mitigate progressive collapse by externally bonded CFRP laminates. *Journal of Composites for Construction*, 17(4), 554–565. [CrossRef]

[36] Saleh, H., Kalfat, R., Abdouka, K., & Al-Mahaidi, R. (2019). Punching shear strengthening of RC slabs using L-CFRP laminates. *Engineering Structures*, 194, 274–289. [CrossRef]

[37] Fayyadh, M. M., & Razak, H. A. (2021). Externally bonded FRP applications in RC structures: A state-of-the-art review. *Jordan Journal of Civil Engineering*, 15(2), 157–179.

[38] Standard, T. (2000). Requirements for Design and Construction of reinforced concrete structures (TS 500). *Institute of Turkish Standard (TSE), Ankara, Turkey*.

[39] Davvari, M. (2018). *Structural analysis of strengthened RC slabs* [Unpublished doctoral dissertation]. University of Manchester.

[40] Sharaf, M. H., Soudki, K. A., & Van Dusen, M. (2006). CFRP strengthening for punching shear of interior slab–column connections. *Journal of Composites for Construction*, 10(5), 410–418. [CrossRef]

[41] Malalanayake, M. L. V. P., Gamage, J. C. P. H., & Silva, M. A. L. (2017). Experimental Investigation on Enhancing Punching Shear Capacity of Flat Slabs Using CFRP. *8th International Conference on Structural Engineering and Construction Management*. Kandy, Sri Lanka.

[42] Moreno, C., Ferreira, D., Bennani, A., & Noverraz, M. (2015). Punching shear strengthening of flat slabs: cfrp and shear reinforcement. In H. Stang, M. Braestrup (Eds.), *Concrete-Innovation and Design, Fib Symposium Proceedings*.

[43] Saadoon, A. M., Mashrei, M. A., & Al Oumari, K. A. (2022). Punching shear strength of recycled aggregate-steel fibrous concrete slabs with and without strengthening. *Advances in Structural Engineering*, 25(10), 2175–2190. [CrossRef]

[44] Mohamed, O. A., Kewalramani, M., & Khattab, R. (2020). Fiber reinforced polymer laminates for strengthening of RC slabs against punching shear: A review. *Polymers*, 12(3), Article 685. [CrossRef]

[45] Chen, C.C., & Li, C.Y. (2005). Punching shear strength of reinforced concrete slabs strengthened with glass fiber-reinforced polymer laminates. *ACI Structural Journal*, 102(4), 535–542. [CrossRef]

[46] American Concrete Institute Committee. (2019). ACI CODE-318-19: *Building code requirements for structural concrete and commentary*. American Concrete Institute, Michigan.

[47] Pani, L., & Stochino, F. (2020). Punching of reinforced concrete slab without shear reinforcement: Standard models and new proposal. *Frontiers of Structural and Civil Engineering*, 14(5), 1196–1214. [CrossRef]

[48] Esfahani, M. R., Kianoush, M. R., & Moradi, A. R. (2009). Punching shear strength of interior slab–column connections strengthened with carbon fiber reinforced polymer sheets. *Engineering Structures*, 31(7), 1535–1542. [CrossRef]

[49] Torabian, A., Isufi, B., Mostofinejad, D., & Pinho Ramos, A. (2020). Shear and flexural strengthening of deficient flat slabs with post-installed bolts and-cfrpcomposites bonded through EBR and EBROG. *Structural Concrete*, 22(2), 1147–1164. [CrossRef]

[50] Abdulrahman, B. (2019). *Strengthening flat slabs at corner columns against punching shear using fibre reinforcing polymer* (FRB) [Unpublished doctoral dissertation]. University of Manchester.

[51] ACI Standart. *Building code requirements for structural concrete (ACI. (2014). 318-14) and commentary (ACI 318R-14)*. Farmington Hills MI: American Concrete Institute.

[52] Rizkalla, S., Hassan, T., & Hassan, N. (2003). Design recommendations for the use of FRP for reinforcement and strengthening of concrete structures. *Progress in Structural Engineering and Materials*, 5(1), 16–28. [CrossRef]

[53] Hu, W., Li, Y., & Yuan, H. (2020). Review of experimental studies on application of FRP for strengthening of bridge structures. *Advances in Materials Science and Engineering*, 6, 1–21. [CrossRef]

[54] Soudki, K., El-Sayed, A. K., & Vanzwol, T. (2012). Strengthening of concrete slab-column connections using CFRP strips. *Journal of King Saud University - Engineering Sciences*, 24(1), 25–33. [CrossRef]

[55] Silva, M. A. L., Dedigamuwa, K. V., & Gamage, J. C. P. H. (2021). Performance of severely damaged reinforced concrete flat slab-column connections strengthened with carbon fiber. *Composite Structures*, 255, Article 112963. [CrossRef]

[56] Sanginabadi, K., Yazdani, A., Mostofinejad, D., & Czaderski, C. (2022). RC members externally strengthened with FRP composites by grooving methods including EBROG and EBRIG: A state-of-the-art review. *Construction and Building Materials*, 324, Article 126662. [CrossRef]

[57] Hollaway, L. C. (2011). Key issues in the use of fibre reinforced polymer (FRP) composites in the rehabilitation and retrofitting of concrete structures. In V. M. Karbhari, L. S. Lee (Eds.), Service Life Estimation and Extension of Civil *Engineering Structures* (pp. 3–74). Woodhead Publishing. [CrossRef]

[58] Qureshi, J. (2022). A review of fibre reinforced polymer structures. *Fibers*, 10(3), Article 27. [CrossRef]

[59] Lukkasse, D., & Meidell, A. (2007). Composites. *Advanced Materials and Structures and their Fabrication Processes* (pp. 55–81). Narvik University College.

[60] Bakis, C. E. (2009). Life cycle analysis issues in the use of FRP composites in civil infrastructure. *Proceedings of US-Japan Workshop on Life Cycle Assessment of Sustainable Infrastructure Materials*.

[61] Lee, L. S. (2011). Rehabilitation and service life estimation of bridge superstructures. In V. M. Karbhari, L.S. Lee (Eds.), *Service Life Estimation and Extension of Civil Engineering Structures* (pp. 117–142). Woodhead Publishing. [CrossRef]

[62] Barbero, E. J. (2010). *Introduction to composite materials design book* (2nd ed.). CRC Press. [CrossRef]

[63] Garg, N., & Shrivastava, S. (2019). Environmental and economical comparison of FRP reinforcements and steel reinforcements in concrete beams based on design strength parameter. *Proceedings of the UKIERI Concrete Congress, Jalandhar, India, 5–8 March 2019*; Dr B R Ambedkar National Institute of Technology: Jalandhar, India, 2019.

[64] Inman, M., Thorhallsson, E. R., & Azrague, K. (2017). A mechanical and environmental assessment and comparison of basalt fibre reinforced polymer (BFRP) rebar and steel rebar in concrete beams. *Energy Procedia*, 111, 31–40. [CrossRef]

[65] Ibrahim, M., Ebead, U., & Al-Ansari, M. (2020). Life Cycle Assessment for Fiber-reinforced polymer (FRP) composites used in concrete beams: A state-of-the-art review. In O. Sirin, U. Ebead, M. Gunduz, & M. Hussein (Eds.), *Proceedings of the international conference on civil infrastructure and construction (CIC 2020)*. (pp. 777–784). Qatar University Press. [CrossRef]

[66] Maxineasa, S. G., Taranu, N., Bejan, L., Isopescu, D., & Banu, O. M. (2015). Environmental impact of carbon fibre-reinforced polymer flexural strengthening solutions of reinforced concrete beams. *The International Journal of Life Cycle Assessment*, 20(10), 1343–1358. [CrossRef]

[67] Gunaslan, S. E., Karasin, A., & Oncu, M. E. (2014). Properties of FRP materials for strengthening. *International Journal of Innovative Science*, 1(9), 656–660.

[68] Lau, D., Qiu, Q., Zhou, A., & Chow, C. L. (2016). Long term performance and fire safety aspect of FRP composites used in building structures. *Construction and Building Materials*, 126, 573–585. [CrossRef]

[69] Chellapandian, M., & Suriya Prakash, S. (2018). Behavior of FRP-strengthened reinforced concrete columns under pure compression—experimental and numerical studies. In A. R. M. & Rao, K. Ramanjaneyulu (Eds.), *Lecture Notes in Civil Engineering Select Proceedings of SEC 2016* (pp. 663–673). Springer. [CrossRef]

[70] Yao, L.Z., & Wu, G. (2016). Fiber-element modeling for seismic performance of square RC bridge columns retrofitted with NSM BFRP bars and/or BFRP sheet confinement. *Journal of Composites for Construction*, 20(4), Article 04016001. [CrossRef]

[71] Ebead, U. (2004). Fiber-reinforced polymer strengthening of two-way slabs. *ACI Structural Journal*, 101(5), 650-659. [CrossRef]

[72] Babaeidarabad, S., Loreto, G., & Nanni, A. (2014). Flexural strengthening of RC beams with an externally bonded fabric-reinforced cementitious matrix. *Journal of Composites for Construction*, 18(5), Article 04014004. [CrossRef]

[73] Attari, N., Amziane, S., & Chemrouk, M. (2012). Flexural strengthening of concrete beams using CFRP, GFRP and hybrid FRP sheets. *Construction and Building Materials*, 37, 746–757. [CrossRef]

[74] Chen, G. M., Teng, J. G., & Chen, J. F. (2013). Shear strength model for FRP-strengthened RC beams with adverse FRP-steel interaction. *Journal of Composites for Construction*, 17(1), 50–66. [CrossRef]

[75] Singh, S. B. (2013). Shear response and design of RC beams strengthened using CFRP laminates. *International Journal of Advanced Structural Engineering*, 5(1), Article 16. [CrossRef]

[76] Hussein, M., Afefy, H. M., & Khalil, A.H. A.K. (2013). Innovative repair technique for R.C. beams predamaged in shear. *Journal of Composites for Construction*, 17(6), 1–8. [CrossRef]

[77] Harajli, M. H., & Soudki, K. A. (2003). Shear strengthening of interior slab–column connections using carbon fiber-reinforced polymer sheets. *Journal of Composites for Construction*, 7(2), 145–153. [CrossRef]

[78] Farghaly, A. S., & Ueda, T. (2011). Prediction of punching shear strength of two-way slabs strengthened externally with FRP sheets. *Journal of Composites for Construction*, 15(2), 181–193. [CrossRef]

[79] Silva, M. A. L., Gamage, J. C. P. H., & Fawzia, S. (2019). Performance of slab-column connections of flat slabs strengthened with carbon fiber reinforced polymers. *Case Studies in Construction Materials*, 11, Article e00275. [CrossRef]

[80] Kim, Y. J., Longworth, J. M., Wight, R. G., & Green, M. F. (2009). Punching shear of two-way slabs retrofitted with prestressed or non-prestressed CFRP sheets. *Journal of Reinforced Plastics and Composites*, 29(8), 1206–1223. [CrossRef]

[81] Abdullah, A., Bailey, C. G., & Wu, Z. J. (2013). Tests investigating the punching shear of a column-slab connection strengthened with non-prestressed or prestressed FRP plates. *Construction and Building Materials*, 48, 1134–1144. [CrossRef]

[82] Abdullah, A., & Bailey, C. G. (2018). Punching behaviour of column-slab connection strengthened with non-prestressed or prestressed FRP plates. *Engineering Structures*, 160, 229–242. [CrossRef]

[83] Palacios-Munoz, B., Gracia-Villa, L., Zabalza-Bribián, I., & López-Mesa, B. (2018). Simplified structural design and LCA of reinforced concrete beams strengthening techniques. *Engineering Structures*, 174, 418–432. [CrossRef]

[84] Vitiello, U., Salzano, A., Asprone, D., Di Ludovico, M., & Prota, A. (2016). Life-cycle assessment of seismic retrofit strategies applied to existing building structures. *Sustainability*, 8(12), Article 1275. [CrossRef]

[85] Shi, C., Wang, J., Liu, Y., Luo, W., Mei, S., Wang, Y., & Yu, J. (2021). Life-cycle study of concrete bridges strengthened with carbon-fibre-reinforced polymer. *Proceedings of the Institution of Civil Engineers - Engineering Sustainability*, 174(6), 289–303. [CrossRef]

[86] Dong, S., Li, C., & Xian, G. (2021). Environmental impacts of glass- and carbon-fiber-reinforced polymer bar-reinforced seawater and sea sand concrete beams used in marine environments: An LCA case study. *Polymers*, 13(1), Article 154. [CrossRef]

[87] Zhang, C. (2014). Life cycle assessment (LCA) of fibre reinforced polymer (FRP) composites in civil applications. In F. Pacheco-Torgal, L. F. Cabeza, J. Labrincha, & A. de Magalhães (Eds.), *Eco-efficient Construction and Building Materials* (pp. 565–591). Woodhead Publishing. [CrossRef]

[88] Hassan, M. M., Schiermeister, L., & Staiger, M. P. (2015). Sustainable production of carbon fiber: Effect of cross-linking in wool fiber on carbon yields and morphologies of derived carbon fiber. *ACS Sustainable Chemistry & Engineering*, 3(11), 2660–2668. [CrossRef]

[89] Sen, T., & Jagannatha Reddy, H. N. (2013). Strengthening of RC beams in flexure using natural jute fibre textile reinforced composite system and its comparative study with CFRP and GFRP strengthening systems. *International Journal of Sustainable Built Environment*, 2(1), 41–55. [CrossRef]

[90] Preinstorfer, P., Huber, T., Reichenbach, S., Lees, J. M., & Kromoser, B. (2022). Parametric design studies of mass-related global warming potential and construction costs of FRP-reinforced concrete infrastructure. *Polymers*, 14(12), Article 2383. [CrossRef]

[91] Alibaba. (2022). Find quality manufacturers, suppliers, exporters, importers, buyers, wholesalers, products and trade leads from our award-winning international trade site. Import & Export on Alibaba.com. http://www.alibaba.com/ Accessed on Nov 22, 2022

[92] Collins, M. P., Gupta, P. R. (2001). Evaluation of shear design procedures for reinforced concrete members under axial compression. *Structural Journal*, 98(4), 537–547. [CrossRef]

[93] Akhundzada, H., Donchev, T., & Petkova, D. (2019). Strengthening of slab-column connection against punching shear failure with CFRP laminates. *Composite Structures*, 208, 656–664. [CrossRef]

[94] Abdel-Kareem, A. H. (2020). Punching strengthening of concrete slab-column connections using near surface mounted (NSM) carbon fiber reinforced polymer (CFRP) bars. *Journal of Engineering Research and Reports*, 9(2), 1–14. [CrossRef]

Appendix A. Key properties of selected studies for database

No	# of sample	Authors	h (mm)	Span/depth ratio	f'_c (MPa)	ρ (%)	ρ_{FRP} (%)	V_{test} (K.N.)
1	12	Harajli et al. [77]	55 and 75	5.18 and 7.70	23.5~34.3	1.01~1.49	0.035~0.155	43.5~130.7
2	14	Chen and Li [45]	100	5.1	16.9~34.4	0.59 and 1.28	1.048 and 1.544	144.4~289.4
3	5	Sharaf et al. [40]	150	7.89	25 and 28	1.37	0.089 and 0.178	420~477
4	9	Esfahani et al. [48]	100	5.82 and 6.16	23 and 46	0.84 and 1.58	0.025~0.076	191~332
5	2	Farghaly et al. [78]	120	7.73	33.5 and 39.6	1.27	0.030 and 0.060	215 and 261
6	3	Kim et al. [80]	150	8.12	32.5	1.12	0.015	392~443
7	5	Soudki et al. [54]	100	7.64	25.8	1.41	0.197 and 0.393	163.8~206.9
8	5	Akhundzada et al. [93]	120	6.62	30~31.5	0.51	0.069~0.138	177~213
9	2	Abdel-Kareem [94]	130	4.32	32.4 and 35.8	0.79	0.02	263.5 and 277.5

Journal of Sustainable Construction Materials and Technologies
Web page info: https://jscmt.yildiz.edu.tr
DOI: 10.47481/jscmt.1190244

JSCMT
Journal of Sustainable Construction Materials and Technologies

Review Article

A review on selected durability parameters on performance of geopolymers containing industrial by-products, agro- wastes and natural pozzolan

Festus Musyimi NGUI[*1], Najya MUHAMMED[1], Fredrick Mulei MUTUNGA[1], Joseph Mwiti MARANGU[2], Ismael Kithinji KINOTI[2]

[1]*Department of Chemistry, Pwani University, Kilifi, Kenya*
[2]*Department of Physical Sciences, Meru University of Science & Technology, Meru, Kenya*

ARTICLE INFO

Article history
Received: 18 October 2022
Revised: 19 November 2022
Accepted: 20 November 2022

Key words:
Agro-industrial waste, calcined clay, coconut ash, durability, geopolymer

ABSTRACT

The applications of geopolymers as cementitious systems are becoming an alternative source of cement daily. The use of potentially suitable aluminosilicate inorganic waste materials incorporated with agro-industrial waste in the production of suitable geopolymer binders has been reported. Calcined clay and some agro-waste ash, such as coconut shells, are examples of aluminosilicate materials that exhibit strong pozzolanic activity because of their high silica-alumina composition. The pozzolanic reaction is primarily caused by the amorphous silica present in properly burned agricultural waste and clay. Based on a variety of available literature on concrete and mortar including geopolymers synthesized from the by-product and agro-industrial waste and natural pozzolan, a critical review of raw materials and the mechanism of synthesis of the geopolymer has been outlined in this work. Also, a brief review of the durability characteristics of this geopolymer concrete and mortar has been done. These include resistance to chloride, corrosion, sulphate and acid attack, depth of carbonation, thermal performance, Creep and drying shrinkage.

Cite this article as: Ngui, FM., Muhammed, N., Mutunga, FM., Marangu, JM., & Kinoti, IK. (2022). A review on selected durability parameters on performance of geopolymers containing industrial by-products, agro- wastes and natural pozzolan. *J Sustain Const Mater Technol*, 7(4), 375–400.

1. INTRODUCTION

The worldwide search for a sustainable and environmentally friendly alternative to today's dominant-natural resource-depleting convectional cement supply is the result of the rising binder innovations. Numerous agro-industrial byproducts and wastes as well as natural pozzolans have the potential to help resolve some of the world's binder and environmental issues due to their well-known silica and/or alumina content. Numerous agricultural wastes have indeed been reported to contain pozzolanic ash, including coconut shell/fiber, olive stones, sugar cane bagasse, cotton stalks, and grape seeds [1–4]. Other reported potential agro-waste are from pine sawdust, almond, nut, hazelnut, and sunflow-

***Corresponding author.**
*E-mail address: festongu@gmail.com

er shells, corn, oat, and rice hulls [5], apricot, peach, and cherry stones, sunflower stalk [5–9]. Amorphous silica and the reactive element in the ash can be utilized as pozzolan in cement manufacturing to provide inexpensive building blocks and as cement, in addition to hardening hazardous wastes [10–12]. Recent studies have shown that some of the ashes can be used to create geopolymer and alkali-activated materials (AAMs) [13].

Geopolymer is an aluminosilicate binder that is made by the use of alkaline as an activator on solid precursor materials that contain silica and alumina at or just above room temperature. The alkaline solution is used to speed up aluminosilicate solubilization for the development of the material's cementing characteristics [14]. Similarly, geopolymer can also be defined as either pure inorganic or organic alkaline-solution substance with a high silica and alumina content, according to Kim et al. [15]. These materials resemble zeolite with a polymeric Si-O-Al framework and their binding properties depend on SiO_2/Al_2O_3 ratio in the framework. In recent decades, this group of minerals has become one of the most important substitutes for conventional cement (OPC) as a binder for the manufacture of pre-cast concrete. This is due to their respectable durability qualities like low shrinkage, fire resistance, acid resistance and environmentally sustainable for the construction industry [16–20]. They are environmentally friendly materials since they have low manufacturing temperature and CO_2 emission which is estimated to be nine times less compared with OPC [16]. The demand for long-established natural raw materials and aggregates in cement as a binder and concrete is greatly brought to a minimal level by the use of industrial by-products in the creation of geopolymers. This directly reduces CO_2 emissions, landfilling, and energy consumption as well [21, 22]. As a result, it has proved to be a "green material," meaning that it utilizes little energy during manufacturing and emits little waste gases [23]. Due to this, geopolymer is now one of the contenders for resolving the conflict between societal growth and environmental pollution caused by the production of binders [24]. Therefore, geopolymer has applications in waste management, biomaterials, fireproofing, building engineering, and other fields [25, 26].

In comparison to PC, processing geopolymer cement uses less fuel, less calcium-based raw material, and lower manufacturing temperatures. As much as 80% to 90% less carbon dioxide is released as a result [16]. Aluminosilicate AAMs are used to create geopolymers, which can have stronger final products and do so more affordably than OPC [18]. Typically, the first four hours of the setting are when 70% of the final compressive strength is reached [27]. Geopolymer constructions exhibit decreased permeability, resilience to fire and acid attack, better unconfined compressive strength, significantly less shrinkage, excellent heavy metal ion solidification, and exceptional freeze-thaw cycle resistance. It's considered a high-strength concrete application that demonstrates strong resistance to fire, acid, and/or chloride penetration. So, for the chemical and nuclear sectors, geopolymers may offer a promising waste immobilization solution.

The favorable effect of geopolymers on the durability performance of the resulting cementitious composite is their principal benefit. This is connected to their dimensional stability, especially with geopolymer compositions that have very low C-S-H levels [28]. The primary reaction occurs when amorphous aluminosilicates in metakaolin-based materials and other amorphous aluminosilicate materials, such as fly ash and volcanic ash with low calcium concentrations, are activated by alkalis. In essence, this causes the creation of polysialates (M-A-S-H). The attack of alkali on aggregates is the secondary reaction, although, in the absence of calcium, this won't have much.

The nature and composition of the reaction products produced by geopolymers or alkali-activated cementitious materials typically rely on the type of agro-industrial by-product of the aluminosilicate precursor used, and they differ from those normally derived from OPC. The production of each of these compounds depends on the Ca/Si and Si/Al and the pH contents of the matrix. For hybrid cementitious materials, Garcia-Lodeiro et al. [29], documented the existence of several gels. This included calcium silicate hydrate (C-S-H) from the usual hydration of PC, calcium aluminosilicate hydrate (C-A-S-H), and (N, C)-A-S-H gels, which are the main by-products of the alkaline activation of aluminosilicate. In comparison to the same type of cement without activation, Palomo et al. [30], found a 50% improvement in strength at an early curing age, a lower heat of hydration, and an early setting time. They explained this as being caused by the availability of C-A-S-H, N-A-S-H, and (N, C)-A-S-H gels, which have previously been noted from hybrid types of cement made of 7:3 of FA: OPC [31].

The alkali-activated gel is created as a result of the exothermic reaction between solid aluminosilicates and hydroxide, silicate, and sulfate solutions of alkali, which promotes the ions dissolution of both Al^{+3} and Si^{+4} from starting materials [32, 33]. This gel exhibits high-quality mechanical and durable properties in the hardened phase.

Geopolymer cement can be classified as fly ash, slag, rock, or ferro-sialate-based geopolymer types of cement. Alkali-activated binder, an inorganic polymer, mineral polymer, hydro ceramics, and alkali-bonded ceramic are some further names for this substance [34, 35]. Substituting waste for Portland cement in the industrial manufacturing of activated alkali materials or geopolymer binders will have positive economic and environmental effects. It would also resolve the issues related to the removal of significant amounts of garbage from industry and building sites that could otherwise threaten the environment, such as coconut shells and calcined clay brick waste.

2. RAW MATERIALS FOR GEOPOLYMER SYNTHESIS

In addition to the alkaline solution, silica-aluminum sources are used as raw ingredients in the production of geopolymer concrete. For the synthesis of geopolymers, there are two types of raw materials. Along with the alkaline activating solution, which is often an alkali metal hydroxide or silicate solution, this also includes the reactive aluminosilicate particles such as fly ash and calcined clays. One-part geopolymer precursors have generated interest [36–38] however, the strength of the materials do not match the requirements for the majority of construction applications. Different aluminosilicate industrial waste materials have traditionally been shown to pose effective options for the synthesis of geopolymer. These include building demolition debris, metallurgical slag, coal fly ash, and a variety of biomass ashes like rice husk ash, coconut shell ash, palm oil fuel ash, and others [39, 40]. The two most often used starting materials in the synthesis of geopolymers for use in the building are fly ash and calcined clay. Industrial waste or by-product created during the production of coal-fired energy is called fly ash [41]. For geopolymers production, a wide range of raw materials with high silica and alumina contents can be employed. Depending on where they come from, the raw materials are categorized into three classes. Among them are primary raw materials, which are composed of natural minerals and secondary raw materials, which are industrial by-products and their wastes and by-products raw materials of natural origin [42].

Natural minerals from the earth's crust, which comprises 65% Al-Si elements, are the main suppliers of raw materials [23, 43]. Several Al-Si minerals and clays, primarily kaolinite and metakaolin, have been found to polymerize in the past [23]. A purer and easily described starting material for geopolymerization is provided by metakaolin. Due to its predictable qualities and stable chemical make-up, it is also commonly employed for industrial and scientific applications. Poorly activated kaolin produces geopolymers based on metakaolin, which are too soft and water-intensive to be of much use in building applications [44–47]. The reactivity of kaolin can be improved by either mechanical or thermal treatment. Mechanical activation involving prolonged grinding decreases the degree of crystallinity and surface energy and hence increases the chemical reactivity [48]. Dehydroxylation of kaolinite at 600–800 °C for 2–5 hours results in metakaolin [44, 47], depending on purity and crystallinity, as shown in Equation (1).

$$Al_2O_3.2SiO_2.2H_2O \dashrightarrow Al_2O_3.2SiO_2 + 2H_2O \quad (1)$$

Metakaolin is a highly reactive anhydrous aluminosilicate-metastable clay that can be produced by calcining kaolin to temperatures between 650 °C and 700 °C, according to [49, 50]. According to earlier studies, the reactivity of metakaolin changes as a result of heat treatment at calcination temperatures between 450 and 600 °C [51, 52]. According to [53] Table 1 displays the normal chemical composition of metakaolin.

Table 1. Typical chemical composition of metakaolin

Chemical compounds	wt %
SiO_2	55.62
Al_2O_3	39.67
Fe_2O_3	0.96
CaO	1.41
MgO	0.18
K_2O	0.87
SO_3	0.00
TiO_2	0.41
Na_2O	0.08
LOI	2.01

Burnt clays' ability to acquire pozzolanic properties is influenced by the raw material's quantity and kind of clay minerals present, the calcination conditions, and the fineness of the finished product [54–57].

Wastes and by-products from industry are secondary raw resources. The secondary raw materials are used in making more environmentally friendly geopolymers which also help in preserving natural resources [58, 59]. These include waste broken bricks, waste glass, fly ash, red mud, and blast furnace slag [60, 61]. Fly ash and slag are the secondary raw materials that are used and studied the most [42]. Fly ash and blast furnace slag are examples of secondary raw materials that are heterogeneous and contain contaminants like calcium and iron. This opens up more chemical pathways during polymerization, which may have an impact on the final product's setting times, slump, strength, and shrinkage [19, 62, 63].

Fly ash which is a by-product of power plants fueled using coal, mostly consists of SiO_2 and Al_2O_3, along with a few minor substances like CaO, Fe_2O_3, MgO, etc. Since it has high alumino-silicate, better workability, low water demand and readily available thus has been a material of concern for geopolymer synthesis. Geopolymerisation of fly ash with alkaline media forms a cementitious material that comprises of alumino-silicate-hydrate (A-S-H) gel [64]. This geopolymer product has improved durability and strong mechanical strength [65]. However, the low reactivity of the material has limited the manufacture of geopolymers by delaying early setting and strength development [64]. Studies in microscopy and microanalysis of residual fly ash particles found in geopolymer cement show that mullite available in fly ash remains unreacted and that calcium appears to be active in the process of alkali activation of fly ash blends [66, 67].

Cooling quickly the molten iron slag from a blast furnace in water or steam, a glassy granular material known as granulated blast furnace slag (GBFS) is produced. This is usual-

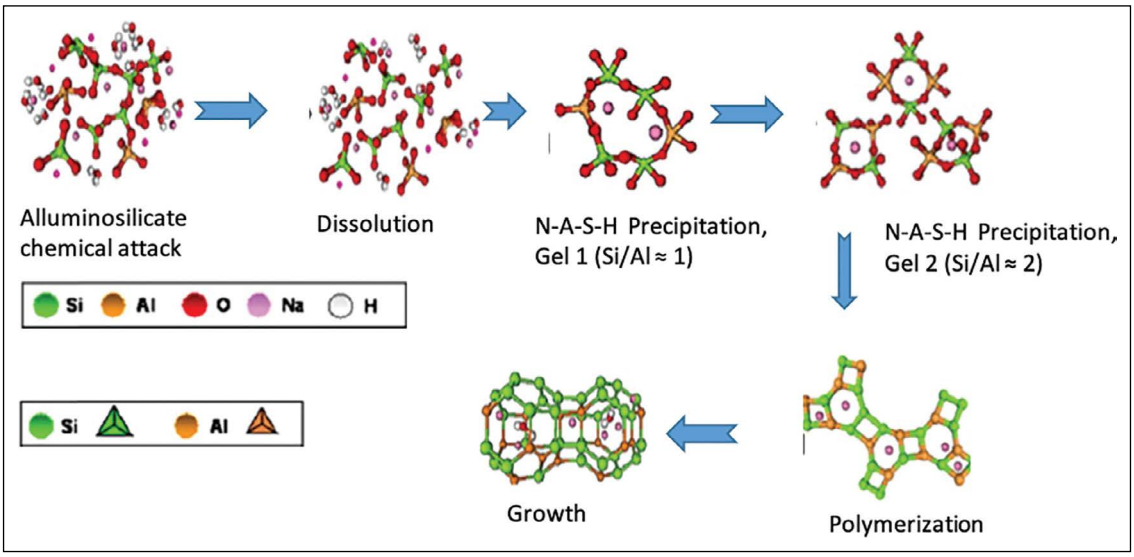

Figure 1. Geopolymerization process [82, 81].

ly very reactive with a mineral composition of SiO_2, CaO, Al_2O_3 and MgO [42, 67, 68]. Due to its small particles, it has effectively increased its strength. As a result, GBFS has been used as a replacement material for making cement for over 75 years [19, 67–69]. A hydrated calcium-silicate (C-S-H) gel with a low C/S ratio is produced as the main reaction product during the alkali activation of GBFS. The strength and setting properties of the geopolymer are enhanced by this gel [70–72]. Hadi et al. [72], worked on a blend of GBFS with fly ash (FA), metakaolin (MK) and silica fume (SF) in nine mix designs. Their formulations gave a better early 7-day compressive strength and setting time compared to conventional cement. In another investigation on the effect of curing conditions on the performance of granulated blast furnace slag and metakaolin-based geopolymer concrete, it was concluded that the use of the GBFS/MK reported good mechanical performance degradation [73].

Red mud is another industrial waste produced during the extraction of alumina from bauxite ores. It mainly consists of Al_2O_3, SiO_2, and NaOH [74]. It is suitable for the synthesis of geopolymers owing to its high alkalinity as well as the presence of alumina [75]. Since its silica component is non-reactive, it is typically utilized in conjunction with other alumino-silicate compounds like fly ash or metakaolin. Roadway building using red mud geopolymers may be a viable option for cementitious materials, helping to lessen the harm that waste has on the environment and human health [16, 76]. Due to its density and resistance to ion penetration, red mud-blast furnace slag geopolymer mortar was found by Liang & Ji [77] to be more durable than PC mortar in terms of protecting steel bars from corrosion. Substitution of 10–15% red mud to alkali-activated fly ash, improved the compressive strength increased by 2.5 times. This was linked to changes in phase composition and activator ratio which inhibits zeolite formation [78].

Wastes and by-products of mineral origin are natural by-products that are produced during the manufacturing process from raw materials. Perlite is an amorphous volcanic glass that contains some crystalline phases and is high in SiO_2 and Al_2O_3. It is reduced in size and heated to create a porous product, which is then used as an agricultural water-absorbent [42, 79]. The perlite that is too fine or has an insufficient ultimate porosity, for example, to be used further, is regarded as trash. Waste perlite that has been geopolymerized, can be utilized to make effective thermally insulating materials, or it can be combined with fly ash or other waste aluminosilicates to make building materials and immobilize hazardous waste [80]. A study by Vance et al. [79], on the use of perlite waste in the preparation of geopolymer, reported that perlite waste in small particles acted as a fairly reactive aluminosilicate constituent with a strong alkali solution in geopolymer formation. Vaou & Panias [80] investigated the foamy geopolymers from perlite. They found that this material had very good thermal insulation and compressive strength of 780 kPa at 2% deformation and a fracture behavior resembling one of the rocks. In addition, it had high fire-resistant properties.

3. MECHANISM OF GEOPOLYMER SYNTHESIS

According to research, the geopolymerization process involves three steps: (1) using an alkaline solution to dissolve (2) diffusion and ion reorganization along with the formation of minute coagulated structures; and (3) soluble species are polycondensed to create hydrated products [18, 81]. The Figure 1 illustrates the geopolymerisation process.

The amorphous, zeolite-like geopolymers are created by the high-pH dissolution of silica- and alumina-containing parent materials. Aluminosilicate raw materials containing Si_2O_3 and Al_2O_3 (or other compatible Metal Oxides such as

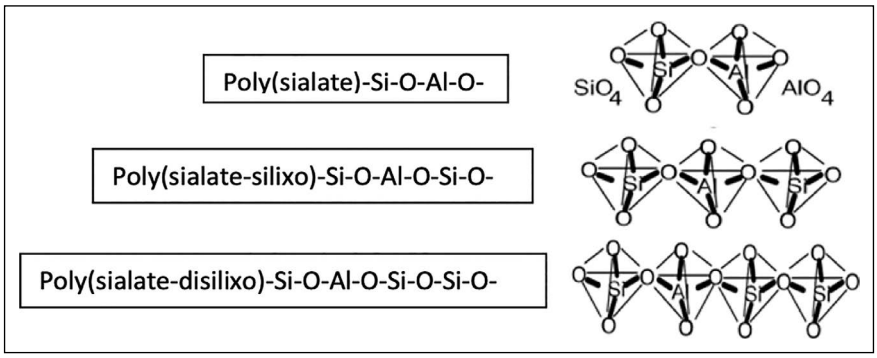

Figure 2. The fundamental process by which various alumino and silicate species co-polymerize to form polysialate.

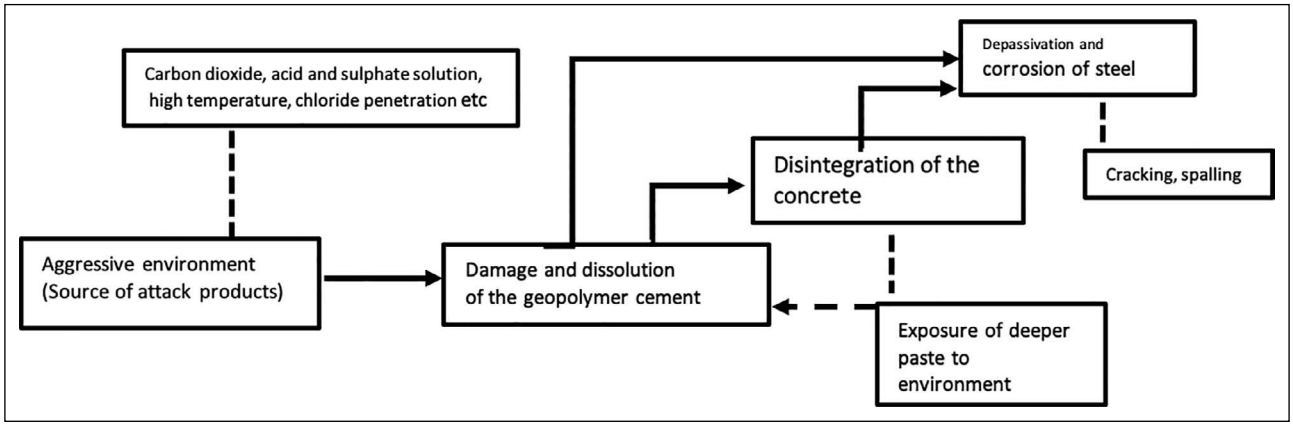

Figure 3. Cement/geopolymer concrete's general mechanism for deterioration [95].

Fe_2O_3) are reacted with a soluble alkali such as K or Na. The Si_2O_3 and Al_2O_3 oxides undergo dissolution into atoms forming a gel. The free atoms within the gel move, forming monomers that form polymers and oligomers. The latter forms 3-dimensional chain networks if the correct ratio of Si: Al is present within the mix expelling water to form the bond, i.e. dehydroxylation. The polymeric bonding continues until a solid hardened structure emerges [83]. Dissolution of these leads to co-polymerization of individual alumino and silicate species [27, 84, 85] to form silico-aluminates i.e poly(sialate). According to Figure 2, Poly (sialates), which can be amorphous or semi-crystalline and feature Si^{4+} and Al^{3+} in IV-fold coordination with oxygen, are chain and ring polymers.

To create the sialate network, AlO_4 and SiO_4 tetrahedra are linked alternately by sharing all of the oxygens. The framework cavities contain positive ions, such as Na^+, K^+, Ca^{2+}, Li+, Ba^{2+}, NH^{4+}, or H_3O^+ to counteract the negative charge of Al3+ in IV-fold coordination. The written empirical formula for poly(sialates); $M_X\{(SiO_2)_ZAlO_2\}_x wH_2O$.

Where, Z is 1, 2, 3.., M is a cation like calcium, sodium, or potassium and x is a polycondensation degree [86]. Geopolymerisation is an exothermic process and involves polycondensation of orthosialate ion monomers as in Equations (2) and (3).

$$n(Si_2O_5Al_2O_2) + 2nSiO_2 + 4nH_2O \xrightarrow{NaOH/KOH} n(OH)_3\text{-}Si\text{-}O\text{-}Al(OH)_2\text{-}O\text{-}Si\text{-}(OH)_3 \quad (2)$$

$$n(OH)_3\text{-}Si\text{-}O\text{-}Al(OH)_2\text{-}O\text{-}Si\text{-}(OH)_3 \xrightarrow{NaOH/KOH} (Na/K)\text{-}(\text{-}Si\text{-}O\text{-}Al(O)_2\text{-}O\text{-}Si\text{-}O\text{-}) + 4nH_2O \quad (3)$$

4. DURABILITY ASPECTS OF GEOPOLYMERS

Alumino-silicate waste can be geopolymerized to provide a variety of mining and construction materials with superior chemical and physical qualities. These characteristics include resistance to fire, chemical stability, acidity, salts such as chlorides and sulfates [40, 87] resistance to humidity or water, freezing action, and weathering [88–90]. The stability and durability characteristics of geopolymers are similar to those of more conventional cements like Portland or blast furnace cement since they have an alkaline nature [91, 92]. Durability is a crucial factor since it measures a material's capacity to operate both temporarily and permanently despite abrasion, chemical attack, and weathering while retaining the necessary qualities [93, 94]. To understand the geopolymers' chemical reactions when exposed

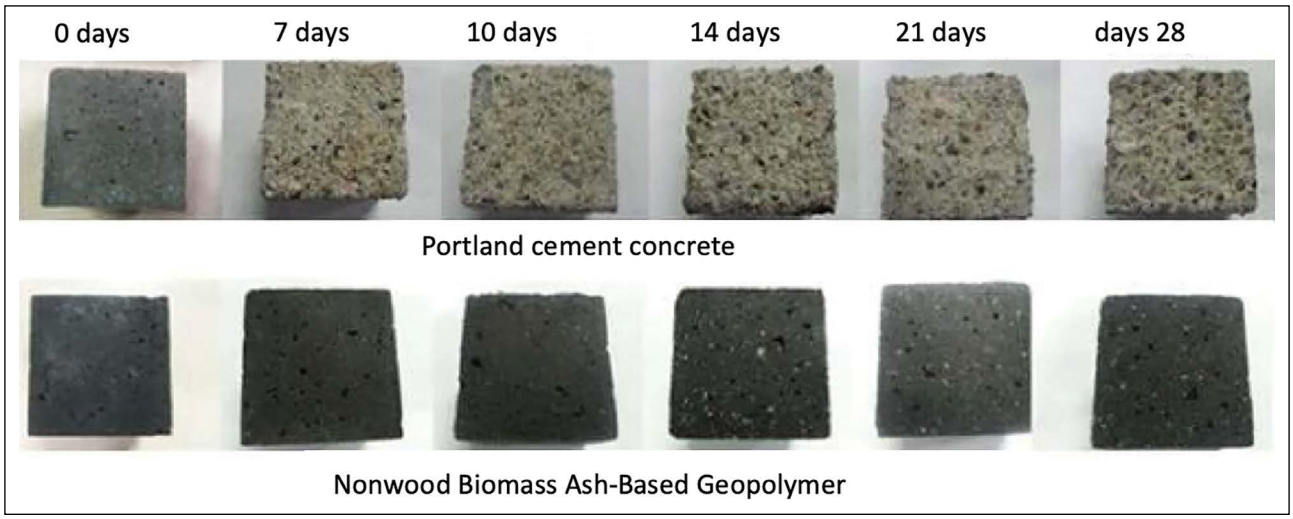

Figure 4. Visual characteristics of non-wood biomass ash-based geopolymer in acid attack on ordinary Portland cement concrete [98].

to aggressive substances, it is required to investigate their durability properties. When materials' compositions alter, the geopolymer degrades, and the paste dissolves and deteriorates when it is exposed to aggressive environments [95], as seen in Figure 3.

4.1. Acid Attack

Cementitious materials are susceptible to reaction with acidic chemicals in a range of applications, including effluents, sewage treatment facilities, power plants, agriculture and in addition to transportation and raw material storage facilities [96]. One of the qualities that building materials should have is resistance to acidic environments. Such an acidic environment can be a result of acid groundwater, acid rain, the acid solution from the sanitary sewer, animal feed and manure, waste stabilization applications, chemical and mining industries [91, 97]. OPC and geopolymer binders are acid attack-prone due to their alkaline nature. As pH decreases, calcium hydroxide and calcium sulfoaluminates breakdown first in the case of PC binder, then C-S-H decalcifies. The hydrated PC paste's main C-S-H component has a comparatively high Ca to Si ratio, leaving a porous structure on its outer layers that is vulnerable to further acid attacks. The typical alkaline earth or alkali aluminosilicate hydrate polymeric binder component, on the other hand, forms a thick silica gel protective layer on its outermost layer in an acidic environment. This slows down additional acid attacks, giving geopolymer binders a better acid attack than PC binders. Matalkah et al. [98], used visual comparisons to contrast normal PC cement concrete concrete specimens with nonwood biomass ash-based geopolymer concrete specimens that were immersed in 5% sulfuric acid solutions for up to 28 days. Figures 4 and 5 show that the PC concrete exhibited significant surface degradation and mass loss in comparison to geopolymer concrete made of

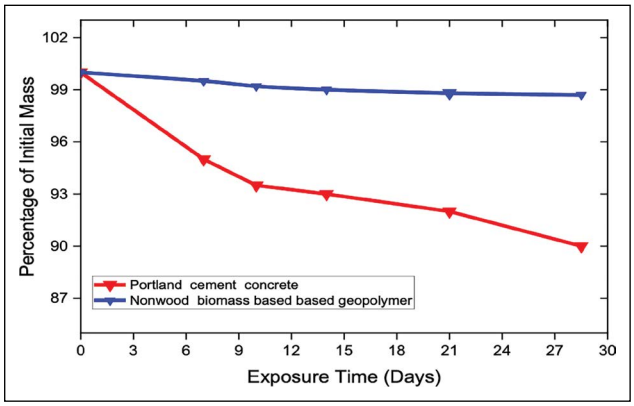

Figure 5. Mass measured against time immersed in acidic solution [98].

nonwood biomass ash. They attributed this to the geopolymer's nonwood biomass ash base's stable chemistry and good barrier properties.

On geopolymer made from palm oil fuel ash, metakaolin or calcined kaolin, fly ash, bottom ash, rice husk ash and slag studies of acid resistance have previously been conducted [99–104]. The method of acid attack varies depending on the type of acid and the characteristics of the calcium salt generated, according to [105]. The structural integrity of the geopolymers will also depend on the dissociation of the cations in either the alkali or acid environments. For instance, the precursor material's iron compounds are prone to acid degradation since they play a little role in the geopolymerization procedure and may dissolve leaving pores [106]. The amorphous aluminosilicate spheres are vulnerable to both alkali and acid damage when left unreacted. This is because Al dissolves more in acids than Si. Also, both Al and Si disintegrate in alkali with Si having the highest solubility. Thus, the amount of amorphous precursor materials

in the geopolymers determines the alkaline or acid resistance behavior. The amorphous compounds have generally a weaker resistance to chemical attack compared to their crystalline counterparts [97].

Conventional concrete constructed with OPC does not offer acid resistance. Alkali-activated or geopolymer concrete has also started to gain favor as most researchers work toward sustainable development because research has proven that it is stronger and more durable than regular concrete [72]. The cementitious materials acid resistance is affected by the concrete matrix's impermeability and the strength-forming phases' resistance [107]. Several approaches have been used to improve the impermeability of the concrete matrix such as the decrease in w/c ratio with minimal impact. According to research, creating a more stable phase is the greatest way to increase acid resistance. For instance, lowering the amount of clinker in Portland cement-based binders by using supplementary materials like metakaolin results in a decrease in the acid-soluble $Ca(OH)_2$. This also leads to the formation of C-A-S-H -phases with lower C/S ratios, hence low leaching property [107, 108]. CASH phases offer more acid resistance than regular CSH phases made from other pozzolanas, such as fly ash.

Working on the acid corrosion resistance of various cementing materials, Shi & Stegemann [109], proposed that the permeability of hardened cement pastes was less important for cement paste resistance to acidic corrosion than the composition of the hydration products. Alkali-activated blast furnace slag cement, lime, and fly ash paste primary hydration product was C-S-H with a low C/S ratio, whereas hardened PC paste primary hydration products was C-S-H with a high C/S ratio and $Ca(OH)_2$. Acid exposure had a deleterious effect on the latter, hardened mortar [109]. As a result of sulphuric acid attack, cementitious phases in the matrix disintegrate and decalcify and sulphate salts crystallize on the exposed surface [110, 111]. This affects both the mechanical and physical characteristics of the concrete, including its porosity and strength, in addition to its density [110, 112]. These alterations in the matrix allow acid to permeate deeper into the concrete layers and neutralize them.

Geopolymer concretes have the potential to replace ordinary PC concrete in construction sites exposed to an aggressive environment [113]. The aluminosilicate secondary raw materials, such as metakaolin, fly ash, and ground granulated blast-furnace slag (GGBS), react with an alkaline activator comprised of metal hydroxide or silicate solution to produce the binders. Highly cross-linked alkali-aluminosilicate is created during the alkali reaction with aluminosilicate and is referred to as geopolymer [114, 115]. The microstructure is made of a three-dimensional network of randomly connected negatively charged $(AlO_4)^{-5}$ and $(SiO_4)^{-4}$ tetrahedrons that are balanced by cation M+ (K^+ or Na^+). Geopolymer binder formed from low calcium aluminosilicate precursor and sodium silicate or hydroxide solutions as an alkaline activator has shown to form an amorphous form of N-A-S-H gel which has shown resilience to an acidic environment [99]. As seen in equation 4, the disintegration of this amorphous gel matrix caused by the liberation and substitution of a proton (H+) with an alkali cation (M+) is what gives geopolymer its chemical resistance.

$$[\text{Si-O-Al-O}\ldots]\text{H+ M}^+ \rightarrow [\text{Si-O-Al-O}\ldots]\text{M+ H}^+ \quad (4)$$

This occurs following the breakdown of the Si-O-Al network and the elimination of alumina. This Al delinking from the aluminosilicate structure results in the formation of Si vacancies, which when combined form an unfinished weak silicic acid [99].

Alkali-activated binders have in recent times shown resilience against aggressive environments like hydrochloric acid, sulphate, sulphuric acid, nitric acid, or acetic acid [97, 116–119]. This contradicts the observation by Lloyd et al. [118], that acid attacks inorganic polymer binders by surface corrosion. Deterioration of inorganic polymer binders is well tested by corroded depth instead of a change in mass. This is because the extremely interconnected aluminosilicate bonds of an inorganic polymer binder are attacked by acid. Instead of wearing away, as has been the case for other binder types, this causes the creation of a physically unstable and porous but intact layer on the sample surface [118].

Acidic corrosion known as nitric acid attack reduces the volume of the damaged layer as a result of the creation of the extremely soluble calcium nitrate salt [120]. According to Thokchom et al. [121], three different specimens made by alkali initializing fly ash with a mixture containing sodium hydroxide and sodium silicate solution containing sodium hydroxide from 5% to 8% of fly ash were tested for the durability of fly ash-based geopolymer mortar samples in nitric acid solution. The researchers submerged samples in a 10% weight solution of nitric acid for 24 weeks. Analyses were carried out in terms of overall aspect, weight change, and compressive strength change. Adjustments in mineralogy and micro-structural caused by nitric acid threat were also investigated. Geopolymer mortar specimens demonstrated outstanding durability in aspects of relatively low weight loss and high compressive strength retention. Also, specimens with a greater alkali content were more resistant to nitric acid.

Previous analysis indicates that geopolymer mortars outperform ordinary Portland cement mortars in terms of sulfuric acid resistance, with lower shrinkage and reduced compressive strength. Similar patterns were seen by Purbasari et al. [122], who studied the resilience and microstructure of geopolymer mortars formed from co-combustion residues of bamboo and kaolin after being subjected to a solution of sulfuric acid at 5% for 2, 4, and 6 weeks. The researchers discovered that when compared to conventional Portland cement mortars, geopolymer mortars

had superior sulfuric acid resistance in terms of lower mass and compressive strength loss. When subjected to a 2% sulphuric acid solution for up to 45 days [123], investigated the durability of geopolymer concrete made with high calcium fly ash and alkaline activators. The findings demonstrated a compressive strength drop of 20% and 28% in the geopolymer concrete and the conventional Portland cement concrete respectively. Song et al. [124], conducted an experiment to see how long concrete made with fly ash will last when exposed to 10% sulfuric acid solutions. With an evaporation rate of less than 3%, the study demonstrated the remarkable sulphuric acid resistance of geopolymer concrete. Furthermore, the Geopolymer cubes were structurally sound and still had a sizable load capacity even after the entire portion had been neutralized by sulfuric acid. Geopolymer concrete subjected to acid and salt was examined for strength by Kumaravel & Girija [125]. The workers claimed that the GPC specimens exhibited outstanding resistance to acid and salt, with a little higher concentration of NaOH as alkali, or 12 M.

The strongest leaching and subsequent quick loss of thickness are caused by citric acid, which has proven to be the most aggressive of all organic acids [126]. Citric acid's polyacidity and the precipitate's lack of protective qualities may be to blame for this. The solubility and acid buffering properties of the organic salts may potentially contribute to the increased harmful effect [127]. Acetic acids found in effluents and damping sites can be aggressive as an acid attack. At equivalent concentrations, the corrosion process is comparable to that of strong acids such as sulphuric acid but less aggressive than that of citric acid [105]. Ukrainczyk et al. [128], did a degradation comparison of GP, Calcium Aluminate and OPC mortar on acetic acid. The results showed that GP concrete was least affected by the exposure to the acetic acid in terms of mass loss, hardness, and porosity. The workers attributed this to the strong aluminosilicate network structure of GP which remains stable after the leaching of alkali ions. The penetrating acid species are highly soluble in the OPC binder phases such as CH, C-S-H, AFt, and AFm, creating a very porous binder matrix. As a result, geopolymer-based mortars have better acid resistance and may be a viable substitute for conventional cement concretes used in a variety of agro-industrial settings.

4.2. Chemical Attack

4.2.1. Sulphate Attack

The long-term endurance of a concrete structure may be threatened by salts and solutions of sulphate-bearing chemicals found in saltwater, industrial water effluents, groundwater, or soils nearby [129]. Depending on the calcium level, geopolymers in a sulphate environment erode in different ways [130, 131]. High calcium alkali-activated systems have similar eroding mechanisms to OPC because hydration products resemble each other [95]. The form and extent of damage to concrete will depend on the sulphate concentration, the type of cation (e.g Na^+ or $Mg2^+$) in the sulphate solution, the pH of the solution, and the microstructure of the hardened cement matrix. Gypsum ($CaSO_4.2H_2O$), ettringite ($[Ca_3Al(OH)_612H_2O]_2(SO_4)_32H_2O$), or thaumasite ($[Ca_3[Si(OH)_612H_2O](CO_3)SO_4$) or mixes of these phases are precipitated as a result of sulfate ions' reaction with the pore [132, 133]. These solid phases' precipitation may cause tension within the material, which may result in expansion, strength loss, spalling, and severe degradation [54]. Calcium hydroxide (CH) consumption lowers pH, which can eventually cause the C-S-H to become decalcified. When the magnesium sulfate solution directly attacks the C-S-H, non-cementious M-S-H is formed [134].

When geopolymer/AAM with little to no calcium content is attacked by sulfate, there typically is an exchange of cations with the sulfate solution. This leads to the formation of N-A-S-H, a less expansive crystalline phase structure hence more resistant to sulfate attack [131]. Geopolymer mortars outperformed Portland cement mortars in terms of durability when exposed to magnesium sulfate solution, according to studies by [135] on Magnesium sulfate resistance. This phenomenon is attributed to the higher amounts of $Ca(OH)_2$ and C_3A in OPC thereby producing gypsum on the attack by sulphate ions (Equation 5). Moreover, calcium silicate hydrate abundant in OPC reacts with sulfuric acid to form SiO_2 in an aqueous state weakening the structure's strength (Equation 6).

$$Ca(OH)_2 + SO_4^{2-} \rightarrow CaSO_4 2H_2O \quad (5)$$

$$CaO.SiO_2 + xH_2SO_4 + xH_2O \rightarrow xCaSO_4 2H_2O + SiO_2 \quad (6)$$

The "sulfate attacking" process that occurs on geopolymer binders is significantly influenced by the cation that the sulfate is connected with [136]. According to research by Ismail et al. [137], it is important to distinguish between "magnesium sulfate attack and broader processes connected to the presence of sulfate along with other, non-damaging cations. It is important to note that both Mg^{2+} and SO_4^{2-} are capable of causing damage to a cement structure. The fly ash/slag binders investigated here were more unfavorable in $MgSO_4$ than Na_2SO_4, though not by as much. This was related to the earlier situation's development of calcium sulfate (gypsum), which expanded and damaged the material [138].

In a study by Albitar et al. [139], geopolymer concrete durability parameters were studied against OPC by immersing mortar cylinders into solutions containing 5% sodium chloride, 5% sodium sulfate, and 5% sodium sulfate + 5% magnesium sulfate and 3% sulfuric acid solutions for 9 months. To investigate the effect of chemical conditions on the durability of the concrete, the authors reported that the geopolymer concrete was most resilient to sulfuric at-

tack. This phenomenon is attributed to the higher amounts of $Ca(OH)_2$ and C_3A in OPC thereby producing gypsum on the attack by sulphuric (Equation 5). Moreover, calcium silicate hydrate abundant in OPC reacts with sulfuric acid to form SiO_2 in an aqueous state weakening the structure's strength (Equations 5 & 6).

Gupta et al. [140], demonstrated a similar resistance of geopolymer concrete to acid attack in a subsequent study examining the mechanical and durability characteristics of a geopolymer composite made of slag and calcined clay. The researchers studied performance at 7, 28 and 56 days using 5% sulfuric and 5% magnesium sulfate. Water permeability was however lower in geopolymer concrete than in conventional, a disagreement with findings by Albitar et al. [139]. This was so probably due to the difference in experimental designs.

Concerns have often arisen concerning the effectiveness of geopolymer concrete modifications due to the uncertainty surrounding this process. Chithambar et al. [138], worked on the durability of fiber-reinforced geopolymer concrete against chloride penetration, sulfuric acid attack, and hydrochloric acid attack among other tests. The geopolymer used in the study was synthesized using M-sand and sodium hydroxide and silicate. The effect of glass and polypropylene fiber on the performance of the concrete was studied. Chloride resistance was reported to increase with polypropylene fiber reinforcement. The reinforced concrete also showed high resistance to acid and sulfate attacks.

According to investigations on geopolymer mortar made of fly-ash produced with various alkali content by Thokchom et al. [121] and Thokchom et al. [141] exhibited variable degrees of degradation when exposed to sulfuric acid. Using an optical microscope, the results showed deterioration of mortar surface with advanced effects on specimens with lesser alkali content.

4.2.2. Chloride Attack Resistance

Attack on the reinforcing steel by chlorides is the most frequent cause of durability failure in reinforced concrete (RC) structures. It adversely affects the service life of an RC structure as a result of effects including reduced steel cross-section, cracking, delamination, and spalling [142]. Therefore, the need to prevent steel corrosion is an important objective in ensuring the durability of steel RC structures. Chloride ions may come from a component of the concrete matrix or an outside source, like saltwater or industrial wastewater. Chloride ions mostly enter concrete under the influence of permeability and porosity [143]. In other words, ions will penetrate pores more deeply the larger they are. The secondary precursor in AACs closes the pores, preventing chloride ions from entering the substance. Additionally, the C-A-S-H gel's dense and compact nature aids in the delayed transport of chloride into geopolymers, resulting in a greater chloride attack durability than OPC paste [144, 145].

The porosity of the geopolymer matrix determines how quickly chloride ions diffuse through it [146]. The precursor that has a larger surface area, along with a high concentration of amorphous silica and alumina, produces an aluminosilicate gel that is denser and less porous. This reduces the chloride ingress rate. Presence of CaO content influences the chloride binding capacity. This lowers the rate of chloride intrusion by causing chloride ions to adsorb on the gel's surface [147]. Ismail et al. [137], and Zhang et al. [148], working on fly ash-slag-based geopolymer found that the chloride binding depended mainly on physical adsorption. Other studies on geopolymer concrete performance against chemical attacks are summarized in Table 2.

4.3. Carbonation

When it comes to the major cause of concrete damage, as a result of steel corrosion, carbonation of concrete is regarded to be one of the most dangerous phenomena. Concrete suffers from the carbonation process because carbon dioxide diffuses through the pore structure and lowers the pH of the pore solution. Rapid destruction of the steel's passivation layer allows for unrestricted corrosion processes [155]. As a result of the internal expansion stress and weakening of the steel bars, structures eventually fail [87, 156].

When gaseous carbon dioxide enters partially wet concrete at a pH >10, a sequence of processes is often triggered. According to equations 8 and 9, it quickly dissociates into the alkaline pore solution before hydrolyzing to HCO_3^- and CO_3^{2-} ions.

$$CO_2 + OH^- \rightarrow HCO_3 \quad (8)$$

$$HCO_3^- \rightarrow CO_3^{2-} + H \quad (9)$$

At pore solution of pH 8, CO_2 hydrates directly forming carbonic acid (H_2CO_3) as shown in equation (10).

$$CO_2 + H_2O \rightarrow H_2CO_3 \quad (10)$$

At a higher pH the carbonic acid normally dissociates into HCO_3^- and CO_3^{2-} ions [157]. To create CO_3^{2-} ions may then attack calcium-containing phases, like CaOH, C-A-H and. C-S-H. The calcium carbonate precipitates into either calcite, aragonite, or vaterite crystal polymorphs, based on the internal concrete conditions and the existence of impurities or additives [158, 159]. Under normal circumstances, calcite is the polymorph that is the most stable. Attack of CSH normally happens probably where the quantity of $Ca(OH)_2$ is less especially in blended or geopolymer types of cement, as shown in Equation 11.

$$CaSiO_3H_2O + CO_2 \rightarrow 3CaCO_3 + SiO_2 + H_2O \quad (11)$$

Table 2. Summary of studies on geopolymer concrete performance against chemical attacks

Precursor(s)	Activator(s)	Other concrete modifiers	Chemical environment	Period of exposure	Observations	Reference
Metakaolin and bottom ash	8M Sodium hydroxide and sodium silicate	–	5% magnesium sulphate	28 days	• GPC concrete had no precipitation on surface • GPC concrete demonstrated higher resistance to sulfate attack	[149]
			2% sulfuric acid	28 days	• No cracks on GPC concrete specimen surface • There was low weight loss in GPC specimens compared to OPC • GPC compressive strength was least affected by acid attack compared to OPC	
Rice husk ash and ultra-fine slag with corn cob ash	8M Sodium hydroxide and sodium silicate	–	Chloride ion environment	28 and 56 days	• Concrete was moderately resistant to chloride ingress	[150]
Class F fly ash	12M Sodium hydroxide and sodium silicate	Oil palm trunk fiber	5% sulfuric acid	90 days	• No significant changes were visually observed, in weight and cross-section. • The outer region color changed from dark grey to light grey (corroded). Intensity corresponded to fiber content	[151]
Granulated blast furnace slag and dolomite	Sodium hydroxide and sodium silicate	Steel fiber	3% sulfuric acid	180 days	• Compressive strength loss 5 times lower than OPC • Weight loss 24 times lower than OPC • Steel fiber does not affect the weight loss/strength	[152]
			3% sodium sulfate	180 days	• Weight loss 5 times lower than OPC • Weight loss not affected by steel fiber	
			Saline water	180 days	• Weight loss 9 times less than OPC • Strength loss 2.6 times less than OPC • Percentage loss in compressive strength reduced by 13-15% with 0.25–0.75% addition in steel fibers	
Class F fly ash	10M Sodium hydroxide and sodium silicate	Granite waste as fine aggregate	5% sulfuric acid	28 days	• When replaced at 5, 10, and 15%, granite waste is favorable to GPC. • Loss in mass and compressive strength was lower than control GPC (best at 20% replacement)	[153]
Granulated blast furnace slag	8M–16M Sodium hydroxide and sodium silicate	–	5% hydrochloric acid	28, 56 and 90 days	• 16 M NaOH GPC showed the highest resistance compared to OPC in 28 days	[154]
			5% sodium chloride	28, 56 and 90 days	• 16M NaOH GPC showed the highest resistance compared to OPC at 28 days	
			5% sulfuric acid	28, 56 and 90 days	• 10M and 12M NaOH GPC performed best at 28 days	
			5% magnesium sulfate	28, 56 and 90 days	• 10M NaOH at 28, 56 and 90 days showed the best resistance to sulfate attack	

This lowers the alkalinity in the cementitious matrix, which allows the corrosion of steel-reinforced bars to spread and affects the mechanical performance of the material. Thus, the durability of the concrete is compromised [160, 161]. On the hand, this attack may be beneficial depending on the time, the extent to which they occur and the environmental exposure [162].

The disparities in the hydrate phase assembly, pore solution chemistry, pore structure, and transport capabilities between geopolymer carbonation concrete and Portland cement (PC) carbonation are related to variations in the concretes' binder compositions, ages, and curing circumstances [163]. The concrete's saturation level and CO_2 partial pressure, which in turn depend on exposure factors such as temperature, relative humidity and the period of contact with water, are all factors in the carbonation mechanism and kinetics [164].

The depth of the CO_2 penetration into cement pastes or concrete at a given time is typically used to describe the materials' resistance to carbonation. This is dependent on the substance's ability to bind CO_2 as well as its porosity and pore size distribution [165]. OPC has shown better binding ability because of the high content of portlandite. In their study of alkali-activated mortars containing waste ceramic powder and GBFS only, Huseien et al. [166], found that increasing the replacement of GBFS with fly ash (FA), increased the carbonation depth. This was attributed to a larger concentration of FA geopolymer materials in the matrix, which resulted in the addition of pore structure as gel formation was constrained to a small amount of Ca, showing a higher permeability and porosity to water than in the control [167, 168].

Compared to geopolymer concrete, ordinary silicate concrete has a different microstructure. and it is impossible to use the tools for carbonation analysis on ordinary concrete. However, geopolymer concrete's carbonation-proof performance is not necessarily superior to that of regular concrete. Prisms of fly ash-based geopolymer concrete were cured in the air for 8 years before their durability test was done by [169]. To assess the effects of carbonation, durability, pore-size distribution, and permeation qualities, large specimens from GPC culverts were compared to standard PC concrete under the same exposure conditions. It was shown that OPC concrete had greater carbonation resistance than GPC. This was attributed to the mix composition or design and the material used in this study.

The curing temperature of geopolymer mortar has been shown to influence the carbonation resistance. The heat-cured GP concrete of HGPC showed greater alkali leaching resistance and stronger carbonation resistance in the wet-dry repeating scenario than the ambient air-cured GP concrete of AGPC. Li & Li. [170], used the test of accelerated carbonation at various intervals and on a wide range of GP mortars and GP concrete to investigate the carbonation depths. At room temperature curing, they observed that the carbonation resistance of GP concrete was lower than the convectional OPC concrete. Heat curing was one of the elements in this study that enhanced GP carbonation resistance, along with other aspects including precursor quantity and fineness, alkali concentration, W/C ratio, and use of retarder.

The alkali solution used to activate the geopolymerization affects the carbonation resistance. The alkali solution's strength and concentration considerably impact both the formation of C-A-S-H gels and the crystallinity of calcium carbonates after carbonation. According to the [171] report, the NaOH slag activated was found to be more carbonation resistant than the NaOH / Na_2SiO_3 slag activated.

It has recently been hypothesized that carbonation affects the porosity and pore size characteristics of GPC concrete [172] studied this phenomenon using three-dimensional thermal neutron tomography, as a conservative analysis technique. They confirmed that carbonation lowered GPC porosity by approximately 30% and pore regions were shifted to smaller regions. This could be associated with the deposition of carbonation reaction products (CO_2 reacting with alkaline hydroxides in the GPC matrix) onto the pores of the concrete. This improves the GPC durability properties as the lower porosity discourages chloride ingress, thereby sustaining strength and corrosion protection [173].

In their investigation to assess the performance of GPC in various exposure conditions, Pasupathy et al. [169], showed that the source material type can also affect the carbonation mechanism and alkalinity of geopolymers. This might be explained by CaO's accessibility in various precursors. In comparison to the GPC with a higher proportion of slag, the fly ash-based geopolymer displayed a lower initial pH value. It was discovered that GPC concrete had higher carbonation levels than OPC concrete in all three environmental situations. However, as the slag component in the geopolymer mix increased, the rate of carbonation decreased. In comparison to the GPC with a higher proportion of slag, the fly ash-based geopolymer displayed a lower initial pH value. The researchers concluded that as compared to OPC, geopolymer concrete is more vulnerable to corrosion and carbonation. Law et al. [174], studied the pH levels of pore water recovered from geopolymer mortar specimens that had undergone 5% rapid carbonation. They suggested a pH level of 11 to safeguard the reinforcing steel after carbonation. In a similar investigation, Li & Li. [175], looked into the connection between GPC's durability and carbonation resistance. The authors reported that the increase in blast furnace slag in the GPC matrix had a corresponding increase in carbonation resistance. Other factors considered in this study were the NaOH content, slag texture and activator solution to active filler ratio.

Calcium carbonate precipitation forms on the OPC concrete's surface as a result of carbonation. This raises the concrete matrix's internal porosity and creates a barrier to carbon dioxide diffusion [176]. Calcium carbonate precipitation in geopolymer may cause volume change because of its poor volumetric stability in the ambient environment thus cracking. Additionally, the rate of carbonation in OPC is lower than that in geopolymer concrete, which is related to a higher Ca/Si ratio in the CSH gel [95, 176]. Based on all these factors, OPC concrete experiences less carbonation-related strength loss compared to geopolymer concrete. According to Marcos-Meson et al. [177], after carbonization, which causes N-A-S-H gel to develop, the compressive strength of fly ash slag-based geopolymers drops linearly. Further, it has been found that after carbonation, the reaction extent and mechanical properties of geopolymer concretes have decreased [156, 178, 179]. Other findings in carbonation have been summarized in Table 3.

4.4. Creep and Shrinkage

Concrete creep and drying shrinkage prediction is still an important parameter in the concrete specification, and it's critical for the long-term durability and serviceability of concrete constructions [183, 184]. While creep refers to the distortion of hardened concrete caused by a steady load, drying shrinkage relates to the cured concrete's internal moisture loss [185, 186]. Most often, shrinkage is described as the volume change in a matrix's geometry brought on by the removal of water from its surface (plastic shrinkage) and the gelling up of the matrix (drying shrinkage). It's also the matrix of a binder's self-desiccation and carbonation of heavier molecules with lighter ones [187]. Non-autogenous shrinkage includes, among other things, thermal deformation, carbonation, shrinkage, drying shrinkage and creep shrinkage [188]. Drying shrinkage is the term used by other researchers to describe a macroscopic dimensional reduction of hardened binders brought on by the evaporation of water or moisture within the products' matrix. When samples are subjected to a certain relative humidity (RH) and ambient temperature, this type of deformation happens [189]. In a comparable situation, plastic shrinkage results from an imbalance in the moisture exchanges between a specimen surface and its surroundings [190].

A chemical reaction on the hydrated concrete, known as autogenous shrinkage, as well as the loss of water as the concrete dries, known as dry shrinkage, are the two main causes of early-age shrinkage of concrete in the hours and days after casting. Typically, autogenous shrinkage increases when the water-to-cement ratio declines for concretes with the same aggregate and binder types, meaning that strength increases and drying shrinkage reduces. Other factors known to influence both creep and drying shrinkage of cement systems include cement type, aggregate type and content, age, temperature, relative humidity of the surroundings, curing, age, and particle size [191].

For moist-cured concrete, the drying shrinkage values suggested in the ACI 209 committee's report shouldn't be more than 800 microstrains, and for steam-cured concrete, they should be between 730 and 788 microstrains [192]. Drying shrinkage causes cracking, and while this may not affect structural integrity, it may raise durability issues, making it one of the most detrimental features of cement concrete. Studies on many components of mixed content and engineering behavior of geopolymers (GP) systems, such as shrinkage and creep, have just lately started to be published. Hardjito & Rangan [193] discovered lower creep coefficient values in their investigation of medium strength GP concrete than the same grade of OPC concrete. These researchers also discovered that as the compressive strength of GP concrete increased, the specific creep dropped. This finding is consistent with traditional OPC concrete. Normal 50 to 60 MPa PC concrete often has particular creep values in the literature that range from 50 to 60 microstrain after one year, with this value decreasing for greater strength concrete. In high-volume performance fly ash concrete, the specific creep was in the range of 30 microstrains per MPa after a year, according to [194].

While the effects of curing on the mechanical properties of GP concrete have not yet been thoroughly established, it has been observed that the drying shrinkage stress of heat-cured concrete specimens is frequently lower than comparable values recorded for ambient-curing concrete [188]. This phenomenon was due to water that is generated during the chemical reaction process of ambient-cured GPs and then evaporates over time, resulting in high drying shrinkage strains, especially during the first two weeks. The engineering performance of GP binders has also been investigated with other material-related features, such as pore network distribution. In their analysis of the pore network distribution of GP binders, Duxson et al. [195] found that there are several clusters of pore diameters that are comparable to those reported in OPC systems. To analyze the basic creep behavior of GP concrete at an early age, this study used similar grade Portland cement concrete as a standard. The studies measured the drying shrinkage response of concrete specimens while assessing the influence of age and stress on real creep at an early age. The drying shrinkage rate was considerably high in the early ages of up to 28 days, according to [196] studies. This research work which was based on GPC based on FA or MK showed drying shrinkage rate decreases beyond this age. They also noted a decrease in drying shrinkage values with an increase in FA and MK contents in the GPC. This is related to the FA or MK enhancing the polymerization process to create high connectivity into the alkali-activated cement matrix. Prior investigations that enhanced the structure have validated the production of products like C-S-H, C-A-S-H, N-A-S-H, and CN-A-S-H [197]. Also, this was due to the decreased calcium content in the cement mix hence reducing the hy-

Table 3. Summary of carbonation finding

Precursor	Activator	Standard used	CO_2 environment	Exposure period	pH	Observations		Reference
						Carbonation depth	Carbonation product	
Low calcium fly ash and granulated blast furnace slag	12M sodium hydroxide +2Ms sodium silicate	AS 1012·9	3% accelerated carbon dioxide	2, 4, 6 weeks	10.9	25 mm	17.4% $NaHCO_3$ in 2 weeks	[156]
			1% accelerated carbon dioxide	2, 4, 6 weeks	<10	2.13	$Na_2CO_3.10H_2O$ in 6 weeks	
			Natural environment	6 months	10.76	3 mm	29% $Na_2CO_3.10H_2O$	
				18 months	10.22	3 mm		
Municipal solid waste incinerator bottom ash and granulated blast furnace slag	Sodium hydroxide (4.8M) and sodium silicate (2.7Ms)	GB /T50107 - 2010	Accelerated 20% carbon dioxide environment, 20+2°C (Lean GPC)	14 days	–	15.53 mm	$NaHCO_3$	[180]
				28 days		20.14 mm		
				60 days		25.65 mm		
			Accelerated 20% carbon dioxide environment, 20+2°C (Modified with 10% slaked lime)	14 days		8.2% reduction	$NaHCO_3$	
				28 days		7.1% reduction		
				60 days		4.8% reduction		
			Accelerated 20% carbon dioxide environment, 20+2°C (Modified with cement)	14 days		37.7% reduction	$NaHCO_3$	
				28 days		37.9% reduction		
				60 days		39.8% reduction		
Class F fly ash	Sodium hydroxide (8M) and sodium silicate	–	Natural environment (Atmospheric exposure conditions)	8 years	9.92–10.41	45 mm fully carbonated, 70 mm partially carbonated	Na_2CO_3	[169]
Class F fly ash	Sodium hydroxide (8M) and sodium silicate	–	Natural environment (saline environment)	6 years	<7.5	135 mm exposed, 90 mm covered	Na_2CO_3	[181]
Class F fly ash	Sodium hydroxide (12M) and sodium silicate	BS EN 14630	Natural saline environment	28–120 days	–	Undetected	Undetected	[182]

dration rate of alkali-activated concrete. Other researchers have shown similar results of GPC concrete exhibiting lower drying shrinkage with the standard sample concrete as well as decreasing dry shrinkage values with an increase in the replacement of alkali-activated concrete [91, 198].

The creep and shrinkage are highly dependent on the curing conditions to which the concrete is exposed GPC concrete can be heat cured or cured in ambient temperatures, practices that induce varying creep and shrinkage effects. To investigate the most suitable curing conditions for GPC Khan et al. [199], studied early age shrinkage and creep. Two GPC mixes were cured at temperatures between 60 °C to 90 °C and ambient temperature. Axial tension was applied to unreinforced dog bone specimens, and it was shown that the curing temperature and time had an impact on the GPC's tensile creep coefficient and shrinkage. High temperatures were related to low early age shrinkage and high tensile creep coefficient. This was in agreement with a study by Frayyeh & Kamil [200] who observed that autogenous shrinkage would further be improved by the use of hooked-end steel fibers. In their study, an increase in hooked-end steel fiber content in the matrix has a corresponding decrease in autogenous shrinkage and tensile creep. They also went further to explore this concept by studying the effect of different reinforcing fibers on the dry shrinkage of geopolymer concrete. They used steel, propylene and carbon fibers. It was reported that improvement was generally seen across all the fibers, but steel fibers showed the highest effect. This was so since metallic fibers are generally stiff and therefore improve the concrete's flexural strength. Non-metallic fibers have a larger surface area and can control plastic shrinkage as a result [201]. Alkaline-activated natural pozzolans geopolymer binder was studied by [202], who claimed that the product's shrinkage was influenced by the curing method and chemical make-up of the basic materials. They also mentioned a connection between shrinkage and the Si/Na ratio.

Another factor that directly influences the creep and shrinkage of GPC is the void structure, which represents the bleeding behavior of concrete. Nazari et al. [203] studied the concept of void distribution patterns and their contribution to strength development in both OPC and GPC. The researchers found a correlation between the bleeding rate of concrete to dry shrinkage and concluded that modification of the bleeding rate is a necessary step to reduce early cracking in hardened concrete. They investigated the effect of slag content on the bleeding rate and found that slag reverses the indirect effect of void volume on the strength development of concrete. Similar conclusions were drawn by Negahban et al. [204] who concluded that pore structure and the distribution of voids are functions of strength development. Other findings on creep and shrinkage have been summarized in Table 4.

4.5. Thermal Performance

The global building and construction industry are very concerned about the longevity of structures made of cement. Cement-based materials are certified to be structurally sound at room temperature. Each year, it is reported that dangerous flames devastate a large number of cement-based structures around the world, causing staggering financial damage. Hazardous fires that affect these structures are largely caused by residential fires and electrical problems. In dangerous fires, these materials are subjected to temperatures that can be destructive. Due to thermal impacts on pore water and products, high temperatures have an impact on the concrete/mortar matrix's physical and chemical properties. Hazardous fires, therefore, shorten the service life of structures made of cement [206, 207].

In recent decades, research has increasingly focused on issues related to building materials' thermal performance and fire resistance. Thermal stability is essential for ensuring that they are safe to use within a specific temperature range with OPC beginning to lose strength irreversibly at 200 °C [208]. This occurs as a result of the principal binding phases, CSH, Ca(OH), and other hydrated products, deteriorating and losing water. Despite this, Jeon et al. [209], found that the breakdown of $Ca(OH)_2$ did not result in a significant loss of strength. However, the main cause of OPC strength reduction is the expansion of lime after chilling.

In past years, there have been a lot of studies done on the thermal characteristic of geopolymers exposed to high heat or fire. Geopolymers, like OPC, lose strength when exposed to high temperatures. Despite this, they maintained a substantially higher binding strength at the temperature range tested. Rivera et al. [210], investigated the effect of elevated temperature on alkali-activated geopolymeric binders compared to portland cement-based binders. The alkali-activated geopolymer showed minimal damage after the temperature exposure of up to 565 °C.

Geopolymer weight decrease is associated with higher strength retention [184]. Geopolymer mortars with a high concentrated slag showed increased strength loss at high temperatures of 600 °C, owing to the decomposition of CSH phases. Despite this, all blended geopolymer mortars-maintained strength between 23 and 25 MPa after being exposed to 600 °C. Compared to geopolymer mortar, geopolymer concrete lost less weight but lost more strength as the temperature increased. The difference in the thermal increase in volume between coarse aggregates as well as binder and the decreased binder concentration in concrete to combat paste shrinkage lead to considerable microcracking. They stated that geopolymers outlast regular concrete and even some high-performance concrete in terms of heat endurance.

Table 4. Summary of shrinkage and creep finding

Precursor	Activator	Modifier	Standard used	Cure conditions	Initial parameters	Shrinkage and creep	Notes	Reference
Fly ash, sodium promotor and sand	10M NaOH and 2.5Ms Na_2SiO_3	1% 3mm polypropylene fiber	RILEM TC 107-CSP (creep strain tests)	75°C for 24h (synthesis conditions) 25 °C, relative humidity 30% (ambient cure conditions)	Compressive = 55.1 MPa @ 28 days	Shrinkage = 0.0002 mm/mm, Creep = 0.0013 mm/mm	• To measure creep and shrinkage strains, 20% of the ultimate compressive force was applied. • Creep and shrinkage data were collected up to the 35th day.	[192]
		5% 3 mm polypropylene fiber			Compressive = 33.9 MPa @ 28 days	Shrinkage = 0.0005 mm/mm, Creep = 0.0007 mm/mm		
		1% 18mm steel fiber			Compressive = 48.4 MPa @ 28 days	Shrinkage = 0.0009 mm/mm, Creep = 0.0021 mm/mm		
		Unmodified (plain GPC)			Compressive = 52.5 MPa @ 28 days	Shrinkage = 0.0006 mm/mm, Creep = 0.0015 mm/mm		
Fly ash	12M NaOH and 2.5Ms $NaSiO_3$	1 wt% carbon fiber	24h at 75 °C	EN 12390-3:2009 (compressive strength)	Compressive loading rate 0.7MPa/s	Creep = 0.00065 mm/mm	1. Creep test at 20% ultimate compressive strength	[188]
Fly ash, granulated blast furnace slag	NaOH and $NaSiO_3$	–	25 °C for 24h (ambient curing), 70 °C for 6h (Accelerated curing)	AS – 1379	Compressive = 62 MPa (ambient), 56.5 MPa (accelerated) Flexural = 7.1 MPa Indirect Tensile =5.1 MPa	Shrinkage = 450 microstrains Creep coefficient = 1.87	2. There was no significant increment in creep after 56 days 3. Compressive, flexural and tensile data was at 28 days	[205]

Furthermore, according to Jiang et al. [211], fly ash, geopolymers preserved strength up to 400 °C and grew stronger at temperatures above 400 °C. In alkali-activated fly ash, crystallization of thermally stable minerals such as sodalite and nepheline was found. XRD diffractograms of geopolymer samples mostly revealed crystalline phases of nepheline when exposed to high temperatures. The presence of thermally stable crystalline phases is critical for geopolymer structure thermal stability. In addition, the solidification of melted stages aided in the development of strength. OPC, on the other hand, maintained compressive strength up to 600 °C before rapidly deteriorating beyond that temperature due to moisture loss and $Ca(OH)_2$ breakdown. The transformation of amorphous aluminosilicates into a geopolymer structure was revealed to be strongly reliant on the geopolymer's compressive strength. The resistance of the material to high temperatures and burning was influenced by the Si/Al ratio and iron content in the fly ash. According to Wang et al. [144], metakaolin-fly ash-based geopolymers have a strength of 46 MPa at 1000 °C. The high-temperature performance was improved with the addition of electrical porcelain as aggregates. The thermal stability of potassium-based metakaolin geopolymers up to 1200 °C was also examined by Jaya et al. [212] in terms of shrinkage and microstructural changes. The optimum densification temperature increases with the addition of quartz sand or alumina powder. When fly ash and metakaolin geopolymers were compared, it was shown that the latter are more tolerant of high temperatures [213]. To improve the thermal characteristics of geopolymer, fibers such as ash wollastonite and basalt fibers could be incorporated. Furthermore, porous materials could serve as a thermal barrier. One of the most important research areas is the creation of lightweight porous materials. Faster construction, improved thermal performance, and fire resistance are all advantages of lightweight building materials. During the foaming process, small pores or linked voids can be added to lightweight porous geopolymer materials which are also known as geopolymer foams. Air bubbles or endogenous gas production could be used to introduce the foam like hydrogen peroxide, aluminum powder or sodium hypochlorite. The gas-forming ingredient in this experiment was hydrogen peroxide. Equation (12) illustrates how hydrogen peroxide breaks down into water and oxygen in an alkaline atmosphere.

$$H_2O_2 \rightarrow 2H_2O + O_2 \quad (12)$$

Regarding the foamed geopolymers' thermal characteristics Cheng-Yong et al. [213], found that when the lightweight porous geopolymer based on glass cullet and red mud were subjected to temperatures between 600 and 800 °C, their volume increased. The foamed geopolymer has a strength of more than 2 MPa and a density of less than 866 kg/m^3. To create greater strength foamed fly ash geopolymers of between 2 MPa to 30 MPa and with densities less than 1000 kg/m^3. Wang et al. [214], utilized 30 percentage slag replacements. The fly ash geopolymer foam maintained its strength well up to 400 °C, and it strengthened much more at 800 °C. According to Cheng-Yong et al. [213], the geopolymer foam did not break or crumble below 1000 °C. Significant shrinkage and sintering are associated with high thermal resistance at high temperatures. As far as we are aware, there is not a lot of literature on the thermal performance and fire resistance of foamed geopolymer materials. Most people believe that porous geopolymer foam behaves similarly to dense geopolymer foam when exposed to high temperatures and fire.

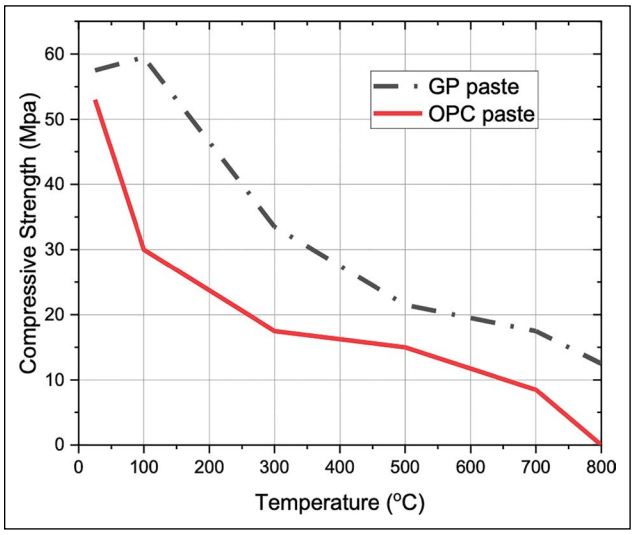

Figure 6. Geopolymer and OPC paste compressive strength comparison [215].

In their research on the creation of MK-FA-based geopolymers for applications requiring fire resistance, geopolymers' compressive strength was higher than OPC pastes', according to research by Zhang et al. [215]. As demonstrated in Figure 6, after exposure to 800 °C, geopolymer paste retained 22% of its compressive strength while OPC paste lost all of it.

According to this, MK-FA-based geopolymer paste showed greater compressive strength than OPC paste at room temperature or after being exposed to high temperatures [168]. At temperatures above 400°, the compressive strength of geopolymer concrete typically remains constant and degrades at a rather gradual rate [216]. Work on FA-slag GPL that was heated up to 1000 o C was done by Chithambaram et al. [217]. The weight reduction rate increased as the temperature rose from 200 °C to 1000 °C, regardless of the alkali content. The reduction of the crystalline nature caused by the inclusion of GGBS resulted in increased strength and polymerization. The rate of polymerization slows down as the temperature is raised above 600 °C, which results in a minor loss of strength.

5. CONCLUSION

This study demonstrated that natural pozzolans, industrial-by products and agro-wastes are a key precursor in the production of geopolymers. The following conclusions are based on the review articles;

1. The geopolymer mortar/ concrete exhibits high resistance to both chemical and acid attack compared to conventional cements
2. OPC concrete possess a greater carbonation resistance than GPC because of its better binding ability associated with high content of portlandite
3. Increasing the alkali activator concentration to some extend demostrates an increase in resilience to both acid and salts attack
4. Temperature, relative humidity and the period of contact with water contribute to the carbonation mechanism and kinetics
5. Geopolymers has shown excellent resistance to temperature extreme compared to convectional cement.

6. AREAS OF FUTURE RESEARCH

There hasn't been any research done on the creation of geopolymer binders using a binary of coconut shell ash and waste from calcined clay bricks. Therefore, based on the research reviewed here, the following topics have been identified for further study in order to decrease the consumption of natural resources and to minimise other environmental effects related to the manufacturing of OPC:

1. Mechanical and durability features of geopolymer cement using alkali-activated calcined clay brick waste from production as well as building sites to ascertain its potential as a geopolymer cement. High alkalinity boasts a higher degree of reaction and maintains a matrix density that tends to prohibit the permeation of corrosive elements into the internal framework of geopolymer cements.
2. Mechanical and durability features of geopolymer cement using alkali-activated coconut shell ash as the primary source materials to ascertain its potential as a geopolymer cement.
3. A blend of alkali-activated coconut shell ash-calcined clay bricks waste mechanical and durability properties to evaluate its binding suitability.
4. Life cycle assessment of geopolymers resulting from coconut shell ash - calcined clay bricks waste to present the sustainability of these products and the potential benefit of such technology.

ETHICS

There are no ethical issues with the publication of this manuscript.

DATA AVAILABILITY STATEMENT

The authors confirm that the data that supports the findings of this study are available within the article. Raw data that support the finding of this study are available from the corresponding author, upon reasonable request.

CONFLICT OF INTEREST

The authors declare that they have no conflict of interest.

FINANCIAL DISCLOSURE

The authors declared that this study has received no financial support.

PEER-REVIEW

Externally peer-reviewed.

REFERENCES

[1] Datau, S. G., Bawa, M. A., Jatau, J. S., Muhammad, M. H., & Bello, A. S. (2020). The potentials of kyanite particles and coconut shell ash as strengthener in aluminum alloy composite for automobile brake disc. *Journal of Minerals and Materials Characterization and Engineering*, 8(3), 84–96. [CrossRef]

[2] Minkova, V., Marinov, S. P., Zanzi, R., Björnbom, E., Budinova, T., Stefanova, M., & Lakov, L. (2000). Thermochemical Treatment of Biomass in a Flow of Steam or in a Mixture of Steam and Carbon Dioxide. *Fuel Processing Technology*, 62(1), 45–52. [CrossRef]

[3] Putun, A. E., Ozbay, N., Onal, E. P., & Putun, E. (2005). Fixed-bed pyrolysis of cotton stalk for liquid and solid products. *Fuel Processing Technology*, 86(11), 1207–1219. [CrossRef]

[4] Savova, D., Apak, E., Ekinci, E., Yardim, F., Petrov, N., Budinova, T., Razvigorova, M., & Minkova, V. (2001). Biomass conversion to carbon adsorbents and gas. *Biomass and Bioenergy*, 21(2), 133–142. [CrossRef]

[5] Tsai, W., Chang, C. Y., & Lee, S. L. (1997). Preparation and characterization of activated carbons from corn cob. *Carbon*, 35(8), 1198–1200. [CrossRef]

[6] Intiya, W., Thepsuwan, U., Sirisinha, C., & Sae-Oui, P. (2017). Possible use of sludge ash as filler in natural rubber. *Journal of Material Cycles and Waste Management*, 19(2), 774–781. [CrossRef]

[7] Jalali, M., & Aboulghazi, F. (2013). Sunflower stalk, an agricultural waste, as an adsorbent for the removal of lead and cadmium from aqueous solutions. *Journal of Material Cycles and Waste Management*, 15(4), 548–555. [CrossRef]

[8] Fan, M., Marshall, W., Daugaard, D., & Brown, R. C. (2004). Steam activation of chars produced from oat hulls and corn stover. *Bioresource Technology*, 93(1), 103–107. [CrossRef]

[9] Ahmedna, M., Marshall, W. E., & Rao, R. M. (2000). Production of granular activated carbons from select agricultural by-products and evaluation of their physical, chemical and adsorption properties. *Bioresource Technology*, 71(2), 113–123. [CrossRef]

[10] El-Dakroury, A., & Gasser, M. S. (2008). Alkali-activated materials. *Journal of Nuclear Materials*, 381(3), 271–277. [CrossRef]

[11] Asavapisit, S., & Macphee, D. E. (2007). Immobilization of metal-containing waste in alkali-activated lime–RHA cementitious matrices. *Cement and Concrete Research*, 37(5), 776–780. [CrossRef]

[12] Nair, D. G., Jagadish, K. S., & Fraaij, A. (2006). Reactive pozzolanas from rice husk ash: An alternative to cement for rural housing. *Cement and Concrete Research*, 36(6), 1062–1071. [CrossRef]

[13] Salas, D. A., Ramirez, A. D., Ulloa, N., Baykara, H., & Boero, A. J. (2018). Life cycle assessment of geopolymer concrete. *Construction and Building Materials*, 190, 170–177. [CrossRef]

[14] Elbasir O. (2020). Influence of cement content on the compressive strength and engineering properties of palm oil fuel ash-based hybrid alkaline cement. Influence of cement content on the compressive strength and engineering properties of palm oil fuel ash-based hybrid alkaline cement. *Third International Conference on Technical Sciences* (ICST2020), 28 - 30 November 2020, Tripoli – Libya.

[15] Kim, D., Lai, H. T., Chilingar, G. V., & Yen, T. F. (2006). Geopolymer formation and its unique properties. *Environmental Geology*, 51(1), 103–111. [CrossRef]

[16] Zhang, Y. J., Wang, Y. C., Xu, D. L., Li, S. (2010). Mechanical performance and hydration mechanism of geopolymer composite reinforced by resin. *Materials Science and Engineering*, 527(24-25), 6574–6580. [CrossRef]

[17] Juenger, M. C. G., Winnefeld, F., Provis, J. L., Ideker, J. H. (2011). Advances in alternative cementitious binders. *Cement and Concrete Research*, 41(12), 1232–1243. [CrossRef]

[18] Duxson, P., Provis, J. L., Lukey, G. C., & Van Deventer, J. S. (2007). The role of inorganic polymer technology in the development of 'Green Concrete'. *Cement And Concrete Research*, 37(12), 1590–1597. [CrossRef]

[19] Duxson, P., Fernández-Jiménez, A., Provis, J. L., Lukey, G. C., Palomo, A., & Van Deventer, J. S. (2007). Geopolymer technology: The current state of the art. *Journal of Materials Science*, 42(9), 2917–2933. [CrossRef]

[20] Palomo, A., Grutzeck, M. W., & Blanco, M. T. (1999). Alkali-activated fly ashes: A cement for the future. *Cement and Concrete Research*, 29(8), 1323–1329. [CrossRef]

[21] Behera, M., Bhattacharyya, S. K., Minocha, A. K., Deoliya, R., & Maiti, S. (2014). Recycled aggregate from C&D waste & its use in concrete–A breakthrough towards sustainability in construction sector: A review. *Construction and Building Materials*, 68, 501–516. [CrossRef]

[22] McLellan, B. C., Williams, R. P., Lay, J., Van Riessen, A., & Corder, G. D. (2011). Costs and carbon emissions for geopolymer pastes in comparison to ordinary Portland cement. *Journal of Cleaner Production*, 19(9-10), 1080–1090. [CrossRef]

[23] Xu, H.P., & Deventer, J.V. (2003). Effect of source materials on geopolymerization. *Industrial & Engineering Chemistry Research*, 42(8), 1698–1706. [CrossRef]

[24] Akcaoglu, T., Cubukcuoglu, B., & Awad, A. (2019). A critical review of slag and fly-ash based geopolymer concrete. *Computers and Concrete*, 24(5), 453–458.

[25] Wang, W., Liu, X., Guo, L., & Duan, P. (2019). Evaluation of properties and microstructure of cement paste blended with metakaolin subjected to high temperatures. *Materials*, 12(6), Article 941. [CrossRef]

[26] Wang, K. (2004). *Proceedings of the International Workshop on Sustainable Development and Concrete Technology*, Beijing, China, May 20-21, 2004. Center for Transportation Research and Education, Iowa State University; 2004.

[27] Khale, D., & Chaudhary, R. (2007). Mechanism of geopolymerization and factors influencing its development: A review. *Journal of Materials Science*, 42(3), 729–746. [CrossRef]

[28] Oh, J. E., Monteiro, P. J., Jun, S. S., Choi, S., & Clark, S. M. (2010). The evolution of strength and crystalline phases for alkali-activated ground blast furnace slag and fly ash-based geopolymers. *Cement and Concrete Research*, 40(2), 189–196. [CrossRef]

[29] Garcia-Lodeiro, I., Donatello, S., Fernández-Jimenez, A., & Palomo, A. (2013). Basic principles of hybrid alkaline cements. *Romanian Journal of Materials*, 42(4), 330–335.

[30] Palomo, Á., Maltseva, O., García-Lodeiro, I., & Fernández-Jiménez, A. (2013). Hybrid alkaline cements. Part II: The clinker factor. *Romanian Journal of Materials*, 43(1), 74–80.

[31] Garcia-Lodeiro, I., Fernandez-Jimenez, A., & Palomo, A. (2013). Hydration kinetics in hybrid binders: Early reaction stages. *Cement and Concrete Composites*, 39, 82–92. [CrossRef]

[32] Provis, J. L. (2018). Alkali-activated materials. *Cement and Concrete Research*, 114, 40–48. [CrossRef]

[33] Singh, B., Ishwarya, G., Gupta, M., & Bhattacharyya, S. K. (2015). Geopolymer concrete: A review of some recent developments. *Construction and Building Materials*, 85, 78–90. [CrossRef]

[34] Naveena, K., & Rao, H. S. (2016). A review on strength and durability studies on geopolymer concrete produced with recycled aggregates. *International Journal for Scientific Research and Development*, 4(07), 27–30.

[35] Givi, A. N., Rashid, S. A., Aziz, F. N. A., & Salleh, M. A. M. (2010). Contribution of rice husk ash to the properties of mortar and concrete: A review. *Journal of American Science*, 6(3), 157–165.

[36] Feng, D., Provis, J. L., & Van Deventer, J. S. J. (2012). Thermal activation of albite for the synthesis of one-part mix geopolymers. *Journal of the American Ceramic Society*, 95(2), 565–572. [CrossRef]

[37] Duxson, P., & Provis, J. L. (2008). Designing precursors for geopolymer cements. *Journal of The American Ceramic Society*, 91(12), 3864–3869. [CrossRef]

[38] Koloušek, D., Brus, J., Urbanova, M., Andertova, J., Hulinsky, V., & Vorel, J. (2007). Preparation, structure and hydrothermal stability of alternative (sodium silicate-free) geopolymers. *Journal of Materials Science*, 42(22), 9267–9275. [CrossRef]

[39] Samadhi, T. W., Wulandari, W., Prasetyo, M.I., & Fernando MR. (2017). Reuse of coconut shell, rice husk, and coal ash blends in geopolymer synthesis. IOP Conference Series: *Materials Science and Engineering*, 248, Article 012008. [CrossRef]

[40] Xu, H., & Van Deventer, J. S. J. (2000). The geopolymerisation of alumino-silicate minerals. *International Journal of Mineral Processing*, 59(3), 247–266. [CrossRef]

[41] Provis, J. L., Palomo, A., & Shi, C. (2015). Advances in understanding alkali-activated materials. *Cement and Concrete Research*, 78, 110–125. [CrossRef]

[42] Mucsi, G., & Ambrus, M. (2017). Raw materials for geopolymerisation. In: *The Publications of the MultiScience - XXXI. MicroCAD International Scientific Conference*. University of Miskolc, 2017. [CrossRef]

[43] Mucsi, G., Kumar, S., Csőke, B., Kumar, R., Molnár, Z., Rácz, Á., Mádai, F., & Debreczeni, Á. (2015). Control of geopolymer properties by grinding of land filled fly ash. *International Journal of Mineral Processing*, 143, 50–58. [CrossRef]

[44] Balczár, I., Korim, T., Kovács, A., & Makó, É. (2016). Mechanochemical and thermal activation of kaolin for manufacturing geopolymer mortars–comparative study. *Ceramics International*, 42(14), 15367–15375. [CrossRef]

[45] Rashad, A. M. (2013). Metakaolin as cementitious material: History, scours, production and composition–A comprehensive overview. *Construction and Building Materials*, 41, 303–318. [CrossRef]

[46] Tironi, A., Trezza, M. A., Scian, A. N., & Irassar, E. F. (2013). Assessment of pozzolanic activity of different calcined clays. *Cement and Concrete Composites*, 37, 319–327. [CrossRef]

[47] Vizcayno, C., De Gutierrez, R. M., Castelló, R., Rodríguez, E., & Guerrero, C. E. (2010). Pozzolan obtained by mechanochemical and thermal treatments of kaolin. *Applied Clay Science*, 49(4), 405–413. [CrossRef]

[48] Marangu, J. M., Riding, K., Alaibani, A., Zayed, A., Thiong'o, J. K., & Wachira, J. M. (2020). Potential for selected kenyan clay in production of limestone calcined clay cement. Springer. [CrossRef]

[49] Yip, C. K., & Van Deventer, J. S. J. (2003). Microanalysis of calcium silicate hydrate gel formed within a geopolymeric binder. *Journal of Materials Science*, 38(18), 3851–3860. [CrossRef]

[50] Charles, E. W., & Lin DP. (2009). The chemistry of clay minerals weaver. Charles E.; Pollard, Lin D. 2009. https://masterpdf.pro/download/4330427-the-chemistry-of-clay-minerals-weaver-charles-e-pollard-lin-d Accessed September 9, 2022.

[51] Kadhim, A., Sadique, M., Al-Mufti, R., & Hashim, K. (2021). Developing one-part alkali-activated metakaolin/natural pozzolan binders using lime waste. *Advances in Cement Research*, 33(8), 342–356. [CrossRef]

[52] Rocha, J., & Klinowski, J. (1990). Solid-state NMR studies of the structure and reactivity of metakaolinite. *Angewandte Chemie International Edition*, 29(5), 553–554. [CrossRef]

[53] Mlinárik, L., & Kopecskó, K. (2013). Impact of metakaolin - a new supplementary material - on the hydration mechanism of cements. *Civil Engineering*, 56(2), Article 11.

[54] Ngui, F. M., Wachira, J. M., Thiong'o, J. K., & Marangu, J. M. (2019). Performance of Ground Clay Brick Mortars in Simulated Chloride and Sulphate Media. *Journal of Engineering*, 2019, Article 6430868. [CrossRef]

[55] Dubois, J., Murat, M., Amroune, A., Carbonneau, X., & Gardon, R. (1995). High-temperature transformation in Kaolinite: The role of the crystallinity and of the firing atmosphere. *Applied Clay Science*, 10(3), 187–198. [CrossRef]

[56] Shvarzman, A., Kovler, K., Grader, G. S., & Shter, G. E. (2003). The effect of dehydroxylation/amorphization degree on pozzolanic activity of kaolinite. *Cement and Concrete Research*, 33(3), 405–416. [CrossRef]

[57] Sha, W., & Pereira, G. B. (2001). Differential scanning calorimetry study of ordinary Portland cement paste containing metakaolin and theoretical approach of metakaolin activity. *Cement and Concrete Composites*, 23(6), 455–461. [CrossRef]

[58] Zhang, Z., Provis, J. L., Reid, A., & Wang, H. (2014). Geopolymer foam concrete: An emerging material for sustainable construction. *Construction and Building Materials*, 56, 113–127. [CrossRef]

[59] Provis, J. L., & Bernal, S. A. (2014). Geopolymers and related alkali-activated materials. *Annual Review of Materials Research*, 44, 299–327. [CrossRef]

[60] Toniolo, N., & Boccaccini, A. R. (2017). Fly ash-based geopolymers containing added silicate waste. A review. *Ceramics International*, 43(17), 14545–14551. [CrossRef]

[61] Payá, J., Monzó, J., Borrachero, M. V., & Tashima, M. M. (2015). Reuse of Aluminosilicate Industrial Waste Materials in the Production of Alkali-Activated Concrete Binders. *In Handbook of Alkali-Activated Cements, Mortars and Concretes*. F. Pacheco-Torgal, J. A. Labrincha, C. Leonelli, A. Palomo, P. Chindaprasirt, (Eds.), (pp. 487–518). Woodhead Publishing. [CrossRef]

[62] Arafa, S. A., Ali, A. Z. M., Awal, A. S. M. A., & Loon, L. Y. (2018). Optimum mix for fly ash geopolymer binder based on workability and compressive strength. *IOP Conference Series: Earth and Environmental Science*, 140, Article 012157. [CrossRef]

[63] Komnitsas, K., & Zaharaki, D. (2007). Geopolymerisation: A review and prospects for the minerals industry. *Minerals Engineering*, 20(14), 1261–1277. [CrossRef]

[64] Swanepoel, J. C., & Strydom, C. A. (2002). Utilisation of fly ash in a geopolymeric material. *Applied Geochemistry,* 17(8), 1143–1148. [CrossRef]

[65] Kumar, S., Djobo, J. N. Y., Kumar, A., & Kumar, S. (2016). Geopolymerization behavior of fine iron-rich fraction of brown fly ash. *Journal of Building Engineering*, 8, 172–178. [CrossRef]

[66] Lloyd, R. R., Provis, J. L., & Van Deventer, J. S. (2009). Microscopy and microanalysis of inorganic polymer cements. 2: The gel binder. *Journal of Materials Science*, 44(2), 620–631. [CrossRef]

[67] Kumar, S., Kumar, R., & Mehrotra, S. P. (2010). Influence of granulated blast furnace slag on the reaction, structure and properties of fly ash based geopolymer. *Journal of Materials Science*, 45(3), 607–615. [CrossRef]

[68] Higuera, I., Varga, C., Palomo, J. G., Gil-Maroto, A., Vázquez, T., Puertas, F. (2012). Mechanical behaviour of alkali-activated blast furnace slag-activated me-takaolin blended pastes, Statistical study. *Materiales de Construcción*, 62(306):163–181. [CrossRef]

[69] Roy, D. M. (1999). Alkali-activated cements opportunities and challenges. *Cement and Concrete Research*, 29(2), 249–254. [CrossRef]

[70] Yip, C. K., Lukey, G. C., & van Deventer Dean, J. S. J. (2012). Effect of blast furnace slag addition on microstructure and properties of metakaolinite geopolymeric materials. In: N. P. Bansal, J. P. Singh, W.M. Kriven, H. Schneider, (Eds,). *Ceramic Transactions Series* (pp. 187–209). John Wiley & Sons, Inc. [CrossRef]

[71] Buchwald, A., Hilbig, H., & Kaps, C. (2007). Alkali-activated metakaolin-slag blends—performance and structure in dependence of their composition. *Journal of Materials Science*, 42(9), 3024–3032. [CrossRef]

[72] Hadi, M. N., Farhan, N. A., & Sheikh, M. N. (2017). Design of geopolymer concrete with GGBFS at ambient curing condition using Taguchi method. *Construction and Building Materials*, 140, 424–431. [CrossRef]

[73] Hasnaoui, A., Ghorbel, E., & Wardeh, G. (2021). Effect of curing conditions on the performance of geopolymer concrete based on granulated blast furnace slag and metakaolin. *Journal of Materials in Civil Engineering*, 33(3), Article 04020501. [CrossRef]

[74] Dani, M., Borad, J., & Shukla, R. (2015). Review on utilization ofmodified red mud by organic modifier in composite material. *International Journal of Advance Research in Science and Engineering*, 4(3), 216–225. [CrossRef]

[75] Alshaaer, M., & Jeon, H. Y. (2020). *Geopolymers and other geosynthetics*. Intech Open. [CrossRef]

[76] Kumar, A., & Kumar, S. (2013). Development of paving blocks from synergistic use of red mud and fly ash using geopolymerization. *Construction and Building Materials*, 38, 865–871. [CrossRef]

[77] Liang, X., & Ji, Y. (2021). Experimental study on durability of red mud-blast furnace slag geopolymer mortar. *Construction and Building Materials*, 267, Article 120942. [CrossRef]

[78] Mucsi G., Szabó, R., Rácz, Á., Kristály, F., & Kumar S. (2019). Combined utilization of red mud and mech,anically activated fly ash in geopolymer. *Rudarsko-Geološko-Naftni Zbornik*. 34(1), Article 44. [CrossRef]

[79] Vance, E. R., Perera, R., Imperia, D. S., Cassidy, P., Davis, D. J., & Gourley, J. T. (2009). Perlite waste as a precursor for geopolymer formation. *Journal of the Australian Ceramic Society*, 45(1), 44-49. [CrossRef]

[80] Vaou, V., & Panias, D. (2010). Thermal insulating foamy geopolymers from perlite. *Minerals Engineering*, 23(14), 1146–1151. [CrossRef]

[81] Fernández-Jiménez, A., García-Lodeiro, I., & Palomo, A. (2007). Durability of alkali-activated fly ash cementitious materials. *Journal of Materials Science*, 42(9), 3055–3065. [CrossRef]

[82] Shi, C., Jiménez, A. F., & Palomo, A. (2011). New cements for the 21st century: The pursuit of an alternative to Portland cement. *Cement and Concrete Research*, 41(7), 750–763. [CrossRef]

[83] Davidovits, J. (1991). Geopolymers: Inorganic polymeric new materials. *Journal of Thermal Analysis and Calorimetry*, 37(8), 1633–1656. [CrossRef]

[84] Catauro, M., Dal Poggetto, G., Sgarlata, C., Ciprioti, S. V., Pacifico, S., & Leonelli, C. (2020). Thermal and microbiological performance of metakaolin-based geopolymers cement with waste glass. *Applied Clay Science*, 197, Article 105763. [CrossRef]

[85] Yousef, R. I., El-Eswed, B., Alshaaer, M., Khalili, F., & Rahier, H. (2012). Degree of reactivity of two kaolinitic minerals in alkali solution using zeolitic tuff or silica sand filler. *Ceramics International*, 38(6), 5061–5067.

[86] Davidovits J. (1994). Properties of geopolymer cements. Geopolymer Institue. [CrossRef]

[87] Khan, H. A., Castel, A., & Khan, M. S. (2020). Corrosion investigation of fly ash based geopolymer mortar in natural sewer environment and sulphuric acid solution. *Corrosion Science*, 168, Article 108586. [CrossRef]

[88] Yan, B., Duan, P., & Ren, D. (2017). Mechanical strength, surface abrasion resistance and microstructure of fly ash-metakaolin-sepiolite geopolymer composites. *Ceramics International*, 43(1), 1052–1060.

[89] Shima, P., Szczotok, A. M., Rodríguez, J. F., Valentini, L., & Lanzón, M. (2016). Effect of freeze-thaw cycles on the mechanical behavior of geopolymer concrete and Portland cement concrete containing micro-encapsulated phase change materials. Elsevier Enhanced Reader. [CrossRef]

[90] Zhao, R., Yuan, Y., Cheng, Z., Wen, T., Li, J., Li, F., & Ma, Z. J. (2019). Freeze-thaw resistance of Class F fly ash-based geopolymer concrete. *Construction and Building Materials*, 222, 474–483. [CrossRef]

[91] Huseien, G. F., & Shah, K. W. (2020). Durability and life cycle evaluation of self-compacting concrete containing fly ash as GBFS replacement with alkali activation. *Construction and Building Materials*, 235, Article 117458. [CrossRef]

[92] Puertas, F., & Fernández-Jiménez, A. (2003). Mineralogical and microstructural characterisation of alkali-activated fly ash/slag pastes. *Cement and Concrete Composites*, 25(3), 287–292. [CrossRef]

[93] Detwiler R. J., & Taylor P. C. (2005). Specifier's guide to durable concrete. Engineering Bulletin 221, https://trid.trb.org/view/900218 Accessed on Sep 27, 2022.

[94] Faten, S., Hani, K., Hubert, R., & Jan, W. (2015). Durability of alkali activated cement produced from kaolinitic clay. *Applied Clay Science*, 104, 229–237. [CrossRef]

[95] Chen, K., Wu, D., Xia, L., Cai, Q., Zhang, Z. (2021). Geopolymer concrete durability subjected to aggressive environments – A review of influence factors and comparison with ordinary Portland cement. *Construction and Building Materials*, 279, Article 122496. [CrossRef]

[96] Koenig, A., & Dehn, F. (2016). Main considerations for the determination and evaluation of the acid resistance of cementitious materials. *Materials and Structures*, 49(5), 1693–1703. [CrossRef]

[97] Temuujin, J., Minjigmaa, A., Lee, M., Chen-Tan, N., & Van Riessen, A. (2011). Characterisation of class F fly ash geopolymer pastes immersed in acid and alkaline solutions. *Cement and Concrete Composites*, 33(10), 1086–1091. [CrossRef]

[98] Matalkah, F., Soroushian, P., Balchandra, A., & Peyvandi, A. (2017). Characterization of Alkali-Activated Nonwood Biomass Ash–Based Geopolymer Concrete. *Journal of Materials in Civil Engineering*, 29(4), Article 04016270. [CrossRef]

[99] Bakharev, T. (2005). Resistance of geopolymer materials to acid attack. *Cement and Concrete Research*, 35(4), 658–670. [CrossRef]

[100] Bouguermouh, K., Bouzidi, N., Mahtout, L., Pérez-Villarejo, L., Lourdes, M., & Martínez-Cartas, M. L. (2017). Effect of acid attack on microstructure and composition of metakaolin-based geopolymers: The role of alkaline activator. *Journal of Non-Crystalline Solids*, 463, 128–137. [CrossRef]

[101] Ariffin, M. A. M., Bhutta, M. A. R., Hussin, M. W., Tahir, M. M., & Aziah, N. (2013). Sulfuric acid resistance of blended ash geopolymer concrete. *Construction and Building Materials*, 43, 80–86. [CrossRef]

[102] Sata, V., Sathonsaowaphak, A., & Chindaprasirt, P. (2012). Resistance of lignite bottom ash geopolymer mortar to sulfate and sulfuric acid attack. *Cement and Concrete Composites*, 34(5), 700–708. [CrossRef]

[103] Bernal, S. A., Rodríguez, E. D., Mejía de Gutiérrez, R., & Provis, J. L. (2012). Performance of alkali-activated slag mortars exposed to acids. *Journal of Sustainable Cement-Based Materials*, 1(3), 138–151. [CrossRef]

[104] Dimas, D., Giannopoulou, I., & Panias, D. (2009). Polymerization in sodium silicate solutions: a fundamental process in geopolymerization technology. *Journal of Materials Science*, 44(14), 3719–3730. [CrossRef]

[105] Ajay, A., Ramaswamy, K. P., & Thomas, A. V. (2020). A critical review on the durability of geopolymer composites in acidic environment. *IOP Conference Series: Earth and Environmental Science*, 491(1), Article 012044. [CrossRef]

[106] Chen-Tan, N. W., Van Riessen, A., Ly, C. V., & Southam, D. C. (2009). Determining the] reactivity of a fly ash for production of geopolymer. *Journal of the American Ceramic Society*, 92(4), 881–887. [CrossRef]

[107] Koenig, A., Herrmann, A., Overmann, S., & Dehn, F. (2017). Resistance of alkali-activated binders to organic acid attack: Assessment of evaluation criteria and damage mechanisms. *Construction and Building Materials*, 151, 405–413. [CrossRef]

[108] Roy, D. M., Arjunan, P., & Silsbee, M. R. (2001). Effect of silica fume, metakaolin, and low-calcium fly ash on chemical resistance of concrete. *Cement and Concrete Research*, 31(12), 1809–1813.

[109] Shi, C., & Stegemann, J. A. (2000). Acid corrosion resistance of different cementing materials. *Cement and Concrete Research*, 30(5), 803–808. [CrossRef]

[110] Mori, T., Nonaka, T., Tazaki, K., Koga, M., Hikosaka, Y., & Noda, S. (1992). Interactions of nutrients, moisture and PH on microbial corrosion of concrete sewer pipes. *Water Research*, 26(1), 29–37. [CrossRef]

[111] Davis, J. L., Nica, D., Shields, K., & Roberts, D. J. (1998). Analysis of concrete from corroded sewer pipe. *International Biodeterioration & Biodegradation*, 42(1), 75–84. [CrossRef]

[112] Marquez-Peñaranda, J. F., Sanchez-Silva, M., Husserl, J., & Bastidas-Arteaga, E. (2016). Effects of biodeterioration on the mechanical properties of concrete. *Materials and Structures*, 49(10), 4085–4099. [CrossRef]

[113] Pacheco-Torgal, F., Castro-Gomes, J., & Jalali, S. (2008). Alkali-activated binders: A review: Part 1. Historical background, terminology, reaction mechanisms and hydration products. *Construction and Building Materials*, 22(7), 1305–1314. [CrossRef]

[114] Bernal, S. A., Provis, J. L., Rose, V., & De Gutiérrez, R. M. (2013). High-resolution X-ray diffraction and fluorescence microscopy characterization of alkali-activated slag-metakaolin binders. *Journal of The American Ceramic Society*, 96(6), 1951–1957. [CrossRef]

[115] Davidovits, J. (1994). Geopolymers: man-made rock geosynthesis and the resulting development of very early high strength cement. *Journal of Materials Education*, 16(2-3), 91–139.

[116] Lee, N. K., & Lee, H. K. (2016). Influence of the slag content on the chloride and sulfuric acid resistances of alkali-activated fly ash/slag paste. *Cement and Concrete Composites*, 72, 168–179. [CrossRef]

[117] Bondar, D., Lynsdale, C. J., Milestone, N. B., & Hassani, N. (2015). Sulfate resistance of alkali activated pozzolans. *International Journal of Concrete Structures and Materials*, 9(2), 145–158. [CrossRef]

[118] Lloyd, R. R., Provis, J. L., & Van Deventer, J. S. (2012). Acid resistance of inorganic polymer binders. 1. Corrosion rate. *Materials and Structures*, 45(1), 1–14. [CrossRef]

[119] Bakharev T. (2005). Geopolymeric materials prepared using Class F fly ash and elevated temperature curing. *Cement and Concrete Research*, 35(6), 1224–1232. [CrossRef]

[120] Senhadji, Y., Escadeillas, G., Mouli, M., Benosman, A. S., & Khelafi, H. (2014). Influence of natural pozzolan, silica fume and limestone fine on strength, acid resistance and microstructure of mortar. *Powder Technology*, 254, 314–323. [CrossRef]

[121] Thokchom, S., Dutta, D., & Ghosh, S. (2011). Effect of incorporating silica fume in fly ash geopolymers. *International Journal of Civil and Environmental Engineering*, 5(12), 750–754.

[122] Purbasari, A., Samadhi, T. W., & Bindar, Y. (2012). Sulfuric acid resistance of geopolymer mortars from co-combustion residuals of bamboo and kaolin. *ASEAN Journal of Chemical Engineering*, 18(2), 22–30.

[123] Lavanya, G., & Jegan, J. (2015). Durability study on high calcium fly ash based geopolymer concrete. Advances in *Materials Science and Engineering*, 6, 1–7. [CrossRef]

[124] Song, Y., Liu, J., Hui, Wang., & Shu, H. (2019). Research progress of nitrite corrosion inhibitor in concrete. *International Journal of Corrosion*, 5, 1–9. [CrossRef]

[125] Kumaravel, S., & Girija, K. (2013). Acid and salt resistance of geopolymer concrete with varying concentration of NaOH. *Journal of Engineering Research and Studies*, 4(4), 1–3.

[126] Ramaswamy, K. P., & Santhanam, M. (2019). Degradation kinetics of cement-based materials in citric acid. In A. R. M. Rao, & K. Ramanjaneyulu (Eds.), *Recent Advances in Structural Engineering, Volume 1* (pp. 891–905). Springer. [CrossRef]

[127] Suiryanrayna, M. V., & Ramana, J. V. (2015). A review of the effects of dietary organic acids fed to swine. *Journal of Animal Science and Biotechnology*, 6(1), 1–11. [CrossRef]

[128] Ukrainczyk, N., Muthu, M., Vogt, O., & Koenders, E. (2019). Geopolymer, calcium aluminate, and Portland cement-based mortars: Comparing degradation using acetic acid. *Materials*, 12(19), Article 3115. [CrossRef]

[129] Xie, F., Li, J., Zhao, G., Zhou, P., & Zheng, H. (2020). Experimental study on performance of cast-in-situ recycled aggregate concrete under different sulfate attack exposures. *Construction and Building Materials*, 253, Article 119144. [CrossRef]

[130] Villa, C., Pecina, E. T., Torres, R., & Gómez, L. (2010). Geopolymer synthesis using alkaline activation of natural zeolite. *Construction and Building Materials*, 24(11), 2084–2090. [CrossRef]

[131] Alcamand, H. A., Borges, P. H., Silva, F. A., & Trindade, A. C. C. (2018). The effect of matrix composition and calcium content on the sulfate durability of metakaolin and metakaolin/slag alkali-activated mortars. *Ceramics International*, 44(5), 5037–5044. [CrossRef]

[132] Taylor, H. F. W. (1997). *Cement Chemistry* (2nd ed.). Thomas Telford Publishing. [CrossRef]

[133] Menéndez, E., Matschei, T., & Glasser, F. P. (2013). Sulfate attack of concrete. In: M. Alexander, A. Bertron, N. De Belie, (Eds,). *Performance of Cement-Based Materials in Aggressive Aqueous Environments* (pp. 7–74). Vol 10. RILEM State-of-the-Art Reports. Springer. [CrossRef]

[134] Alexander, M., Bertron, A., & De Belie, N., (Eds.). (2013). *Performance of Cement-Based Materials in Aggressive Aqueous Environments: State-of-the-Art Report*. RILEM TC 211 - PAE. Vol 10. Springer. [CrossRef]

[135] Elyamany, H. E., Abd Elmoaty, M., & Elshaboury, A. M. (2018). Magnesium sulfate resistance of geopolymer mortar. *Construction and Building Materials*, 184, 111–127. [CrossRef]

[136] Ismail, I., Bernal, S. A., Provis, J. L., Hamdan, S., & Van Deventer, J. S. (2013). Microstructural changes in alkali activated fly ash/slag geopolymers with sulfate exposure. *Materials and Structures*, 46(3), 361–373.

[137] Ismail, I., Bernal, S. A., Provis, J. L., San Nicolas, R., Brice, D. G., Kilcullen, A. R., Hamdan, S., & Van Deventer, J. S. (2013). Influence of fly ash on the water and chloride permeability of alkali-activated slag mortars and concretes. *Construction and Building Materials*, 48, 1187–1201. [CrossRef]

[138] Chithambar Ganesh, A., Rajesh Kumar, K., Vinod Kumar, M., et al. (2020). Durability Studies on the Hybrid Fiber reinforced Geopolymer concrete made of M-sand under ambient curing. *IOP Conf Ser: Mater Sci Eng*. 981(3):032074. doi:10.1088/1757-899X/981/3/032074. [CrossRef]

[139] Albitar, M., Ali, M. M., Visintin, P., & Drechsler, M. (2017). Durability evaluation of geopolymer and conventional concretes. *Construction and Building Materials*, 136, 374–385. [CrossRef]

[140] Gupta, A., Gupta, N., Saxena, K. K. (2021). Experimental study of the mechanical and durability properties of Slag and Calcined Clay based geopolymer composite. *Advances in Materials and Processing Technologies*, 10, 1–15.

[141] Thokchom, S., Ghosh, P., & Ghosh, S. (2009). Acid resistance of fly ash based geopolymer mortars. *International Journal of Recent Trends in Engineering*, 1(6), 36-40.

[142] Choi, Y. S., Kim, J. G., & Lee, K. M. (2006). Corrosion behavior of steel bar embedded in fly ash concrete. *Corrosion Science*, 48(7), 1733–1745. [CrossRef]

[143] Noushini, A., Castel, A., Aldred, J., & Rawal, A. (2020). Chloride diffusion resistance and chloride binding capacity of fly ash-based geopolymer concrete. *Cement and Concrete Composites*, 105, Article 103290. [CrossRef]

[144] Wang, A., Zheng, Y., Zhang, Z., Liu, K., Li, Y., Shi, L., & Sun, D. (2020). The durability of alkali-activated materials in comparison with ordinary Portland cements and concretes: A review. *Engineering*, 6(6), 695–706. [CrossRef]

[145] Yuan, Q., Shi, C., De Schutter, G., Audenaert, K., & Deng, D. (2009). Chloride binding of cement-based materials subjected to external chloride environment–a review. *Construction and Building Materials*, 23(1), 1–13. [CrossRef]

[146] Gunasekara, C., Law, D., Bhuiyan, S., Setunge, S., & Ward, L. (2019). Chloride induced corrosion in different fly ash based geopolymer concretes. *Construction and Building Materials*, 200, 502–513. [CrossRef]

[147] de Oliveira, L. B., De Azevedo, A. R., Marvila, M. T., Pereira, E. C., Fediuk, R., & Vieira, C. M. F. (2022). Durability of geopolymers with industrial waste. *Case Studies in Construction Materials*, 16, Article e00839. [CrossRef]

[148] Zhang, J., Shi, C., & Zhang, Z. (2019). Chloride binding of alkali-activated slag/fly ash cements. *Construction and Building Materials*, 226, 21–31. [CrossRef]

[149] Logesh Kumar, M., & Revathi, V. (2021). Durability Performance On Alkali Activated Metakaolin And Bottom Ash Based Geopolymer Concrete. Preprint. https://doi.org/10.21203/rs.3.rs-703480/v1[CrossRef]

[150] Parveen, S., Pham, T. M., Lim, Y. Y., Pradhan S. S., Jatin, & Kumar, J. (2021). Performance of rice husk Ash-Based sustainable geopolymer concrete with Ultra-Fine slag and Corn cob ash. *Construction and Building Materials*, 279, Article 122526. [CrossRef]

[151] Mashaly, A. O., El-Kaliouby, B. A., Shalaby, B. N., El–Gohary, A. M., & Rashwan, M. A. (2016). Effects of marble sludge incorporation on the properties of cement composites and concrete paving blocks. *Journal of Cleaner Production*, 112, 731–741. [CrossRef]

[152] Saranya, P., Nagarajan, P., & Shashikala, A. P. (2021). Performance studies on steel fiber–Reinforced GGBS-dolomite geopolymer concrete. Journal of Materials in *Civil Engineering*, 33(2), Article 04020447. [CrossRef]

[153] Saxena, R., Gupta, T., Sharma, R. K., & Panwar, N. L. (2021). Influence of granite waste on mechanical and durability properties of fly ash-based geopolymer concrete. *Environment, Development and Sustainability*, 23(12), 17810–17834. [CrossRef]

[154] Sravanthi, D., Himath Kumar, Y., Sarath Chandra Kumar, B.. (2020). Comparative study on flow characteristics, strength and durability of GGBS based geopolymer concrete. IOP Conference Series: *Materials Science and Engineering*, 912(6), Article 062032. [CrossRef]

[155] De Ceukelaire, L., & Van Nieuwenburg, D. (1993). Accelerated carbonation of a blast-furnace cement concrete. *Cement and Concrete Research*, 23(2), 442–452. [CrossRef]

[156] Khan, M. S. H., Castel, A., & Noushini, A. (2017). Carbonation of a low-calcium fly ash geopolymer concrete. *Magazine of Concrete Research*, 69(1), 24–34.

[157] Adamczyk, K., Prémont-Schwarz, M., Pines, D., Pines, E., & Nibbering, E. T. J. (2009). Real-time observation of carbonic acid formation in aqueous solution. *Science*, 326(5960), 1690–1694. [CrossRef]

[158] Dubina, E., Korat, L., Black, L., Strupi-Šuput, J., & Plank, J. (2013). Influence of water vapour and carbon di-oxide on free lime during storage at 80°C, studied by Raman spectroscopy. *Spectrochimica Acta Part A: Molecular and Biomolecular Spectroscopy*, 11, 299– 303. [CrossRef]

[159] Fernández-Díaz, L., Fernández-González, Á., & Prieto, M. (2010). The role of sulfate groups in controlling CaCO3 polymorphism. *Geochimica et Cosmochimi-ca Acta*, 74(21), 6064–6076. [CrossRef]

[160] Johannesson, B., & Utgenannt, P. (2001). Microstructural changes caused by carbonation of cement mortar. *Cement and Concrete Research*, 31(6), 925–931. [CrossRef]

[161] Bernal, S. A., de Gutierrez, R. M., Provis, J. L., & Rose, V. (2010). Effect of silicate modulus and metakaolin incorporation on the carbonation of alkali silicate-activated slags. *Cement and Concrete Research*. 40(6), 898–907. [CrossRef]

[162] Liu, J., Yao, S., Ba, M., He, Z., & Li, Y. (2016). Effects of carbonation on micro structures of hardened cement paste. *Journal Wuhan University of Technology, Materials Science Edition*, 31(1), 146–150. [CrossRef]

[163] Zhang, R., & Panesar, D. K. (2020). Carbonated binder systems containing reactive MgO and Portland cement: Strength, chemical composition and pore structure. *Journal of Cleaner Production*, 271, Article 122021. [CrossRef]

[164] von Greve-Dierfeld, S., Lothenbach, B., Vollpracht, A., Wu, B., Huet, B., Andrade C., Medina, C., Thiel, C., Gruyaert, E., Vanoutrive, H., Saez del Bosque, I. F., Ignjatovic, I., Elsen, J., Provis, J. L., Scrivener, K., Thienel K-C., Sideris, K., Zajac, M., Alderete N., Cizer, Ö., Van den Heede, P., Hooton, R.D., Kamali-Bernard, S., Bernal, S. A., Zhao, Z., Shi, Z., & De Belle, N. (2020). Understanding the carbonation of concrete with supplementary cementitious materials: a critical review by RILEM TC 281-CCC. *Materials and Structure*, 53(6), Article 136. [CrossRef]

[165] Leemann A., & Moro, F. (2016). Carbonation of concrete: the role of CO2 concentration, relative humidity and CO2 buffer capacity. *Materials and Structures*, 50(1), Article 30. [CrossRef]

[166] Huseien, G. F., Sam, A. R. M, Shah, K. W., Mirza, J., & Tahir, M. (2019). Evaluation of alkali-activated mortars containing high volume waste ceramic powder and fly ash replacing GBFS. *Construction and Building Materials*, 210, 78–92. [CrossRef]

[167] Morandeau, A. (2014). Investigation of the carbonation mechanism of CH and C-S-H in terms of kinetics, microstructure changes and moisture properties. *Cement and Concrete Research*, 2014, Article 18. [CrossRef]

[168] Aziz, I. H., Al Bakri Abdullah, M. M., Cheng Yong, H., Yun Ming, L., Hussin, K., Azimi, E. A. (2015). A review on mechanical properties of geopolymer composites for high temperature application. *KEM*, 660, 34–38. [CrossRef]

[169] Pasupathy, K., Berndt, M., Sanjayan, J., Rajeev, P., Cheema, D. S. (2018). Durability performance of precast fly ash–based geopolymer concrete under atmospheric exposure conditions. *Journal of Materials in Civil Engineering*, 30(3), Article 04018007. [CrossRef]

[170] Li, Z., & Li, S. (2020). Effects of wetting and drying on alkalinity and strength of fly ash/slag-activated materials. *Construction and Building Materials*, 254, Article 119069. [CrossRef]

[171] Li, N., Farzadnia, N., & Shi, C. (2017). Microstructural changes in alkali-activated slag mortars induced by accelerated carbonation. *Cement and Concrete Research*, 100, 214–226. [CrossRef]

[172] Vu, T. H., Gowripalan, N., De Silva, P., Paradowska, A., Garbe, U., Kidd, P., & Sirivivatnanon, V. (2020). Assessing carbonation in one-part fly ash/slag geopolymer mortar: Change in pore characteristics using the state-of-the-art technique neutron tomography. *Cement and Concrete Composites*, 114, Article 103759. [CrossRef]

[173] Morla, P., Gupta, R., Azarsa, P., & Sharma, A. (2021). Corrosion evaluation of geopolymer concrete made with fly ash and bottom ash. *Sustainability*, 13(1), Article 398. [CrossRef]

[174] Law, D. W., Adam, A. A., Molyneaux, T. K., Patnaikuni, I., & Wardhono, A. (2015). Long term durability properties of class F fly ash geopolymer concrete. *Materials and Structures*, 48(3), 721–731. [CrossRef]

[175] Li, Z., & Li, S. (2018,). Carbonation resistance of fly ash and blast furnace slag based geopolymer concrete. *Construction and Building Materials*, 163, 668–680. [CrossRef]

[176] Bakharev, T., Sanjayan, J. G., Cheng, Y. B. (2001). Resistance of alkali-activated slag concrete to carbonation. *Cement and Concrete Research*, 31(9), 1277–1283. [CrossRef]

[177] Marcos-Meson, V., Fischer, G., Edvardsen, C., Skovhus, T. L., & Michel, A. (2019). Durability of steel fibre reinforced Concrete (SFRC) exposed to acid attack – a literature review. *Construction and Building Materials*, 200, 490–501. [CrossRef]

[178] Park, J. W., Ann, K. Y., & Cho, C. G. (2015). Resistance of alkali-activated slag concrete to chloride-induced corrosion. *Advances in Materials Science and Engineering*, 2015, 1–7. [CrossRef]

[179] Nkwaju, R. Y., Djobo, J. N. Y., Nouping, J. N. F., Huisken, P. W. M., Deutou, J.G. N., & Courard, L. (2019). Iron-rich laterite-bagasse fibers based geopolymer composite: Mechanical, durability and insulating properties. *Applied Clay Science*, 183, Article 105333. [CrossRef]

[180] Huang, G., Ji, Y., Li, J., Hou, Z., & Jin, C. (2018). Use of slaked lime and Portland cement to improve the resistance of MSWI bottom ash-GBFS geopolymer concrete against carbonation. *Construction and Building Materials*, 166, 290–300. [CrossRef]

[181] Pasupathy, K., Berndt, M., Sanjayan, J., Rajeev, P., & Cheema, D. S. (2017). Durability of low calcium fly ash based geopolymer concrete culvert in a saline environment. *Cement and Concrete Research*, 100, 297–310. [CrossRef]

[182] Yahya, Z., Bakri Abdullah, M. M. A., Jing, L. Y., Li, L.Y., & Razak, R. A. (2020). Seawater exposure effect on fly ash based geopolymer concrete with inclusion of steel fiber. IOP Conference Series: *Materials Science and Engineering*, 743(1), Article 012013. [CrossRef]

[183] Xu, T., Huang, J., Castel, A., Zhao, R., & Yang, C. (2018). Influence of steel–concrete bond damage on the dynamic stiffness of cracked reinforced concrete beams. *Advances in Structural Engineering*, 21(13), 1977–1989. [CrossRef]

[184] Liang, G., Liu, T., Li, H., Dong, B., & Shi, T. (2022). A novel synthesis of lightweight and high-strength green geopolymer foamed material by rice husk ash and ground-granulated blast-furnace slag. *Resources, Conservation and Recycling*. 176, Article 105922. [CrossRef]

[185] Liang, M., Chang, Z., Wan, Z., Gan, Y., Schlangen, E., & Šavija, B. (2022). Interpretable Ensemble-Machine-Learning models for predicting creep behavior of concrete. *Cement and Concrete Composites*, 125, Article 104295. [CrossRef]

[186] Rovnaník, P. (2010). Effect of curing temperature on the development of hard structure of metakaolin-based geopolymer. *Construction and Building Materials*, 24(7), 1176–1183. [CrossRef]

[187] Yusuf, M. O., Megat Johari, M. A., Ahmad, Z. A., & Maslehuddin, M. (2014). Shrinkage and strength of alkaline activated ground steel slag/ultrafine palm oil fuel ash pastes and mortars. *Materials & Design*, 63, 710–718. [CrossRef]

[188] Seneviratne, C., Gunasekara, C., Law, D. W., Setunge, S., & Robert, D. (2020). Creep, shrinkage and permeation characteristics of geopolymer aggregate concrete: long-term performance. *Archive of Civil and Mechanical Engineering*, 20(4), Article 140. [CrossRef]

[189] Mechtcherine, V., & Hans-Wolf Reinhardt, W. (2012). *Application of super absorbent polymers (SAP) in concrete construction*. Springer. [CrossRef]

[190] Slowik, V., & Ju, J. W. (2011). Discrete modeling of plastic cement paste subjected to drying. *Cement and Concrete Composites*, 33(9), 925–935. [CrossRef]

[191] Gettu, R., Patel, A., Rathi, V., Prakasan, S., Basavaraj, S., & Maity, S. (2019). Influence of supplementary cementitious materials on the sustainability parameters of cements and concretes in the Indian context. *Materials and Structures*, 52(1), Article 10. [CrossRef]

[192] Neupane, K., & Hadigheh, S. A. (2021). Sodium hydroxide-free geopolymer binder for prestressed concrete applications. *Construction and Building Materials*, 293, Article 123397. [CrossRef]

[193] Hardjito, D., & Rangan, B. V. (2005). Development and properties of low-calcium fly ash-based geopolymer concrete. Research Report GC 1 Faculty of Engineering Curtin University of Technology Perth, Australia.

[194] Mehta, A., Siddique, R., Ozbakkaloglu, T., Uddin Ahmed Shaikh, F., & Belarbi, R. (2020). Fly ash and ground granulated blast furnace slag-based alkali-activated concrete: Mechanical, transport and microstructural properties. *Construction and Building Materials*, 257, Article 119548. [CrossRef]

[195] Duxson, P., Provis, J. L., Lukey, G. C., Mallicoat, S. W., Kriv-en, W. M., & Van Deventer, J. S. (2005). Understanding the relationship between geopolymer composition, microstructure and mechanical properties. *Colloids and Surfaces A: Physicochemical and Engineering Aspects*, 269(1-3), 47–58. [CrossRef]

[196] Amin, N., Alam, S., & Gul, S. (2016). Effect of thermally activated clay on corrosion and chloride resistivity of cement mortar. *Journal of Cleaner Production*, 111, 155–160. [CrossRef]

[197] Saloni, P., & Pham, T. M. (2020). Enhanced properties of high-silica rice husk ash-based geopolymer paste by incorporating basalt fibers. *Construction and Building Materials*, 245, Article 118422. [CrossRef]

[198] Saha, A. K. (2018). Effect of class F fly ash on the durability properties of concrete. *Sustainable Environment Research*, 28(1), 25–31. [CrossRef]

[199] Khan, M. S. H., Castel, A., & Noushini A. (2017). The effect of adding fibers on dry shrinkage of geopolymer concrete. *Civil Engineering Journal*, 7(12), 2099–2108. [CrossRef]

[200] Frayyeh, Q. J., & Kamil, M. H. (2021). The effect of adding fibers on dry shrinkage of geopolymer concrete. *Civil Engineering Journal*, 7(12), 2099–2108. [CrossRef]

[201] Banthia, N., & Gupta, R. (2006). Influence of polypropylene fiber geometry on plastic shrinkage cracking in concrete. *Cement and Concrete Research*, 36(7), 1263–1267. [CrossRef]

[202] Kani, E. N., & Allahverdi, A. (2011). Investigating shrinkage changes of natural pozzolan based geopolymer cementpaste. *Iranian Journal of Materials Science and Engineering*, 8(3), 50–60.

[203] Nazari, A., Bagheri, A., Sanjayan, J., Yadav, P. N. J. A., & Tariq, H. (2019). A comparative study of void distribution pattern on the strength development between opc-based and geopolymer concrete. *Advances in Materials Science and Engineering*, 2019, Article 1412757. [CrossRef]

[204] Negahban, E., Bagheri, A., & Sanjayan, J. (2021). Pore gradation effect on Portland cement and geopolymer concretes. *Cement and Concrete Composites*, 122, Article 104141. [CrossRef]

[205] Amin, M., Elsakhawy, Y., Abu El-hassan, K., A., Abdelsalam, B. A. (2021). Behavior evaluation of sustainable high strength geopolymer concrete based on fly ash, metakaolin, and slag. *Case Studies in Construction Materials*, 16, Article e00976. [CrossRef]

[206] Aydın, S., & Baradan, B. (2007). Effect of pumice and fly ash incorporation on high temperature resistance of cement-based mortars. *Cement and Concrete Research*, 37(6), 988–995. [CrossRef]

[207] Lahoti, M., Tan, K. H., Yang, E. H. (2019). A critical review of geopolymer properties for structural fire-resistance applications. *Construction and Building Materials*, 221, 514–526. [CrossRef]

[208] Lin, W., Zhou, F., Luo, W., & You, L. (2021). Recycling the waste dolomite powder with excellent consolidation properties: Sample synthesis, mechanical evaluation, and consolidation mechanism analysis. *Construction and Building Materials*, 290, Article 123198. [CrossRef]

[209] Jeon, D., Yum, W. S., Song, H., Sim, S., & Oh, J. E. (2018). The temperature-dependent action of sugar in the retardation and strength improvement of Ca(OH)2-Na2CO3-activated fly ash systems through calcium complexation. *Construction and Building Materials*, 190, 918–928. [CrossRef]

[210] Rivera, O. G., Long, W. R., Weiss Jr., CA, Moser, R. D., Williams, B. A., Gore, E. R., & Allison, P. G. (2016). Effect of elevated temperature on alkali-activated geopolymeric binders compared to portland cement-based binders. *Cement and Concrete Research*, 90, 43–51. [CrossRef]

[211] Jiang, X., Xiao, R., Ma, Y., Zhang, M., Bai, Y., & Huang, B. (2020). Influence of waste glass powder on the physico-mechanical properties and microstructures of fly ash-based geopolymer paste after exposure to high temperatures. *Construction and Building Materials*, 262, Article 120579. [CrossRef]

[212] Jaya, N. A., Yun-Ming, L., Cheng-Yong, H., Abdullah, M. M. A. B., & Hussin, K. (2020). Correlation between pore structure, compressive strength and thermal conductivity of porous metakaolin geopolymer. *Construction and Building Materials*, 247, Article 118641. [CrossRef]

[213] Cheng-Yong, H., Yun-Ming, L., Abdullah, M. M. A. B., & Hussin, K. (2017). Thermal resistance variations of fly ash geopolymers: foaming responses. *Scientific Report*, 7(1), Article 45355. [CrossRef]

[214] Wang, J., Basheer, P., Nanukuttan, S., & Bai, Y. (2014). Influence of compressive loading on chloride ingress through concrete," Civil Engineering Research Association of Ireland (CERAI) Proceedings August 2014, Queen's University Belfast, UK.

[215] Zhang, H. Y., Kodur, V., Qi, S. L., Cao, L., & Wu, B. (2014). Development of metakaolin–fly ash based geopolymers for fire resistance applications. *Construction and Building Materials*, 55, 38–45. [CrossRef]

[216] Abdulkareem, O. A., Mustafa Al Bakri, A. M., Kamarudin, H., Khairul Nizar, I., & Saif, A. A. (2014). Effects of elevated temperatures on the thermal behavior and mechanical performance of fly ash geopolymer paste, mortar and lightweight concrete. *Construction and Building Materials*, 50, 377–387. [CrossRef]

[217] Chithambaram, S. J., Kumar, S., & Prasad, M. M. (2019). Thermo-mechanical characteristics of geopolymer mortar. *Construction and Building Materials*, 213, 100–108. [CrossRef]